

**Investigation of Intermolecular Interactions of Chiral Molecules
Using Vibrational Circular Dichroism Spectroscopy and
Density Functional Theory Calculations**

by

Angelo Shehan Perera

A thesis submitted in partial fulfillment of the requirements for the degree of

Doctor of Philosophy

Department of Chemistry
University of Alberta

© Angelo Shehan Perera, 2019

Abstract

Vibrational circular dichroism (VCD) spectroscopy is the chiral version of infrared (IR) spectroscopy. The sensitivity of VCD spectroscopy towards absolute configuration and conformational aspects of chiral molecules makes it an effective experimental tool for analyzing chiral solute-chiral solute and chiral solute-solvent intermolecular interactions. In this thesis, both IR and VCD spectroscopic methods have been utilized to characterize the intermolecular interactions between water and some prototype chiral molecules as well as the self-aggregation behavior of chiral molecules in both solution and in low temperature rare gas matrices. Motivated by the need to understand the biologically important water solvation effects in detail in order to model them effectively, I examined the experimental and theoretical data available from our group and other groups and proposed the *clusters-in-a-liquid* solvation model. This model not only recognizes the contributions of both explicit and implicit solvation effects of water, but also the concept of “long-lived” solute-water_n species.

In Chapter 3, I examined the variations of the IR and VCD spectra of methyl glycidate (MG), a prototype chiral molecule with multiple hydrogen-bonding sites, in water and CCl₄. It was demonstrated that by considering experimental VCD features, especially the induced solvent VCD signatures at the water bending region, one can identify the MG-(H₂O)_{1,2} complexes as the *long-lived* species in water. The simulated spectral features of the MG-(H₂O)_{1,2} complexes in bulk water, modelled by the polarizable continuum model (PCM), correctly predict all the IR and VCD spectral features observed.

Furthermore, all the Raman and Raman optical activity (ROA) spectra of MG in water were also predicted correctly with the same model.

In Chapter 5, IR and VCD spectra of methyl- β -D-glucose, a complicated model system with a large number of OH groups, were investigated. The solvation effects of water related to experimental spectra were modelled using the *clusters-in-a-liquid* solvation model. The methyl- β -D-glucose-(H₂O)₈ clusters were identified as the main *long-lived* species in aqueous solution, based on the current and the previous experimental and theoretical investigations.

In Chapter 4, the self-aggregation behavior of lactic acid (LA) was studied in cold rare gas matrices and in solution using both IR and VCD spectroscopic methods, complemented with DFT calculations. The well-resolved matrix-isolation (MI)-IR and VCD spectra of LA obtained at 10 K were interpreted correctly using the simulated spectral features of the LA monomer, whereas the theoretical interpretation of MI-IR and MI-VCD spectra obtained at 16 K and 24 K provides clear insights into the formation of the larger LA aggregates. Comparing the MI-IR and MI-VCD spectra obtained at several temperatures with the corresponding solution spectra of LA obtained in solution allows one to remove the uncertainties in the band assignments of solution spectra, thus providing a good level of understanding about the self-aggregation behavior of LA in solution. The present work showcases the power of MI-VCD spectroscopy in aiding solution spectral assignment and in providing insight into the complex self-aggregation behavior of LA in solution.

Preface

The contents of this thesis are based on the research work that I have undertaken during my graduate study in the period of January 2013 to December 2018 in the Department of Chemistry at the University of Alberta. The contribution made by each author in each research project is summarized below.

Chapter 1 and Chapter 6 are based partially on the published review article: A. S. Perera, J. Thomas, M. R. Poopari, Y. Xu: “The clusters-in-a-liquid approach for solvation: New insights from the conformer specific gas phase spectroscopy and vibrational optical activity spectroscopy”, *Front. Chem.*, **2016**, 4-9, 1-17. DOI: 10.3389/fchem.2016.00009. I wrote the initial review about the solution studies, Dr. J. Thomas wrote the initial review of the gas phase studies, and Dr. M. R. Poopari contributed ideas to and commented on the draft. Professor Y. Xu was the supervisory author and was involved in editing and finalizing the manuscript.

Chapter 3 is based on the published article: “IR, Raman, and Vibrational Optical Activity Spectra of Methyl Glycidate in Chloroform and Water: The Clusters-in-a-liquid Solvation Model”, A. S. Perera, J. Cheramy, C. Merten, J. Thomas, Y. Xu, *Chem. Phys. Chem.*, **2018**, 19, 17, 2234–2242. In this research project, I carried out the IR and VCD experiments of methyl glycidate (MG) in water, the simulations of spectra, and the initial manuscript preparation. J. Cheramy carried out the Raman and ROA experiments of MG in water and helped with the spectral simulations and the manuscript preparation. Dr. C. Merten worked with me on the initial IR and VCD experiments of MG in CCl₄. Dr. J. Thomas did some initial *ab initio* calculations of the MG conformer and the MG-(H₂O)_{1,2}

complexes. This paper was chosen as a VIP paper and was highlighted on ChemistryViews.org. Professor Y. Xu was the supervisory author and was involved in the concept formation, data analysis, and manuscript composition.

The basis for Chapter 4 is from the published material: “Aggregation of lactic acid in cold rare-gas matrices and the link to solution: a matrix isolation-vibrational circular dichroism study”, A. S. Perera, J. Cheramy, M. R. Poopari, Y. Xu, *Phys. Chem. Chem. Phys.*, **2018**, DOI: 10.1039/c8cp04748k. I undertook all the matrix isolation (MI)-IR and VCD experiments of LA, the solution IR and VCD experiments of LA, the simulations of spectra, and the initial preparation of the manuscript. J. Cheramy performed some additional simulations of spectra and helped with the manuscript preparation. Dr. M. R. Poopari was involved in the initial *ab initio* calculations of the LA monomer and the (LA)_{2,3,4} aggregates. Professor Y. Xu was the supervisory author and was involved in the concept formation, data analysis, and manuscript composition.

Chapter 5 is yet to be submitted. I carried out all the aqueous phase IR and VCD measurements, the simulations of spectra, and initial manuscript preparation. Professor Y. Xu was the supervisory author and was involved in the concept formation and manuscript composition.

Acknowledgement

I'm grateful to my supervisor Prof. Yunjie Xu for admitting me into her research group as a graduate student and also for all the assistance and guidance provided during my PhD research studies. I would like to thank to the both current and past Xu and Jager group members for all their support and advice during my research studies. I would like to thank Prof. Wolfgang Jager for his valuable advice and inspiring scientific discussions. I also acknowledge Prof. Gabriel Hanna, Prof. James Harynuk, Prof. Sarah Styler, Prof. Arthur Mar and Prof. Yujun Shi for generously agreeing to be part of my supervisory committee. Also, I would like to thank my lab coordinators, Dr. Norman Gee (10X general chemistry), Dr. Anna Jordan and Dr. M. R. Poopari (37X physical chemistry) for their assistance and advice provided during my time period as a graduate student. I'm grateful for Dr. Anna Jordan for her vital contribution provided during the editing of my thesis. I would like to thank Dr. Christian Merten, Dr. Javix Thomas, Dr. Prasanta Das and Dr. M. R. Poopari for their support and advice provided during the commencement of matrix isolation experiments. I would also like to thank Prof. Todd Lowary and Chun-Jui (Anthony) Chu for providing the synthetic assistance. I appreciate the support provided by the staff of analytical and instrumentation lab, machine shop, electric shop and glass shop during my research studies.

I'm really grateful to my parents for their valuable inspiration and advice in many difficult situations. I would also like to thank my friends in both Sri Lanka and Canada for their encouragement. Also, I'm grateful to Almighty God for being both my strength and guidance in the difficult situations.

Table of contents

Chapter 1 Introduction	1
1.1 Molecular Chirality.....	1
1.2 The Importance of Vibrational Circular Dichroism (VCD) Spectroscopy in the Determination of Absolute Configurations and Dominating Conformations of Chiral Molecules	4
1.3 The Vital Role of VCD Spectroscopy in the Investigation of Intermolecular Interactions of Chiral Molecules in Solution	7
1.4 References	13
Chapter 2 Experimental and Theoretical Methods	16
2.1 Experimental Methods.....	16
2.1.1 Introduction.....	16
2.1.2 VCD Spectroscopy.....	17
2.1.3 Matrix Isolation (MI)-VCD Spectroscopy	24
2.2 Theoretical Aspects	28
2.2.1 Basic Concepts of IR and VCD Spectroscopy.....	28
2.2.2 Theoretical IR and VCD Spectra	31
2.3 References	34
Chapter 3 IR, Raman and Vibrational Optical Activity Spectra of Methyl Glycidate in Chloroform and Water: The <i>Clusters-in-a-Liquid</i> Solvation Model.....	38
3.1 Introduction.....	38
3.2 Experimental Section	40
3.2.1 Experimental Details	40
3.2.2 Computational Details.....	41
3.3 Results and Discussion.....	42
3.3.1 Experimental IR and VCD Spectra of MG in CCl ₄ and H ₂ O	42
3.3.2 Implicit Solvation.....	43
3.3.3 The <i>Clusters-in-a-Liquid</i> Solvation Model for IR and VCD of MG in Water	48
3.4 Conclusions.....	59
3.5 Acknowledgements	60
3.6 References	60
Chapter 4 Aggregation of Lactic Acid in Cold Rare-Gas Matrices and the Link to Solution: a Matrix Isolation-Vibrational Circular Dichroism Study	64
4.1 Introduction	64
4.2 Experimental Section.....	66

4.2.1 Experimental Details.....	66
4.2.2 Computational Details.....	68
4.3 Results and Discussion.....	68
4.3.1 Experimental MI-IR and MI-VCD Spectra	68
4.3.2 Energetics and Geometries of the LA Monomer and (LA) _n n = 2, 3, 4 Aggregates.....	71
4.3.3 Assignment of the MI-IR and MI-VCD Spectra at 10 K.....	77
4.3.4 Assignments of the 16 K and 24 K MI-IR and MI-VCD Spectra and the Self- aggregation of LA in an Ar Matrix.....	80
4.3.5 Re-examination of Self-aggregation of LA in CDCl ₃	84
4.4 Conclusions	87
4.5 Acknowledgements	88
4.6 References.....	88
Chapter 5 IR and Vibrational Circular Dichroism Spectra of Methyl-β-D- glucopyranose in Water: The Application of the <i>Clusters-in-a-Liquid</i> Solvation Model	92
5.1 Introduction.....	92
5.2 Experimental Section	93
5.2.1 Experimental Details.....	93
5.2.2 Computational Details.....	94
5.3 Results and Discussion.....	95
5.3.1 Implicit Solvation.....	95
5.3.2 The Clusters-in-a-Liquid Solvation Model in the Simulation of IR and VCD Spectra of Methyl-β-D-glucopyranose in Water.....	101
5.4 Conclusions	108
5.5 Acknowledgement.....	109
5.6 References.....	109
Chapter 6 Conclusions and Future Work.....	113
6.1 Conclusions	113
6.2 Future Work	117
6.3 References.....	118
Bibliography.....	120
Appendix A.....	128
Appendix B.....	135

List of Tables (Chapters)

Table	Page
Table 3.1. The relative free energies, ΔG (in kJ mol^{-1}), and Boltzmann factors (Pop) at 298 K (in %), of the two main MG conformers under three environments.....	44
Table 4.1. Comparison of the relative free energies (ΔG in kJ mol^{-1}) and Boltzmann factors (Bf in %) at 298 K of the LA monomer conformers computed at the B3LYP/6-311++G(2d,p), B3LYP-D3BJ/6-311++G(2d,p) and the B3LYP-D3BJ/def2-TZVPD levels of theory.....	72
Table 4.2. Comparison of the relative free energies (ΔG in kJ mol^{-1}) and Boltzmann factors (Bf in %) at 298 K ^a of the LA dimer conformers computed at the B3LYP/6-311++G(2d,p), B3LYP-D3BJ/6-311++G(2d,p) and the B3LYP-D3BJ/def2-TZVPD levels of theory.....	73
Table 4.3. Comparison of the relative free energies (ΔG in kJ mol^{-1}) and Boltzmann factors (Bf in %) at 298 K ^a of the LA trimers and tetramers computed at the B3LYP/6-311++G(2d,p), B3LYP-D3BJ/6-311++G(2d,p) and the B3LYP-D3BJ/def2-TZVPD levels of theory. ^b	76
Table 5.1. The relative free energies, ΔG , (in kJ mol^{-1}) and the Boltzmann factors at 298 K (in %) of the conformer of me- β -D-gluc with the PCM of water.....	98

List of Tables (Appendices)

Table	Page
Table A1. General assignment of the IR and VCD bands of MG-I and MG-II in the PCM of CCl ₄	132
Table B1. Comparison of the relative energies (ΔE in kJ mol ⁻¹) and Boltzmann factor (Bf in %) at 298 K of the LA monomer conformers computed at the B3LYP/6-311++G(2d,p) and B3LYP-D3BJ/6-311++G(2d,p) and the B3LYP-D3BJ/def2-TZVPD levels of theory.	137
Table B2. Comparison of the relative energies (ΔE in kJ mol ⁻¹) and Boltzmann factor (Bf in %) at 298 K ¹ of the LA dimer conformers computed at the B3LYP/6-311++G(2d,p) and B3LYP-D3BJ/6-311++G(2d,p) and the B3LYP-D3BJ/def2-TZVPD levels of theory.....	138
Table B3. Comparison of the relative free energies (ΔE in kJ mol ⁻¹) and Boltzmann factor (Bf in %) at 298 K ¹ of the LA trimers and tetramers computed at the B3LYP/6-311++G(2d,p) and B3LYP-D3BJ/6-311++G(2d,p) and the B3LYP-D3BJ/def2-TZVPD levels of theory. ²	139
Table B4. The α^1 values of the C=O stretching modes of the most stable conformers of each LA species calculated.	140

List of Figures (Chapters)

Figure	Page
Figure 1.1. Different forms of molecular chirality: a) point chirality, b) axial chirality, and c) helical chirality.	2
Figure 1.2. The R and S absolute configuration assignments a) at a stereogenic center and b) about a chiral axis. The numbers 1, 2, 3, 4 reflect the priority order of substituents at a stereogenic center or about a chiral axis.	3
Figure 2.1. The schematic diagram of the FTIR-VCD instrumentation.	18
Figure 2.2. The schematic diagram of Michelson interferometer.	19
Figure 2.3. The components of the photoelastic modulator (PEM).	21
Figure 2.4. The modulation cycle of the photoelastic modulator (PEM); the figure is obtained directly from reference [6].	22
Figure 2.5. The schematic diagram of the MI experimental setup.	26
Figure 3.1. Comparisons of the experimental IR (left) and VCD (right) spectra of MG in water (top) and in CCl ₄ (bottom). In addition, VCD spectra (dashed lines) of S-MG are presented.	43
Figure 3.2. The optimized geometries of the two most stable conformers of MG in the gas phase.	44
Figure 3.3. Comparison of the experimental IR (bottom-left) and VCD (bottom-right) spectra of MG in CCl ₄ with the corresponding simulated IR (a) and VCD (b) spectra of the MG-I and MG-II conformers in the PCM of CCl ₄ , the population weighted IR (c) and VCD (d) spectra based on their relative free energies, and the fitted IR (e) and VCD (f) spectra with $C_{MG-I}=0.62$ and $C_{MG-II}=0.38$. Please see text for details.	46
Figure 3.4. The optimized geometries of the MG-H ₂ O complexes with the PCM of water. The relative free energy (in kJ mol ⁻¹) and the Boltzmann factor at room temperature for	

each MG-H₂O complex are given in parenthesis. The intermolecular H-bond lengths (in Å) are indicated with dashed lines. The relative stabilities within the MG-I-H₂O and MG-II-H₂O series are indicated with an Arabic number, with 1 being the most stable in each case.

.....51

Figure 3.5. Comparisons of the experimental IR (a) and VCD (b) spectra of MG in water with the simulated IR (g) and VCD (h) conformer spectra of MG-H₂O in the PCM of water, the population weighted IR (e), VCD (f) spectra based on the calculated relative free energy of each MG-H₂O complex, and the fitted IR (c), VCD (d) spectra. Please see text for details regarding the fitting procedure and the contribution of each dominant species. 52

Figure 3.6. The optimized geometries of the most stable conformers of MG-2H₂O in the PCM of water. The relative free energy (in kJ mol⁻¹) and the Boltzmann abundance (%) at room temperature for each conformer are given in parentheses. The intermolecular H-bond lengths (in Å) between water and MG are indicated with dashed lines. The relative stabilities within the MG-I-H₂O and MG-II-H₂O series are indicated with an Arabic number, with 1 being the most stable in each case.55

Figure 3.7. Comparisons of the experimental IR (a) and VCD (b) spectra (bottom) of MG in water with the related theoretical IR (g) and VCD (h) spectra of the MG-2H₂O conformers, the population weighted IR (e), VCD (f) spectra of MG-2H₂O, and the final fitted (fitted with “all”) IR (c), VCD (d) spectra containing both MG-H₂O and MG-2H₂O conformers. Please see the main text for details.57

Figure 3.8. Comparison of the experimental Raman (bottom-left) and ROA (bottom-right) spectra of S-MG in water with the calculated population weighted Raman (left) and ROA (right) spectra of the MG monomer (a), MG-H₂O (b), and MG-2H₂O (c) in the PCM of water. Also included are the “fitted” Raman (left) and ROA (right) spectra using just the conformers of MG-H₂O (d) and “all” (e). Please see text for details.59

Figure 4.1. Comparison of the experimental MI-IR and MI-VCD spectra of LA obtained at 10 K, 16 K, and 24 K. The dashed lines indicate the contribution from the LA monomer, while the dashed-dotted lines indicate the contribution from LA aggregates, such as the LA dimer, trimer, and tetramer. Please see text for discussion. The broad feature indicated with * is an artifact due to some minor baseline variation in the MI measurements. 70

Figure 4.2. The optimized geometries of the four most stable conformers of the LA monomer in the gas phase are shown in the first row, where the name “M” stands for monomer. The names in the brackets are the corresponding names used in Ref. 25. The optimized geometries of the most stable dimer (D) and the representative trimer (T) and

tetramer (Te) conformers of LA in the gas phase are given in the subsequent rows. The intra- and intermolecular H-bond lengths (in Å) are indicated with dashed lines for each structure, as well as the OH...O H-bond angles (θ s).....74

Figure 4.3. Comparisons of the experimental MI-IR (a) and MI-VCD (b) spectra of LA obtained at 10 K with the simulated IR (c) and VCD (d) spectra of the monomeric LA conformers in the gas phase and also with the related population weighted spectra. The dashed lines connect the corresponding experimental IR and VCD features with the simulated ones. * indicates the contributions from the larger LA aggregates. See the main text for discussion.79

Figure 4.4. Comparisons of the experimental MI-IR and MI-VCD spectra of LA obtained at 10 K, 16 K, and 24 K with the simulated IR and VCD spectra of the monomeric (M), binary (D), ternary (T), and quaternary (Te) LA species in the gas phase. The band assignment made for the 10 K spectra in Figure 4.3 is used as the basis to recognize the new features at 16 K and 24 K. The largest contribution to the 16 K spectra is from the LA dimer, identified with bands labelled with a', b', etc. The additional contribution to the 24 K spectra from the LA trimer, LA tetramer are identified with bands labelled with a'', b'', and so on. The empirically population weighted spectra at 16 K (a) and 24 K (b) also are presented. () indicates that an assignment is only tentative. Please see the main text for the detailed discussions.....83

Figure 4.5. Top: comparisons of the solution IR and VCD spectra of LA in CDCl₃ recorded at 0.1 M and 0.2 M with the MI-IR and MI-VCD spectra of LA obtained at 24 K. The 0.1 M trace also is rescaled and superimposed on the 0.2 M trace for easy comparison. Bottom: the population weighted IR and VCD spectra of the LA monomer (M-PCM), dimer (D-PCM), trimer (T-PCM), and tetramer (Te-PCM) in CDCl₃ at 298 K. The peak assignments are indicated by the dashed lines.....87

Figure 5.1. Methyl- β -D-glucopyranose is depicted in the ⁴C₁ chair conformation. The two small arrows indicate the rotation about the C5—C6 and C6—O6 bonds corresponding to the O5—C5—C6—O6 and C5—C6—O6—H dihedral angles, respectively. The large arrow indicates the direction of the cooperative H-bonds.96

Figure 5.2. The stable conformers of me- β -D-gluc obtained at the B3LYP/6-311++G(2d,p) level of theory with the PCM of water. Please refer to the main text for the definition of the letter symbols.97

Figure 5.3. Comparisons of experimental IR and VCD spectra of methyl- β -D-glucopyranose in water with the population weighed VA(IR) (a) and VCD (b) spectra of the me- β -D-gluc monomer in the PCM of water and also with the simulated VA(IR) (c) and VCD (d) spectra of stable conformers of me- β -D-gluc in the PCM of water. The dashed lines indicate the corresponding experimental and theoretical features. The gray traces behind the experimental data are the population weighted IR and VCD spectra, which are shifted slightly by the same amount to guide the comparison. 100

Figure 5.4. Optimized geometries of the 20 most stable me- β -D-gluc-(H₂O)₈ complexes containing a) G-g+ and b) G+g- me- β -D-gluc conformers in the PCM of water. The relative free energies (in kJ mol⁻¹) and Boltzmann factors of each cluster at room temperature also are listed. The Arabic numbers indicate the relative stability of the hydration clusters containing a particular me- β -D-gluc conformer, with 1 being the most stable one. 104

Figure 5.5. The strong cooperative H-bonding chains are indicated with the arrowed lines in the a) most stable cG-g+-8W-1 and the b) second most stable ccG+g+-8W-1 octahydrate complexes. 105

Figure 5.6. The simulated IR (a) and VCD (b) spectra of the me- β -D-gluc-(H₂O)₈ complexes are shown in the top section, while the comparisons of the Boltzmann weighted IR (c) and VCD (d) spectra with the experimental data are provided at the bottom section. 107

List of Figures (Appendices)

Figure	Page
Figure A1. The raw, experimental VCD spectra of R-MG and S-MG a) in water, recorded with a concentration of 6 M and a pathlength of 3 μm and b) in CCl_4 , recorded with a concentration of 0.16 M and a pathlength of 25 μm	129
Figure A2. Comparisons of the experimental IR and VCD spectra of MG in CCl_4 with the simulated IR and VCD features of MG-I and MG-II in the gas phase and the corresponding population weighted IR and VCD spectra. The population weighted IR and VCD spectra of MG with the PCM of CCl_4 are also included for comparison.	130
Figure A3. Comparisons of the experimental IR (left) and VCD (right) spectra of MG in water with the simulated IR and VCD spectra of MG-I and MG-II in the PCM of water and the corresponding population weighted IR and VCD spectra.	131
Figure A4. The electrostatic potential distribution diagrams of a) MG-I and b) MG-II...	132
Figure A5. The simulated Raman and ROA spectra of MG-I, MG-II, MG-I- H_2O and MG-II- H_2O complexes in the PCM of water.	134
Figure A6. The simulated Raman and ROA spectra of MG-I-2 H_2O and MG-II-2 H_2O complexes in the PCM of water.	135
Figure B1. The raw, experimental VCD spectra of D-LA and L-LA in the cold Ar matrices at 10 K, 16 K and 24 K and in a 0.2 M solution in CDCl_3	136
Figure B2. Geometries of the additional conformers of the LA trimer and tetramer in the gas phase. The relative free energy values in kJ mol^{-1} at the B3LYP-D3BJ/def2-TZVPD level of theory are indicated in brackets.	141
Figure B3. Predicted IR and VCD spectra of the four most stable conformers of the LA monomer in the gas phase at the B3LYP/6-311++G(2d,p) and B3LYP-D3BJ/6-311++G(2d,p) and the B3LYP-D3BJ/def2-TZVPD levels of theory from top to bottom.	142

Figure B4. Predicted IR and VCD spectra of the six most stable conformers of the LA dimer in the gas phase at the B3LYP/6-311++G(2d,p) and B3LYP-D3BJ/6-311++G(2d,p) and the B3LYP-D3BJ/def2-TZVPD levels of theory from top to bottom.	143
Figure B5. Predicted IR and VCD spectra of the five stable conformers of the LA trimer in the gas phase at the B3LYP/6-311++G(2d,p) and B3LYP-D3BJ/6-311++G(2d,p) and the B3LYP-D3BJ/def2-TZVPD levels of theory from top to bottom.	144
Figure B6. Predicted IR and VCD spectra of the five stable conformers of the LA tetramer in the gas phase at the B3LYP/6-311++G(2d,p) and B3LYP-D3BJ/6-311++G(2d,p) and the B3LYP-D3BJ/def2-TZVPD levels of theory from top to bottom.	145
Figure B7. Optimized geometries of T3 in the gas phase obtained with and without the dispersion correction (D3BJ) with the basis set 6-311++G(2d,p). The optimized geometry obtained at the B3LYP-D3BJ/def2-TZVPD level is very similar to that at the B3LYP-D3BJ/6311++G(2d,p) and the dipole moment is 1.4 D.....	146
Figure B8. Predicted IR and VCD spectra of the four most stable conformers of the LA monomer in the PCM of CDCl ₃ at the B3LYP-D3BJ/def2-TZVPD level of theory.....	147
Figure B9. Predicted IR and VCD spectra of the six most stable conformers of the LA dimer in the PCM of CDCl ₃ at the B3LYP-D3BJ/def2-TZVPD level of theory.....	148
Figure B10. Predicted IR and VCD spectra of the seven (LA) ₃ conformers in the PCM of CDCl ₃ at the B3LYP-D3BJ/def2-TZVPD level of theory. The Boltzmann factors for T1-T7 (in %) at 298 K are: 60.9, 28.9, 0.2, 0.2, 0.0, 3.4, and 6.4.	149
Figure B11. Predicted IR and VCD spectra of the five (LA) ₄ conformers in the PCM of CDCl ₃ at the B3LYP-D3BJ/def2-TZVPD level of theory. The Boltzmann factors for Te1-Te5 (in %) at 298 K are: 76.9, 5.1, 17.9, 0.1, and 0.0.....	150
Figure B12. Comparison of the experimental IR and VCD spectra at 24 K, in 0.1 M and in 0.2M solution with the empirically population weighted IR and VCD spectra of the LA monomer, dimer, trimer and tetramer calculated at the B3LYP-D3BJ/def2-TZVPD level of theory. The population weighted spectra contain 20% LA dimer, 30% LA trimer and 50 % LA tetramer.	151

Chapter 1

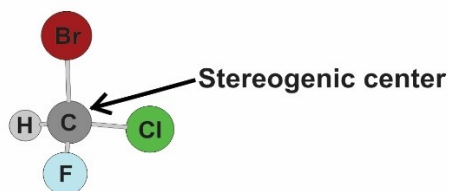
Introduction

1.1 Molecular Chirality

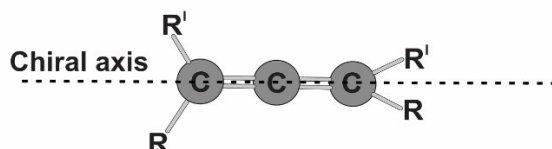
It is important to reiterate some basic aspects of chirality as part of the introduction, since the central theme of this thesis is based on chirality. If a molecule consists of a mirror image that cannot/can be superimposed on itself, then that molecule is designated as a/an chiral/achiral molecule. In the language of molecular symmetry group theory, a molecule is chiral only if it does not contain an improper rotation axis (S_n). The S_n improper rotation axis is identified as a combination of the rotation with respect to an axis, accompanied by the reflection via a plane perpendicular to the axis of rotation. The chiral molecule and its mirror image, which are called enantiomers, have the same atomic connectivity but different spatial orientations of atoms. There are several forms of molecular chirality: point chirality, axial chirality, and helical chirality. A chiral molecule may possess a stereogenic center, an axis of chirality, or a helix.^[1]

A stereogenic center is created when a C atom binds to four different substituents. A stereogenic center also can be generated with respect to a N (or P) atom when it attaches itself to three different substituents. For example, in the situation of the N center, the lone pair on the N atom can be considered as the fourth substituent. In terms of axial chirality, the chirality is generated with respect to an axis in the molecule about which a set of four substituents are arranged so that the pair of mirror images cannot be superimposed. The main reason for the axial chirality comes from the nonplanar arrangement of the substituents about the chiral axis causing the rotation around the chiral axis to be hindered due to the steric effects of the substituents. In helical chirality, the spiral arrangement of bonds is responsible for the generation of two non-superimposable mirror images.

a) Point Chirality



b) Axial Chirality



c) Helical Chirality

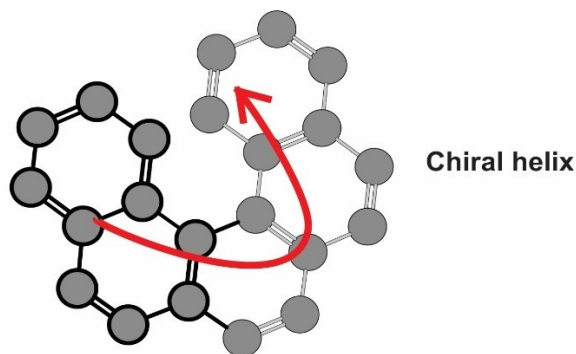


Figure 1.1. Different forms of molecular chirality: a) point chirality, b) axial chirality, and c) helical chirality.

The absolute configuration of a chiral molecule defines its spatial orientation of bonds with respect to its stereogenic centers, chiral axis, or chiral helix. The absolute configurations at stereogenic centers are labelled as R (rectus) or S (sinister) according to the Cahn-Ingold-Prelog naming rules.^[2] In the Cahn-Ingold-Prelog nomenclature, the priorities of four substituents attached to the stereogenic center are decided based on the increasing order of atomic masses of substituents that are bonded directly to the center. By placing the substituent which binds to the center through the lowest atomic mass away from the viewer, the absolute configuration of the center is assigned as R if the atomic mass priority order of the three remaining substituents at the center follows in the clockwise direction. The counterclockwise atomic mass variation of substituents at the

center corresponds to the S absolute configuration. An example is provided in Figure 1.1 (a). The absolute configurations of chiral amino acids and carbohydrates are sometimes labelled using the D and L nomenclature, where the absolute configuration is assigned based on the comparison of the Fischer projection of carbohydrate or amino acid with respect to the Fischer projection of glyceraldehyde. Sometimes, additional labelling is used based on the optical rotation character. For example, an enantiomer that rotates the plane of linearly polarized light in the clockwise direction is labelled as dextrorotatory (d or (+)), whereas the enantiomer that rotates the plane of linearly polarized light in the counterclockwise direction is labelled as levorotatory (l or (-)).^[3]

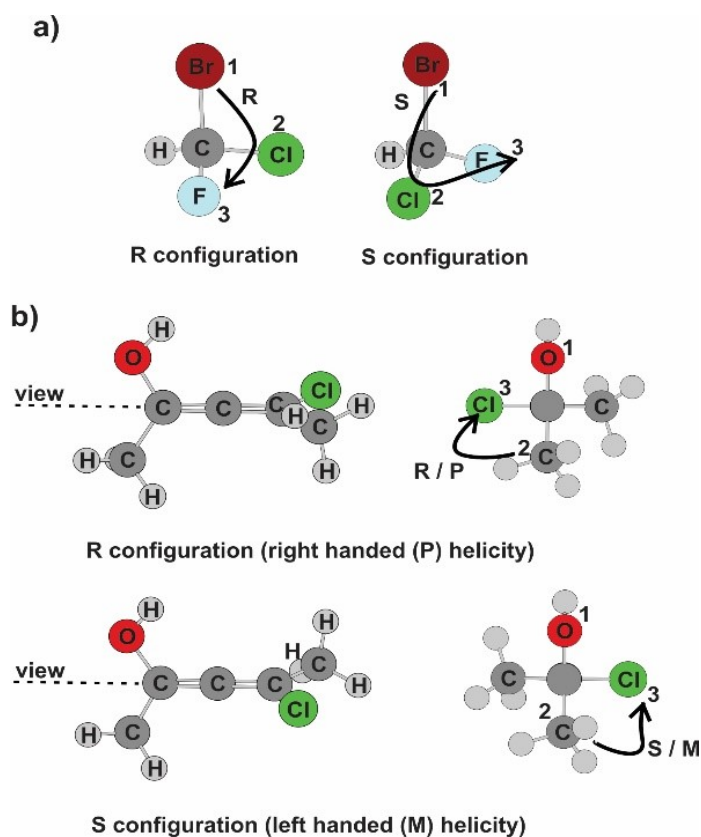


Figure 1.2. The R and S absolute configuration assignments a) at the stereogenic center of (Br)HCF(Cl) and b) about the chiral axis of (CH₃)(HO)C=C=C(Cl)(CH₃). The numbers 1, 2, 3, 4 reflect the priority order of substituents at a stereogenic center or about a chiral axis.

In axial chirality, the absolute configuration about the chiral axis can be defined using the same Cahn-Ingold-Prelog nomenclature system.^[2] If the priority order of atomic masses from the nearest group to the farthest group varies in the clockwise manner, the

absolute configuration about the chiral axis is defined as an R axial absolute configuration (See Figure 1.2 (b)) or P helicity (right-handed helicity). On the other hand, if the priority order of atomic masses from the nearest group to the farthest group changes in the counterclockwise manner, the absolute configuration about the chiral axis is defined as an S axial absolute configuration or M helicity (left-handed helicity). In helical chirality, the absolute configurations of clockwise and counterclockwise spatial orientations of spiral structures are defined based on the P and M helicity notations, respectively.

1.2 The Importance of Vibrational Circular Dichroism (VCD) Spectroscopy in the Determination of Absolute Configurations and Dominating Conformations of Chiral Molecules

Most of the biological molecules that perform vital roles in living systems are chiral, and their three-dimensional structures play a key role in their biological functions. Therefore, a good level of understanding about both absolute configurations and dominating conformations of biologically significant molecules are required for the associated development of new drugs. Several spectroscopic methods have been implemented to investigate the absolute configurations of biologically important molecules, but each has its own concerns. In the application of X-ray crystallography, the absolute configuration of the molecule of interest can be identified only with the formation of a well-defined single crystal.^[4] In the case of NMR spectroscopy, the determination of the absolute configuration requires a chiral derivatizing agent for the chiral molecule of interest.^[5] On the other hand, electronic circular dichroism (ECD) spectroscopy, which measures the differential absorption of left circularly polarized light with respect to the right circularly polarized light for an electronic transition,^[6] is suitable only for chiral molecules with chromophores. The fairly broad bandwidth of ECD spectral features makes it difficult at times to interpret the experimental data based on theoretical simulations.^[7] Furthermore, the simulation of ECD spectral features requires knowledge of excited states, which is difficult to obtain.

VCD spectroscopy measures the differential absorption of left-circularly polarized light with respect to right-circularly polarized light for a vibrational transition. A chiral molecule with N number of atoms has $3N-6$ fundamental vibrational modes, and its VCD spectral features may contain information from all $3N-6$ vibrational modes. Often, many well-resolved VCD bands can be detected which contain stereochemical details of a chiral molecule. Also, unlike X-ray crystallography, the experimental VCD spectrum of a chiral molecule can be obtained directly in solution. Most importantly, being an optical spectroscopic method, VCD spectroscopy reveals sensitivity towards the conformational variations of a chiral molecule, which in turn allows the experimental VCD spectrum of a chiral molecule to register VCD features corresponding to individual conformers of a chiral molecule. Furthermore, unlike ECD calculations, which require knowledge of the excited electronic states, VCD simulations only require one to deal with the ground electronic state *ab initio* computations, which therefore provides reliability in the prediction of corresponding experimental spectra. One major shortcoming of VCD spectroscopy is that the anisotropic ratios, i.e., the intensity ratio between the VCD and IR spectral features are typically in the range of 10^{-4} – 10^{-6} , much smaller than those (10^{-2} – 10^{-3}) of ECD. Therefore, a reasonably long VCD measurement time often is necessary to accomplish a good signal-to-noise ratio level.

The recent instrumental and theoretical advancements of VCD spectroscopy have addressed some of the challenges successfully and have increased its applications on the world stage drastically.^[8, 9, 10] Today, VCD spectrometers are manufactured by many companies, such as BioTools, Bruker Optics, Jasco, and Thermo Electron. To extract the structural information, including absolute configuration and the dominating conformation of a chiral molecule in solution, it is necessary to have high-quality theoretical calculations of VCD spectral features for comparison with the experimental ones. The computational software packages, such as Gaussian,^[11, 12] Amsterdam DF (ADF),^[13] and Dalton, all provide codes for IR and VCD simulations by density functional theory (DFT). The important experimental aspects of VCD spectroscopy and the relevant details regarding the DFT calculations of IR and VCD spectra are discussed in more detail in Chapter 2.

Another vibrational optical activity technique used in this thesis is Raman optical activity (ROA). Unlike VCD, ROA measures chiral responses of Raman scattering, which include four major forms: incident circularly polarized (ICP)-ROA; scattered circularly polarized (SCP)-ROA; in-phase dual CP or DCP_I-ROA; and out-of-phase CP or DCP_{II}-ROA.^[14] These can be expressed, respectively, as follows:

$$\text{VCD } \Delta A(\bar{\nu}) = A_L(\bar{\nu}) - A_R(\bar{\nu}) \quad (1.1)$$

In the above equation of VCD, A_L is the absorption of left circularly polarized light and A_R is the absorption of right circularly polarized light, where $\bar{\nu}$ corresponds to the wavenumber (cm^{-1}), and:

$$\text{ICP - ROA (Incident CP) } \Delta I_\alpha(\bar{\nu}) = I_\alpha^R(\bar{\nu}) - I_\alpha^L(\bar{\nu}) \quad (1.2)$$

$$\text{SCP - ROA (Scattered CP) } \Delta I^\alpha(\bar{\nu}) = I_R^\alpha(\bar{\nu}) - I_L^\alpha(\bar{\nu}) \quad (1.3)$$

$$\text{DCP}_I \text{ - ROA (In-Phase Dual CP) } \Delta I_I(\bar{\nu}) = I_R^R(\bar{\nu}) - I_L^L(\bar{\nu}) \quad (1.4)$$

$$\text{DCP}_{II} \text{ - ROA (Out-of-Phase DCP) } \Delta I_{II}(\bar{\nu}) = I_L^R(\bar{\nu}) - I_R^L(\bar{\nu}) \quad (1.5)$$

In the above equations of ROA, the I term corresponds to the scattered Raman intensity, where the superscript and subscript notifications depict the polarization states of incident and scattered light, respectively. The R , L and α terms used as superscript or subscript notifications corresponds to the right, left, and arbitrary polarization states of incident or scattered light, respectively.

In ICP-ROA, the right- and left-circularly polarized light are used as the incident light to excite the chiral sample and the intensity difference of the resulting Raman scattered light is measured at an arbitrary polarization direction. In SCP-ROA, the randomly polarized light is used as the incident light to excite the chiral sample and the difference in the Raman scattered intensity of the right- versus left-circularly polarized light is monitored. This is the most commonly reported scheme, and all commercial SCP-ROA instruments use the back-scattering geometry. The remaining DCP-ROA forms are

the combinations of both ICP-ROA and SCP-ROA forms. In DCP_I-ROA and DCP_{II}-ROA measurements, the right- and left-circularly polarized light are used as the incident radiation. In DCP_I-ROA, the differential Raman scattered intensity of right- versus left-circularly polarized light is measured, whereas in DCP_{II}-ROA, the differential Raman scattered intensity of left- versus right-circularly polarized light is detected. The anisotropic ratio between Raman and ROA intensities is 10^{-2} – 10^{-4} . The weak nature of Raman intensities makes the ROA intensities even weaker, and as a result, the ROA instrument development was slower than that of VCD, although much has happened in recent years. The recent improvements in both instrumental and theoretical aspects of ROA have transformed it into a useful spectroscopic method in the investigation of stereochemical aspects of chiral molecules in solution, especially in the aqueous medium.^[15] One of the main challenges encountered in the investigation of stereochemical properties of chiral molecules in solution by vibrational optical activity spectroscopic methods is the simulation of solvation effects on the solution VCD and ROA spectral features. Such effects can be quite drastic when solvent molecules form hydrogen (H)-bonding interactions with the chiral solute. In such cases, for example in water, the interpretation of solution VCD and ROA spectral features may become a very difficult task.

1.3 The Vital Role of VCD Spectroscopy in the Investigation of Intermolecular Interactions of Chiral Molecules in Solution

The following text includes some paragraphs which are published in the paper titled “The Clusters-in-a-Liquid Approach for Solvation: New Insights from the Conformer Specific Gas Phase Spectroscopy and Vibrational Optical Activity Spectroscopy”, A. S. Perera, J. Thomas, M. R. Poopari, Y. Xu, Front. Chem., 2016, 4, 1–17. These are indicated with quotation marks.

Most biologically important reactions involve chiral reactants and occur in an aqueous medium, therefore, the interactions formed between chiral biomolecules and water play a vital role in life sciences “It has been recognized for some time that water is not a simple

bystander but rather an active participant in these biological events. For example, water is not only required to maintain enzymes in their natural conformation to deliver their full functionality, but it can also participate directly in enzymatically catalyzed reactions. [16] Increasingly, researchers are pushing for a detailed and accurate description of solute-water interactions at the molecular level, even in much more complex biological systems.”[17]

The high sensitivity of VCD spectroscopy to the structure of a chiral molecule and especially to the structural changes induced by its non-covalent interactions with the solvent and other chiral solute molecules has made it a vital experimental tool in revealing explicit non-covalent interactions, such as hydrogen bonding and halogen bonding, and also implicit solvation effects.[18,19,20] Dezhahang et al. have investigated the conformational aspects of chiral binaphthyl diphosphine ligands and their complexes with palladium in CDCl_3 using IR and VCD spectroscopic methods.[18] In the interpretation of solution spectra of the above study, the simulated spectral features of conformers above chiral ligands and their complexes with palladium in the gas phase could not account for all the solution spectral features. However, the introduction of the implicit polarizable continuum model (PCM)[21] creates a good correlation between the experimental and simulated spectra. The correct interpretation of solution VCD spectra achieved via the PCM model reveals the sensitivity of VCD spectroscopy towards implicit solvation effects. Merten et al. have investigated the interactions of a chiral amine-borane system in solution using IR and VCD spectroscopy.[19] During the interpretation of solution VCD spectra, they have recognized the specificity of VCD spectral features according to different dihydrogen bonding topologies of the amine-borane dimer. The above evidence illustrates the sensitivity of VCD spectroscopy towards different explicit H-bonding interactions.

The interpretation of VCD spectra obtained in water, on the other hand, is usually much more complicated due to a number of factors. The first concern is that water can act both as a strong H-bond donor and acceptor at the same time. This character allows water to form extensive H-bonding networks among themselves. When modelling a chiral solute in water, it is challenging to know how many explicit water molecules are needed for the modelling of the experimental VCD features. Secondly, the dynamic nature of water

H-bonded clusters generates questions about the lifetime of H-bonding networks and how to account for such dynamics in the simulation. Thirdly, the conformational flexibility of the interested chiral solute may be influenced strongly by the surrounding water, making the theoretical modelling even more challenging.

“For more than two decades, spectroscopists working in the field of cluster science have been using the bottom-up approach to probe solute-water hydrogen (H)-bonding interactions in great detail. The general idea is that by adding water molecules one at a time, one may gain significant insight into the first few steps of solvation and ultimately “bridge” the gap between the behavior of an isolated solute to that in aqueous solution. For example, Wester and co-workers demonstrated that interaction with just one water molecule is enough to affect the outcome of the nucleophilic substitution reaction of $\text{CH}_3\text{I} + \text{OH}^-$,^[22] highlighting the significance of such explicit H-bonding interaction. Spectroscopists have used isomer and sometimes even conformer-specific spectroscopic techniques to provide direct, bond-specific information about local solute-water interactions in the gas phase. For example, using the conformer-selective double resonance laser spectroscopy such as IR–UV ion dip and UV–IR and UV–UV hole burning methods, Simons and co-workers found that while gas phase monosaccharides may prefer somewhat different conformations, interaction with just a single water molecule was enough to lock all of them into the same type of conformation.^[23] As highlighted by Cocinero and Çarçabal in their recent review, the first bound water molecule plays the role of a “conformational lock” in these cases by replacing the weakest intramolecular H-bond interaction with two strong intermolecular H-bonds and strengthening the H-bond cooperativity effects.^[24] Pate and co-workers reported a rotational spectroscopic study of sequential solvation of β -propiolactone with one to five water molecules using a chirped pulse Fourier transform microwave (CP-FTMW) spectrometer and revealed the associated micro solvation structures of water surrounding the simple organic molecule.”^[25]

Although the solute-water complexes identified in the above sequential solvation studies in the gas phase provide some insights about the explicit solvation effects, their existence in aqueous solution is unclear. “In 1996, for the first time, Jalkanen et al.

attempted to include the explicit H-bonding interaction between water molecules and N-acetyl-L-alanine N'-methylamide (L-AANMA) in their interpretation of the observed VCD spectrum.^[26] They optimized geometries of eight low-energy conformers of L-AANMA in the gas phase and solvated one conformer with four additional water molecules and calculated their IR and VCD spectra. The authors commented that adding water molecules has a significant effect on the appearance of VCD spectrum. Only a few VCD studies concerning water-solvent effects had been reported before 2007.^[27] Since 2007, Xu and co-workers have reported a series of VCD studies of prototype chiral molecules such as propylene oxide (PO),^[28] methyl lactate (ML),^[29] lactic acid,^[30] and glycidol^[31] in water.” Interestingly these VCD investigations conducted in water have identified VCD spectral features for the water bending vibrations.

The achiral water bending vibrations cannot give rise to any VCD intensities on their own since water is an achiral molecule. Therefore, it is logical to hypothesize that when water forms H-bonding interactions with the chiral solute, the H-bonded water molecules of the chiral solute-water complexes could gain VCD intensities because they are part of the new chiral entities. On the other hand, if the arrangement of water molecules surrounding a chiral solute fluctuates very rapidly and/or changes to many possible orientations, the probability to observe such induced solvent VCD features of water is very low, since the VCD features generated by chiral solute-water complexes with a wide range of H-bonding topologies, are expected to give rise to a very broad line width and the resulting VCD features with opposite signs tend to cancel each other out, leading to zero intensity. Therefore, the observation of the induced solvent VCD features of water in the aforementioned VCD investigations have provided strong evidence for the existence of *long-lived* chiral solute-water clusters in aqueous solution.^[28, 29, 30, 31] The above findings of aqueous phase VCD investigations have provided the basis for the emergence of the *clusters-in-a-liquid* solvation model.^[32] The main idea of the *clusters-in-a-liquid* solvation model is that the experimental vibrational optical activity (VCD and/or ROA) features obtained in water are generated not by the chiral solute itself but by the *long-lived* chiral solute-water complexes. Since the *clusters-in-a-liquid* solvation model accounts for the explicit solvation effects by means of the *long-lived* chiral solute-(water)_n complexes, the

investigation of the solute-water clusters in sequential solvation studies of chiral molecules in the gas phase could provide insights in the modelling of *long-lived* chiral solute-(water)_n clusters in solution. In addition, the *clusters-in-a-liquid* solvation model simulates the implicit solvation effects of bulk water by means of the polarizable continuum model (PCM)^[21] of water. Most importantly, the *clusters-in-a-liquid* solvation model facilitates the identification of *long-lived* chiral solute-(water)_n complexes in water via experimental vibrational optical activity features obtained in water. In this thesis, I have addressed the challenges encountered in the interpretation of vibrational optical activity features of chiral molecules in water by applying the concept of the *clusters-in-a-liquid* solvation model. The remainder of the thesis is organized as outlined below.

In Chapter 2, I have discussed the instrumental aspects of IR and VCD spectroscopic methods in detail. The important conditions that are required to obtain a good quality experimental VCD spectrum are emphasized. I have highlighted the significance of the matrix isolation (MI) technique and have specified the advantages that can be achieved through the combination of the MI technique with IR and VCD spectroscopic methods. In the second part of Chapter 2, I have presented the basic theoretical concepts of IR and VCD spectroscopy and emphasized the important concerns related to the simulation of IR and VCD of chiral molecules. The *clusters-in-a-liquid* solvation model is introduced to interpret the implicit and explicit solvation effects on solution VCD and ROA spectra of chiral molecules.

In Chapter 3, I have investigated the solvation effects of methyl glycidate (MG) in both water and CCl₄ using VCD spectroscopy and ROA spectroscopy. These two very different solvents were selected so that one can compare the effects of solvent on the IR, VCD, Raman, and ROA spectra. Furthermore, I aim to illustrate how well different current solvent models perform in reproducing the experimental results. For example, I applied the PCM model to both CCl₄ and H₂O solvents to interpret the experimental data, and the shortcomings of this model in interpreting the experimental data obtained in aqueous solution are discussed. Since the PCM model only accounts for implicit solvation effects, the experimental spectral features that are generated due to explicit H-bonding interactions cannot be predicted via the PCM model. Therefore, in the next part of the analysis, I have applied the *clusters-in-a-liquid* solvation model^[32] to interpret the experimental spectral

features of MG in water. Through the *clusters-in-a-liquid* solvation model, I have considered the aqueous phase VCD features of MG and, especially, the induced VCD signature of water to recognize the *long-lived* species of MG in water. The *long-lived* species of MG identified via *the clusters-in-a-liquid* solvation model are verified eventually through the interpretation of all four experimental spectra of MG in water.^[33]

In Chapter 4, I have investigated the self-aggregation of lactic acid (LA) in the gas phase using the combined matrix isolation (MI)–VCD spectroscopic method to probe the self-aggregation behavior of LA in detail. Application of the MI technique allows one to control the degree of self-aggregation of LA molecules better and record IR and VCD spectra at a very low temperature of 10–30 K with our MI setup. Through the low temperature MI technique, one may trap isolated sample molecules in an inert gas matrix, reducing their chances to interact with each other if desired. In addition, the low temperature used means that essentially only vibrational transitions from the vibrational ground state are detected. The above favorable aspects achieved via the MI technique allows us to record much better resolved IR and VCD spectra. Generally, a large number of solvated species produced by many possible intermolecular interactions in solution, in addition to the conformational flexibility of the targeted chiral molecule, often result in a fairly broad linewidth for the solution IR and VCD spectra of chiral molecules. At the same time, the accuracy of the theoretical predictions of IR and VCD band positions and intensities gets worse as the aggregates and the solute-solvent complexes of the targeted chiral solute get larger. All these factors make the interpretation of the solution IR and VCD spectra of chiral molecules challenging. One further goal of this research is to use the resolved MI-IR and MI-VCD experimental spectral features to clarify the ambiguous vibrational band assignments of the related solution IR and VCD spectra of LA.^[34]

In Chapter 5, the *clusters-in-a-liquid* solvation model^[32] has been applied to interpret the IR and VCD spectra of methyl- β -D-glucopyranose (me- β -D-gluc) in water. The conformational flexibility of the selected monosaccharide model, me- β -D-gluc, can generate many conformers. Since each possible conformer of me- β -D-gluc contains many H-bonding donor and acceptor sites, it is not surprising that the simulated IR, VCD features of me- β -D-gluc monomer in the PCM of water fail to interpret the corresponding experimental data. Therefore, in order to account for both the explicit and implicit

solvation effects of water, I have considered the *clusters-in-a-liquid* solvation model to interpret the aqueous phase spectral features of MG. By implementing the *clusters-in-a-liquid* solvation model to the challenging system of me- β -D-gluc in water, I have evaluated the performance of the *clusters-in-a-liquid* solvation model in comparison to the other solvation models reported on monosaccharides.^[35]

In the final chapter, I summarize the main conclusions of each chapter and discuss the links among these studies and the general solvation picture emerging from my thesis work. In addition, some remarks are made about future improvements to the *clusters-in-a-liquid* solvation model. Finally, several appendices that include the supporting information of each chapter are enclosed in the last part of the thesis.

1.4 References

1. L. A. Nafie, "Molecular Chirality and Optical Activity", In *Vibrational Optical Activity: Principles and Applications*, John Wiley and Sons, Ltd., Chichester, 2011.
2. R. S. Cahn, C. K. Ingold, V. Prelog, *Angew. Chem., Int. Ed.*, **1966**, 5, 385.
3. a) J. B. Biot, *Bull. Soc. Philomath.*, **1815**, 190; b) D.F. Arago, *Mem. de L'Inst.*, **1811**, 12, part1, 93.
4. H. D. Flack, G. Bernardinelli, *Acta Crystallogr. Sect. A*, **1999**, 55, 908–915.
5. T. J. Wenzel, J. D. Wilcox, *Chirality*, **2003**, 15, 256–270.
6. L. A. Nafie, *J. Mol. Struct.*, **1995**, 347, 83–100.
7. G. Pescitelli, S. Gabriel, Y. Wang, J. Fleischhauer, R. W. Woody, N. Berova, *J. Am. Chem. Soc.*, **2003**, 125, 7613–7628.
8. a) T. B. Freedman, X. Cao, R. K. Dukor, L. A. Nafie, *Chirality*, **2003**, 15, 9, 743–58; b) T. A. Keiderling, *Curr. Opin. Chem. Biol.*, **2002**, 6, 5, 682–688; c) P. J. Stephens, F. J. Devlin, *Chirality*, **2000**, 12, 172–179; d) G. Yang, Y. Xu, "Vibrational Circular Dichroism Spectroscopy of Chiral Molecules", In *Top. Curr. Chem., Volume: Electronic and Magnetic Properties of Chiral Molecules and Supramolecular Architectures*, edited by R. Naaman, D. N. Beratan, D. H. Waldeck, Springer-Verlag Berlin Heidelberg, 2011, vol 298, pp 189–236; e) R. K. Dukor, L. A. Nafie, "Vibrational Optical activity of pharmaceuticals and biomolecules", In *Encyclopedia of Analytical Chemistry*, edited by R. A. Meyers, John Wiley & Sons, 2000, pp 662–676; f) L. A. Nafie, T. B. Freedman, R. K. Dukor, "Vibrational Circular dichroism", In *Handbook of Vibrational Spectroscopy*, edited by J. M. Chalmers and P. R. Griffiths, John Wiley & Sons,

-
- 2002; g) Z. Dezhahang, C. Merten, M. R. Poopari, Y. Xu, *Dalton Trans.*, **2012**, 41, 10817–10824; h) G. Holzwarth, E. C. Hsu, H. S. Mosher, T. R. Freedman, A. Moscowitz, *J. Am. Chem. Soc.*, **1974**, 96, 1, 251–252; i) L. A. Nafie, J. C. Cheng, P. J. Stephens, *J. Am. Chem. Soc.*, **1975**, 97, 13, 3842–3843.
9. B. E. Maryanoff, D. F. McComsey, R. K. Dukor, L. A. Nafie, T. B. Freedman, X. Cao, V. W. Day, *Bioorg. Med. Chem.*, **2003**, 11, 11, 2463–2470.
10. R. D. Shah, L. A. Nafie, *Curr. Opin. Drug. Discov. Devel.*, **2001**, 4, 6, 764–775.
11. Gaussian 03, Revision E.01, M. J. Frisch, G. W. Trucks, H. B. Schlegel, G. E. Scuseria, M. A. Robb, J. R. Cheeseman, J. A. Montgomery, Jr., T. Vreven, K. N. Kudin, J. C. Burant, J. M. Millam, S. S. Iyengar, J. Tomasi, V. Barone, B. Mennucci, M. Cossi, G. Scalmani, N. Rega, G. A. Petersson, H. Nakatsuji, M. Hada, M. Ehara, K. Toyota, R. Fukuda, J. Hasegawa, M. Ishida, T. Nakajima, Y. Honda, O. Kitao, H. Nakai, M. Klene, X. Li, J. E. Knox, H. P. Hratchian, J. B. Cross, V. Bakken, C. Adamo, J. Jaramillo, R. Gomperts, R. E. Stratmann, O. Yazyev, A. J. Austin, R. Cammi, C. Pomelli, J. W. Ochterski, P. Y. Ayala, K. Morokuma, G. A. Voth, P. Salvador, J. J. Dannenberg, V. G. Zakrzewski, S. Dapprich, A. D. Daniels, M. C. Strain, O. Farkas, D. K. Malick, A. D. Rabuck, K. Raghavachari, J. B. Foresman, J. V. Ortiz, Q. Cui, A. G. Baboul, S. Clifford, J. Cioslowski, B. B. Stefanov, G. Liu, A. Liashenko, P. Piskorz, I. Komaromi, R. L. Martin, D. J. Fox, T. Keith, M. A. Al-Laham, C. Y. Peng, A. Nanayakkara, M. Challacombe, P. M. W. Gill, B. Johnson, W. Chen, M. W. Wong, C. Gonzalez, and J. A. Pople, Gaussian, Inc., Wallingford CT, 2004.
12. Gaussian 09, Revision C.01, M. J. Frisch, G. W. Trucks, H. B. Schlegel, G. E. Scuseria, M. A. Robb, J. R. Cheeseman, G. Scalmani, V. Barone, B. Mennucci, G. A. Petersson, H. Nakatsuji, M. Caricato, X. Li, H. P. Hratchian, A. F. Izmaylov, J. Bloino, G. Zheng, J. L. Sonnenberg, M. Hada, M. Ehara, K. Toyota, R. Fukuda, J. Hasegawa, M. Ishida, T. Nakajima, Y. Honda, O. Kitao, H. Nakai, T. Vreven, J. A. Montgomery, Jr., J. E. Peralta, F. Ogliaro, M. Bearpark, J. J. Heyd, E. Brothers, K. N. Kudin, V. N. Staroverov, R. Kobayashi, J. Normand, K. Raghavachari, A. Rendell, J. C. Burant, S. S. Iyengar, J. Tomasi, M. Cossi, N. Rega, J. M. Millam, M. Klene, J. E. Knox, J. B. Cross, V. Bakken, C. Adamo, J. Jaramillo, R. Gomperts, R. E. Stratmann, O. Yazyev, A. J. Austin, R. Cammi, C. Pomelli, J. W. Ochterski, R. L. Martin, K. Morokuma, V. G. Zakrzewski, G. A. Voth, P. Salvador, J. J. Dannenberg, S. Dapprich, A. D. Daniels, Ö. Farkas, J. B. Foresman, J. V. Ortiz, J. Cioslowski, and D. J. Fox, Gaussian, Inc., Wallingford CT, 2009.
13. Amsterdam Density Functional Program; Vrije Universiteit: Amsterdam, The Netherlands; <http://www.scm.com>. E.J. Baerends, T. Ziegler, J. Autschbach, D. Bashford, A. Bérces, F.M. Bickelhaupt, C. Bo, P.M. Boerrigter, L. Cavallo, D.P. Chong, L. Deng, R.M. Dickson, D.E. Ellis, M. van Faassen, L. Fan, T.H. Fischer, C. Fonseca Guerra, M. Franchini, A. Ghysels, A. Giammona, S.J.A. van

-
- Gisbergen, A.W. Götz, J.A. Groeneveld, O.V. Gritsenko, M. Grüning, S. Gusarov, F.E. Harris, P. van den Hoek, C.R. Jacob, H. Jacobsen, L. Jensen, J. W. Kaminski, G. van Kessel, F. Kootstra, A. Kovalenko, M. V. Krykunov, E. van Lenthe, D.A. McCormack, A. Michalak, M. Mitoraj, S.M. Morton, J. Neugebauer, V.P. Nicu, L. Noodleman, V.P. Osinga, S. Patchkovskii, M. Pavanello, P.H.T. Philipsen, D. Post, C.C. Pye, W. Ravenek, J.I. Rodríguez, P. Ros, P. R. T. Schipper, G. Schreckenbach, J.S. Seldenthuis, M. Seth, J.G. Snijders, M. Solà, M. Swart, D. Swerhone, G. te Velde, P. Vernooijs, L. Versluis, L. Visscher, O. Visser, F. Wang, T.A. Wesolowski, E.M. van Wezenbeek, G. Wiesenekker, S. K. Wolff, T.K. Woo, A.L. Yakovlev.
14. a) L. D. Barron, M. P. Bogaard, A. D. Buckingham, *J. Am. Chem. Soc.*, **1973**, *95*, 2, 603–605; b) L. A. Nafie, *Annu. Rev. Phys. Chem.*, **1997**, *48*, 357–386.
15. a) L. D. Barron, A. D. Buckingham, *Chem. Phys. Lett.*, **2010**, *492*, 199–213; b) L. D. Barron, F. Zhu, L. Hecht, G. E. Tranter, N. W. Isaacs, *J. Mol. Struct.*, **2007**, *834–836*, 7–16.
16. K. Rezaei, E. Jenab, F. Temelli, *Critical Rev. Biotech.*, **2007**, *27*, 183–195.
17. G. Hummer, A. Tokmakoff, *J. Chem. Phys.*, **2014**, *141*, 22D101.
18. Z. Dezhahang, C. Merten, M. R. Poopari, Y. Xu, *Dalton Trans.*, **2012**, *41*, 10817–10824.
19. C. Merten, C. J. Berger, R. McDonald, Y. Xu, *Angew. Chem. Int. Ed.*, **2014**, *53*, 9940–9943.
20. a) P. Zhu, G. Yang, M. R. Poopari, Z. Bie, Y. Xu, *Chem. Phys. Chem.*, **2012**, *13*, 1272–1281; b) M. R. Poopari, Z. Dezhahang, G. Yang, Y. Xu, *Chem. Phys. Chem.*, **2012**, *13*, 2310–2321; c) M. R. Poopari, Z. Dezhahang, Y. Xu, *Spectrochim. Acta A Mol. Biomol. Spectrosc.*, **2013**, *136*, 131–140.
21. B. Mennucci, *WIREs Comput. Mol. Sci.*, **2012**, *2*, 386–404.
22. R. Otto, J. Brox, S. Trippel, M. Stei, T. Best, R. Wester, *Nat. Chem.*, **2012**, *4*, 534–538.
23. a) P. Carcabal, R. A. Jockusch, I. Hunig, L. C. Snoek, R. T. Kroemer, B. G. Davis, et al., *J. Am. Chem. Soc.*, **2005**, *127*, 11414–11425; b) L. Drouin, E. C. Stanca-Kaposta, P. Saundh, A. J. Fairbanks, S. Kemper, T. D. W. Claridge et al., *Chem. Eur. J.*, **2009**, *15*, 4057–4069.
24. E. J. Cocinero, P. Carcabal, “Carbohydrates”, In *Gas-Phase IR Spectroscopy and Structure of Biological Molecules. Top. Curr. Chem.*, edited by A. Rijs, J. Oomens, Springer, Cham, 2015, vol 364, pp 299–334.
25. a) C. Perez, J. L. Neill, M. T. Muckle, D. P. Zaleski, I. Pena, J. C. Lopez et al., *Angew. Chem. Int. Ed.*, **2015**, *54*, 979–982; b) C. Perez, J. L. Neill, M. T. Muckle, D. P. Zaleski, I. Pena, J. C. Lopez et al., *Angew. Chem.*, **2015**, *127*, 993–996.
26. K. Jalkanen, S. Suhai, *Chem. Phys.*, **1996**, *208*, 81–116.

-
27. J. Sadlej, J. C. Dobrowolski, J. E. Rode, *Chem. Soc. Rev.*, **2010**, *39*, 1478–1488.
28. M. Losada, P. Nguyen, Y. Xu, *J. Phys. Chem. A*, **2008**, *112*, 5621–5627.
29. M. Losada, Y. Xu, *Phys. Chem. Chem. Phys.*, **2007**, *9*, 3127–3135.
30. M. Losada, H. Tran, Y. Xu, *J. Chem. Phys.*, **2008**, *128*, 014508.
31. G. Yang, Y. Xu, *J. Chem. Phys.*, **2009**, *130*, 164506.
32. A. S. Perera, J. Thomas, M. R. Poopari, Y. Xu, *Front. Chem.*, **2016**, *4*, 1–17.
33. A. S. Perera, J. Cheramy, C. Merten, J. Thomas, Y. Xu, *Chem. Phys. Chem.*, **2018**, *19*, 2234–2242.
34. a) G. Tarczay, G. Magyarfalvi, E. Vass, *Angew. Chem. Int. Ed.*, **2006**, *45*, 1775–1777; b) C. H. Pollok, C. Merten, *Phys. Chem. Chem. Phys.*, **2016**, *18*, 13496–13502.
35. a) J. R. Cheeseman, M. S. Shaik, P. L. A. Popelier, E. W. Blanch, *J. Am. Chem. Soc.*, **2011**, *133*, 4991–4997; b) S. T. Mutter, F. Zielinski, J. R. Cheeseman, C. Johannessen, P. L. A. Popelier, E. W. Blanch, *Phys. Chem. Chem. Phys.*, **2015**, *17*, 6016; c) A. Melcrova, J. Kessler, P. Bour, J. Kaminsky, *Phys. Chem. Chem. Phys.*, **2016**, *18*, 2130; d) F. Zielinski, S. T. Mutter, C. Johannessen, E. W. Blanch, P. L. A. Popelier, *Phys. Chem. Chem. Phys.*, **2015**, *17*, 21799.

Chapter 2

Experimental and Theoretical Methods

2.1 Experimental Methods

2.1.1 Introduction

In this thesis, I have utilized IR, VCD, Raman, ROA, MI-IR, and MI-VCD spectroscopic methods to investigate the intermolecular interactions associated with chiral molecules in solution and in cold rare gas matrices. While IR and Raman spectral features provide some information about intermolecular interactions containing chiral molecules, their sensitivity and specificity towards such interactions are low, especially in solution where broader line widths may obscure the small red (bathochromic) or blue (hypsochromic) shifts induced by such interactions. The chiral versions of IR and Raman spectroscopy, namely VCD and ROA, also can distinguish a pair of enantiomers, whereas the IR and Raman spectra of a pair of enantiomers are identical. Furthermore, VCD and ROA spectral features are in general substantially more sensitive to such intermolecular interactions than those of IR and Raman. Not only the frequency and intensity of a VCD or ROA band but also its sign may change due to intermolecular interactions, such as solute-solute and solute-solvent interactions. As mentioned in Chapter 1, the identification of structural changes of chiral molecules via VCD spectroscopy can be accomplished only with the aid of theoretical interpretation of the experimental VCD features. In this thesis, the ROA spectroscopic method has been used mainly to support the findings of solution phase VCD investigations. The combination of matrix isolation (MI) technique with IR and VCD spectroscopic methods provides a much narrower line width because both the low temperature and the separation of different sample conditions, where the number of possible intermolecular interactions can be reduced, lead to the possible identification of individual chiral molecule/chiral cluster or even its specific conformers.

In this chapter, I will give a brief description of the history of VCD spectroscopy, the IR and VCD instruments (focusing mainly on the VCD instrument which is newer), and some important details of my MI-VCD experiments. I will end with a short summary of IR and VCD theories and the related *ab initio*/density functional theory (DFT) calculations.

2.1.2 VCD Spectroscopy

2.1.2.1 The History of the Development of VCD Spectroscopy

The first VCD investigation was conducted for the neat sample of 2,2,2-trifluoromethyl-1-phenylethanol by Holzwarth et al. in 1974 when they obtained VCD spectra of both the enantiomers and the racemic mixture in the C—H stretching absorption region.^[1] The experimental VCD features of 2,2,2-trifluoromethyl-1-phenylethanol identified by Holzwarth et al. were reproduced later by Nafie et al. through their VCD investigations of the same chiral molecule.^[2] In the latter study, the experimental VCD features were obtained also in the O—H stretching absorption region. Later VCD measurements were extended to the whole —H stretching absorption region for a different set of chiral molecules.^[3] All these early VCD investigations were undertaken using dispersive scanning VCD instruments; these instruments only allow the VCD spectra to be recorded in a narrow wavenumber region. The first Fourier transform (FT)-VCD study was undertaken by Nafie et al. when they recorded the C—H stretching vibrations of camphor in the mid-IR region.^[4] Later, the use of HgCdTe (MCT) detectors allowed the FT-VCD measurements to be undertaken in the fingerprint region (800–1800 cm⁻¹) for a wide range of chiral molecules.^[5] The initial commercialization of VCD instrumentation was undertaken by both BioRad (Digilab) and Nicolet (Thermo Nicolet) companies in the 1980s without much success. In 1997, the ChiralIR FT-VCD instrument, which turns out to be the first stand-alone VCD spectrometer that was designed solely for VCD measurements, was introduced by Bomen and BioTools companies. Later, in 2009, the ChiralIR-2X FT-VCD spectrometer was invented by BioTools as an improvement over the first generation of VCD spectrometers. In this new FT-VCD spectrometer, all the necessary electronic processing happens in a single PC card of the computer of a FT-VCD

spectrometer, a ‘black box’ design which may be aiming at pharmaceutical companies. Since 2000, essentially all major FTIR companies carry their own FT-VCD products.

2.1.2.2 FT-IR and FT-VCD Instrumentation

The IR section of electromagnetic radiation corresponds to the wavenumber region of 10 cm^{-1} – 14000 cm^{-1} . This IR radiation range can be divided further into far-IR (10 cm^{-1} – 400 cm^{-1}), mid-IR (400 cm^{-1} – 4000 cm^{-1}), and near-IR (4000 cm^{-1} – 14000 cm^{-1}) regions. In the mid-IR region, the 800 cm^{-1} – 1800 cm^{-1} region is defined as the fingerprint region. This is mainly because the bending and stretching vibrations in the fingerprint region are unique and quite specific for each molecule. Therefore, the interpretation of the experimental IR and VCD features recorded in the fingerprint region can be used to extract stereochemical details of chiral molecules.

In this thesis, the FTIR-VCD instrument, which consists of an FTIR spectrophotometer (Vertex 70, Bruker) and a VCD module (PMA 50, Bruker), was used to undertake all the IR and VCD measurements. The schematic diagram of the FTIR-VCD instrumentation is presented in Figure 2.1.

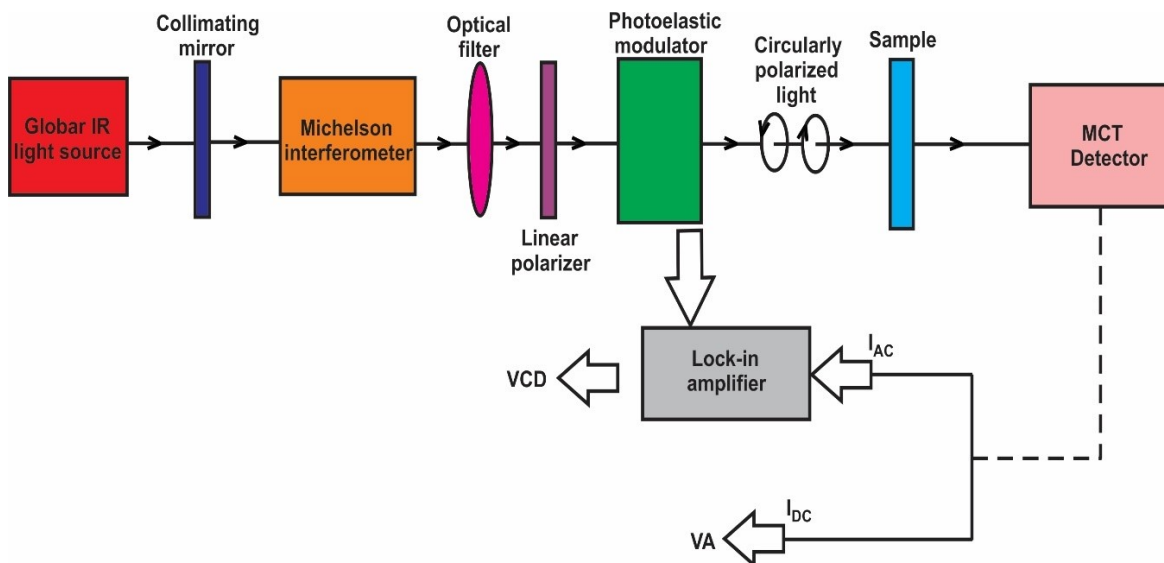


Figure 2.1. The schematic diagram of the FTIR-VCD instrumentation.

The mid-IR radiation (400 cm^{-1} – 4000 cm^{-1}) required for both the FT-IR and the FT-VCD measurements is obtained from the Globar (silicon carbide) source. The Michelson interferometer, which consists of a beam splitter and two mirrors (one fixed and one moving), is an important component of FTIR-VCD instrumentation. The schematic diagram of the Michelson interferometer is presented in Figure 2.2. The mid-IR light generated via a Globar light source is directed to the center of the beam splitter by a collimating optical mirror. At the beam splitter, half of the IR light is transmitted towards the direction of the moving mirror, while the other half is reflected towards the fixed mirror. Next, the reflected IR beams from the fixed and the moving mirrors are joined at the beam splitter again where they can interact constructively or destructively. The difference in the total distance traveled by the moving versus the fixed mirror IR light is $2x$.

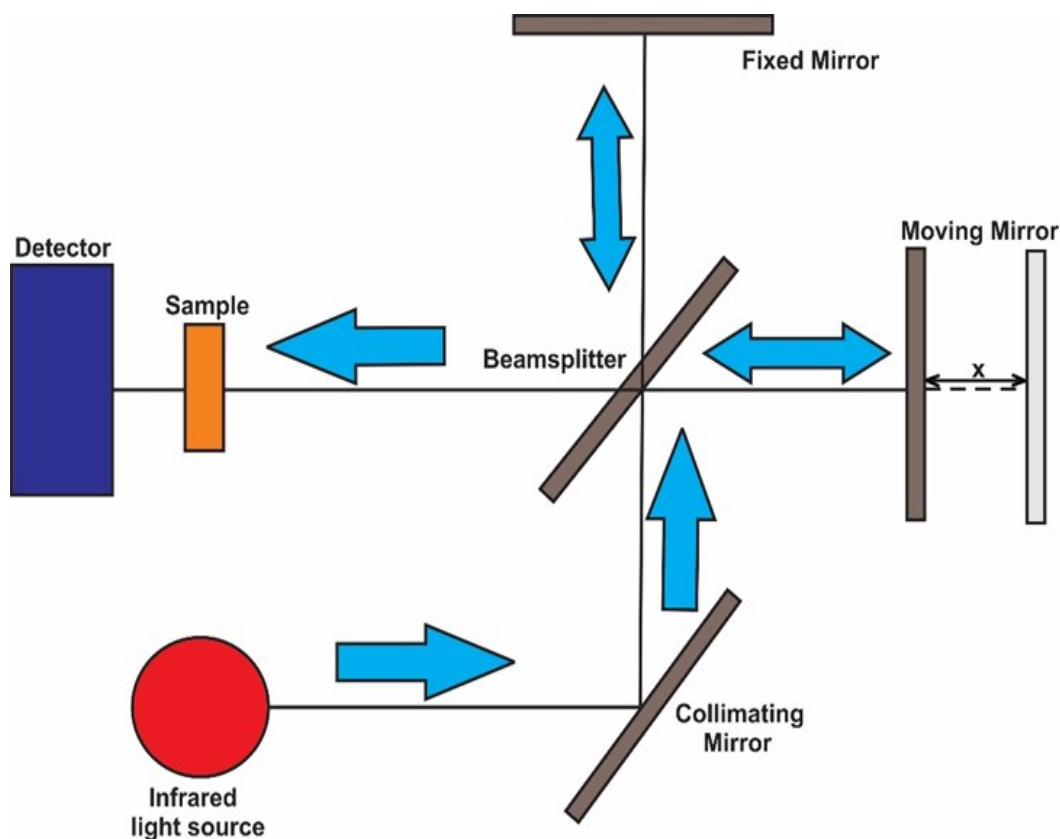


Figure 2.2. The schematic diagram of Michelson interferometer.

If the $2x$ path length difference is an exact multiple ($n = 0, 1, 2, \dots$) of the wavelength (λ) of IR light, then the interference at the beam splitter will be constructive and given by:

$$2x = n\lambda \quad (n = 0, 1, 2, \dots) \quad (2.1)$$

On the other hand, if the $2x$ path length difference is an odd multiple ($n = 1, 3, 5, \dots$) of half the wavelength ($\lambda/2$) of IR light, then the interference at the beam splitter will be destructive and given by:

$$2x = n \frac{\lambda}{2} \quad (n = 1, 3, 5, \dots) \quad (2.2)$$

The resulting combined stream of IR light then travels through the sample and finally reaches the mid-IR detector. The mid-IR detector records the intensity of combined IR streams as a function of the displacement of the moving mirror. The resulting interferogram is subjected to Fourier transformation (FT), which eventually generates the frequency dependent signal at each wavenumber.

For a FT-VCD measurement, the IR light emerging after the Michelson interferometer beam splitter is directed into the VCD chamber. It passes through an optical filter that has an upper cut-off in the 1800 cm^{-1} region; the optical filter can be changed to provide the desired wavenumber range for a VCD measurement. The IR light that comes through the optical filter is not polarized in any specific direction. The wire-grid linear polarizer only allows one specific polarization direction of IR light to go through it, therefore, the IR light coming through it is polarized in one specific direction; in our experiments, this is selected at 45° (vide infra).

It is essential to generate right- and left-circularly polarized IR light at a 50 kHz modulation frequency to distinguish the VCD signal from other instrumental noise since the experimental VCD intensities are 10^{-4} – 10^{-6} times less than their corresponding IR intensities. This goal is accomplished by the next key optical element, the photoelastic modulator (PEM). The PEM is composed of a transparent silica bar connected to a piezoelectric transducer, which is in turn connected to a 50 kHz alternating current (AC)

source (Figure 2.3). When a transparent solid material, such as the silica bar, is stressed by compression or stretching generated by the piezoelectric transducer, it becomes birefringent, and as a consequence, the polarized components parallel or perpendicular to the modular axis travel at slightly different speeds through the silica bar.

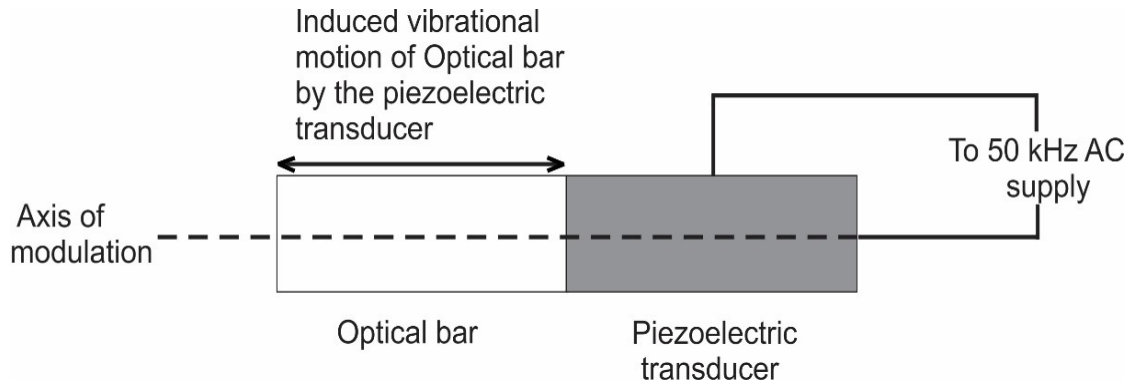


Figure 2.3. The components of the photoelastic modulator (PEM).

For the VCD experiments, the incoming linearly polarized light is oriented at an angle of 45° to the optical axis of the PEM, and this can be viewed as a combination of two equal vertically and horizontally polarized light beams. When there is no stress applied on the silica bar, the horizontal and vertical linearly polarized light beams travel through the silicon bar without being influenced and recombine as the same 45° linearly polarized light beam as before. When the silica bar is stretched, the refractive index of the silica bar along the vertical axis (n_v) is reduced compared to the refractive index of the silica bar along the horizontal axis (n_h). As a result, the horizontally polarized beam lags in comparison to the vertically polarized beam after they pass the PEM, generating a phase difference between the two beams. This phase difference is called the *retardation*, and it oscillates as a function of time (Figure 2.4). The importance of the above *retardation* to the VCD experiments is the special condition when the maximum (peak) retardation reaches exactly $1/4$ of the wavelength. Essentially, the PEM acts as an oscillating $1/4$ waveplate and produces the right circularly polarized light at the maximum stretching limit of the piezoelectric cycle, and the left circularly polarized light is generated at the maximum compressing limit of the piezoelectric cycle (Figure 2.4). It is also clear from the above discussion that each PEM setting operates only in a small wavenumber or wavelength region because of the $1/4$ wave requirement. If one wants to move to a much different

wavenumber region, one needs to reset the PEM center frequency to the desired region and redo all the calibration procedures.

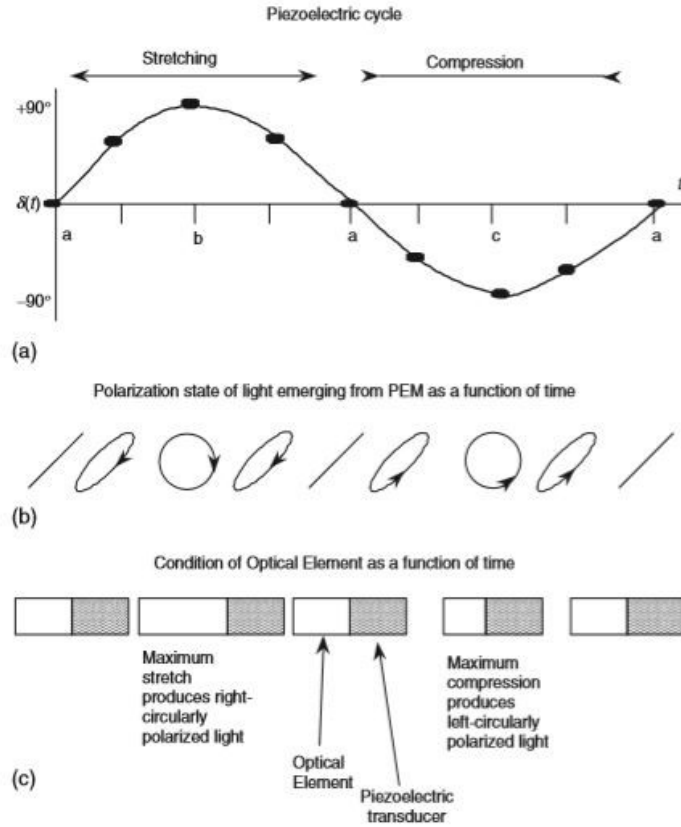


Figure 2.4. The modulation cycle of the photoelastic modulator (PEM); the figure is obtained directly from reference [6].

Next, the right and left circularly polarized IR lights generated by the PEM are passed through the sample and registered at the HgCdTe (MCT) detector cooled by liquid N₂. The MCT detector converts the optical signal to an electrical signal. The high-frequency AC signal, which is related to the experimental VCD spectrum, is separated using a high-pass filter, whereas the low-frequency DC signal, which corresponds to the experimental IR spectrum, is obtained using a low-pass filter. The resulting high-frequency AC signal is directed towards the lock-in amplifier, which plays a vital role in the extraction of weak VCD signals from a noisy background. In the lock-in amplifier, the demodulated signal from the high-frequency AC signal is obtained through the synchronous demodulation process^[6] where the required reference for the demodulation process is provided by the

input modulation frequency of the PEM. Both the demodulated signal from the AC path and the low-frequency signal from the DC path are converted to the frequency dependent AC and DC spectra, respectively, via Fourier transformation. The final experimental VCD spectrum is obtained as a ratio between the frequency dependent AC and DC spectra.

The success of a VCD experiment depends on the selection of several important parameters. The first factor is the selection of the solvent. Besides the desirable solubility, the solvent should not contain any strong IR bands in the fingerprint region in order to avoid solvent interference. Secondly, it is also important to identify the correct window material for the IR and VCD measurements. Normally, windows made of KBr, CsI, BaF₂, CaF₂, and ZnSe are considered for the measurements, but each material has its advantages as well as disadvantages. Although the low cutoff wavenumbers of KBr and CsI windows are placed at $\sim 400\text{ cm}^{-1}$ and $\sim 200\text{ cm}^{-1}$, respectively, both are soluble in water, therefore, they are not good options for aqueous phase measurements. On the other hand, windows made of ZnSe turn out to be much more expensive than the windows of other materials. The CaF₂ windows have a relatively high cutoff at 1100 cm^{-1} , which in turn limits the accessibility of the fingerprint region. In this thesis, all the VA and VCD measurements were performed using the BaF₂ windows, which provide a cutoff at $\sim 800\text{ cm}^{-1}$. The third factor is the selection of the correct concentration and path length conditions for VCD measurements. Typically, we aim at an IR absorption in the range of 0.2 to 0.9 for VCD measurements to avoid both saturation effects and very low photon counts. The above desirable IR intensity range of chiral samples can be achieved through the manipulation of concentration and path length conditions.

The VCD intensities of a chiral sample depend on the variation of the phase angle of the PEM with the wavenumber.^[7] To extract the proper VCD information, one needs to go through a calibration procedure to set the dependency of VCD intensities on the unknown function of the PEM. In this calibration process, the sample is replaced by a combined setup of the quarter wavelength plate and the linear polarizer. The CD intensities are recorded for the parallel and 90° orientations of the above linear polarizer with respect to the linear polarizer placed prior to the PEM. The combination of the two sets of CD intensities generates a calibration curve that defines the variation of the phase angle of the

PEM with the wavenumber. In situations where there is a change in either the resolution of the VCD experiment or the selected wavenumber region of the PEM, the above calibration process needs to be performed before the commencement of the VCD measurements of the sample. Since experimental VCD features exhibit very weak intensities, it is important to achieve a decent signal-to-noise ratio for their subsequent interpretation. Typically, a VCD measurement time of 3 to 6 h, which includes 12000 to 24000 scans, generates a good quality VCD spectrum.

2.1.3 Matrix Isolation (MI)-VCD Spectroscopy

2.1.3.1. The Importance of MI-VCD Spectroscopy

A chiral solute in solution can exist in many different forms, such as different conformers of the chiral solute monomer, self-aggregates of the chiral solute, and chiral solute-solvent clusters. Therefore, when IR and VCD spectra of a chiral molecule are recorded in solution, the resulting solution IR and VCD features often are not generated by a single species of the chiral solute but by several species of the chiral solute. The contribution of many different species of the chiral solute may produce broadened solution IR and VCD features. Such broadening often hinders the theoretical interpretation of solution spectra. For example, the final signs of the solution VCD features may be the result of many overlapping features of several chiral solute species, making their spectral assignments challenging. Furthermore, cancellation of VCD signatures with opposite signs also reduces the final intensities of solution VCD features, making it difficult to obtain high-quality data. This is where MI-IR and MI-VCD spectroscopic methods come into the picture.

The MI technique enables the trapping of diluted sample molecules (chiral solutes in our cases) in an inert gas at very low temperatures, for example at 10 K to 15 K. The MI technique was introduced first by G. C. Pimentel et al. in 1954 when they implemented it to stabilize reactive species which cannot be studied under normal experimental conditions.^[8] Although initially this technique was implemented to trap unstable species, the highly resolved nature of spectral features obtained has excelled its application beyond the initial investigations of reactive species.^[9] In the MI technique, the interactive solvent

medium is replaced by an inert gas matrix, thus eliminating any spectral features due to chiral solute-solvent clusters. The use of very low temperatures means that the chiral solute is typically in its ground vibrational state. The tight arrangement of chiral molecules within the cages of an inert gas matrix typically does not provide the required freedom for molecular rotations; as a result, no rotational splitting is observed in MI-IR and VCD spectra. Also, an inert gas matrix is transparent in the IR region, offering no interference to the species of interest. In addition, MI experiments can be performed using much different sample conditions such that a particular species of interest may be tuned to be the dominant one. Together, these aspects usually produce much better resolved MI-IR and VCD features, facilitating definite theoretical interpretation. Furthermore, by varying the experimental conditions, one may use MI-IR and VCD spectra to follow the processes of chiral solute aggregation and of solvation of chiral molecules and clarify ambiguous theoretical interpretations of solution IR and VCD spectra of chiral molecules.

2.1.3.2 The Challenges of MI-VCD Spectroscopy

Despite the powerful nature of MI-VCD spectroscopy, the application of the MI-VCD technique was affected by the stringent requirements on the quality of the matrix. Since VCD intensities are only 10^{-4} to 10^{-6} times those of their parent IR intensities, it is important to obtain a high degree of transparency for the matrix. The absence of transparency in the matrix promotes the light scattering effects and in the case of circularly polarized experiments, the left- and right-circularly polarized IR light may experience different extents of scattering effects. As a consequence, a VCD spectrum recorded of a nontransparent matrix tends to generate a distorted set of VCD signatures. The transparency of the matrix depends sensitively on the deposition rate of the gas mixture (sample + inert gas) and the temperature of the cold surface. The recent improvements of MI-VCD instrumentation have provided a good control over both the temperature of the cold surface and the rate of introduction of the gas mixture to the cold surface.^[10, 11] The transparency of the matrix also influences the trapping sites of chiral molecules in the inert gas matrix. The defined crystal structure of the transparent inert gas matrix provides a specific set of trapping sites for isolated sample molecules. When two conformationally

equivalent sample molecules are trapped, one would expect identical MI-IR (and MI-VCD) features under ideal conditions. On the other hand, two different trapping sites may create differences in the weak interactions between the matrix and the trapped molecules, leading to the so-called “site-splitting” and greatly complicating the assignment of MI-IR and MI-VCD spectral features. Typically, the MI-VCD features of “site-splitting” tend to have the same sign. This is mainly because the stereochemical aspects of chiral molecules are not influenced strongly by the differences of the trapping sites.

2.1.3.3 MI-VCD Instrumentation

The experimental set up of matrix isolation consists of a cryostat, a vacuum system, and a sample injection system. The schematic diagram of the MI experimental setup is presented in Figure 2.5.

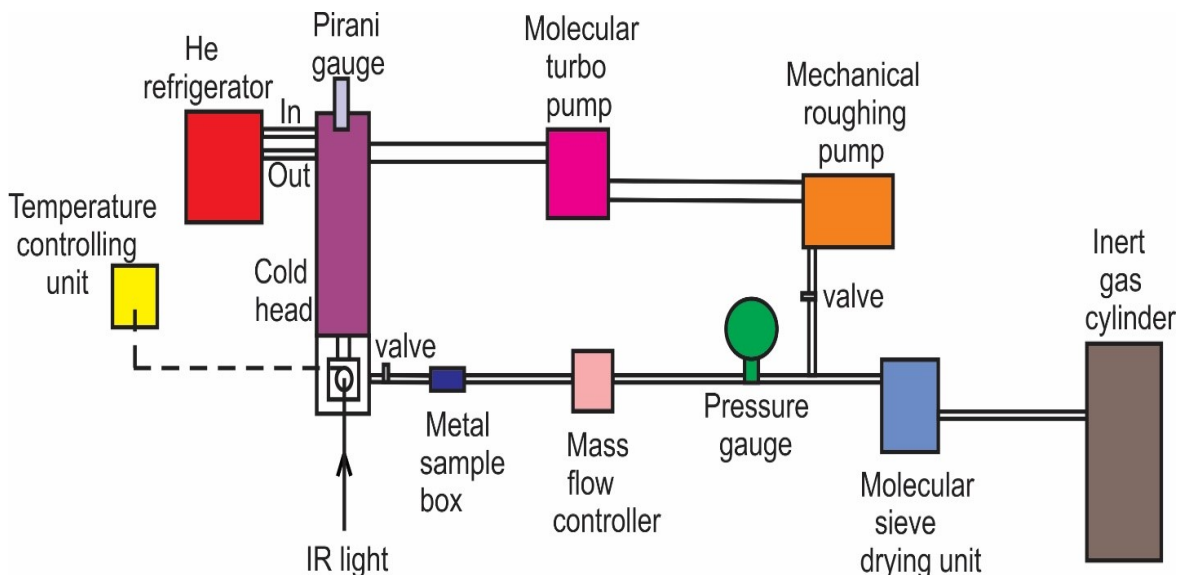


Figure 2.5. The schematic diagram of the MI experimental setup.

The low-temperature environment required for MI-VCD experiments is provided by the cryostat system. The cryostat from Advanced Research System is comprised of a cold head and a helium compressor (Advanced Research System, model no HC-4E1). The cold head, also known as the expander of a closed cycle cryocooler, undertakes the Gifford-McMahon refrigeration cycle.^[12] The expander is connected to the helium compressor via two gas

lines. One of the gas lines introduces the high pressure He gas into the cold head. The high pressure He gas is expanded in the cold head; as a result, the temperature of the cold head decreases. After the expansion process, the resulting low pressure He gas in the cold head is taken back to the He compressor through the returning gas line. The heat developed in the He compressor is dissipated through a cold-water circulating system. The cold head is connected to a sample holder, and the sample holder retains the cold surface of the BaF₂ window on which the gas mixture of sample and inert gas is deposited. The cold surface of the BaF₂ window is enclosed in a radiant heat shield, which is then inserted inside a vacuum shroud leading to a vacuum region around the cold surface of BaF₂. All these efforts minimize any heat exchange between the cold surface of BaF₂ windows and the vacuum shroud whose outer surface is exposed to the room temperature. The lowest temperature that the cryostat system from Advance Research System can attain is around 4 K.

In order to achieve the high vacuum condition, the Leybold molecular turbopump supported by a mechanical roughing pump is connected to the cold head. Typically, it takes about 6 h to achieve the required high vacuum condition in the cold head. During the cryogenic cooling process of the cold head when the temperature of the cold head goes below 150 K, the cold head is isolated from the pumping system using a special shatter valve. The temperature of the cold head is controlled using the Lake Shore 311 model temperature controller, which employs the usual PID feedback loop system. Two silicon diode temperature sensors were inserted to the cryostat system, one directly at the BaF₂ window and the other on the cold head. These two temperatures are used as input for the temperature controlling system. Typically, the temperature difference from the cold head to the BaF₂ window is less than 1 K.

The sample molecules are injected into the stream of inert gas via two methods. If the sample molecule of interest is a liquid with a reasonable vapor pressure at room temperature or a gas, we mix the sample molecules and inert gas molecules in a desirable ratio. If the sample is a solid, we flow a rare gas over the solid sample placed inside a stainless-steel container that is near the cold head, bringing the sample vapor into the cold head for deposition. Unlike the first case, the exact ratio between the sample molecules and

the inert gas molecules is unknown. Instead, the temperature of the sample and the flow rate of the inert gas can be manipulated to assist in the formation of different sizes of aggregates.

The flow rate of the sample mixture is controlled by the MKS mass flow controller instrument. We monitor the IR spectrum while deposition is in progress. If there are any issues with the baseline tilting or IR features, the deposition is stopped and the temperature of the cold surface of BaF₂ is raised to room temperature. Then, the system is pumped clean, and a new experiment is performed with the implemented changes.

2.2 Theoretical Aspects

2.2.1 Basic Concepts of IR and VCD Spectroscopy

The vibrational spectra are modelled using the harmonic oscillation approximation. The potential energy of a harmonic oscillator can be written with respect to both the force constant (k) and the displacement from the equilibrium position ($r - r_{\text{eq}}$) as follows:

$$V = \frac{1}{2}k(r - r_{\text{eq}})^2 \quad (2.3)$$

The application of quantum mechanics to the harmonic oscillator system of two nuclei defines its energy levels by:

$$E_n = \left(n + \frac{1}{2}\right)\hbar\omega \quad (2.4)$$

where $\hbar = \frac{h}{2\pi}$ and $\omega = 2\pi\nu$. Here ν is the fundamental vibrational frequency and can be calculated as $\nu = \frac{1}{2\pi} \left(\frac{k}{\mu}\right)^{\frac{1}{2}}$, where k and μ are the force constant and the reduced mass of the system, respectively. The vibrational quantum numbers are represented by $n = 0, 1, 2, 3$ etc., and the energy of E_0 defines the zero-point energy level. The energy levels of the

harmonic oscillator system maintain a constant energy gap, and the transitions between vibrational energy levels are permitted according to the $\Delta n = \pm 1$ selection rule.

The intensity of a vibrational absorption (IR) transition is decided by the dipole strength. The dipole strength (D_{ge}) of a vibrational absorption transition from the vibrational ground state Ψ_g to the first vibrational excited state Ψ_e is defined as follows:

$$D_{ge} = |\langle \psi_e | \boldsymbol{\mu} | \psi_g \rangle|^2 \quad (2.5)$$

In the above equation, $\boldsymbol{\mu}$ corresponds to the electric dipole moment operator and the $\langle \psi_e | \boldsymbol{\mu} | \psi_g \rangle$ term is defined as the electric transition dipole moment.

VCD spectroscopy measures the absorption difference of left versus right circularly polarized light for a vibrational transition. The sign and intensity of a VCD signal are determined by the parameter called rotational strength. The rotational strength (R_{ge}) of a vibrational transition from the ground vibrational state Ψ_g to the first vibrational excited state Ψ_e is defined as follows:

$$R_{ge} = \text{Im}\{\langle \psi_g | \boldsymbol{\mu} | \psi_e \rangle \cdot \langle \psi_e | \mathbf{m} | \psi_g \rangle\} \quad (2.6)$$

where the \mathbf{m} defines the magnetic dipole moment operator and the $\langle \psi_e | \mathbf{m} | \psi_g \rangle$ term is defined as the magnetic transition dipole moment. The above equation also can be written as $R = |\boldsymbol{\mu}| \cdot |\mathbf{m}| \cdot \cos \theta$, where $|\boldsymbol{\mu}|$ and $|\mathbf{m}|$ correspond to the absolute values of the electric and magnetic dipole transition moments, respectively. The θ defines the angle between the electric and magnetic transition dipole moment vectors. If $0^\circ < \theta < 90^\circ$ and $270^\circ < \theta < 360^\circ$, the resulting $\cos \theta$ term will have a positive value, therefore, the sign of the VCD signature will be positive. For $270^\circ > \theta > 90^\circ$, the $\cos \theta$ term is a negative value, therefore, the resulting VCD signature will be negative. The rotational strength of a vibrational transition reaches zero at $\theta = 90^\circ$ and 270° , leading to a zero VCD intensity.

Although the determination of the dipole strength of a vibrational transition can be achieved with the evaluation of the electric transition dipole moment, the determination of the rotational strength of a vibrational transition requires the determination of both the electric and magnetic transition dipole moments.^[13,14] Even though the vibrational electric

transition dipole moment can be evaluated within the Born Oppenheimer (BO) approximation, the situation is not the same for the computation of the vibrational magnetic transition dipole moment. In the determination of the vibrational magnetic transition dipole moment within the BO approximation, the electronic contribution of the vibrational magnetic transition dipole moment attains zero.^[15] This is mainly because the electronic contribution of the vibrational magnetic transition dipole moment is generated via the velocities of nuclei related to vibrational motions. But within the BO approximation, the nuclei velocities are not allowed to reveal any dependency on the electronic variables; as a result, the electronic contribution of the vibrational magnetic transition dipole moment vanishes under the BO approximation. In order to account for the above consequence, several theoretical approaches, like the fixed partial charge (FPC) model,^[16] the coupled oscillator (CO) model,^[17] the dynamic polarization (DP) model,^[18] the localized molecular orbital model,^[19] the nuclear electric shielding tensor model,^[20] and the vibronic coupling model,^[21] have been put forward to evaluate the vibrational magnetic transition dipole moment. Despite the above theoretical models, the widespread implementation of calculations of the vibrational magnetic transition dipole moment was achieved only with the invention of the magnetic field perturbation (MFP) theory by Stephens^[22, 14] and Buckingham.^[23] In the MFP theory, corrections are introduced to the BO approximation so that the electronic contribution made by vibrational motions towards the magnetic transition dipole moment is calculated by taking the first derivatives of the ground state wave function with regard to the nuclear coordinate displacements and the applied magnetic field.

The vibrational electric transition dipole moments and the vibrational magnetic transition dipole moments of normal modes are determined, respectively, via atomic polar tensor (APT)^[24] and atomic axial tensor (AAT)^[23] evaluations. The Hessian matrix (harmonic force field), along with APT^[25] and eventually the AAT^[26] (based on MFP theory) calculations, have been included into common electronic structure packages, such as Gaussian, Dalton, GAMESS, etc. The dipole strength (D in $\text{esu}^2 \text{ cm}^2$) and rotational strength (R in $\text{esu}^2 \text{ cm}^2$) entities of the normal modes determined are related to molar

extinction coefficients (ε) and molar differential extinction ($\Delta\varepsilon$) coefficients via the following relationships:^[27]

$$\varepsilon(v) = \frac{v}{9.184 \times 10^{-39}} \sum_i D_i f(v, v_i) \quad (2.7)$$

where $f(v, v_i) = \frac{\gamma_i/\pi}{(v-v_i)^2 + \gamma_i^2}$

$$\Delta\varepsilon(v) = \frac{v}{2.296 \times 10^{-39}} \sum_i R_i f(v, v_i) \quad (2.8)$$

where ε and $\Delta\varepsilon$ (in $M^{-1} \text{ cm}^{-1}$) are a function of frequency (v) in wavenumber (cm^{-1}), and the $f(v, v_i)$ function corresponds to a Lorentzian line shape function with γ_i and v_i depicting the half-width of the band at half maximum and the transition frequency of normal mode “ i ”, respectively.

2.2.2 Theoretical IR and VCD Spectra

The simulation of IR and VCD spectra of chiral molecules requires equilibrium geometries and, subsequently, the Hessian matrixes (harmonic force fields), atomic polar tensors (APT), and atomic axial tensors (AAT) evaluations of equilibrium geometries. The selection of the *ab initio* method plays a key role in the prediction of experimental IR and VCD spectra. The Hartree-Fock (HF) method is recognized as the simplest and computationally most inexpensive *ab initio* method for the prediction of the ground electronic state properties of chiral molecules.^[28] The electron correlation effects that are neglected in the HF method can be accounted for by using post-Hartree-Fock methods, such as configuration interaction (CI), coupled cluster (CC), and Moller-Plesset (MP) perturbation theory. However, the computational cost of the above post-HF methods has hindered their application in the prediction of experimental IR and VCD spectra.^[29] In contrast to the HF method, the density functional theory (DFT)^[30] determines the electron

correlation effects through functionals of electron density, and unlike post-HF methods, the computational cost of DFT is at the same level as the HF method.^[31]

The functionals of DFT that account for electron exchange-correlation effects have been developed from two main approximations. The functionals that are centered on the local density approximation (LDA) are defined as local functionals, whereas the functionals that are based on the generalized gradient approximation (GGA) are termed nonlocal functionals. The hybrid functionals of DFT that include not only local and nonlocal functionals but also contain some contribution from the HF method provide a much-improved representation of electron exchange-correlation effects when compared to either local or nonlocal functionals.^[32] Some of the well-known hybrid functionals of DFT are B3LYP (Becke's three parameter,^[33] Lee-Yang-Parr functional^[34]) and B3PW91 (Becke's three parameter,^[33] Perdew and Wang functional^[35]).^[36] The B3LYP hybrid functional is recognized for its effective nature in the simulation of IR and VCD spectra of chiral molecules.^[37]

The next important concern is the selection of a basis set for the *ab initio* calculation. Since the basis set reflects the spatial distribution of electrons in a molecule, the selection of a large basis set provides the required flexibility to account for the electron distributions of molecular orbitals. As a result, the implementation of a large basis set improves the theoretical interpretation of experimental results; however, the use of a large basis set also increases the computation cost.^[27] In order to confront the above challenge, split-valence basis sets were introduced by J. Pople and coworkers as the first set of large basis sets.^[38] Some examples of split-valence basis sets are 6-31G, 6-311G, etc. In split-valence basis sets, the electrons in the valence orbitals are represented by more than one basis function. In the above examples, although both the 6-31G and 6-311G basis sets allocate only one basis function (with a degree of contraction of 6) for a core orbital, the former uses two basis functions (with a degree of contraction of 3 and 1) and the latter uses three basis functions (with a degree of contraction of 3, 1, and 1) to account for a valence orbital. The cooperation of polarization functions with split-valence basis sets provides flexibility in the representation of the shapes of orbitals. A polarization function that is assigned to a specific orbital contains a higher angular momentum than the angular

momentum of the orbital. Thus, the use of p and d polarization functions with the respective basis functional representations of 1s and 2p orbitals, respectively, improves the flexible nature of basis functions. The inclusion of diffuse functions with split-valence basis sets also improves the flexibility of basis functions. In a situation where the electron distribution of an orbital spreads far away from the nucleus, the inclusion of diffuse functions provides an improved representation of the electron distribution. The correlation-consistent basis sets^[39] and the Karlsruhe basis sets^[40] are two other categories of basis sets that can be used as large sets to represent the electron distributions of molecular orbitals.

In this thesis, the identification of equilibrium geometries, the Hessian matrix evaluations that ultimately provide the frequencies of the normal modes, and the APT and AAT computations that eventually generate the IR and VCD intensities were performed using the Gaussian 09^[41] program package via DFT-based methodologies. The well recognized DFT hybrid functionals of B3LYP and B3LYP with Grimme's dispersion correction, including the Becke-Johnson damping (D3BJ) factor^[42] and 6-311++G(2d,p) basis set^[43] combination, were selected as the main hybrid functionals and basis set combination to perform the computations of the above-mentioned ground state molecular properties of different chiral systems. This combination of hybrid functionals and the basis set combination was selected mainly due to their well-earned recognition in predicting experimental IR and VCD spectra of different chiral systems correctly.^[37,44] In the above computations, the implicit solvation effects generated on the chiral solute are modelled using the polarizable continuum model (PCM).^[45]

In many situations, the solvent that provides the medium for the chiral solute can form intermolecular interactions with the chiral solutes. In those cases, the interpretation of experimental IR and VCD spectra of solutions cannot be accomplished with the sole consideration of the implicit solvent effects. The situation gets even more complicated in the interpretation of IR and VCD spectra of chiral molecules in water. The capability of water to act as both the H-bond acceptor and the H-bond donor at the same time facilitates the formation of extensive H-bonding networks. The above characteristic feature of water complicates the identification of dominant solute-(water)_n clusters in an aqueous solution. In this thesis, the challenge of the interpretation of IR and VCD features of chiral

molecules in water is performed via the *clusters-in-a-liquid* solvation model developed by our research group.^[46] The main idea of the *clusters-in-a-liquid* solvation model is that the experimental IR and VCD features of chiral molecules in water are generated not by the chiral solute itself but by the solute-(water)_n clusters. Therefore, the *clusters-in-a-liquid* solvation model uses the experimentally observed VCD features of chiral molecules as a guidance in the identification of the long-lived solute-(water)_n clusters in water. The induced VCD signatures of water molecules^[47] due to explicit chiral solute-water interactions play an especially vital role in the recognition of the long-lived solute-(water)_n clusters in water. In the *clusters-in-a-liquid* solvation model, the implicit solvation effects generated in a chiral solute by the rest of the water molecules in the bulk medium are captured through the PCM of water.

2.3 References

1. G. Holzwarth, E. C. Hsu, H. S. Mosher et al., *J. Am. Chem. Soc.*, **1974**, *96*, 251–252.
2. L. A. Nafie, J. C. Cheng, P. J. Stephens, *J. Am. Chem. Soc.*, **1975**, *97*, 3842–3843.
3. L. A. Nafie, T. A. Keiderling, P. J. Stephens, *J. Am. Chem. Soc.*, **1976**, *98*, 2715–2723.
4. a) L. A. Nafie, M. Diem, *Appl. Spectrosc.*, **1979**, *33*, 130–135; b) L. A. Nafie, M. Diem, D. W. Vidrine, *J. Am. Chem. Soc.*, **1979**, *101*, 496–498.
5. E. D. Lipp, C. G. Zimba, L. A. Nafie, *Chem. Phys. Lett.*, **1982**, *90*, 1–5.
6. K.W. Busch, M. A. Busch, (Eds), *Chiral Analysis: Instrumental aspects of chiroptical detection*, Elsevier, Amsterdam, 2006.
7. L. A. Nafie, *Vibrational Optical Activity: Principles and Applications*, John Wiley and Sons, Ltd., Chichester, 2011.
8. a) E. Whittle, D. A. Dows, G. C. Pimentel, *J. Chem. Phys.*, **1954**, *22*, 1943; b) E. D. Becker, G. C. Pimentel, *J. Chem. Phys.*, **1956**, *25*, 224; c) I. Norman, G. Porter, *Nature (London)*, **1954**, *174*, 58.
9. a) M. Van Thiel, E. D. Becker, G. C. Pimentel, *J. Chem. Phys.*, **1957**, *27*, 95; b) M. Van Thiel, E. D. Becker, G. C. Pimentel, *J. Chem. Phys.*, **1957**, *27*, 486; c) D. W. Schlosser, F. Devlin, K. Jalkanen, P. J. Stephens, *Chem. Phys. Lett.*, **1982**, *88*, 286.

-
10. a) I. R. Dunkin, *Matrix Isolation Techniques*, Oxford University Press, New York, 1998; b) J. W. L. Kohler, *Sci. Amer.*, **1965**, *212*, 119; c) M. Moskovits, G. A. Ozin, (Editors) *Cryochemistry*, Wiley-Interscience, New York, 1976; d) H. E. Hallam, (Editor) *Vibrational Spectroscopy of Trapped Species*, J. Wiley, London, 1973.
11. a) D. W. Schlosser, F. Devlin, K. Jalkanen, P. J. Stephens, *Chem. Phys. Lett.*, **1982**, *88*, 286; b) D. O. Henderson, P. L. Polavarapu, *J. Am. Chem. Soc.*, **1986**, *108*, 7110; c) G. Tarczay, G. Magyarfalvi, E. Vass, *Angew. Chem. Int. Ed.*, **2006**, *45*, 1775–1777.
12. W.E. Gifford, R.C. Longworth, *Adv. Cryog. Eng.*, **1966**, *11*, 171.
13. a) M. A. Lowe, G. A. Segal, P. J. Stephens, *J. Am. Chem. Soc.*, **1986**, *108*, 248–256.
14. a) P. J. Stephens, *J. Phys. Chem.*, **1985**, *89*, 748–752.
15. a) N. V. Cohan, H. F. Hameka, *J. Am. Chem. Soc.*, **1966**, *88*, 2136; b) T. R. Faulkner, C. Marcott, A. Moscovitz, J. Overend, *J. Am. Chem. Soc.*, **1977**, *99*, 8160.
16. J. A. Schellman, *J. Chem. Phys.*, **1973**, *58*, 2882.
17. G. Holzwarth, I. Chabay, *J. Chem. Phys.*, **1972**, *57*, 1632.
18. C. J. Barnett, A. F. Drake, R. Kuroda, S. F. Mason, *Mol. Phys.*, **1980**, *41*, 455.
19. a) L. A. Nafie, T. H. Walnut, *Chem. Phys. Lett.*, **1977**, *49*, 441; b) T. H. Walnut, L. A. Nafie, *Chem. Phys.*, **1977**, *67*, 1501.
20. a) K. L. C. Hunt, R. A. Harris, *J. Chem. Phys.*, **1991**, *94*, 6995; b) P. Lazzeretti, M. Malagoli, R. Zanasi, *Chem. Phys. Lett.*, **1991**, *179*, 297.
21. a) L. A. Nafie, T. B. Freedman, *J. Phys. Chem.*, **1983**, *78*, 7108; b) R. Dutler, A. Rauk, *J. Am. Chem. Soc.*, **1989**, *111*, 6957; c) D. Yang, A. Rauk, *J. Chem. Phys.*, **1992**, *97*, 6517.
22. P.J. Stephens, *J. Phys. Chem.*, **1987**, *91*, 1712–1715.
23. A. D. Buckingham, P. W. Fowler, P. A. Galwas, *Chem. phys.*, **1987**, *112*, 1–14.
24. W. B. Person, J. H. Newton, *J. Chem. Phys.*, **1974**, *61*, 1040.
25. a) B. G. Johnson, M. J. Frisch, *Chem. Phys. Lett.*, **1993**, *216*, 133–140; b) B. G. Johnson, M. J. Frisch, *J. Chem. Phys.*, **1994**, *100*, 7429–7442.
26. J. R. Cheeseman, M. J. Frisch, F. J. Devlin, P. J. Stephens, *Chem. Phys. Lett.*, **1996**, *252*, 211–220.

-
27. P. J. Stephens, F. J. Devlin, J. R. Cheeseman, *VCD Spectroscopy for Organic Chemists*, CRC Press, Taylor & Francis Group, Boca Raton, FL, USA, 2012.
28. W. J. Hehre, L. Radom, P. V. R. Schleyer, J. A. Pople, *Ab Initio Molecular Orbital Theory*, John Wiley & Sons, New York, 1986.
29. a) P. J. Stephens, K. J. Jalkanen, F. J. Devlin, C. F. Chabalowski, *J. Phys. Chem.*, **1993**, *97*, 6107–6110; b) F. J. Devlin, P. J. Stephens, *J. Am. Chem. Soc.*, **1994**, *116*, 5003–5004; c) D. Y. Yang, A. Rauk, *J. Chem. Phys.*, **1994**, *100*, 7995–8002.
30. a) P. Hohenberg, W. Kohn, *Phys. Rev.*, **1964**, *136*, 3B, B864; b) W. Kohn, L. J. Sham, *Phys. Rev.*, **1965**, *140*, A1133; c) J. K. Labanowski, J. W. Andzelm, *Density functional Methods in Chemistry*, Springer-Verlag: New York, 1991.
31. P. J. Stephens, F. J. Devlin, *Chirality*, **2000**, *12*, 172–179.
32. a) A. D. Becke, *J. Chem. Phys.*, **1993**, *98*, 1372–1377; b) A. D. Becke, *J. Chem. Phys.*, **1993**, *98*, 5648–5652.
33. A.D. Becke, *Phys. Rev. A*, **1988**, *38*, 6, 3098.
34. C. Lee, W. Yang, and R.G. Parr, *Phys. Rev. B*, **1988**, *37*, 2, 785.
35. J. P. Perdew, Y. Wang, *Phys. Rev. B*, **1992**, *45*, 23, 13244.
36. P. J. Stephens, F. J. Devlin, C. F. Chabalowski, M. J. Frisch, *J. Phys. Chem.*, **1994**, *98*, 11623–11627.
37. a) P. J. Stephens, F. J. Devlin, C. F. Chabalowski, M. J. Frisch, *J. Phys. Chem.*, **1994**, *98*, 11623; b) T. Kuppens, W. Langenaeker, J. P. Tollenaere, P. Bultinck, *J. Phys. Chem. A*, **2003**, *107*, 542; c) T. Kuppens, K. van der Vandyck, J. Eycken, W. Herrebout, B. J. van der Veken, P. Bultinck, *J. Org. Chem.*, **2005**, *70*, 9103; d) T. Kuppens, W. Herrebout, B. van der Veken, P. Bultinck, *J. Phys. Chem. A*, **2006**, *110*, 10191; e) Ducasse, F. Castet, A. Fritsch, I. Huc, T. Buffeteau, *J. Phys. Chem. A*, **2007**, *111*, 5092; f) T. Brotin, D. Cavagnat, J. P. Dutasta, T. Buffeteau, *J. Am. Chem. Soc.*, **2006**, *128*, 5533.
38. W. J. Hehre, R. Ditchfield, J. A. Pople, *J. Chem. Phys.*, **1972**, *56*, 5, 2257.
39. T. H. Dunning Jr, *J. Chem. Phys.*, **1989**, *90*, 1007.
40. F. Weigend, F. Furche, R. Ahlrichs, *J. Chem. Phys.*, **2003**, *19*, 12753.
41. a). Gaussian 09, Revision B.01, M. J. Frisch, G. W. Trucks, H. B. Schlegel, G. E. Scuseria, M. A. Robb, J. R. Cheeseman, G. Scalmani, V. Barone, B. Mennucci, G. A. Petersson, H. Nakatsuji, M. Caricato, X. Li, H. P. Hratchian, A. F. Izmaylov, J. Bloino, G. Zheng, J. L. Sonnenberg, M. Hada, M.

-
- Ehara, K. Toyota, R. Fukuda, J. Hasegawa, M. Ishida, T. Nakajima, Y. Honda, O. Kitao, H. Nakai, T. Vreven, J. A. Montgomery, Jr., J. E. Peralta, F. Ogliaro, M. Bearpark, J. J. Heyd, E. Brothers, K. N. Kudin, V. N. Staroverov, R. Kobayashi, J. Normand, K. Raghavachari, A. Rendell, J. C. Burant, S. S. Iyengar, J. Tomasi, M. Cossi, N. Rega, J. M. Millam, M. Klene, J. E. Knox, J. B. Cross, V. Bakken, C. Adamo, J. Jaramillo, R. Gomperts, R. E. Stratmann, O. Yazyev, A. J. Austin, R. Cammi, C. Pomelli, J. W. Ochterski, R. L. Martin, K. Morokuma, V. G. Zakrzewski, G. A. Voth, P. Salvador, J. J. Dannenberg, S. Dapprich, A. D. Daniels, Ö. Farkas, J. B. Foresman, J. V. Ortiz, J. Cioslowski, D. J. Fox, Gaussian, Inc., Wallingford CT, 2009; b) Gaussian 09, Revision D.01, M. J. Frisch, G. W. Trucks, H. B. Schlegel, G. E. Scuseria, M. A. Robb, J. R. Cheeseman, G. Scalmani, V. Barone, B. Mennucci, G. A. Petersson, H. Nakatsuji, M. Caricato, X. Li, H. P. Hratchian, A. F. Izmaylov, J. Bloino, G. Zheng, J. L. Sonnenberg, M. Hada, M. Ehara, K. Toyota, R. Fukuda, J. Hasegawa, M. Ishida, T. Nakajima, Y. Honda, O. Kitao, H. Nakai, T. Vreven, J. A. Montgomery, Jr., J. E. Peralta, F. Ogliaro, M. Bearpark, J. J. Heyd, E. Brothers, K. N. Kudin, V. N. Staroverov, R. Kobayashi, J. Normand, K. Raghavachari, A. Rendell, J. C. Burant, S. S. Iyengar, J. Tomasi, M. Cossi, N. Rega, J. M. Millam, M. Klene, J. E. Knox, J. B. Cross, V. Bakken, C. Adamo, J. Jaramillo, R. Gomperts, R. E. Stratmann, O. Yazyev, A. J. Austin, R. Cammi, C. Pomelli, J. W. Ochterski, R. L. Martin, K. Morokuma, V. G. Zakrzewski, G. A. Voth, P. Salvador, J. J. Dannenberg, S. Dapprich, A. D. Daniels, Ö. Farkas, J. B. Foresman, J. V. Ortiz, J. Cioslowski, and D. J. Fox, Gaussian, Inc., Wallingford CT, 2009.
42. a) A. D. Becke, E. R. Johnson, *J. Chem. Phys.*, **2005**, *123*, 154101; b) S. Grimme, S. Ehrlich, L. Goerigk, *J. Comput. Chem.*, **2011**, *32*, 1456–1465.
43. R. Krishnan, J. S. Binkley, R. Seeger, J. A. Pople, *J. Chem. Phys.*, **1980**, *72*, 650–654.
44. J. R. Chessman, J. Frisch, J. Devlin, J. P. Stephens, *Chem. Phys. Lett.*, **1996**, *252*, 211–220.
45. B. Mennucci, J. Tomasi, R. Cammi, J. R. Cheeseman, M. J. Frisch, F. J. Devlin, S. Gabriel, P. J. Stephens, *J. Phys. Chem. A*, **2002**, *106*, 6102–6113.
46. A. S. Perera, J. Thomas, M. R. Poopari, Y. Xu, *Front. Chem.*, **2016**, *4*, 1–17.
47. a) M. Losada, H. Tran, Y. Xu, *J. Chem. Phys.*, **2008**, *128*, 014508; b) G. Yang, Y. Xu, *J. Chem. Phys.*, **2009**, *130*, 164506; c) M. Losada, P. Nguyen, Y. Xu, *J. Phys. Chem. A*, **2008**, *112*, 5621–5627; d) M. Losada, Y. Xu, *Phys. Chem. Chem. Phys.*, **2007**, *9*, 3127–3135.

Chapter 3

IR, Raman and Vibrational Optical Activity Spectra of Methyl Glycidate in Chloroform and Water: The *Clusters-in-a-Liquid* Solvation Model

The contents of this chapter have been copied and/or adapted from the following publication: A. S. Perera, J. Cheramy, C. Merten, J. Thomas, Y. Xu, *Chem. Phys. Chem.*, **2018**, *19*, 17, 2234–2242.

3.1 Introduction

Vibrational circular dichroism (VCD) and Raman optical activity (ROA) have been utilized increasingly as two effective experimental techniques for the determination of absolute configurations and conformations of chiral molecules in solutions.^[1,2] This is in part due to the significant developments in the associated instrumentation^[3,4] and *ab initio* density functional theory (DFT)^[5,6] treatment in the last two decades. More recently, the applications of these two chiroptical techniques have been extended to the studies of intermolecular interactions directly in solution, in particular chiral solute-solvent interactions.^[7, 8, 9] These studies pointed out the importance of both explicit and implicit solute-solvent interactions in modelling solvent effects, for example, for solvents that can serve as a H-bond donor/acceptor to a solute. For many common solvents, such as chloroform and dimethyl sulfoxide (DMSO), one can account adequately for solvent effects by constructing small solute-solvent H-bonded complexes and placing them in a bulk solvent, which is commonly modelled by the polarizable continuum model (PCM).^[5,6, 10]

The situation in aqueous solution, however, is more complicated. First, water is capable of forming extensive H-bonding networks, making it difficult to justify how many water molecules should be included. Second, H-bonding networks in bulk water are known to exhibit short time dynamics.^[11,12] One may, therefore, question the life time of the chiral solute-water_n clusters in aqueous solution. For these reasons, some researchers advocate a molecular dynamics (MD) simulation approach and sample several thousand snapshots in order to catch such dynamics in modelling water solvent effects.^[13,14,15] Some researchers use the combined explicit and implicit model discussed above and have dubbed it the “ad hoc hydration” model^[10] since the selection of possible chiral solute-water_n complexes seemed random. These approaches will be commented on further in the main text.

While many experimental spectroscopic techniques, such as NMR, ultrafast far-IR (FIR), IR, and Raman have been utilized to investigate H-bonding interactions between (chiral) solutes and water,^[16] it is often challenging to distinguish the water molecules H-bonded to a solute from those in the bulk and to identify the solute-water_n binding topologies.^[17,18] In this study, we utilize four vibrational spectroscopies, namely IR, VCD, Raman, and ROA to evaluate solvent effects on methyl glycidate (MG), methyl oxiranecarboxylate (according to IUPAC nomenclature), in CCl₄ and in water with the aid of DFT calculations. One main goal is to illustrate that VCD and ROA, especially induced solvent VCD features,^[19] offer the unique opportunity to differentiate water molecules that form *long-lived* direct contacts with the chiral solute from those in the bulk water environment. For example, the induced water VCD signatures at the water bending vibrational region were observed experimentally,^[20, 21, 22, 23] and such induced chirality VCD features are due exclusively to the water molecules that are part of the chiral solute-water_n complexes. A second goal is to evaluate the utility of the recently proposed “*clusters-in-a-liquid*” solvation model.^[24] This model uses the combined explicit and implicit solvation approach discussed above; more importantly, it offers insight into the construction and selection of the chiral solute-water_n complexes. In particular, this model recognizes that the main species in aqueous solution are these *long-lived* chiral solute-water_n clusters rather than the chiral solute itself. We will discuss the lifetime of these

hydration complexes in light of the recent MD modelling report.^[25] We further aim to test this model stringently with both IR and VCD as well as Raman and ROA spectra.

MG is selected for a number of reasons. First, MG exhibits two main conformational preferences as revealed by rotational spectroscopic studies of MG and its monohydrate in the gas phase.^[26, 27] This system, therefore, allows a detailed examination on how solvents alter the conformational ratio. Second, MG contains an epoxy, a carbonyl, and a methyl ester functional groups, since these functional groups are polarized permanent bond dipoles, they can form strong H-bonding interactions with the highly polarized permeant bond dipoles of water molecules. Third, MG has good solubility in both polar and nonpolar solvents, allowing a direct comparison to be made between the solute-solvent interactions formed in the polar and nonpolar solvent mediums. Finally, MG is also relatively small, suitable for high-level *ab initio* modelling of the intermolecular H-bonding interactions with water.

3.2 Experimental Section

3.2.1 Experimental Details

Both S-MG (98%) and R-MG (97%) were obtained from Sigma-Aldrich and were used without further purification. The IR and VCD measurements were performed using a Bruker Vertex 70 Fourier transform IR spectrometer with a PMA50 VCD model with 4 cm^{-1} resolution at room temperature. A variable path length cell that contains two BaF_2 windows and a low pass filter of 1800 cm^{-1} was used for the measurements. The solutions for the IR and VCD measurements were prepared using deionized water or reagent grade (99.9%) CCl_4 . To avoid saturation by strong water absorption at $\sim 1640 \text{ cm}^{-1}$, a high concentration (6 M) was used. In addition, the sample was placed directly between the pair of BaF_2 windows, and a short path length of $\sim 3 \text{ }\mu\text{m}$, estimated as before.^[28] The IR and VCD measurements in CCl_4 were carried out with a concentration of 0.16 M and a path length of 25 μm . The total measurement time is about 3 to 3.5 h. The final VCD spectra in H_2O and CCl_4 were obtained by using the well-known opposite enantiomer background

correction method, i.e., $(R-S)/2$.^[3] The IR spectra in water and CCl₄ were solvent corrected.

Raman and ROA spectra of S-MG in H₂O were measured using a BioTools ChiralRaman2X spectrometer (532 nm excitation laser) with an illumination time of 1.029 s in a quartz cell. Only S-MG was used because R-MG contained a trace amount of fluorescent impurity which interferes with the measurement. The water solution (6 M) was measured for 2048 complete cycles (32 scans per cycle) at a laser power of ~90 mW at the sample. A baseline correction was applied to both the Raman and ROA spectra.

3.2.2 Computational Details

All geometry optimizations, harmonic frequency calculations, IR, VCD, Raman, and ROA intensity calculations were carried out using Gaussian09 program package.^[29] We note that Raman and ROA intensities were computed in a “one-step” procedure^[5] using the gauge-including atomic orbitals (GIAOs) with an incident light frequency of 532 nm. The calculations were done with the Becke, three-parameter, Lee-Yang-Parr (B3LYP) functional^[30] and the 6-311++G(2d,p) basis set,^[31] and with Grimme’s dispersion correction,^[32] including the Becke-Johnson damping (D3BJ)^[33] factor. The B3LYP functional and the basis set were chosen for their proven accuracy in simulating VCD and ROA intensities.^[5, 34] We also used the aug-cc-pVTZ basis set and obtained very similar Raman and ROA spectra (not shown) for the MG conformers. In addition, the functional and basis set combination above has been used extensively in rotational spectroscopic studies of structures of non-covalently bonded molecular aggregates and their complexes with water and demonstrated excellent agreements with the experimental data.^[35]

The implicit solvent effects were modelled using the integral equation formalism (IEF) version of PCM.^[36] All optimized geometries of the molecule and its clusters with water were carried out in the gas phase and in the two solvents modelled by PCM for comparison with the experiment. All optimized geometries were confirmed to be true minima without any imaginary frequencies.

The IR and VCD spectra were simulated using Lorentzian line shapes of 4 cm^{-1} and 8 cm^{-1} halfwidth at half height (HWHH) for CCl_4 and water, respectively, while Lorentzian line shapes of 10 cm^{-1} (HWHH) were used for the simulation of Raman and ROA spectra. We note that the simulation of Raman and ROA spectra with GaussView does not include comprehensively the temperature factor, which is important for correct intensities (See Eq. (1) in Ref. 2). This effect is particularly noticeable in the low frequency region where intensities of bands were severely underestimated.^[2,37] A script^[38] which properly accounts for the Boltzmann factors was used in the current simulations. No frequency scaling factors were used.

3.3 Results and Discussion

3.3.1 Experimental IR and VCD Spectra of MG in CCl_4 and H_2O

In Figure 3.1, we compare the experimental IR and VCD spectra of MG in CCl_4 and water in the $1000\text{--}1800\text{ cm}^{-1}$ region. The IR spectra of MG in water and CCl_4 display similar band features, although there are several noticeable differences. In the $1700\text{--}1800\text{ cm}^{-1}$ region, the only IR feature observed shows a narrow splitting in CCl_4 , whereas it is a broader band in water, which is red shifted (bathochromic shifted) by $\sim 10\text{ cm}^{-1}$ compared to that in CCl_4 . The IR feature discussed above can be assigned easily to the carbonyl stretching vibrational mode. The red shift (bathochromic shift) in water suggests the presence of H-bonding interactions between the $\text{C}=\text{O}$ of MG and H_2O . Next, there is an extra IR band in the water bending region, even after solvent correction. In the region below 1350 cm^{-1} , there are some minor differences in band intensity in these two solvents.

The VCD spectra in general appear much different in water and in CCl_4 . The most significant difference is in the $1600\text{--}1800\text{ cm}^{-1}$ region where a strong positive VCD feature centred at $\sim 1640\text{ cm}^{-1}$ is observed in water and not in CCl_4 . Since water is achiral, we tentatively attribute the experimental VCD feature at 1640 cm^{-1} to the H-bonded MG-water_n complexes. In Figure A1, Appendix A, the raw VCD spectra of both S-MG and R-MG in water and in CCl_4 are provided to show their good mirror-image quality. In addition, the $-/+$ VCD feature in CCl_4 in the $1700\text{--}1800\text{ cm}^{-1}$ region becomes just a

positive VCD signal in water. There are also many more changes in the lower cm^{-1} region between CCl_4 and water. Overall, IR and VCD spectra, especially VCD spectra, of MG in CCl_4 and in H_2O appear to be quite different, indicating the presence of some very different solute-solvent interactions in these two solvents. Please note that R-MG was used for all modelling and experimental spectra, unless otherwise specified.

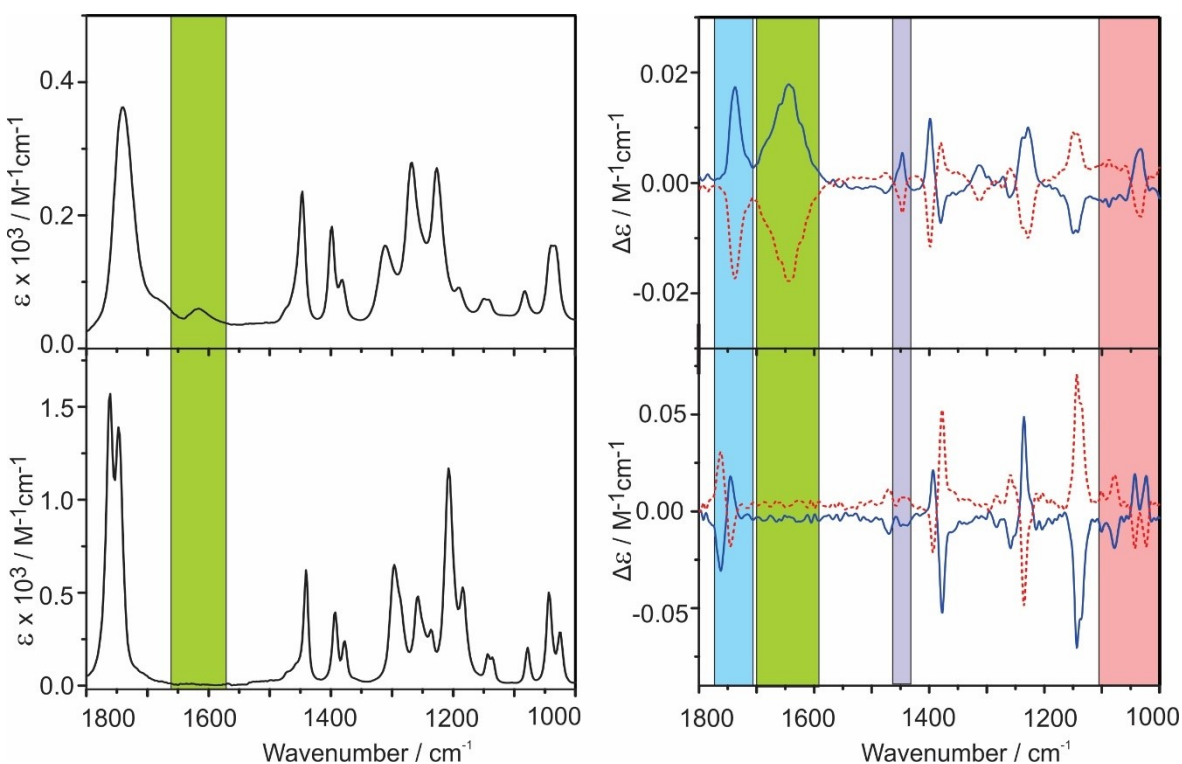


Figure 3.1. Comparisons of the experimental IR (left) and VCD (right) spectra of MG in water (top) and in CCl_4 (bottom). In addition, VCD spectra (dashed lines) of S-MG are presented.

3.3.2 Implicit Solvation

The conformers of MG had been investigated in the gas phase experimentally using rotational spectroscopy and theoretically at the MP2/6-311++G(2d,p) level of theory.^[26] The same conformers were identified in this study in the gas phase, consistent with the previous experimental rotational spectroscopic results. MG has two main conformers, MG-I and MG-II (Figure 3.2), where the epoxy and carbonyl groups are in the *syn* or *anti* relative orientation, respectively.

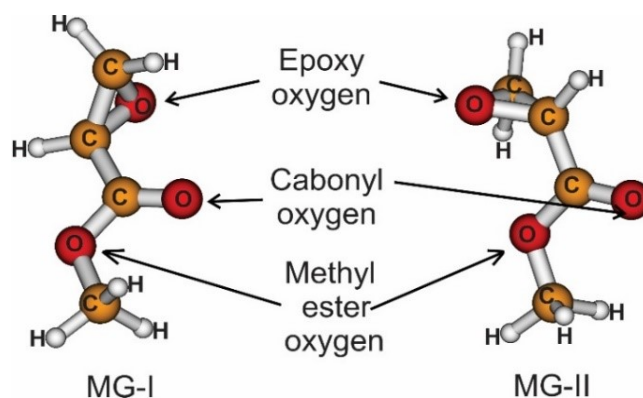


Figure 3.2. The optimized geometries of the two most stable conformers of MG in the gas phase.

The computed relative free energies and Boltzmann factors (Pop) at 298 K for the MG-I and MG-II conformers in the gas phase, in CCl₄ and in water are given in Table 3.1. The calculated Boltzmann factors indicate that an environment with a larger dielectric constant clearly favours MG-I over MG-II. This preference can be understood from the fact that MG-I has a much larger electric dipole moment than MG-II.^[26]

Table 3.1. The relative free energies, ΔG (in kJ mol⁻¹), and Boltzmann factors (Pop) at 298 K (in %), of the two main MG conformers under three environments.

Conformer	Gas phase		CCl ₄		H ₂ O	
	ΔG	Pop	ΔG	Pop	ΔG	Pop
MG-I	0.00	53.2	0.00	54.6	0.00	69.8
MG-II	0.32	46.5	0.46	45.4	2.07	30.2

The calculated IR and VCD spectra of MG-I and MG-II in the PCM of CCl₄ are depicted in Figure 3.3, while the corresponding results in the gas phase are given in Figure A2, Appendix A. There is little change in the IR or VCD spectra in going from the gas phase to the PCM of CCl₄. This is not surprising since CCl₄ has a fairly small dielectric constant. On the other hand, the IR spectrum of MG-I appears very different compared to that of MG-II, especially in the region below 1300 cm⁻¹. The corresponding vibrational motions in MG-I and MG-II are labelled as 1, 2, 3,... and 1', 2', 3',... respectively, based on a detailed examination of the vibrational motions. A brief summary of the vibrational

description of these bands is given in Table A1, Appendix A. If one ignores 6 and 6', the mode with the largest frequency shift, one can correlate the rest of the bands based on their frequency ordering in a relatively straightforward manner, although the relative intensity pattern changes a bit from MG-I to MG-II. Different orientations of the epoxy and carbonyl groups produce much different electrostatic potential diagrams of MG-I and MG-II (Figure A4, Appendix A). The frequency of band 6, largely related to the C—O_{ester} stretching motion, moves to a much higher frequency in 6'. This can be understood in terms of a much larger stereoelectronic hindrance in MG-II where O_{epoxy} and O_{ester} are only about 2.7 Å apart, in comparison to that in MG-I where these two atoms are on opposite sides. Similarly, one can rationalize the higher C=O stretching frequency (11) in MG-I where O_{carbonyl} is close to O_{epoxy}, while in MG-II, O_{carbonyl} is far away from both O_{ester} and O_{epoxy}. The related VCD spectra exhibit an even larger difference between MG-I and MG-II. Such sensitivity to structural dihedral angles is common with VCD (see Ref. ³⁹ for a pictorial explanation).

A cursory inspection of the experimental and theoretical spectra shows that both conformers make significant contributions to the experimental IR and VCD spectra. The comparisons between experimental IR and VCD spectra of MG in CCl₄ and the population weighted ones with the PCM of CCl₄ are provided in Figure 3.3. Overall, the Boltzmann-weighted IR and VCD spectra of MG in the PCM of CCl₄ correctly predict most of the experimental spectral features, including the carbonyl stretching doublet in the IR spectrum and the corresponding bisignate VCD features. We note that the Boltzmann weighted gas phase IR and VCD (Figure A2, Appendix A) appear quite similar to those in the PCM of CCl₄. All these comparisons confirm that CCl₄ is a fairly inert solvent and exercises little influence on MG.

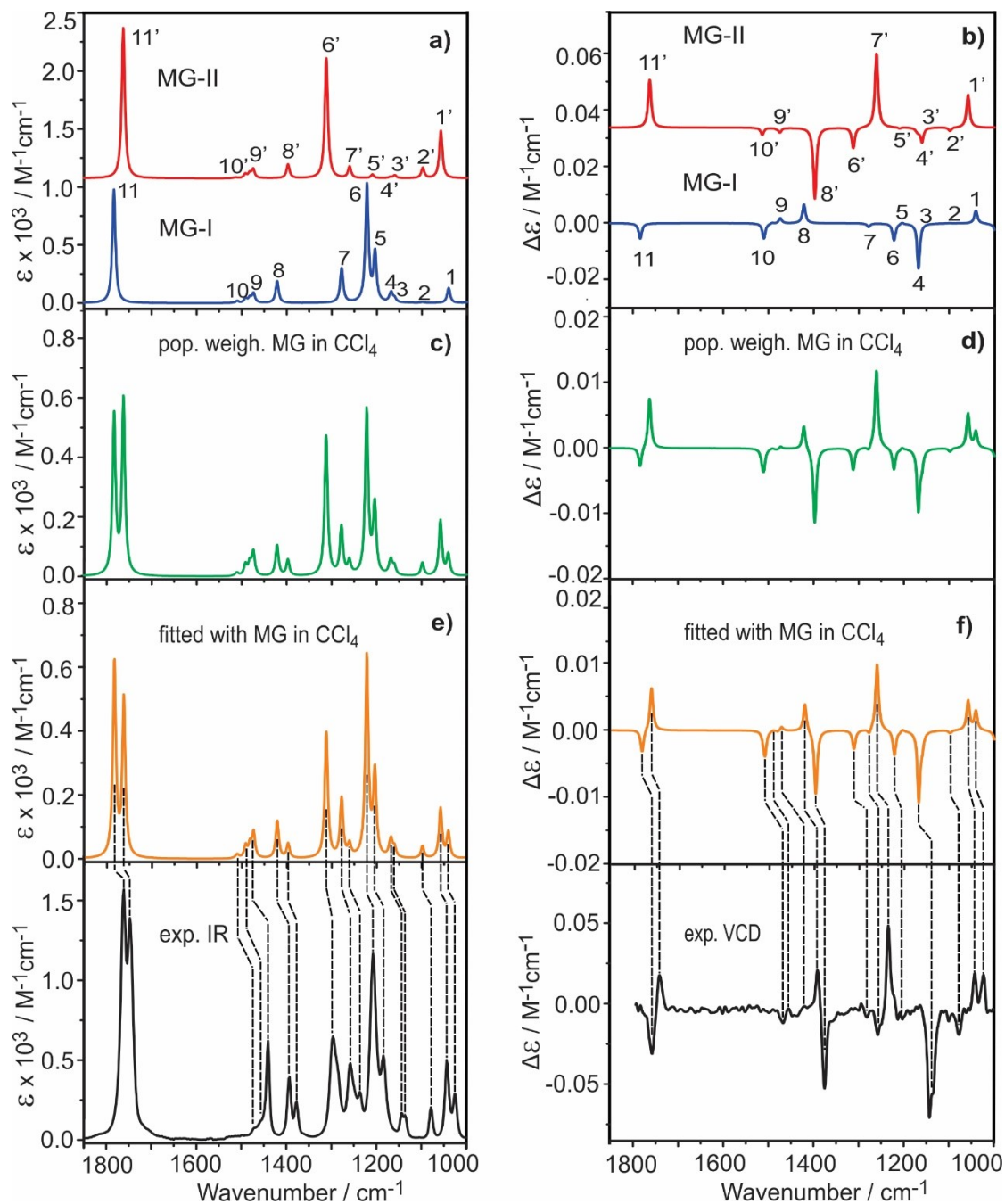


Figure 3.3. Comparison of the experimental IR (bottom-left) and VCD (bottom-right) spectra of MG in CCl_4 with the corresponding simulated IR (a) and VCD (b) spectra of the MG-I and MG-II conformers in the PCM of CCl_4 , the population weighted IR (c) and VCD (d) spectra based on their relative free energies, and the fitted IR (e) and VCD (f) spectra with $C_{\text{MG-I}}=0.62$ and $C_{\text{MG-II}}=0.38$. Please see text for details.

Since MG-I and MG-II have very distinctive IR and VCD features, a small change in the relative Boltzmann factors may alter the appearance of the final Boltzmann-weighted

IR and VCD spectra. In order to fine tune the agreement between the experimental and theoretical spectra of MG in CCl₄, we have adopted a spectral fitting procedure used in a number of previous investigations.^[12,40] The fitting equation is given below:

$$\sigma = \int_{V_i}^{V_f} \left(g \left(IR_{\text{exp}} - \sum_n (c_n IR_{n,\text{calc}}) \right) \right)^4 + \int_{V_i}^{V_f} \left(VCD_{\text{exp}} - \sum_n (c_n VCD_{n,\text{calc}}) \right)^4 \quad (3.1)$$

where $IR_{n,\text{calc}}$ and $VCD_{n,\text{calc}}$ are the theoretical IR and VCD spectra of the n^{th} conformer, i.e., the MG-I and MG-II conformers, while IR_{exp} and VCD_{exp} are the experimental IR and VCD spectra, respectively; c_n refers to the weight (or population factor) of the n^{th} conformer to be obtained from the fitting procedure and the summation over all conformers, i.e. $\sum_n c_n$, should be 1; g denotes the anisotropy ratio between VCD and IR intensities. Instead of the usual least square fitting routine, the exponent in the above equation was set to 4 to minimize influences arising from noise and to obtain a positive value for σ .^[12] The fitting range, associated with the V_i and V_f values, was set to 1000–1800 cm^{-1} . The σ function is minimized through the variation of c_n factors of conformers so that the c_n factors are determined at the minimum value of σ function. In applying this fitting procedure, we implicitly acknowledge that the calculated IR and VCD features of conformers are trustworthy and can be used to identify specific conformers, whereas the calculated abundance may deviate from the actual experimental ones. Such practice has been used frequently in previous IR and/or VCD spectroscopic studies.^[41] Overall, the fitted IR and VCD spectra generate similar or arguably better agreement with the experimental data than the DFT population weighted ones. For example, the agreement with the experimental data for the relative intensity ratios of the VCD bisignate features around 1770 cm^{-1} and 1050 cm^{-1} seems better. The fitted parameters suggest a slightly stronger preference for MG-I versus MG-II than predicted.

The situation with water is much different from CCl₄. The calculated IR and VCD spectra of MG-I and MG-II in the PCM of water and the related population-weighted ones are compared with the experimental data in Figure A3, Appendix A. While different dielectric constants of the environments modify the relative abundance of the MG-I versus MG-II conformer greatly, the associated conformer IR and VCD spectra in gas phase, CCl₄ and water reveal only minor differences. One interesting variation is that the VCD band 7 (corresponding mainly to the C—O_{epoxy} stretching vibrations) of MG-I changes from a small positive band in the gas phase, to a small negative band in CCl₄, and finally to a medium negative band in H₂O, reflecting the interesting effect of dielectric environment on VCD features. Obviously, the simulated IR and VCD spectra with the PCM of water generate most of the experimental features in the 1000–1500 cm⁻¹ region, although some exceptions were noted. For example, the medium negative VCD feature predicted in the 1200–1250 cm⁻¹ region is not present in the experiment spectrum. The big discrepancy appears in the 1600–1800 cm⁻¹ region. For example, the eminent experimental VCD feature at ~1640 cm⁻¹ is not present in the simulated spectrum. The implicit solvation model, which works beautifully for CCl₄, fails for H₂O. Unlike CCl₄, water is a protic solvent, and its strong intermolecular H-bonding interactions with MG need to be considered in order to reproduce the experimental data. This is elaborated in the following section.

3.3.3 The *Clusters-in-a-Liquid* Solvation Model for IR and VCD of MG in Water

As mentioned before, it is challenging to model the explicit interactions between MG and water for a number of reasons. First, water is unique in its ability to form extensive H-bonding networks, making it challenging to evaluate the number of explicit water molecules needed in order to capture the experimental spectral signatures adequately. Second, it is unclear how the dynamic behaviour of water molecules surrounding a chiral solute influences the spectra observed. Several approaches have been used by researchers.

One elaborative approach is to utilize classical MD or Car-Parrinello MD (CPMD) to create a chiral solute in equilibrium with a box of water molecules.^[10,12] Very recently, the first fully *ab initio* MD calculation of the dynamical VCD spectrum of propylene oxide in the liquid phase was reported. It reproduced much of the experimental data, although the theoretical prediction of the induced solvent VCD signal was still buried in simulation noise.^[42] Typically, in the MD approach, one would then choose a (somewhat arbitrary) radius from the chiral solute with some water molecules included, sample a large number (for example 2000) of snapshots, and finally place these in the PCM of water for subsequent geometry optimizations, harmonic frequency calculations, and IR and VCD intensity calculations.^[10,12] The final simulated IR or VCD spectra are taken as the average of the IR or VCD spectra of all the snapshots, respectively. One main goal of this approach is to capture the potential dynamic fluctuation associated with the water molecules surrounding a chiral solute. On the other hand, it is not certain if the so-selected chiral solute-water_n clusters are important species in aqueous solution,^[10,43] and mixed outcomes have been reported.^[10,12]

The second method is the combined explicit and implicit solvation approach mentioned before. One main challenge is to decide how many water molecules to include in the chiral hydration clusters. Some of us used the radial distribution functions obtained from a MD simulation to aid in deciding the number of water molecules to be included.^[10,44] The *clusters-in-a-liquid* model applies the second approach but also provides guidelines for the selection of the small hydration clusters. One main hypothesis is that there are some relatively *long-lived*, *small* chiral hydration clusters in aqueous solution that are responsible for the observed spectra rather than the chiral solute itself.^[18] This hypothesis is based on the examination of the induced solvent VCD features of small prototype systems, such as propylene oxide^[18] and methyl lactate^[19] in water together with the related structural and energetic studies of their small hydration clusters, using rotational spectroscopy.^[45] In addition, it was suggested that typically just one water molecule is needed to be considered at each (strong) H-bonding site of a chiral solute. This is, in part, because in a number of previous studies, it was recognized that a more extensive H-bonded water network tends to generate unusually large multi-signate induced solvent VCD

features at the water bending region,^[18,19,20] which have not been detected experimentally. Furthermore, the recent MD simulation study of methyl lactate in water indicates that larger hydration clusters, such as the 1:2 chiral solute:water complexes, have a much shorter lifetime than the smaller 1:1 complexes.^[22] In terms of lifetime, it would also seem that the large hydration clusters with many water molecules simultaneously H-bonded to a chiral solute, which are used as MD snapshots, are less likely to be a main species compared to the smaller clusters with just one or two water molecules H-bonded to the solute at different sites at a time.

Applying the *clusters-in-a-liquid* model, we first constructed the 1:1 MG-H₂O complexes. The geometries of 14 optimized MG-H₂O complexes are shown in Figure 3.4, together with their relative free energy values and Boltzmann factors at room temperature. It is interesting to see how explicit and implicit solvation changes the conformational distribution. The H-bonding interaction with just one water molecule already creates a preferential stabilization effect for MG-II over MG-I in the PCM of water, with the theoretical abundance of MG-I:MG-II dropping to ~46%:54% versus 70%:30% with just the PCM of water. It is further interesting to note that while MG-II-H₂O-1 is the most preferred structure predicted in the PCM of water, MG-I-H₂O-1 is the most stable structure predicted and observed experimentally in the gas phase.^[27]

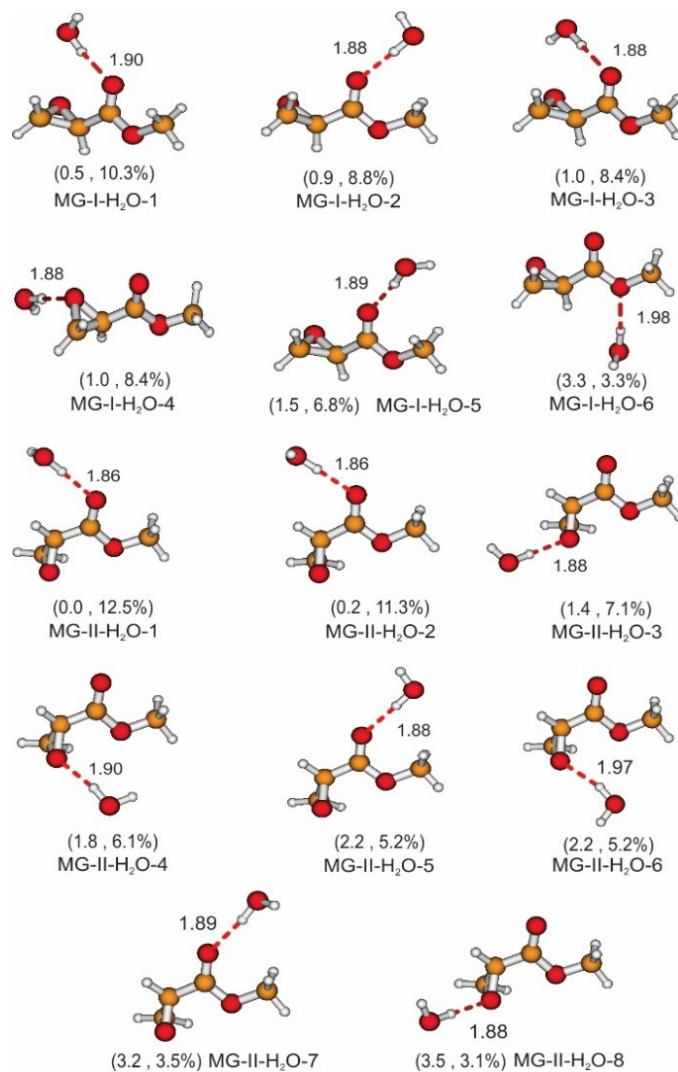


Figure 3.4. The optimized geometries of the MG-H₂O complexes with the PCM of water. The relative free energy (in kJ mol⁻¹) and the Boltzmann factor (%) at room temperature for each MG-H₂O complex are given in parenthesis. The intermolecular H-bond lengths (in Å) are indicated with dashed lines. The relative stabilities within the MG-I-H₂O and MG-II-H₂O series are indicated with an Arabic number, with 1 being the most stable in each case.

The conformer IR and VCD spectra of the monohydrates are summarized in Figure 3.5. The most striking new feature is the induced solvent VCD signature at the water bending band at ~ 1640 cm⁻¹. Not only does the VCD intensity vary a lot among different monohydrates, but also its signs, i.e., positive or negative. While most major VCD bands of MG-II remain similar as in its monomeric form, some more noticeable changes were predicted for MG-I-H₂O compared to MG-I, especially in the 1100–1400 cm⁻¹ region. In

addition, there are small vibrational frequency shifts in many bands among these hydrates, one reason for the generally broader width observed in water.

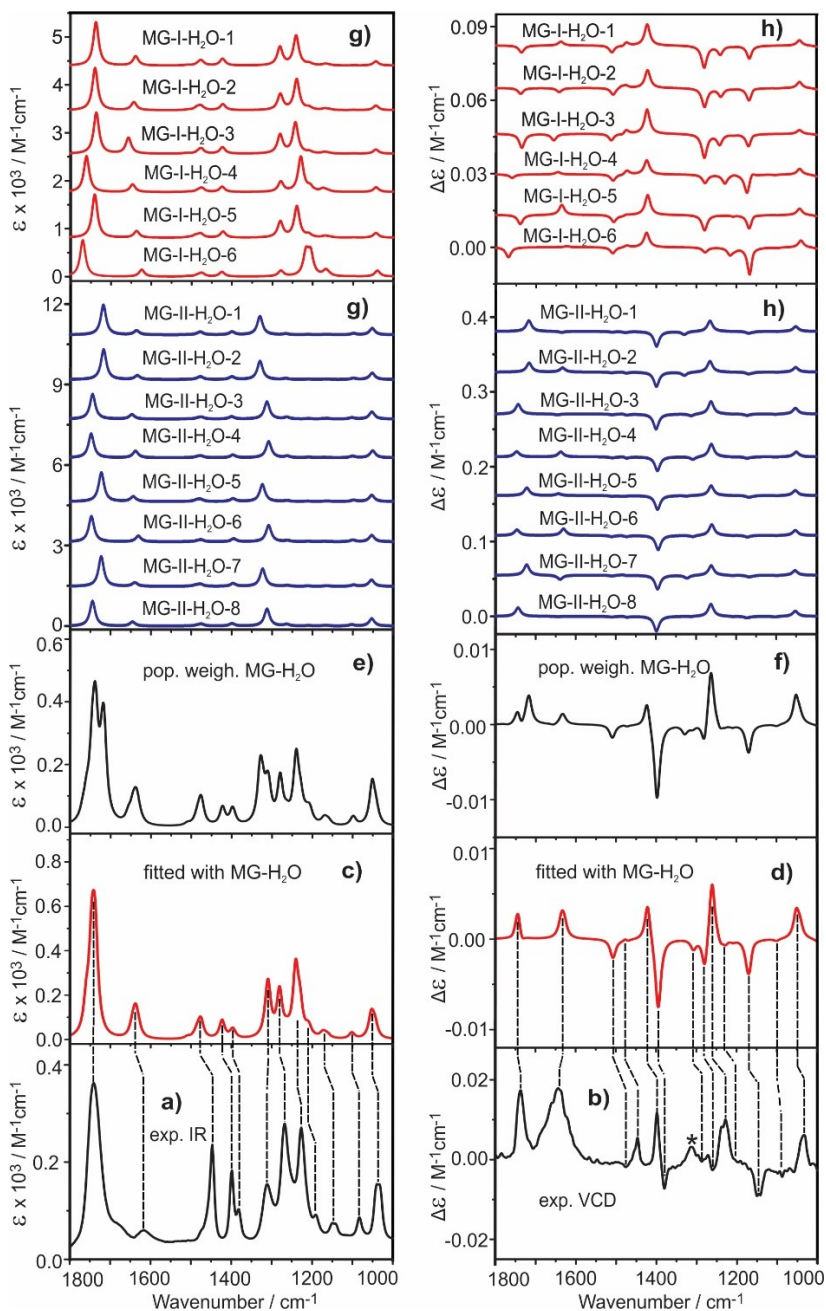


Figure 3.5. Comparisons of the experimental IR (a) and VCD (b) spectra of MG in water with the simulated IR (g) and VCD (h) conformer spectra of MG-H₂O in the PCM of water, the population weighted IR (e), VCD (f) spectra based on the calculated relative free energy of each MG-H₂O complex, and the fitted IR (c), VCD (d) spectra. Please see text for details regarding the fitting procedure and the contribution of each dominant species.

Also included in Figure 3.5 are the corresponding Boltzmann weighted IR and VCD spectra of MG-H₂O complexes in the PCM of water and the experimental IR and VCD spectra of MG in water. Although the experimental IR and the positive VCD signals at ~1640 cm⁻¹ generally are simulated by the Boltzmann weighted spectra, the C=O stretching region (1700–1800 cm⁻¹) is not reproduced well for both IR and VCD. It is noted that the C=O stretching bands of the MG-H₂O complexes show a very wide frequency distribution, much wider than the experimental band width of the main C=O band. Perhaps the more striking observation is that the experimental VCD C=O band is strongly positive, with a narrow band width. A closer examination indicates that all MG-I-H₂O complexes have a negative C=O stretching VCD band predicted, in contrast to the strong, positive VCD band observed. On the other hand, the simulated VCD spectra of MG-I-H₂O-1, MG-I-H₂O-4 and MG-I-H₂O-5 complexes have the positive induced solvent VCD bands at ~1650 cm⁻¹, consistent with the experimental data. Furthermore, the simulated VCD spectra of MG-II-H₂O-4 and MG-II-H₂O-6 complexes exhibit both positive VCD features at the C=O stretching region (1700–1800 cm⁻¹) and water bending band region (~1640 cm⁻¹), in agreement with the experiment. Clearly, both MG-I-H₂O and MG-II-H₂O complexes are required to model the experimentally observed IR and VCD features of MG in water.

Acknowledging that the IR and VCD spectral features generally are predicted correctly, whereas the relative stabilities of species in solution are much more challenging to predict correctly, we utilized the same spectral fitting procedure used in the case of MG in CCl₄. The resulting fitted IR and VCD spectra of MG-H₂O complexes in the PCM of water are presented in Figure 3.5. Overall, the fitted IR and VCD spectra provide very good agreement with the experimental data, noticeably better than the population weighted spectra. In particular, the experimental VCD features in the 1600–1800 cm⁻¹ region are captured well. Some minor differences between the experimental and fitted spectra still exist. For example, the relative IR intensity pattern in the 1200–1350 cm⁻¹ region is not reproduced, and the positive experimental VCD signature at 1450 cm⁻¹ is underestimated. It is also noted that the positive band marked with * at ~1310 cm⁻¹ is not predicted. A detailed examination indicates that none of the MG-H₂O complexes exhibits a positive

VCD here. The following contributions were identified using the spectral fitting procedure: MG-I-H₂O-1 (22.9%), MG-I-H₂O-4 (16.8%), MG-I-H₂O-5 (16.8%), MG-II-H₂O-3 (4.8%), MG-II-H₂O-4 (16.8%), MG-II-H₂O-6 (16.8%), MG-II-H₂O-8 (4.8%). It is interesting to note that all these selected complexes have explicit solvation at the carbonyl or epoxy oxygen atoms, indicating that these are the preferred solvation sites of MG in water. Based on the spectral analysis, MG-I and MG-II account for 57% and 43% of total abundance, respectively.

Next, we examined the influence of the MG-2H₂O complexes on IR and VCD. The second water molecule was introduced into MG-I-H₂O and MG-II-H₂O complexes in two ways. One way is to form an intermolecular H-bonding interaction with the first water molecule, which can act either as a H-bond donor or acceptor. The second way is to form an intermolecular H-bonding interaction with one of the remaining H-bonding sites at MG. The geometries of the ten most stable MG-2H₂O complexes in the PCM of water are depicted in Figure 3.6. While the most stable MG-II-2H₂O-1 complex features two H-bonds to the carbonyl and epoxy O atoms of MG, the most stable MG-I-2H₂O-1 takes on a cooperative intermolecular H-bonded ring.

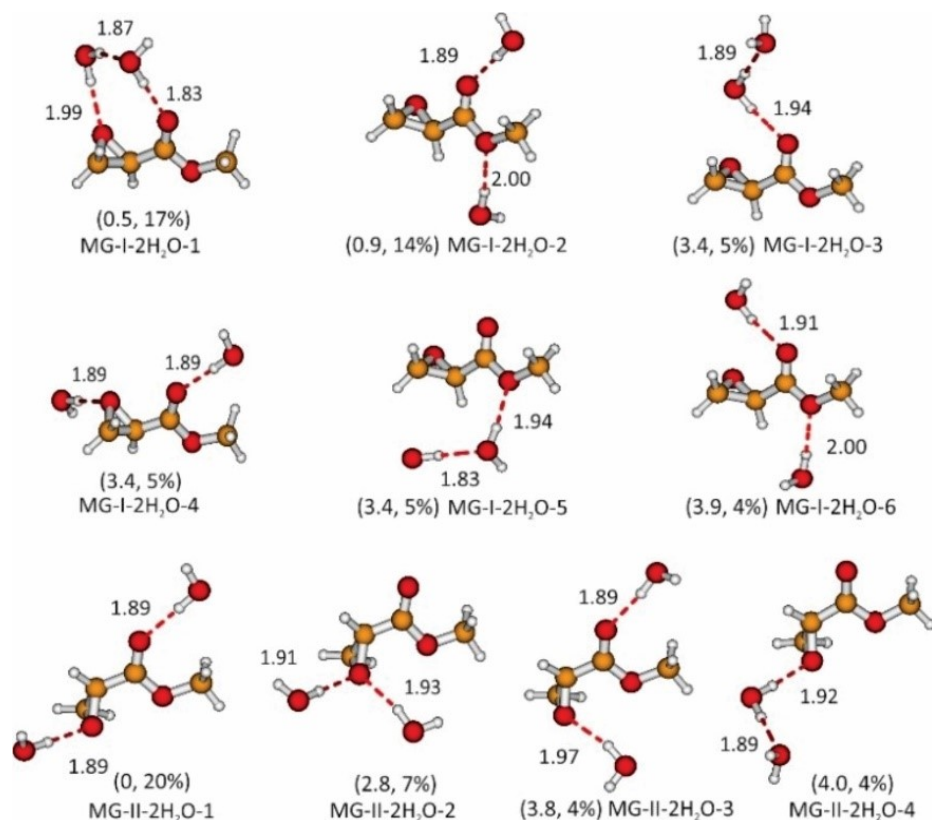


Figure 3.6. The optimized geometries of the most stable conformers of MG-2H₂O in the PCM of water. The relative free energy (in kJ mol⁻¹) and the Boltzmann abundance (%) at room temperature for each conformer are given in parentheses. The intermolecular H-bond lengths (in Å) between water and MG are indicated with dashed lines. The relative stabilities within the MG-I-H₂O and MG-II-H₂O series are indicated with an Arabic number, with 1 being the most stable in each case.

The simulated IR and VCD spectra of the MG-2H₂O complexes in the PCM of water are presented in Figure 3.7. The simulated IR features among the complexes of MG-I-2H₂O, except MG-I-2H₂O-5, generally are quite similar, except in the region above 1600 cm⁻¹. The same can be said for the MG-II-2H₂O complexes. The VCD signatures, on the other hand, vary drastically between them. Especially those complexes that contain cooperative H-bonding water molecules tend to exhibit strong induced VCD features at ~1650 cm⁻¹, far different from the experimental features. A closer examination indicates that only MG-II-2H₂O-3 correctly predicts the positive experimental VCD features at the water bending and the C=O stretching regions. While MG-I-2H₂O-4 exhibits fairly weak VCD features in the 1600–1800 cm⁻¹ region, its VCD features in the lower wavenumber region appear very similar to those of MG-I-H₂O-1. The population weighted IR and VCD

of the MG-2H₂O conformers also are provided in Figure 3.7. Generally speaking, the experimental IR features are reproduced roughly by the population weighted spectrum. For VCD, the region below 1600 cm⁻¹ is well reproduced, and even the positive VCD corresponding to the feature marked as “*” is predicted. On the other hand, the prominent positive VCD signal at the water bending region obviously is not predicted correctly by the negative VCD feature.

We then applied the same spectral fitting procedure by including both MG-H₂O and MG-2H₂O complexes. The weighting factors obtained from the fitting procedure with MG-H₂O and from the preliminary examination with MG-2H₂O were used as the starting point. The final fitted IR and VCD spectra, i.e., fitted with “all”, are compared with the experimental ones in Figure 3.7. The following population factors were obtained from the fitting procedure: MG-I-H₂O-1 (13.9%), MG-I-H₂O-4 (8.2%), MG-I-H₂O-5 (12.8%), MG-I-2H₂O-4 (12.8%), MG-I-2H₂O-6 (8.2%), MG-II-H₂O-3 (4.6%), MG-II-H₂O-4 (12.8%), MG-II-H₂O-6 (12.8%), MG-II-H₂O-8 (4.6%), MG-II-2H₂O-1 (4.6%), and MG-II-2H₂O-3 (4.6%). While the same MG-H₂O complexes are kept with slightly less percentage abundance to accommodate the MG-2H₂O complexes, the added MG-2H₂O complexes show again the preferred solvation at the carbonyl and epoxy oxygen atoms. It is further interesting to note that none of the MG-2H₂O complexes selected by the fitting procedure contains two water molecules H-bonded to each other or to the same O atom. From the IR and VCD spectral analysis, MG-I accounts for 56% of the population and MG-II accounts for 44%. Overall, the fitted IR and VCD spectra are in excellent agreement with the experimental data in water. The inclusion of MG-II-2H₂O-1 also provides the positive VCD band at 1310 cm⁻¹ indicated with a *.

It is perhaps beneficial to say a few cautious words about the spectral fitting procedure. Assuming that the spectral features of each species are predicted well by the level of theory, the fitting procedure works very well if the spectral features are species distinctive, as in the current case. For example, MG-I and MG-II have drastically different IR and VCD features. For the MG-H₂O and MG-2H₂O complexes, the IR and VCD features of the C=O stretching band and VCD features of the H₂O bending band also are very species dependent. In our fitting trials, it was recognized that the C=O stretching and

the H₂O bending regions serve very well as discriminators against many MG-H₂O and MG-2H₂O complexes; the resulting IR and VCD spectra would differ greatly from the experiment ones if these species were included.

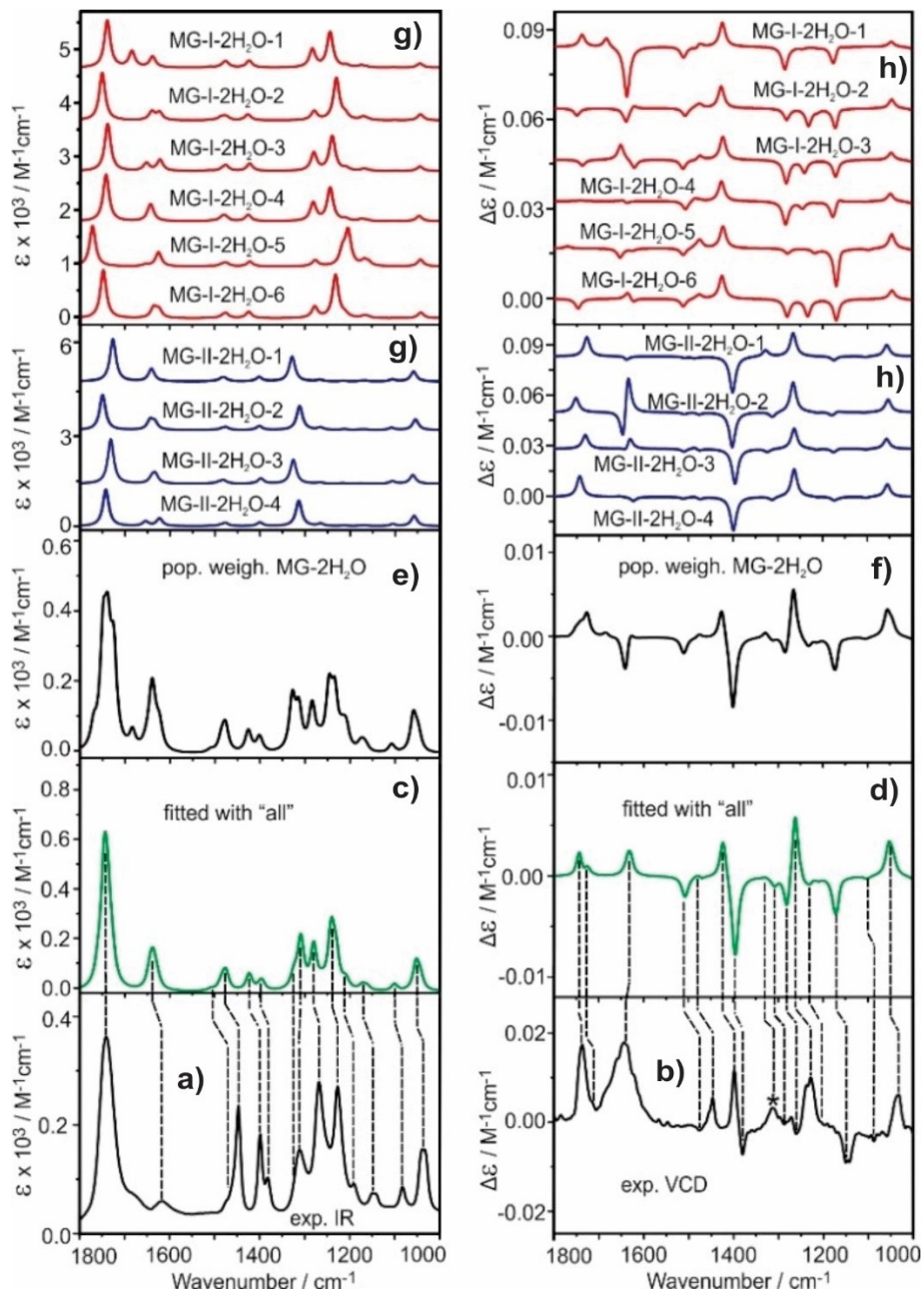


Figure 3.7. Comparisons of the experimental IR (a) and VCD (b) spectra (bottom) of MG in water with the related theoretical IR (g) and VCD (h) spectra of the MG-2H₂O conformers, the population weighted IR (e), VCD (f) spectra of MG-2H₂O, and the final fitted (fitted with “all”) IR (c), VCD (d) spectra containing both MG-H₂O and MG-2H₂O conformers. Please see the main text for details.

3.3.4 Raman and ROA of MG in Water

To test the *clusters-in-a-liquid* approach further and to verify the population factors obtained from the IR and VCD spectral analysis, we carried out measurements and simulations of Raman and ROA spectra of S-MG in water. The theoretical Raman and ROA spectra of MG-I, MG-II, and MG-H₂O complexes are provided in Figure A5, Appendix A, and those of MG-2H₂O are in Figure A6, Appendix A. Similar to the case of IR and VCD, the two conformers exhibit distinctive Raman and ROA features from each other. The population weighted Raman and ROA spectra of MG-I and MG-II in the PCM of H₂O are given in Figure 3.8. These population weighted spectra already capture much of the experimental features, in contrast to the case of IR and VCD. It is noted that some MG-H₂O and MG-2H₂O complexes exhibit noticeably different ROA features compared to their monomeric forms. On the other hand, these conformers play a relatively minor role in their respective population weighted spectra, which are also provided in Figure 3.8. Finally, the fitted spectra with just MG-H₂O and with “all” (considering both MG-H₂O and MG-2H₂O complexes) are depicted in Figure 3.8 using the same species and population factors obtained from the corresponding fits of the IR and VCD. Overall, one could say subjectively that the fitted with “all” spectra are in the best agreement with the experimental one. For example, the relative Raman and ROA band intensities in the <600 cm⁻¹ region and the ROA features around 1250 cm⁻¹ are better reproduced with the fitted with “all” than others.

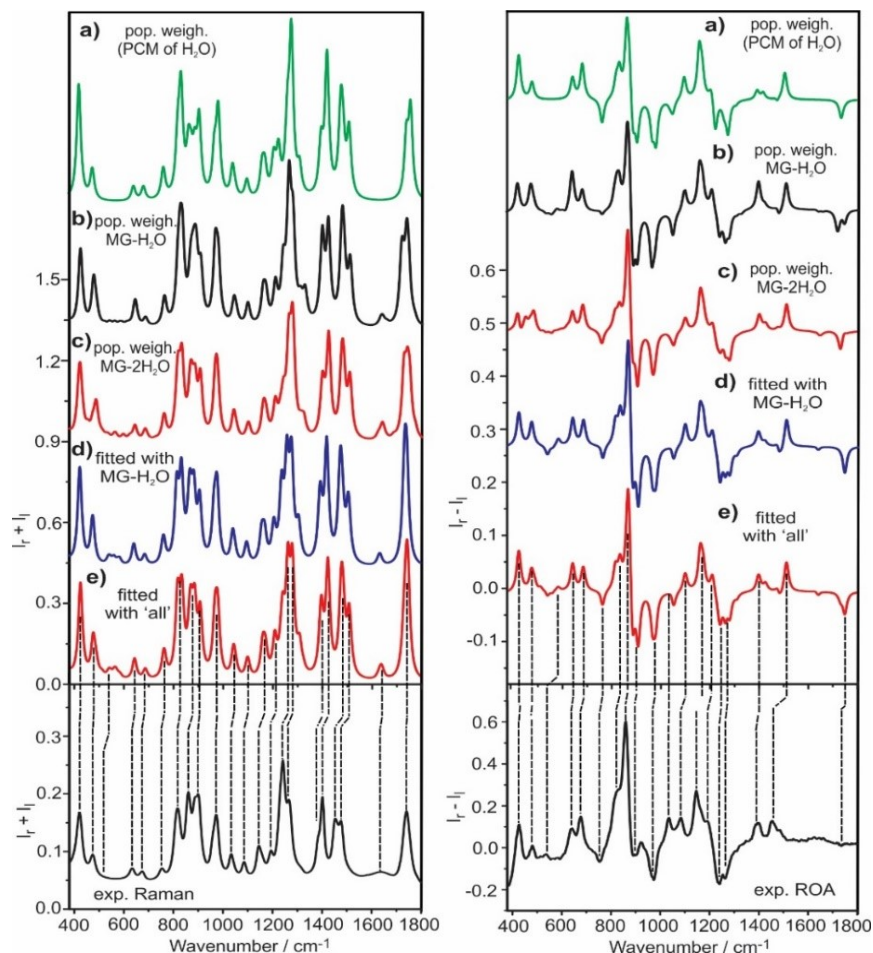


Figure 3.8. Comparison of the experimental Raman (bottom-left) and ROA (bottom-right) spectra of S-MG in water with the calculated population weighted Raman (left) and ROA (right) spectra of the MG monomer (a), MG-H₂O (b), and MG-2H₂O (c) in the PCM of water. Also included are the “fitted” Raman (left) and ROA (right) spectra using just the conformers of MG-H₂O (d) and “all” (e). Please see text for details.

3.4 Conclusions

In this work, we have examined how solvent effects influence the appearance of IR, VCD, Raman, and ROA spectra of MG in water and CCl₄. Noticeably, the different IR, VCD, Raman, and ROA spectra have been observed in these two solvents reflect the much different nature of the intermolecular interactions between solute and solvent molecules in CCl₄ and in H₂O as well as the different dielectric environment. We have discussed the pros and cons of different solvation approaches and provided a rationale for the *clusters-in-*

a-liquid model. In particular, we have pointed out the existence of *small, long-lived* solute-solvent complexes, which contribute significantly to the observed spectra. In the current work, this model has been put through stringent tests with all four vibrational and vibrational optical activity spectra. The excellent agreement between the experimental and theoretical of all four types of spectra in water strongly supports the *clusters-in-a-liquid* approach and indicates that the MG-(H₂O)_{1,2} complexes are the relatively *long-lived* species in water that make the dominant contributions to the observed IR, VCD, Raman, and ROA spectra.

3.5 Acknowledgements

This work was funded by the Natural Sciences and Engineering Research Council of Canada, Canada Foundation for Innovation, and by the University of Alberta. We gratefully acknowledge access to the computing facilities by the Shared Hierarchical Academic Research Computing Network, the Western Canada Research Grid (Westgrid), and Compute/Calcul Canada. CM thanks the Humboldt Foundation for a Feodor Lynen postdoctoral fellowship, the Fonds der Chemischen Industrie for a Liebig fellowship, and the Deutsche Forschungsgemeinschaft for support through the Cluster of Excellence RESOLV (“Ruhr Explores SOLVation”, EXC 1069). YX is a Tier I Canada Research Chair in Chirality and Chirality Recognition.

3.6 References

-
1. a) L. A. Nafie, *Vibrational Optical Activity: Principles and Applications*, John Wiley & Sons, Ltd., UK, 2011; b) G. Yang and Y. Xu, *Top. Curr. Chem.*, **2011**, 298, 189–236; c) P. L. Polavarapu, *Chirality*, **2012**, 24, 909–920.
 2. V. Parchaňský, J. Kapitán, P. Bouř, *RSC Adv.*, **2014**, 4, 57125–57136.
 3. W. Hug, *Appl. Spectrosc.*, **2003**, 57, 1–13.
 4. X. L. Cao, R. K. Dukor, L. A. Nafie, *Theo. Chem. Acc.*, **2008**, 119, 69–79.

-
5. J. R. Chessman, J. Frisch, J. Devlin, J. P. Stephens, *Chem. Phys. Lett.*, **1996**, 252, 211–220.
 6. J. R. Cheeseman, M. J. Frisch, *J. Chem. Theo. Comput.*, **2011**, 7, 3323–3334.
 7. a) M. Srebro-Hooper and J. Autschbach, *Annual Rev. Phys. Chem.*, **2017**, 68, 399–420; b) M. Passarello, S. Abbate, G. Longhi, S. Lepri, R. Ruzziconi, V. P. Nicu, *J. Phys. Chem. A*, **2014**, 118, 4339–4350; c) Y. Zhang, M. R. Poopari, X. Cai, A. Savin, Z. Dezhahang, J. Cheramy, Y. Xu, *J. Nat. Prod.*, **2016**, 79, 1012–1023.
 8. K. Bünnemann and C. Merten, *Phys. Chem. Chem. Phys.*, **2017**, 19, 18948–18956.
 9. J. E. Rode, J. C. Dobrowolski, K. Lyczko, A. Wasiewicz, D. Kaczorek, R. Kawęcki, G. Zajac, M. Baranska, *J. Phys. Chem. A*, **2017**, 121, 6713–6726.
 10. M. R. Poopari, Z. Dezhahang and Y. Xu, *Phys. Chem. Chem. Phys.*, **2013**, 15, 1655–1665.
 11. M. Yves, *The hydrogen bond and the water molecule*, Elsevier, New York, 2007.
 12. G. Hummer, A. Tokmakoff, *J. Chem. Phys.*, **2014**, 141, 22D101.
 13. K. H. Hopmann, K. Ruud, M. Pecul, A. Kudelski, M. Dračinský, P. Bouř, *J. Phys. Chem. B.*, **2011**, 115, 4128–4137.
 14. A. Melcrova, J. Kessler, P. Bouř, J. Kaminsky, *Phys. Chem. Chem. Phys.*, **2016**, 18, 2130–2142.
 15. M. Kamiński, A. Kudelski, M. Pecul, *J. Phys. Chem. B*, **2012**, 116, 4976–4990.
 16. P. L. Geissler, *Annu. Rev. Phys. Chem.*, **2013**, 64, 317–337.
 17. M. Thämer, L. De Marco, K. Ramasesha, A. Mandal, A. Tokmakoff, *Science*, **2015**, 350, 78–82.
 18. F. Dahms, R. Costard, E. Pines, B. P. Fingerhut, E. T. J. Nibbering, T. Elsaesser, *Angew. Chem. Int. Ed.*, **2016**, 55, 10600–10605; *Angew. Chem.*, **2016**, 128, 10758–10763.
 19. J. Sadlej, J. C. Dobrowolski and J. E. Rode, *Chem. Soc. Rev.*, **2010**, 39, 1478–1488.
 20. M. Losada, H. Tran, Y. Xu, *J. Chem. Phys.*, **2008**, 128, 014508.
 21. G. Yang, Y. Xu, *J. Chem. Phys.*, **2009**, 130, 164506.
 22. M. Losada, P. Nguyen, Y. Xu, *J. Phys. Chem. A*, **2008**, 112, 5621–5627.
 23. M. Losada and Y. Xu, *Phys. Chem. Chem. Phys.*, **2007**, 9, 3127–3135.
 24. A. S. Perera, J. Thomas, M. R. Poopari, Y. Xu, *Front. Chem.*, **2016**, 4, 1–17.

-
25. S. Palchowdhury, B. L. Bhargava, *J. Phys. Chem. B*, **2018**, *122*, 2113–2120.
26. J. Thomas, J. Yiu, J. Rebling, W. Jäger, Y. Xu, *J. Phys. Chem. A*, **2013**, *117*, 13249–13254.
27. J. T. A. Gall, J. Thomas, F. Xie, Z. Wang, W. Jäger, Y. Xu, *Phys. Chem. Chem. Phys.*, **2017**, *19*, 29508–29515.
28. a) C. Guo, R. D. Shah, R. K. Dukor, T. B. Freedman, X. Cao, L. A. Nafie, *Vib. Spectrosc.*, **2006**, *42*, 254–272; b) X. Cao, R. D. Shah, R. K. Dukor, T. B. Freedman, C. Guo, L. A. Nafie, *Appl. Spectrosc.*, **2004**, *58*, 1057–1064.
29. Gaussian 09 (Revision D.01), M. J. Frisch, G. W. Trucks, H. B. Schlegel, G. E. Scuseria, M. A. Robb, J. R. Cheeseman, G. Scalmani, V. Barone, B. Mennucci, G. A. Petersson, H. Nakatsuji, M. Caricato, X. Li, H. P. Hratchian, A. F. Izmaylov, J. Bloino, G. Zheng, J. L. Sonnenberg, M. Hada, M. Ehara, K. Toyota, R. Fukuda, J. Hasegawa, M. Ishida, T. Nakajima, Y. Honda, O. Kitao, H. Nakai, T. Vreven, J. A. Montgomery, Jr., J. E. Peralta, F. Ogliaro, M. Bearpark, J. J. Heyd, E. Brothers, K. N. Kudin, V. N. Staroverov, T. Keith, R. Kobayashi, J. Normand, K. Raghavachari, A. Rendell, J. C. Burant, S. S. Iyengar, J. Tomasi, M. Cossi, N. Rega, J. M. Millam, M. Klene, J. E. Knox, J. B. Cross, V. Bakken, C. Adamo, J. Jaramillo, R. Gomperts, R. E. Stratmann, O. Yazyev, A. J. Austin, R. Cammi, C. Pomelli, J. W. Ochterski, R. L. Martin, K. Morokuma, V. G. Zakrzewski, G. A. Voth, P. Salvador, J. J. Dannenberg, S. Dapprich, A. D. Daniels, O. Farkas, J. B. Foresman, J. V. Ortiz, J. Cioslowski, D. J. Fox, Gaussian, Inc., Wallingford CT, 2013.
30. A. D. Becke, *J. Chem. Phys.*, **1993**, *98*, 5648–5652.
31. R. Krishnan, J. S. Binkley, R. Seeger, J. A. Pople, *J. Chem. Phys.*, **1980**, *72*, 650–654.
32. S. Grimme, S. Ehrlich and L. Goerigk, *J. Comput. Chem.*, **2011**, *32*, 1456–1465.
33. A. D. Becke, E. R. Johnson, *J. Chem. Phys.*, **2005**, *123*, 154101–154109.
34. a) P. J. Stephens, F. J. Devlin, C. F. Chabalowski, M. J. Frisch, *J. Phys. Chem.*, **1994**, *98*, 11623–11627; b) T. Kuppens, K. Vanduyck, J. Van der Eycken, W. Herrebout, B. J. van der Veken, P. Bultinck, *J. Org. Chem.*, **2005**, *70*, 9103–9114.
35. a) W. Huang, J. Thomas, W. Jäger and Y. Xu, *Phys. Chem. Chem. Phys.*, **2017**, *19*, 12221–12228; b) J. Thomas, N. A. Seifert, W. Jäger and Y. Xu, *Angew. Chem. Int. Ed.*, **2017**, *56*, 6289–6293; *Angew. Chem.*, **2017**, *129*, 6386–6390.
36. a) B. Mennucci, J. Tomasi, R. Cammi, J. R. Cheeseman, M. J. Frisch, F. J. Devlin, S. Gabriel and P. J. Stephens, *J. Phys. Chem. A*, **2002**, *106*, 6102–6113; b) B. Mennucci, *WIREs Comput Mol Sci*, **2012**, *2*, 386.

-
37. J. Neugebauer, M. Reiher, C. Kind, B. A. Hess, *J. Comput. Chem.*, **2002**, *23*, 895–910.
38. J. Cheeseman, private communication.
39. C. Merten, *Phys. Chem. Chem. Phys.*, **2017**, *19*, 18803–18812.
40. A. Melcrova, J. Kessler, P. Bour and J. Kaminsky, *Phys. Chem. Chem. Phys.*, **2016**, *18*, 2130–2142.
41. a) M. Schneider, C. Masellis, T. Rizzo, and C. Baldauf, *J. Phys. Chem. A*, **2017**, *121*, 6838–6844; b) C. Merten and Y. Xu, *Angew. Chem. Int. Ed.*, **2013**, *52*, 2073–2076.
42. A. Scherrer, R. Vuilleumier and D. Sebastiani, *J. Chem. Phys.*, **2016**, *145*, 084101.
43. S. Lubber, M. Reiher, *J. Phys. Chem. A*, **2009**, *113*, 8268–8277.
44. a) M. R. Poopari, Z. Dezhahang, G. Yang, Y. Xu, *Chem. Phys. Chem.*, **2012**, *13*, 2310–2321; b) M. R. Poopari, P. Zhu, Z. Dezhahang and Y. Xu, *J. Chem. Phys.*, **2012**, *137*, 194308.
45. a) Z. Su, Q. Wen, Y. Xu, *J. Am. Chem. Soc.*, **2006**, *128*, 6755–6760; b) Z. Su and Y. Xu, *Angew. Chem. Int. Ed.*, **2007**, *46*, 6163–6166; *Angew. Chem.*, **2007**, *119*, 2326–2329; c) J. Thomas, O. Sukhorukov, W. Jäger and Y. Xu, *Angew. Chem. Int. Ed.*, **2014**, *53*, 1156–1159; *Angew. Chem.*, **2014**, *126*, 1175–1178.

Chapter 4

Aggregation of Lactic Acid in Cold Rare-Gas Matrices and the Link to Solution: a Matrix Isolation-Vibrational Circular Dichroism Study

The contents of this chapter have been copied and/or adapted from the following publication: A. S. Perera, J. Cheramy, M. R. Poopari, Y. Xu, *Phys. Chem. Chem. Phys.*, **2018**, DOI: 10.1039/c8cp04748k

4.1 Introduction

Vibrational circular dichroism (VCD) spectroscopy^[1] is used extensively nowadays in the determination of absolute configurations and conformations of chiral molecules in solution.^[2,3,4,5] In recent years, this technique has emerged as an important tool for probing non-covalent interactions, such as solute-solute and solute-solvent interactions of chiral molecules in solution.^[6,7,8,9,10] In particular, such non-covalent interactions between a chiral solute and achiral solvent molecules may induce significant VCD intensities in the vibrational modes of the achiral solvent molecules, offering significant insight into solvent effects.^[11,12,13,14]

On the other hand, the existence of multiple conformers, in addition to many more species generated through non-covalent interactions, such as hydrogen (H)-bonding and halogen-bonding of solute-solute and solute-solvent molecules in solution, tend to generate broader and weaker IR and VCD bands in the solution, rendering concrete, detailed spectral assignments difficult. It is, therefore, highly desirable to minimize some of these line broadening factors. The combined approach of matrix isolation (MI) and VCD spectroscopy, i.e., MI-VCD spectroscopy, offers a powerful new way to achieve this goal.

Generally, the replacement of an interactive solvent environment by a cold inert-gas matrix environment removes the severe solute-solvent interactions encountered in solution, thus reducing the number of possible species containing the chiral solute of interest. This reduction, in addition to the low temperature environment, generates much better resolved MI-IR and especially MI-VCD features, which can be critical in clarifying the ambiguous band assignments in solution IR and VCD spectra of chiral molecules.^[15,16] Furthermore, by varying the deposition matrix temperature and sample composition,^[17,18,19] one can alter the degree of self-aggregation of chiral solutes or the complexation of the chiral solute with another molecule of interest. Since VCD intensities are typically only in the range of 10^{-4} to 10^{-5} times those of the corresponding parent IR intensities, this places stringent requirements on the quality of the prepared cold rare gas matrices. It is also highly desirable to measure the MI-VCD spectra of both enantiomers to verify the reliability of the bands observed. Such measurements may be difficult in practice because one enantiomer may be quite rare naturally, difficult to synthesize, or can contain different impurities that may interfere with the final measurements. Nevertheless, very good quality mirror image MI-VCD spectra have been demonstrated.^[17,18]

The system of interest in the current study is the lactic acid (LA) monomer and its aggregates. LA belongs to the group of chiral alpha hydroxy acids. Biologically, LA is considered to be important mainly because of its involvement in biological reactions as a metabolite. Also, the biodegradable character of LA-based polymer derivatives has extended their applications to a range of different fields,^[20,21] therefore, LA has been the focus of many experimental and theoretical investigations. The most stable monomer of LA, M1, and one higher energy conformer, M4, were identified using microwave spectroscopy in the gas phase.^[22, 23, 24] M1–4 are the four most stable LA monomer conformations predicted in the gas phase that will be discussed in the main section in detail.

Borda et al. carried out an MI-IR study of LA and identified not only the most stable conformer (M1) but also M2 and M4 in their MI-IR spectrum aided by DFT calculations.^[25] Because of its propensity to form larger aggregates, the aggregation behaviour of LA in solution and solid-state has been the subject of interest in many prior

investigations. Shouten et al. investigated the crystalline structure of LA at 100 K using the X-ray diffraction technique.^[26] The aggregation of LA in water was studied using IR and Raman spectroscopic methods,^[27,28] where possible intermolecular association compounds connected by H-bonds between the hydroxyl groups were proposed tentatively in the early 90s, although no specific species were identified. The dominant existence of the cyclic OH---O eight-membered ring LA dimer as the main species in water was suggested by Fekete et al. using both IR spectroscopy and *ab initio* calculations.^[29] Later on, Losada et al. applied both IR and VCD spectroscopy with *ab initio* calculations to investigate the aggregation of LA in CDCl₃, water, and CH₃OH.^[30] In the interpretation of IR and VCD spectra of LA in CDCl₃, they considered the contribution of LA up to the binary size, although possible contributions from even larger aggregates were mentioned briefly since further assignment was hampered by the broad spectral width and the potential existence of many species.

In this study, we take advantage of the much narrower linewidth and the better sample control provided by the MI technique to unravel the aggregation behaviour of LA. We first aim to obtain a high-quality MI-VCD spectrum of the LA monomer, which is extremely difficult to do in solution because of severe aggregation even at low LA concentration. Secondly, we will utilize the MI technique to assist the selective formation of different sizes of LA aggregates with controlled sample conditions in a cold rare-gas matrix and obtain their corresponding MI-IR and MI-VCD spectra. By comparing the MI-IR and especially the MI-VCD features obtained under controlled conditions to those obtained in solution, we aim to achieve the concrete assignment of the solution species with the aid of high-level theoretical calculations.

4.2 Experimental Section

4.2.1 Experimental Details

Both L-(+)-LA ($\geq 98\%$) and D-(-)-LA ($\geq 90\%$) were obtained from Sigma-Aldrich and used without further purification. One main difference in their purity seems to be the amount of water in the sample. The solid powder samples were placed in a stainless-steel

sample reservoir situated right before the sample injection tube mounted at the cold head and were kept at room temperature (25 °C). The stainless-steel reservoir was evacuated for one or two hours to remove water trapped in the samples. The flow rate of the Ar backing gas was held constant at 14 sccm and 1.5 sccm (sccm = standard cubic centimeters per minute) for the MI experiments of the LA monomer and the LA aggregates, respectively, using a flow controller (MKS 1179A). The matrix isolation experimental setup contains a closed-cycle helium cryostat from Advanced Research Systems, Inc. (ARS 4HW compressor with a DE 204SI expander) and a stainless-steel vacuum line. Several deposition temperatures (10 K, 16 K, and 24 K) were used. At a 10 K deposition temperature with the flow rate set to 14 sccm, the deposition was carried out for 1 h; at 16 K and 24 K with the flow rate set to 1.5 sccm, the deposition was performed for 3.5 h. The high Ar flow rate at 10 K was used to optimize the generation of the LA monomer in the matrix, while the about ten-times slower flow rate at 16 K and 24 K was to aid the formation of the LA aggregates.

The experimental IR and VCD spectra were measured using a Bruker Vertex 70 supplemented with a PMA 50 module for polarization modulated measurements. All MI-IR and MI-VCD spectra were measured with a spectral resolution of 2 cm^{-1} . The MI-VCD spectra were collected with ~30,000 scans (12 h acquisition time) that were carried out as four individual sets, where each set corresponds to a 3 h acquisition time. The photoelastic modulator (PEM) was set to 1700 cm^{-1} , which improves the reliability of the MI-VCD features obtained in the carbonyl stretching absorption region. Measurements done with the PEM at 1400 cm^{-1} show little difference for all the lower wavenumber bands. Since the purity of the L-(+)-LA and D(-)-LA samples was much higher than that reported in ref. 30 where L-(+)-LA (90%) and racemic LA (85%) were used, we also re-measured the 0.1 M and 0.2 M solution IR and VCD spectra of LA in CDCl_3 . For solution preparation, chloroform-d, 99.8% D from Sigma-Aldrich was used. The final MI-VCD and solution VCD spectra were produced using the standard (S-R)/2 procedure, while the final solution IR spectra were solvent subtracted; the raw VCD data are provided in Figure B1, Appendix B.

4.2.2 Computational Details

All geometry optimizations, harmonic frequency calculations, and IR and VCD intensity calculations were performed using Gaussian 16^[31] program package. All computations initially were undertaken using the Becke, three-parameter, Lee-Yang-Parr (B3LYP)^[32] functional and the 6-311++G(2d,p)^[33] basis set. The B3LYP hybrid functional was selected mainly due to its reasonable accuracy in simulating VCD intensities.^[34,35] More recently, it was recognized that the inclusion of the dispersion-correction^[36] with Becke-Johnson damping^[37] (B3LYP-D3BJ) provides much more accurate conformational geometries and energies than without,^[38] as also demonstrated by many rotational spectroscopic studies of monomers and H-bonded molecular systems, for example the trifluoroethanol trimer.^[39] Therefore, calculations with the B3LYP-D3BJ functional were carried out. Furthermore, since diffuse functions are considered important for chiroptical calculations,^[34] we also performed the calculations with 6-311++G(2d,p) and def2-TZVPD basis sets for comparison.^[40] The theoretical IR and VCD spectra were simulated using a Lorentzian line shape with half-width at half maximum (HWHM) of 4 cm⁻¹ for the comparison with the experimental MI-IR and MI-VCD spectra. No frequency scaling was applied. Please note that we use the S-enantiomer, L-(+)-LA for all the calculations and comparisons with the experimental data throughout this paper, unless otherwise specified explicitly.

4.3 Results and Discussion

4.3.1 Experimental MI-IR and MI-VCD Spectra

In this study, we aim to obtain MI-IR and MI-VCD spectra corresponding to the LA monomer and larger aggregates. The goal is to obtain well separated and distinctive IR and VCD spectral features for these species experimentally in order ultimately to achieve the concrete assignment of solution spectra. After many trial experiments at several source temperatures, it was recognized that to achieve good-quality MI-VCD spectra it is best to leave the sample at 25 °C and evacuate the sample reservoir for one to two hours to remove residual water. This step seems to be crucial to obtaining good mirror-imaged MI-VCD spectra of D- and L-LA enantiomers, possibly because the D- and L-samples

purchased came with much different amounts of water, and excessive heating and less pumping before the start of deposition tended to cause a noticeable variation in the exact species composition in the D- versus L-experiments.

The experimental MI-IR and MI-VCD spectra of LA obtained are presented in Figure 4.1. The MI-IR features recorded at 10 K are sharp in nature and generally agree with the MI-IR results recorded in the Ar matrix at 9 K by Borda et al.^[25] Please note that there is a gap from 1700–1600 cm^{-1} in Figure 4 of Ref. 25. The raw experimental MI-VCD spectra of L- and D-forms of LA reveal clear mirror images for the sharp bands and the MI-VCD spectra in Figure 4.1 show, in general, a good baseline.

The strong MI-IR peak obtained at 10 K at 1767.3 cm^{-1} loses a significant portion of its IR intensity at 16 K and even more at 24 K. In the previous MI-IR study, this band at 1767.3 cm^{-1} at 10 K was assigned to the C=O stretching of M1, and the weak bands observed at higher wavenumber were assigned to M2 and M4.^[25] The three weak MI-IR bands observed at 10 K at a wavenumber lower than 1767.3 cm^{-1} seem to line-up well with the corresponding bands of the 16 K spectrum, i.e., at 1750.7 cm^{-1} (shoulder), 1729.2 cm^{-1} , and 1713.2 cm^{-1} , with a noticeable increase in their relative intensity with respect to 1767.3 cm^{-1} when compared to those at 10 K. At 24 K, the relative intensity of the bands below 1740 cm^{-1} increases further at the expense of those above 1740 cm^{-1} . Based on the above comparison, we hypothesize that the three lower wavenumber MI-IR peaks in the 1700–1800 cm^{-1} region likely are associated with larger LA aggregates, i.e., the LA dimer, trimer, and tetramer, etc. The appearance of larger aggregates can be seen also in the IR bands below 1200 cm^{-1} where the three sharp peaks at 10 K become broader and with obvious shoulders at 16 K and 24 K. In the 1200–1300 cm^{-1} region, we observe a significant relative intensity increase in going from 10 K to 16/24 K. In contrast, the two bands at ~1327.5 cm^{-1} and 1320.4 cm^{-1} exhibit a noticeable decrease in their relative intensity, while those centered at 1378.7 cm^{-1} show noticeable broadening.

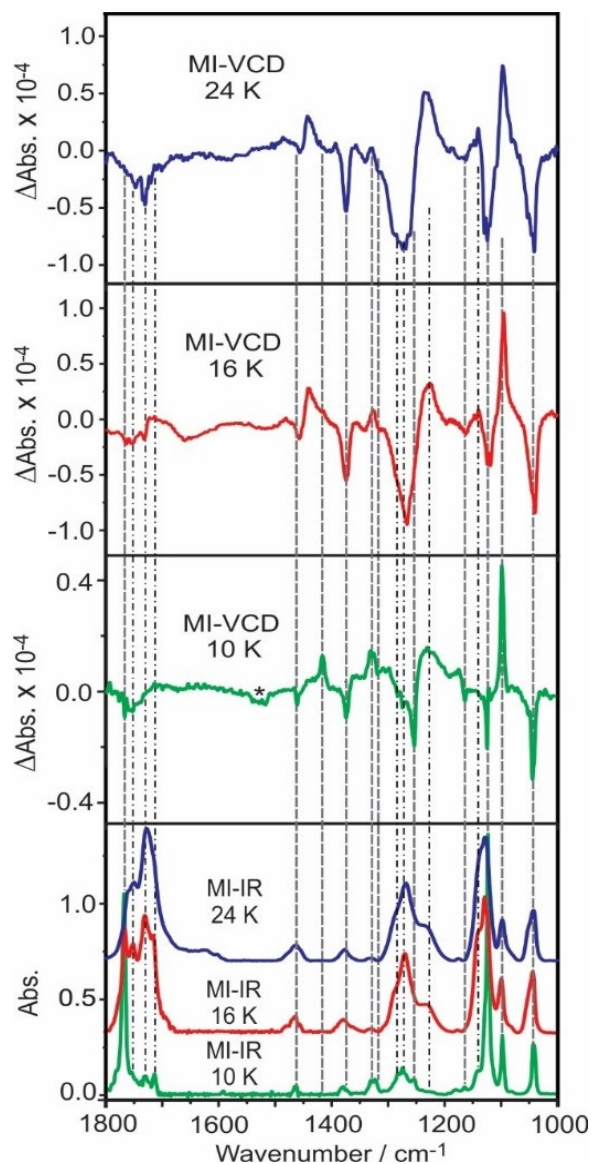


Figure 4.1. Comparison of the experimental MI-IR and MI-VCD spectra of LA obtained at 10 K, 16 K, and 24 K. The dashed lines indicate the contribution from the LA monomer, while the dashed-dotted lines indicate the contribution from LA aggregates, such as the LA dimer, trimer, and tetramer. Please see text for discussion. The broad feature indicated with * is an artifact due to some minor baseline variation in the MI measurements.

To assist the discussion, we use dashed lines to mark the VCD features at 10 K and extend them to all IR and VCD spectra at the three temperatures in order to correlate the corresponding features, a task made easy by many sharp MI-VCD features observed at 10 K. Interestingly, a close examination shows that all these sharp VCD features have their corresponding sharp IR features in the 10 K spectrum. Furthermore, these bands generally

become relatively less intense as one moves to higher temperatures, supporting the aforementioned assignment that they belong to the LA monomer. A further interesting observation is that the MI-IR and MI-VCD features at 16 K and 24 K have broader bands and look fairly alike, suggesting that the dominant species at these two temperatures may be similar. Furthermore, the overall VCD/IR intensity ratios at 16 K and 24 K are similar to each other and are much larger than those at 10 K. To assign the observed spectral features, we need to simulate IR and VCD spectra for the LA monomer and its larger aggregates. The associated calculations are discussed in the next section.

4.3.2 Energetics and Geometries of the LA Monomer and (LA)_n n = 2, 3, 4 Aggregates

Here, we examine the possible monomeric, binary, ternary, and quaternary conformations of LA. The structural aspects of the LA monomer were discussed in several previous investigations.^[7, 25, 41, 42] The four energetically relevant conformations at 298 K identified before^[7, 25] have been reoptimized at the B3LYP-D3BJ/6-311++G(2d,p) and B3LYP-D3BJ/def2-TZVPD levels of theory. Similar geometries were obtained with the inclusion of D3BJ and are summarized in Figure 4.2. M1, M2/M3, and M4 exhibit an OH_{alcohol}···O_{carbonyl}, OH_{alcohol}···O_{acid}, and OH_{acid}···O_{alcohol} intramolecular H-bond, respectively. The subtle difference in M2 and M3 conformers comes from which electronic lone pair of O_{acid} is used for the intramolecular H-bond. Please note that M1, M2, M3, and M4 correspond to *SsC*, *GskC*, *G'sk'C*, and *AaT* in Ref. 25, respectively, and are shown in order of decreasing stability according to calculations at the B3LYP/6-311++G(d,p) level of theory. Also note that this relative stability order may alter depending on the levels of theory and whether the molecule is in the gas phase or in solution. Their relative free energies calculated at the three levels of theory at 298 K in the gas phase and with the PCM of CDCl₃ are compared in Table 4.1, as are the associated Boltzmann factors. Other additional higher energy conformers are without the intramolecular H-bonds shown above and make negligible contribution at 298 K. We note that the changes in the relative free energies among the three levels of theory are small in the gas phase, whereas the addition

of the PCM of CDCl₃ alters the stability ordering of the higher energy conformers and the Boltzmann factors noticeably.

Table 4.1. Comparison of the relative free energies (ΔG in kJ mol⁻¹) and Boltzmann factors (Bf in %) at 298 K of the LA monomer conformers computed at the B3LYP/6-311++G(2d,p), B3LYP-D3BJ/6-311++G(2d,p) and the B3LYP-D3BJ/def2-TZVPD levels of theory.

Conf.	B3LYP/ 6-311++G(2d,p)		B3LYP-D3BJ/ 6-311++G(2d,p)		B3LYP-D3BJ/ def2-TZVPD	
	ΔG	Bf	ΔG	Bf	ΔG	Bf
M1	0.0 (0.0) ^a	92.9 (80.4)	0.0 (0.0)	92.5 (77.7)	0.0 (0.0)	92.5 (83.7)
M2	8.2 (6.0)	3.3 (7.3)	8.4 (5.9)	3.1 (7.0)	8.5 (6.3)	3.0 (6.5)
M3	9.1 (6.9)	2.4 (4.9)	8.9 (7.0)	2.5 (4.6)	9.0 (7.0)	2.5 (4.9)
M4	10.4 (7.4)	1.4 (7.4)	9.6 (4.9)	1.9 (10.7)	9.4 (7.0)	2.0 (4.9)

^a The values in brackets are obtained with the PCM of CDCl₃ added to the calculations.

The formation of LA aggregates is facilitated readily by the availability of aliphatic hydroxyl and carboxylic acid functional groups in LA, which can serve both as H-bond acceptors and donors. An extensive set of LA dimer conformations can be generated from these H-bond donor and acceptors sites utilizing different intermolecular H-bonding topologies. The preliminary calculations by Fekete et al. at the HF level identified the cyclic carboxylic-carboxylic binary conformations (Figure 4.2) as by far the most stable ones, whereas all the other binding topologies resulted in structures which are about 30 kJ mol⁻¹ less stable.^[29] For this reason, we may expect six cyclic carboxylic-carboxylic LA dimers, i.e. M1M1, M1M2, M1M3, M2M2, M2M3, and M3M3, which utilize the carboxylic acid functional groups for the intermolecular H-bonds. These structures were reported previously by Losada et al.^[30] and are re-optimized in this study with the inclusion of the dispersion correction with the damping factor. The geometries of the six stable LA dimer conformations are shown in Figure 4.2, and the corresponding relative energies and

Boltzmann factors of these stable dimers of LA in the gas phase and with the PCM of CDCl_3 are compared at the three levels of theory in Table 4.2.

Table 4.2. Comparison of the relative free energies (ΔG in kJ mol^{-1}) and Boltzmann factors (Bf in %) at 298 K^a of the LA dimer conformers computed at the B3LYP/6-311++G(2d,p), B3LYP-D3BJ/6-311++G(2d,p) and the B3LYP-D3BJ/def2-TZVPD levels of theory.

Dimer Conf.	B3LYP/6-311++G(2d,p)		B3LYP-D3BJ/6-311++G(2d,p)		B3LYP-D3BJ/def2-TZVPD	
	ΔG	Bf	ΔG	Bf	ΔG	Bf
D1	0.0 (0.0) ^b	86.4 (92.0)	0.0 (0.0)	86.2 (78.3)	0.0 (0.0)	83.7 (72.1)
D2	6.4 (8.1)	6.5 (3.5)	6.5 (5.0)	6.4 (10.5)	6.0 (4.6)	7.5 (11.3)
D3	6.8 (8.2)	5.6 (3.4)	6.6 (5.4)	6.0 (8.9)	6.3 (4.3)	6.7 (12.7)
D4	12.6 (13.9)	0.5 (0.3)	12.7 (10.9)	0.5 (0.9)	11.8 (9.3)	0.7 (1.7)
D5	13.2 (14.6)	0.4 (0.4)	12.8 (11.6)	0.5 (0.7)	12.0 (9.8)	0.7 (1.4)
D6	12.9 (13.2)	0.5 (0.3)	12.7 (12.0)	0.5 (0.6)	11.8 (10.8)	0.7 (0.9)

^a For the relevant cold matrix temperatures of 10 K, 16 K, and 24 K, only the most stable conformer D1 contributes (~100%) to the experimental spectra. See text for discussion.

^b The values in brackets are obtained with the PCM of CDCl_3 added to the calculations.

Again, the relative energy ordering of the LA dimer conformers and their Boltzmann factors in the gas phase appear very similar among the three levels of theory. Much more noticeable differences are observed among the three levels of theory when the PCM of CDCl_3 is introduced. It is interesting to note that the relative dimer stability hinges largely on the respective monomeric subunits. For example, D1, which consists of two M1 (by far the most stable monomeric unit), is by far the most stable dimer, followed by D2 and D3, which contain one M1 each. This is perhaps not surprising because the central intermolecular H-bonding topologies are essentially the same among all these dimers.

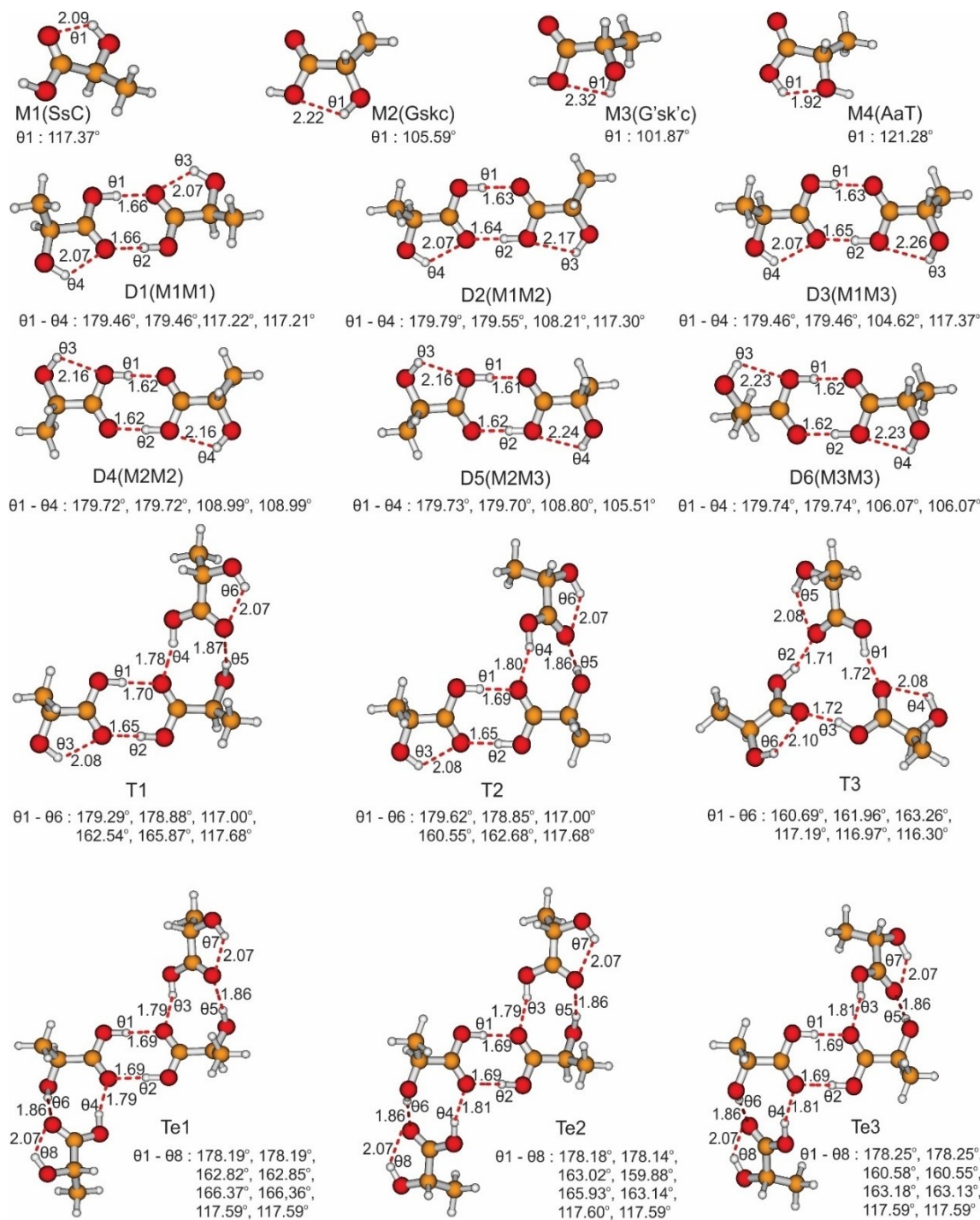


Figure 4.2. The optimized geometries of the four most stable conformers of the LA monomer in the gas phase are shown in the first row, where the name “M” stands for monomer. The names in the brackets are the corresponding names used in Ref. 25. The optimized geometries of the most stable dimer (D) and the representative trimer (T) and tetramer (Te) conformers of LA in the gas phase are given in the subsequent rows. The intra- and intermolecular H-bond lengths (in Å) are indicated with dashed lines for each structure, as well as the OH \cdots O H-bond angles (θ s).

We also have explored larger LA aggregates in light of the experimental data presented in the previous section. A third LA molecule can form H-bonding interactions with the most stable M1M1 dimer in two main ways: (1) insertion of the third LA molecule into one of the intramolecular H-bonded rings of the dimer; (2) insertion of the third LA molecule into the existing intermolecular H-bonded ring. When the third M1 utilizes its carboxylic acid group to form the new intermolecular H-bonded ring, this results in T1 and T2 (Figure 4.2), each of which consists of three M1 subunits. In T1, the insertion of the third M1 molecule happens above the plane of the intramolecular H-bonded ring, whereas in T2, the insertion of the third M1 molecule happens below the aforementioned plane. If the third M1 molecule instead uses its C=O and OH (aliphatic) groups to form the new intermolecular H-bonded ring, the resulting trimer structures, T4 and T5, are much less stable than T1 and T2. If one replaces the third M1 with M2 or M3 in T1, two additional structures, T6 and T7, which are much less stable than T1 and T2, are obtained. The geometries of T4–T7 are given in Figure B2, Appendix B. In the second scenario, the existing eight-member intermolecular H-bonded ring in the M1M1 dimer gets extended into a twelve-member intermolecular H-bonded ring, resulting in T3 (Figure 4.2). Again, T3 is much less stable than T1 and T2.

In terms of tetramers, the remaining intramolecular H-bonded rings of T1 and T2 trimers could assist the insertion of the fourth M1 to form a LA tetramer. As in the case of trimers, the most stable tetramer, Te1, is generated from the T1 trimer, where the insertion of the fourth M1 also happens above the plane of the intramolecular H-bonded ring. The second stable tetramer, Te2, also is generated from the most stable T1 trimer. But unlike Te1, the insertion of a fourth M1 comes below the plane of the intramolecular H-bonded ring, i.e., with the third and fourth M1 molecules above and below, respectively. Te3 has the third and fourth M1 molecules approaching the D1 dimer below the planes of the intramolecular H-bonded rings. We further confirmed that if the third and/or fourth M1 uses instead its C=O and OH (aliphatic) groups to form the new intermolecular H-bonded ring, the resulting tetramers (Te4 and Te5 in Figure B2, Appendix B) are much less stable. The geometries of the three most stable tetramer structures, Te1–Te3, are provided in Figure 4.2.

Table 4.3. Comparison of the relative free energies (ΔG in kJ mol^{-1}) and Boltzmann factors (Bf in %) at 298 K^a of the LA trimers and tetramers computed at the B3LYP/6-311++G(2d,p), B3LYP-D3BJ/6-311++G(2d,p) and the B3LYP-D3BJ/def2-TZVPD levels of theory.^b

(LA) ₃ & (LA) ₄ Conf.	B3LYP/ 6-311++G(2d,p)		B3LYP-D3BJ/ 6-311++G(2d,p)		B3LYP-D3BJ/ def2-TZVPD	
	ΔG	Bf	ΔG	Bf	ΔG	Bf
T1	0.0 (0.0) ^c	43.5 (50.9)	0.0 (0.3)	61.2 (46.8)	0.0 (0.0)	63.0 (67.5)
T2	0.8 (0.6)	31.8 (39.2)	1.2 (0.0)	38.1 (52.2)	1.4 (1.8)	35.4 (32.0)
T3	1.4 (4.0)	24.7 (9.9)	11.2 (11.2)	0.7 (0.6)	9.1 (13.9)	1.6 (0.3)
Te1	0.0 (1.4)	49.4 (28.1)	0.0 (0.0)	44.4 (57.7)	0.0 (0.0)	48.0 (76.9)
Te2	2.5 (1.9)	18.1 (22.6)	0.6 (4.9)	35.4 (8.0)	1.0 (6.7)	32.2 (5.1)
Te3	1.0 (0.0)	32.5 (49.4)	1.9 (1.3)	20.4 (34.2)	2.2 (3.6)	19.8 (17.9)

^a For the relevant cold matrix temperatures of 10 K, 16 K, and 24 K, only the most stable conformers, T1 and Te1, contribute predominantly ($\geq 98\%$) to the experimental spectra.

^b Only the three conformers listed are included in the Boltzmann factor calculations for easy comparison among different levels of theory. Additional high energy conformers were optimized, and their relative energies calculated at the B3LYP-D3BJ/def2-TZVPD level; the results are given in Appendix B.

^c The values in brackets are obtained with the PCM of CDCl_3 added to the calculations.

For easy comparison of the computational results of the representative structures, the relative free energies and the Boltzmann factors of T1–T3 and Te1–Te3 in the gas phase and with the PCM of CDCl_3 at the three levels of theory are summarized in Table 4.3. Here, we observe very noticeable changes in the relative free energies and, therefore, their Boltzmann factors among the ternary (T1–T3) and quaternary (Te1–Te3) LA complexes with the inclusion of the D3BJ correction; some stability orderings are reversed in the gas phase. Such variations due to the inclusion of the D3BJ correction become even more drastic when these complexes are placed in the PCM of the solvent. While the calculations with the inclusion of D3BJ dispersion correction generally appear consistent

with each other with the two different basis sets used, the discrepancies in the relative free energies are still large as the molecular system gets larger. Since the weakness of the calculations is known to affect the entropic component more severely, we also listed the corresponding relative energies in Table B1–B3, Appendix B. The trend observed for ΔG is still there for ΔE , although the corresponding discrepancies are smaller for ΔE than ΔG . All these observations highlight the difficulties one may face in modelling larger aggregates in solution. The sensitivity of the IR and VCD spectral features to the D3BJ correction and the inclusion of PCM will be discussed later on. For consistency, all theoretical interpretations are based on the calculations at the B3LYP-D3BJ/def2-TZVPD level, performed either in the gas phase or with the PCM of CDCl₃ for the remainder of the paper.

4.3.3 Assignment of the MI-IR and MI-VCD Spectra at 10 K

As discussed in the experimental results section, the sharp bands observed in both the MI-IR and MI-VCD spectra of LA obtained at 10 K provide a solid experimental foundation for the interpretation using the simulated IR and VCD features of the LA monomer. While the assignment of the MI-IR spectrum to the LA monomer had been discussed previously in Ref. 25, there were considerable uncertainties in the assignment in the 1150–1500 cm⁻¹ region, where poor agreement between the experimental MI-IR features and the calculated ones was attributed to matrix site splitting and Fermi resonance. Here, we take advantage of the unique MI-VCD features to complement the MI-IR features to nail down the assignment.

The simulated IR and VCD spectra of the four most stable conformers of the LA monomer in the gas phase at the B3LYP-D3BJ/def2-TZVPD level of theory are shown in Figure 4.3. For completeness, the simulated IR and VCD features for the four conformers at the three levels of theory are compared in Figure B3, Appendix B. For the LA monomeric conformers, the variation in the geometries, relative energies, and spectral features are all relatively small among the three levels of theory used. The previous microwave spectroscopic study^[24] identified that the abundance of M4 is about 2% that of M1, pretty close to the predictions by the two B3LYP-D3BJ calculations. In Figure 4.3, we

use the dashed lines to connect the sharp experimental VCD and IR features and then correlate them to the simulated spectral features. To assist discussions, we label all main IR and the corresponding VCD bands in M1 with a, b, c, etc. and label the assigned bands in the experimental data accordingly. Because of the positive and negative VCD features of these sharp bands, it is straightforward to assign the IR and VCD bands. Every band in M1 has its spectral features identified in the experimental MI-IR and MI-VCD spectra. Overall, the agreement between experiment and theory for both IR and VCD spectra is excellent. It is interesting to note a few differences in the current assignment and the one in Ref. 25. The shoulder band e at 1250.5 cm^{-1} now can be assigned definitely to M1, based on its distinctively large negative VCD. The split bands marked with *, which were previously assigned to M1, are mainly contributions from the larger LA aggregates, which will be discussed later on. Instead, we assign the experimental bands at 1328.6 cm^{-1} (g) and 1323.1 cm^{-1} (f) approximately to the bending mode of $\text{CC}_{\text{alcohol}}\text{H}$ (g) and the bending mode of $\text{HOC}_{\text{acid}}/\text{CO}_{\text{alcohol}}\text{H}$ (f) of M1, respectively, which exhibit a distinctive positive/negative VCD couplet. In the $1350\text{--}1500\text{ cm}^{-1}$ region, the assignment of the three weak IR bands, i.e., i, j, and k, were not certain before. Now, with the corresponding distinctive medium to strong -/+/- VCD pattern, one can identify them confidently.

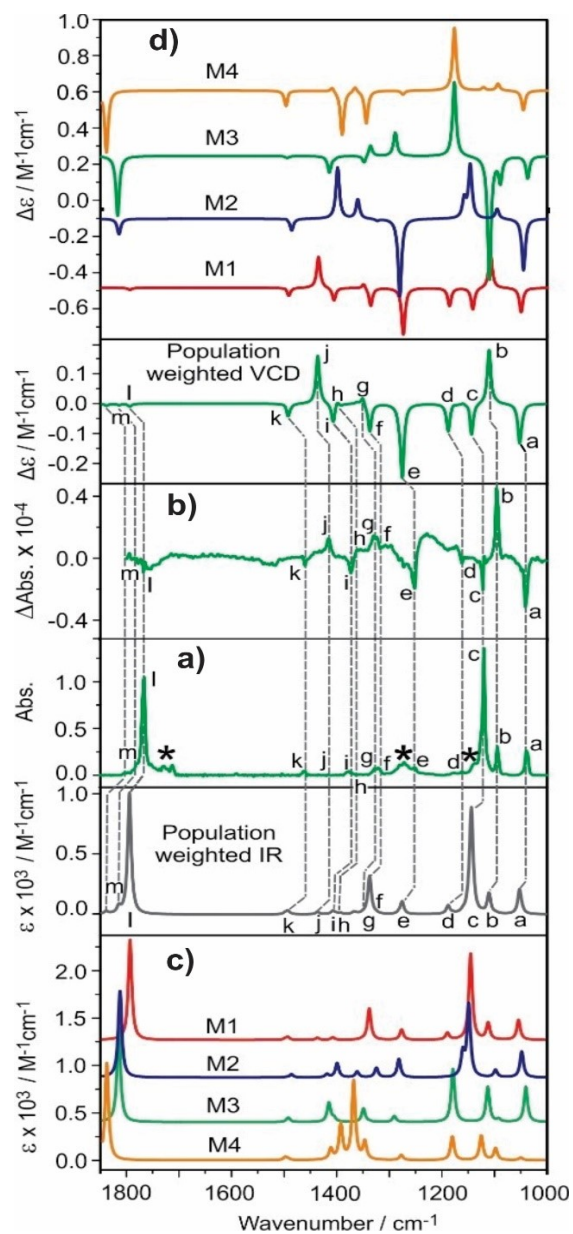


Figure 4.3. Comparisons of the experimental MI-IR (a) and MI-VCD (b) spectra of LA obtained at 10 K with the simulated IR (c) and VCD (d) spectra of the monomeric LA conformers in the gas phase and also with the related population weighted spectra. The dashed lines connect the corresponding experimental IR and VCD features with the simulated ones. * indicates the contributions from the larger LA aggregates. See the main text for discussion.

How about the contribution from the less stable LA monomeric conformers? So far, the assigned MI-IR and MI-VCD spectral features are all consistent with those of M1, which has a dominant population of $\sim 93\%$ of the total monomer population. Because of the interference from the LA aggregates, the only clear indication of the higher energy

conformers resides in the region higher in wavenumber than the C=O stretching band of M1. Since M2 and M3 are close in terms of their structures and also close in energy, we verified their interconversion barrier, which is 1.9 kJ mol⁻¹ from M3 to M2 at the B3LYP-D3BJ/def2-TZVPD level. We further estimated the zero-point energy corrected barrier, which is predicted to be 0.7 kJ mol⁻¹ at the same level of theory. This small barrier can be overcome at 10 K based on the Barnes relation.^[43] With this consideration in mind, we have the following populations: M1 (92.5%), M2 (5.5%), and M4 (2.0%) for the MI spectra at 10 K. Without consideration of conformational conversion from M3 to M2, one would have obtained a stronger negative C=O stretching VCD band of M2/M3 than that of M1. This is because this M3 VCD band is much more negative than the VCD band of M2, and they are at essentially the same C=O stretching wavenumber. Such a prediction would be inconsistent with the experimental VCD data, where M1 has the most negative VCD intensity. The two small IR bands observed at 1788 cm⁻¹ and 1781 cm⁻¹ can be assigned to M4 and M2/M3, respectively. While the 1788 cm⁻¹ band is too weak and too close to the cut off of the IR filter for a good VCD measurement, the negative VCD band associated with M2 is visible in the experiment. Some weaker experimental MI-IR peaks observed in the 1700–1760 cm⁻¹, 1250–1300 cm⁻¹, and 1130–1150 cm⁻¹ regions and marked with * have no corresponding features in the simulated IR/VCD spectra of the LA monomer. As discussed in the previous section, these are likely from the larger LA aggregates. Their detailed assignments will be discussed in the next section in relation to the MI-IR and MI-VCD spectra obtained at 16 K and 24 K.

4.3.4 Assignments of the 16 K and 24 K MI-IR and MI-VCD Spectra and the Self-aggregation of LA in an Ar Matrix

The gradual variations of the MI-IR and MI-VCD spectral features in going from 10 K, to 16 K, and finally to 24 K have provided insights into the self-aggregation of LA. In order to evaluate the spectral features associated with the LA aggregates, the IR and VCD spectra of the binary, ternary, and quaternary LA aggregates in the gas phase have been simulated and are shown in Figure B4–B6, Appendix B, respectively, at all three levels of theory. Generally speaking, both the IR and VCD spectral features are fairly consistent

among the three levels of theory, although with some small variations in the wavenumber positions. This provides confidence in using them to interpret the MI data. The only exception is T3, which shows much different VCD features in the C=O stretching region at the B3LYP level versus those at the B3LYP-D3BJ level. This VCD alternation is associated with the obvious change in the optimized T3 geometry when D3BJ is included (See Figure B7, Appendix B, for a comparison). The two different basis sets, 6-311++G(2d,p) and def2-TZVPD, using the B3LYP-D3BJ functional provide very consistent results across the board.

Since the depositions were done at the low temperatures of 16 K and 24 K over a long period of time, we assume that the conformational temperatures of the H-bonded LA aggregates are the same as the matrix temperatures. At such low temperatures, only the most stable conformer is dominantly populated ($\geq 98\%$) for every LA aggregate size. Even if the conformational temperature is slightly higher than the one assumed, the resulting MI-IR and MI-VCD spectra are expected to be dominated still by the most stable conformer of each species. For this reason, the simulated IR and VCD spectra of the most stable conformer of LA dimer, trimer, and tetramer are shown in Figure 4.4, together with the experimental MI-IR and MI-VCD spectra obtained at 10 K, 16 K, and 24 K. For the monomer, the same population weighted IR and VCD spectra used before are depicted in Figure 4.4. Based on the experimental analysis presented above and the simulated IR and especially VCD features, we can assign the IR and VCD bands. We label the IR/VCD bands of the LA dimer with a', b', and c', etc., while those of the LA trimer /tetramer are with a''/a''', b''/b''', and c''/c''', etc., respectively. For the LA trimer/tetramer, only relevant bands are labelled for simplicity.

At 16 K, the three IR bands to the red shift (bathochromic shift) direction of the C=O stretching band of M1, visible at 10 K, become much stronger relative to that of M1. These bands can be assigned tentatively to the LA dimer, trimer, and tetramer, based on the comparison to the simulated spectra of each aggregated species. While the furthest red shifted (bathochromic shifted) band, l', can be assigned to the LA dimer, the positions of the trimer and tetramer are predicted to be essentially overlapped in contrast to the separated bands observed. This small, although crucial, deviation in the predicted versus experimental band positions could have a dramatic consequence for the appearance of the

VCD signatures in this region because of the multi-signate nature of the associated VCD bands. For example, the +/- VCD bands underneath l'' may overlap more to produce just a negative band.

The contribution of the LA monomer also can be recognized from the distinctive -/+/- VCD feature associated with a/b/c bands, along with some other similarities to the 10 K spectral features. With the availability of the distinctive experimental MI-IR and MI-VCD spectral features at 10 K, we can estimate the contribution from the LA monomer to the -/+/- feature to be about 10% of its total intensity. Please note that the experimental VCD intensity at 10 K is on the right side, and if it were plotted on the same scale as the VCD intensities at 16 K and 24 K, it would be about half the height as currently depicted. The calculated LA monomer and dimer VCD spectra are amplified by a factor of two for easy visualization of the spectral features. Interestingly, the distinctive -/+/- feature mentioned above is predicted not only for the LA monomer but also for its aggregates, with only a minor variation in the band positions, although the relative intensity of the positive centre band versus the two negative side bands drops in moving from the monomer to the dimer and the trimer. Therefore, it is not surprising that this distinctive feature remains very much the same at different deposition temperatures. On the other hand, the observed broadening of the bands and the drop in the relative intensity of the positive centre band versus the two negative side bands points to the contributions by the LA dimer and also the trimer. A further detailed examination of the IR and VCD features in the 1500–1200 cm⁻¹ region indicates that the overall IR and especially the VCD features can be attributed largely to the LA dimer, with some contributions from the trimer and monomer. For example, the experimental VCD features, e' and e'' at 16 K/24 K, are blue shifted (hypsochromic shifted) from those at 10 K, consistent with the predicted positions of the e' of the LA dimer and e'' of the LA trimer. Similarly, the very noticeable blue shift (hypsochromic shift) of the positive j' at 16 K/24 K from j at 10 K is captured by the prediction of the blue shift (hypsochromic shift) j' of the dimer with respect to j of the monomer.

The detailed band assignments are indicated in Figure 4.4 for the 16 K spectra. The 24 K spectra are very similar to those at 16 K, except that they contain a bit more relative contribution from the larger LA aggregates and less from monomer than at 16 K. For

conciseness, in the 24 K spectra, we label only the bands with more obvious contribution from the LA trimer at 24 K than at 16 K. The empirically population weighted IR and VCD spectra at 16 K with 31% monomer, 60% dimer, 8.5% trimer, and 0.5% tetramer and those at 24 K with 20% monomer, 65% dimer, 12% trimer, and 3% tetramer also are included in Figure 4.4 for comparison. Overall, the agreement with the experimental data is very good, except in the C=O stretching region, in part due to the inaccuracy in the predicted relative band positions for larger aggregates and the cancellation of the multi-signate VCD features.

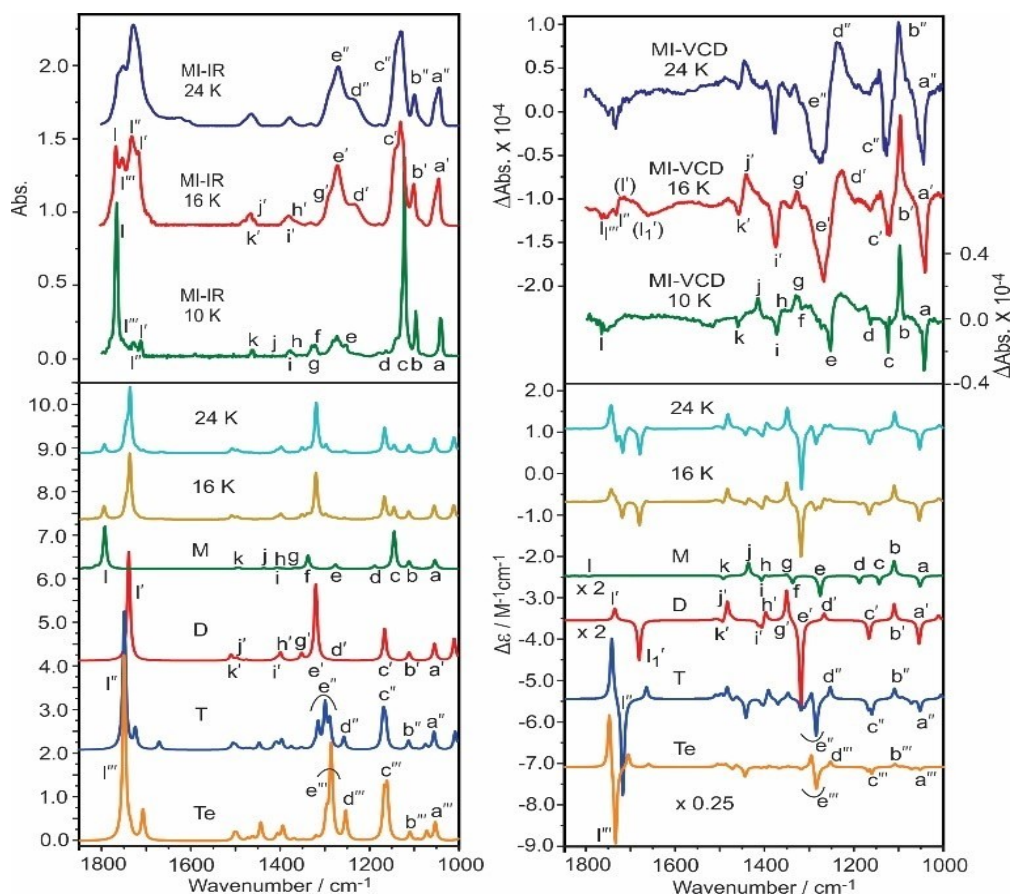


Figure 4.4. Comparisons of the experimental MI-IR and MI-VCD spectra of LA obtained at 10 K, 16 K, and 24 K with the simulated IR and VCD spectra of the monomeric (M), binary (D), ternary (T), and quaternary (Te) LA species in the gas phase. The band assignment made for the 10 K spectra in Figure 4.3 is used as the basis to recognize the new features at 16 K and 24 K. The largest contribution to the 16 K spectra is from the LA dimer, identified with bands labelled with a', b', etc. The additional contribution to the 24 K spectra from the LA trimer, LA tetramer are identified with bands labelled with a'', b'', and so on. The empirically population weighted spectra at 16 K (a) and 24 K (b) also are presented. (') indicates that an assignment is only tentative. Please see the main text for the detailed discussions.

From Figure 4.4, one may consider assigning the 10 K spectra to the LA trimer, even though the agreement is worse for some VCD bands. For example, the experimental a, b, and c VCD bands are very sharp, whereas (LA)₃ has additional VCD bands predicted close to a'', and its c'' band shows splitting, inconsistent with the experiment. The d VCD band observed has no corresponding feature in (LA)₃. Furthermore, at a deposition temperature of 10 K, the main species trapped in the matrix are the species already present in the gas phase, based on our own and others' experience.^[17, 18, 25] The rotational spectroscopic (gas phase) studies show that the LA monomer dominates the experimental rotational spectrum.^[24] It was clear that we had mostly the LA monomer in the gas phase before deposition.

We recognize that it is still quite challenging to obtain an accurate theoretical prediction of band position and intensity, especially for larger aggregates. Such deficiency makes it very difficult to reproduce experimental data with many different species since minor frequency shifts and intensity variation can generate very different final VCD patterns. This deficiency is particularly acute in the current case in the C=O stretching region, where the trimer and tetramer exhibit an extremely strong VCD intensity due to exciton coupling,^[44,45,46] a concept recently illustrated by Abbate and co-workers using bicamphor molecules.^[47] A minor inaccuracy in the band positions and/or intensities of these extremely strong VCD couplets may change the pattern and appearance completely. We caution against over interpreting the VCD signatures at the C=O region under such conditions. The availability of the MI-IR and MI-VCD at multiple temperatures and experimental conditions allows one to follow the aggregation process sequentially and makes the assignment conclusive.

4.3.5 Re-examination of Self-aggregation of LA in CDCl₃

Self-aggregation of LA in CDCl₃ is considerably more complicated than in a cold rare-gas matrix because at 298 K many more conformers of each species are populated and because of solvent effects. It is also clear from the discussion in the theoretical modelling section, that the relative free energies and their Boltzmann factors at 298 K for the larger LA aggregates in solution change very noticeably from the gas phase to solution (see Table

4.3). To complicate the interpretation further, the aforementioned variations strongly depend on the levels of theory used. We, therefore, aim to use the experimental MI-IR and MI-VCD spectra obtained at multiple temperatures to aid the solution assignment. In Figure 4.5, the solution IR and VCD spectra obtained at 0.1 M and 0.2 M are compared with the experimental MI data at 24 K.

Also included in Figure 4.5 are the population weighted IR and VCD spectra of the LA monomer, dimer, trimer, and tetramer species at 298 K. We use the predicted Boltzmann population factors at the B3LYP-D3BJ/def2-TZVPD level of theory because of its reliability in terms of conformational geometries and relative energies.^[38] The individual conformer IR and VCD spectra of the LA monomer, dimer, trimer, and tetramer, and their population weighted spectra at 298 K are provided in Figure B8–B11, Appendix B for comparison. It is interesting to note that with the PCM of CDCl₃, the negative C=O VCD band of M1 now becomes positive. Since the sign of a VCD band is determined by the sign of $\cos\alpha$, where α is the angle between the electric and magnetic dipole transition moment vectors of the VCD mode, one labels such a mode non-robust if α is near 90°.^[48] The α values of the C=O stretching modes are listed in Table B4, Appendix B, for the main conformers of each LA species calculated. For M1 and some angles in D1 and T1, these α values are in the range of 82.1–90.2°, indicating that these are the non-robust modes. Another intriguing observation is that the C=O VCD features for the most stable and the second most stable conformers of the dimer, trimer, and tetramer are essentially opposite in sign in every aggregate size. Any change in the α values and in the population factors for these two most stable conformers can alter the final appearance of the VCD features in this region. A similar issue associated with non-robust conformer population also was reported recently.^[49] Again, this highlights the challenge one faces to correctly predict the C=O stretching VCD signatures.

Overall, the IR and VCD spectra obtained at 0.1 M and 0.2 M share similar spectral features, and they also are similar to the MI-IR and MI-VCD spectra obtained at 24 K. There are, however, some small yet informative changes, especially in the VCD spectra. The broadening of the VCD bands at 0.2 M compared to those at 0.1 M suggest that larger LA aggregates become more dominant at higher concentration. The VCD features in the C=O stretching region become more intense relative to the VCD features in the lower

wavenumber region in the 0.2 M solution versus the 0.1 M solution. This would suggest strongly the contribution from the LA tetramer since this is the only species that could generate such an increase based on the theoretical modelling. A detailed analysis allows one to assign most of the observed VCD bands to the tetramer, indicated by the dashed lines in Figure 4.5, with some small contributions from the LA dimer and trimer. The observed positive VCD band marked with 3 is reproduced by the LA tetramer. A minor shift in the predicted C=O band positions marked with 1 and 2 may generate the negative band observed, although the current prediction shows a +/- VCD pattern for 1/2. Based on the gradual evolution of the IR and VCD spectral features from the 10 K, to 16 K, 24 K, and finally to the 0.1 M and 0.2 M solution conditions, we can conclude confidently that even for the 0.2 M solution there is significant contribution to the observed IR and VCD spectra from the large LA aggregates, such as the LA tetramer. The simulated IR and VCD spectra with empirical Boltzmann factors of 20% LA dimer, 30% LA trimer, and 50 % LA tetramer are compared with the experimental data obtained at 24 K and in the 0.1 M and 0.2 M solution in Figure B12, Appendix B; a very good agreement was obtained with the 0.2 M experimental data.

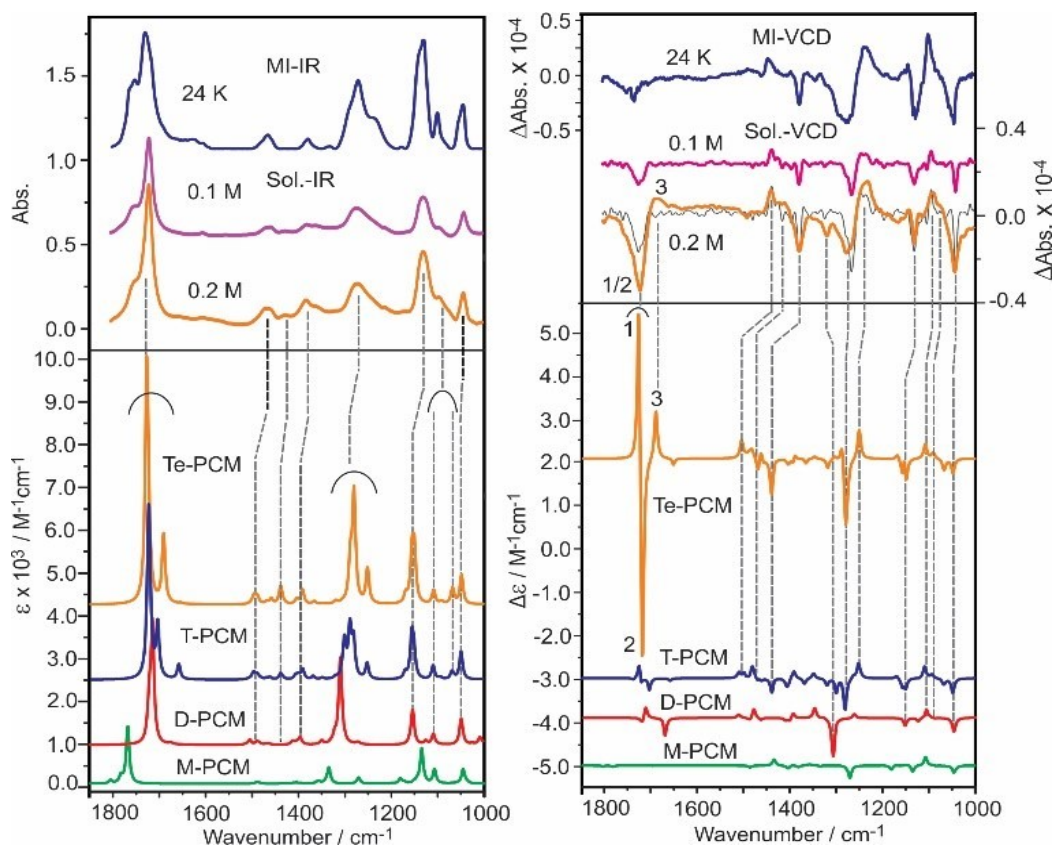


Figure 4.5. Top: comparisons of the solution IR and VCD spectra of LA in CDCl_3 recorded at 0.1 M and 0.2 M with the MI-IR and MI-VCD spectra of LA obtained at 24 K. The 0.1 M trace also is rescaled and superimposed on the 0.2 M trace for easy comparison. Bottom: the population weighted IR and VCD spectra of the LA monomer (M-PCM), dimer (D-PCM), trimer (T-PCM), and tetramer (Te-PCM) in CDCl_3 at 298 K. The peak assignments are indicated by the dashed lines.

4.4 Conclusions

In this study, we have undertaken MI-IR and MI-VCD measurements of LA at 10 K, 16 K, and 24 K temperatures and obtained spectra of LA dominated by the monomer and by larger aggregates sequentially. The sharp and characteristic MI-VCD spectral features at 10 K provide the essential experimental tool to assign the IR bands belonging to the LA monomer conclusively; they show excellent agreement with the theoretical calculations. By following the experimental trend observed in the MI-IR and especially MI-VCD spectral features at the higher deposition temperatures, and aided with the B3LYP-D3BJ/def2-TZVPD calculations, we have been able to identify the LA dimer confidently as the main species at 16 K and 24 K. Finally, through the comparison of the experimental

MI-VCD spectral features and those in the 0.2 M solution, in conjunction with the theoretical simulations, the main carriers have been identified as the LA tetramer and trimer in solution. This is different from the previous studies, which identify the LA dimer as the main species at even higher concentrations. It is worth emphasizing that the characteristic VCD features are essential in achieving the conclusive assignment since IR features alone do not allow a clear assignment. The experimental data obtained with different degrees of LA self-aggregation also are crucial in facilitating the spectral assignment since the theoretical uncertainties in the vibrational band positions and the IR/VCD intensities, as well as the relative abundance of conformers, become larger as one moves to larger aggregates. In addition, we show that the B3LYP functional (without the D3BJ dispersion correction) commonly used in VCD research gives very different relative energies as the molecular systems get larger and are placed in solution when compared to those with the D3BJ correction. The current work highlights the importance of utilizing extensive, controlled experimental data, in addition to the high level DFT calculations, to aid the IR and VCD spectroscopic interpretation.

4.5 Acknowledgements

This work was funded by the Natural Sciences and Engineering Research Council of Canada and by the University of Alberta. We thank Dr. Javix Thomas for his involvement at the early stage of the matrix isolation experiments. We gratefully acknowledge access to the computing facilities of the Shared Hierarchical Academic Research Computing Network, the Western Canada Research Grid (Westgrid), and Compute/Calcul Canada. YX is a Tier I Canada Research Chair in Chirality and Chirality Recognition.

4.6 References

-
1. L. A. Nafie, *Vibrational Optical Activity: Principals and Applications*, Wiley, Chichester, 2011.
 2. J. M. Batista Jr., E. W. Blanch, V. da Silva Bolzan, *Nat. Prod. Rep.*, **2015**, 32, 1280–1302.
 3. A. C. Chamayou, G. Makhouloufi, L. A. Nafie, C. Janiak, S. Ludeke, *Inorg. Chem.*, **2015**, 54, 2193–2203.

-
4. Y. Zhang, M. R. Poopari, X. Cai, A. Savin, Z. Dezhahang, J. Cheramy, Y. Xu, *J. Nat. Prod.*, **2016**, *79*, 1012–1023.
 5. T. Wu, X. X. You, P. Bour, *Coord. Chem. Rev.*, **2015**, *284*, 1–18.
 6. C. Merten, C. J. Berger, R. McDonald, Y. Xu, *Angew. Chem., Int. Ed.*, **2014**, *53*, 9940–9943.
 7. M. Passarello, S. Abbate, G. Longhi, S. Lepri, R. Ruzziconi, V. P. Nicu, *J. Phys. Chem. A*, **2014**, *118*, 4339–4350.
 8. J. E. Rode, J. C. Dobrowolski, K. Lyczko, A. Wasiewicz, D. Kaczorek, R. Kawecki, G. Zajac, M. Baranska, *J. Phys. Chem. A*, 2017, *121*, 6713–6726.
 9. C. Merten, *Phys. Chem. Chem. Phys.*, **2017**, *19*, 18803–18812.
 10. G. Yang, Y. Xu, *Top. Curr. Chem.*, **2011**, *298*, 189–236.
 11. J. Sadlej, J. C. Dobrowolski, J. E. Rode, *Chem. Soc. Rev.*, **2010**, *39*, 1478–1488.
 12. M. R. Poopari, Z. Dezhahang, G. Yang, Y. Xu, *Chem. Phys. Chem*, **2012**, *13*, 2310–2321.
 13. A. S. Perera, J. Thomas, M. R. Poopari, Y. Xu, *Front. Chem.*, **2016**, *4*, 1–17.
 14. A. S. Perera, J. Cheramy, C. Merten, J. Thomas, Y. Xu, *Chem. Phys. Chem*, **2018**, *19*, 2234–2242.
 15. G. Tarczay, G. Magyarfalvi, E. Vass, *Angew. Chem., Int. Ed.*, **2006**, *45*, 1775–1777.
 16. C. H. Pollok, C. Merten, *Phys. Chem. Chem. Phys.*, **2016**, *18*, 13496–13502.
 17. C. Merten, Y. Xu, *Chem. Phys. Chem*, **2013**, *14*, 213–219.
 18. C. Merten, Y. Xu, *Angew. Chem., Int. Ed.*, **2013**, *52*, 2073–2076.
 19. W. Sander, M. Gantenberg, *Spectrochim. Acta, Part A*, **2005**, *62*, 902–909.
 20. M. Kleerebezem, J. Hugenholtz, *Curr. Opin. Biotechnol.*, **2003**, *14*, 232–237.
 21. A. Narladkar, E. Balnois, Y. Grohens, *Macromol. Symp.*, **2006**, *241*, 34–44.
 22. B. P. van Eijck, *J. Mol. Spectrosc.*, **1983**, *101*, 133–138.
 23. L. Pszczolkowski, E. Białkowska-Jaworska, Z. Kisiel, *J. Mol. Spectrosc.*, **2005**, *234*, 106–112.
 24. Z. Kisiel, E. Białkowska-Jaworska, D. P. Zaleski, J. L. Neill, A. L. Steber, B. H. Pate, WH10, *66th Int. Sym. on Mol. Spectrosc.*, Columbus, Ohio, 2011.
 25. A. Borda, A. Gomez-Zavaglia, L. Iapinski, R. Fausto, *Phys. Chem. Chem. Phys.*, **2004**, *6*, 2101–2108.

-
26. A. Shouten, J. Kanters, J. van Krieken, *J. Mol. Struct.*, **1994**, *323*, 165–168.
27. G. Cassanas, M. Morssli, E. Fabregue, L. Bardet, *J. Raman Spectrosc.*, **1991**, *22*, 409–413.
28. G. Cassanas, G. Kister, E. Fabregue, M. Morssli, L. Bardet, *Spectrochim. Acta, Part A*, **1993**, *49*, 271–279.
29. Z. Fekete, T. Kortvelyesi, J. Andor, I. Palinko, *J. Mol. Struct.: THEOCHEM*, **2003**, *666*, 159–162.
30. M. Losada, H. Tran, Y. Xu, *J. Chem. Phys.*, **2008**, *128*, 014508.
31. Gaussian 16, Revision B.01, M. J. Frisch, G. W. Trucks, H. B. Schlegel, G. E. Scuseria, M. A. Robb, J. R. Cheeseman, G. Scalmani, V. Barone, G. A. Petersson, H. Nakatsuji, X. Li, M. Caricato, A. V. Marenich, J. Bloino, B. G. Janesko, R. Gomperts, B. Mennucci, H. P. Hratchian, J. V. Ortiz, A. F. Izmaylov, J. L. Sonnenberg, D. Williams-Young, F. Ding, F. Lipparini, F. Egidi, J. Goings, B. Peng, A. Petrone, T. Henderson, D. Ranasinghe, V. G. Zakrzewski, J. Gao, N. Rega, G. Zheng, W. Liang, M. Hada, M. Ehara, K. Toyota, R. Fukuda, J. Hasegawa, M. Ishida, T. Nakajima, Y. Honda, O. Kitao, H. Nakai, T. Vreven, K. Throssell, J. A. Montgomery, Jr., J. E. Peralta, F. Ogliaro, M. J. Bearpark, J. J. Heyd, E. N. Brothers, K. N. Kudin, V. N. Staroverov, T. A. Keith, R. Kobayashi, J. Normand, K. Raghavachari, A. P. Rendell, J. C. Burant, S. S. Iyengar, J. Tomasi, M. Cossi, J. M. Millam, M. Klene, C. Adamo, R. Cammi, J. W. Ochterski, R. L. Martin, K. Morokuma, O. Farkas, J. B. Foresman, and D. J. Fox, Gaussian, Inc., Wallingford CT, 2016.
32. A. D. Becke, *J. Chem. Phys.*, **1993**, *98*, 5648–5652.
33. R. Krishnan, J. S. Binkley, R. Seeger, J. A. Pople, *J. Chem. Phys.*, **1980**, *72*, 650–654.
34. J. Cheeseman, M. Frisch, *J. Chem. Theory Comput.*, **2007**, *7*, 3323–3334.
35. T. Kuppens, K. Vandyck, J. van der Eycken, W. Herrebout, J. vander Veken, P. Bultinck, *J. Org. Chem.*, **2005**, *70*, 9103–9114.
36. S. Grimme, S. Ehrlich, L. Goerigk, *J. Comput. Chem.*, **2011**, *32*, 1456–1465.
37. A. D. Becke, E. R. Johnson, *J. Chem. Phys.*, **2005**, *123*, 154101.
38. M. K. Kesharwani, A. Karton, J. M. L. Martin, *J. Chem. Theory Comput.*, **2016**, *12*, 444–454.
39. J. Thomas, N. A. Seifert, W. Jager, Y. Xu, *Angew. Chem., Int. Ed.*, **2017**, *56*, 6289–6293 (*Angew. Chem.*, **2017**, *129*, 6386–6390).
40. D. Rappoport, F. Furche, *J. Chem. Phys.*, **2010**, *133*, 134105.

-
41. J. Sadlej, J. Dobrowolski, J. Rode, M. Jamroz, *Phys. Chem. Chem. Phys.*, **2006**, *8*, 101–113.
42. M. Pecul, A. Rizzo, J. Leszczynski, *J. Phys. Chem. A*, **2002**, *106*, 11008–11016.
43. A. Barnes, *J. Mol. Struct.*, **1984**, *113*, 161–174.
44. G. Holzwarth, I. Chabay, *J. Chem. Phys.*, **1972**, *57*, 1632–1635.
45. V. Setnicka, M. Urbanova, P. Bour, V. Kral, K. Volka, *J. Phys. Chem. A*, **2001**, *105*, 8931–8938.
46. T. Taniguchi, K. Monde, *J. Am. Chem. Soc.*, **2012**, *134*, 3695–3698.
47. S. Abbate, G. Mazzeo, S. Meneghini, G. Longhi, S. E. Boiadjev, D. A. Lightner, *J. Phys. Chem. A*, **2015**, *119*, 4261–4267.
48. V. P. Nicu, E. J. Baerends, *Phys. Chem. Chem. Phys.*, **2009**, *11*, 6107–6118.
49. G. Longhi, M. Tommasini, S. Abbate, P. L. Polavarapu, *Chem. Phys. Lett.*, **2015**, *639*, 320–325.

Chapter 5

IR and Vibrational Circular Dichroism Spectra of Methyl- β -D-glucopyranose in Water: The Application of the *Clusters-in-a- Liquid* Solvation Model

5.1 Introduction

Carbohydrates perform vital biological functions in living systems.^[1, 2, 3] The biological importance of carbohydrates has made them the subject of interest for many investigations.^[4] Water often is the medium for the biologically important reactions of carbohydrates, and one may expect water to interact strongly with the OH and other functional groups of carbohydrates. These interactions between carbohydrate molecules and water play crucial roles in deciding the outcomes of biologically important reactions of carbohydrates;^[2, 3, 5] therefore, the outcomes of these reactions can be interpreted only with the proper description of water solvation effects. Monosaccharides are the building units of carbohydrates and are recognized for their involvement in many biologically important reactions.^[6]

The vibrational optical activity methods of Raman optical activity (ROA) and vibrational circular dichroism (VCD) spectroscopic methods have become powerful experimental techniques in the investigations of both the absolute configurations and the dominating conformations of a wide range of chiral molecules in solution.^[7, 8] This is mainly due to improvements in both the *ab initio* density functional theory (DFT)^[9] calculations and the associated instrumentation.^[10] Both ROA and VCD spectroscopic methods have been applied in the investigation of solvation effects.^[11, 12, 13, 14] In particular, the VCD and ROA spectra of monosaccharides in solution have revealed sensitivities

towards the different anomer, epimer, and homomorphic configurations of monosaccharides.^[15,16] Several solvation studies on monosaccharides have implemented a combined molecular dynamics (MD) and *ab initio* DFT approach to model the experimental Raman and ROA features of monosaccharides in water.^[17,18,19,20]

In this study, we focus on methyl- β -D-glucopyranose (me- β -D-gluc), a representative monosaccharide, and apply the clusters-in-a-liquid solvation model^[21] to interpret the experimental IR and VCD spectra of me- β -D-gluc in water. The clusters-in-a-liquid solvation model hypothesizes that the experimental vibrational optical activity features of a chiral solute in water are generated not by the chiral solute itself but rather by the long-lived chiral solute-water_{*n*} complexes. The evidence of such long-lived chiral solute-water clusters is the unique induced solvent VCD signature^[22] of the water bending modes, which have been detected experimentally in a range of small chiral molecules in water.^[23] Since water is an achiral molecule, only water in the long-lived chiral solute-water_{*n*} complexes can give rise to such induced VCD signatures.

One significant challenge is that me- β -D-gluc has many H-bond donor and acceptor sites, making the evaluation of the required number of explicit water molecules quite complicated. In this regard, the previous NMR,^[24] ultrasound,^[25] NIR,^[26] and combined IR and *ab initio*^[27] investigations of other monosaccharides in water have provided some insight into the existence of monosaccharide-water_{*n*} complexes in water. We will utilize these reported findings in identifying the long-lived me- β -D-gluc-(water)_{*n*} clusters in water.

5.2 Experimental Section

5.2.1 Experimental Details

Methyl- β -D-glucose (99%) was obtained from Sigma-Aldrich and was used without further purification. The IR and VCD measurements were performed using a Bruker Vertex 70 Fourier transform infrared spectrometer coupled to a PMA 50 VCD model at room temperature. A variable path length cell that contains BaF₂ windows and a low pass

filter with a cutting wave number of 1800 cm^{-1} was used for the measurements. The spectral resolution of 4 cm^{-1} was used for solution IR and VCD measurements. Since experimental VCD measurements in water are affected by the water bending absorbance band in the 1650 cm^{-1} region, the interference from solvent water can be minimized through using both high concentration and low path length conditions. A concentration of 200mg/ml of methyl- β -D-glucose in water and a path length of $3\text{ }\mu\text{m}$ (without spacer) were selected for the IR and VCD measurements. All the solutions required for IR and VCD measurements were prepared using double distilled water. The VCD measurement of me- β -D-gluc in water was undertaken for a 10 h (5×2 h) time period mainly because the VCD signals are 10^4 times inferior than the corresponding VA signals. The resulting 10 h averaged raw VCD spectrum of me- β -D-gluc in water were corrected for background effects using the 10 h averaged VCD spectrum of water. The IR spectrum of me- β -D-gluc in water was corrected for the solvent absorbance.

5.2.2 Computational Details

All geometry optimizations, harmonic frequency calculations, and IR as well as VCD intensity calculations were carried out using the Gaussian09 program package.^[28] The calculations were done using the Becke, three-parameter, Lee-Yang-Parr (B3LYP) functional^[29] and the 6-311++G (2d,p) basis set.^[30] The B3LYP functional and the basis set were selected mainly due to their proven accuracy in simulating VCD and ROA intensities.^[31] The implicit solvent effects were modelled using the integral equation formalism (IEF) version of PCM.^[32] All optimized geometries of the me- β -D-gluc monomer and its clusters with water were obtained in the PCM of water for comparison with the experiment. All optimized geometries were confirmed to be true minima without any imaginary frequencies. The IR and VCD spectra were simulated using Lorentzian line shapes of 8 cm^{-1} half width at half height (HWHH) for the water. No frequency scaling factors were used.

5.3 Results and Discussion

5.3.1 Implicit Solvation

The conformational space of D-glucopyranose and its derivatives has been the subject of many theoretical investigations.^[33, 34, 35, 36, 37] While the flexibilities of the six-member pyranose ring, ring hydroxy groups, and exocyclic hydroxymethyl group offer many conformational possibilities,^[33] Simons and co-workers showed that phenyl- β -D-glucopyranose contains only a limited number of stable conformations.^[36, 37] This is because the 4C_1 chair conformation is favoured strongly over the other possible six-member ring conformations.^[38] Note that 4C_1 stands for chair configuration with carbon atom C4 up and C1 down (See Figure 5.1 for atom labels). The ring hydroxyl groups of D-glucopyranose may orient in either the clockwise (c) or counter clockwise (cc) fashion to form cooperative intramolecular hydrogen bonding interactions.^[39] The condensed phase investigations of D-glucopyranose-based monosaccharides show strong contributions from the G(+60°) and G(-60°) conformations and a negligible contribution from the T(180°) conformation, where the notation refers to the O5—C5—C6—O6 dihedral angle.^[40] The G+ and G- conformations of exocyclic hydroxymethyl group favours the operation of stabilizing hyperconjugation interactions between the C-O anti bonding orbital and the C—C/C—H bonding orbitals, whereas the T conformation does not allow the operation of such stabilizing hyperconjugation interactions between the C-O anti bonding orbital and the C—C/C—H bonding orbitals.^[41] The above conformational preferences reported on the D-glucopyranose structure have provided the basis for the investigation of the conformational space of me- β -D-gluc. In addition, the g(+60°), g(-60°), and t(180°) notations are used for the conformations associated with the C5—C6—O6—H dihedral angle. In Figure 5.1, the variation of these two dihedral angles and the cooperative H-bonding topology directions that can generate all possible conformations are indicated.

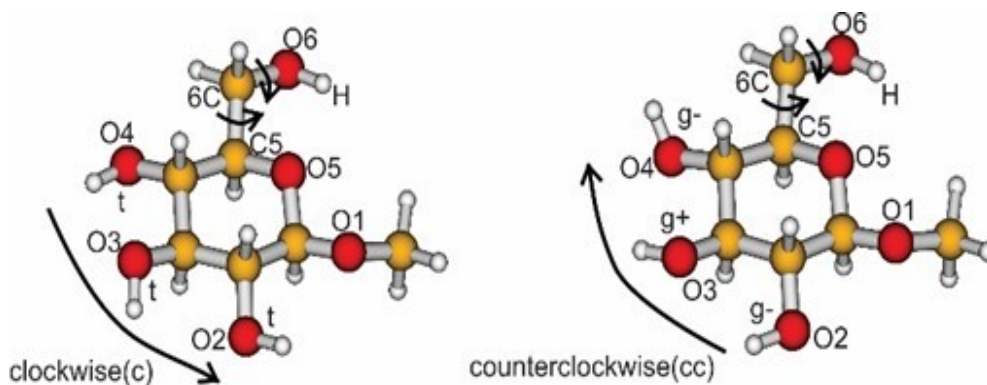


Figure 5.1. Methyl- β -D-glucopyranose is depicted in the 4C_1 chair conformation. The two small arrows indicate the rotation about the C5—C6 and C6—O6 bonds corresponding to the O5—C5—C6—O6 and C5—C6—O6—H dihedral angles, respectively. The large arrow indicates the direction of the cooperative H-bonds.

The conformational search of me- β -D-gluc results in 12 conformations at the B3LYP/6-311++G(2d,p) level of theory with the PCM of water, which are presented in Figure 5.2. The computed relative free energies and Boltzmann factors of all conformations of me- β -D-gluc at 298 K are presented in Table 5.1.

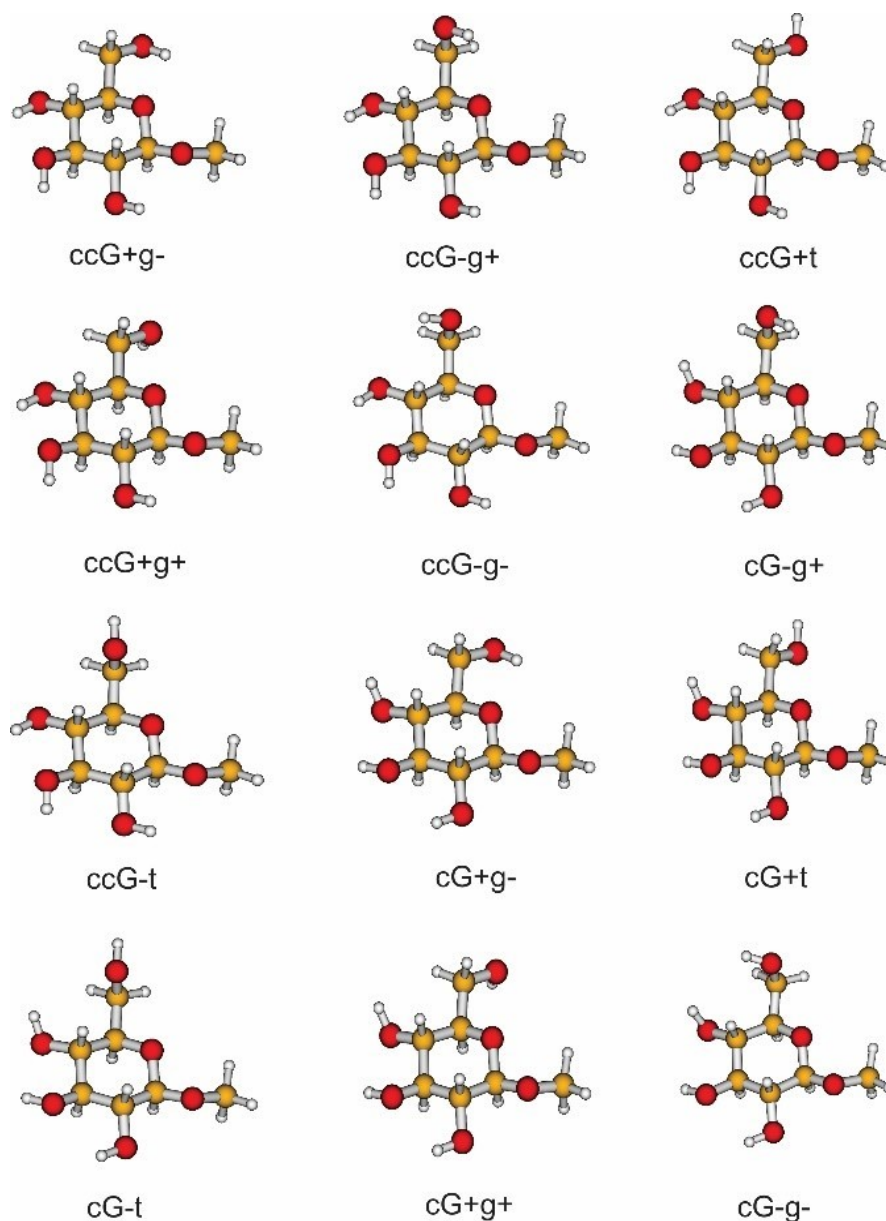


Figure 5.2. The stable conformers of me-β-D-gluc obtained at the B3LYP/6-311++G(2d,p) level of theory with the PCM of water. Please refer to the main text for the definition of the letter symbols.

The ccG+g- and ccG-g+ conformers, which have been identified as the most and second most stable conformations of phenyl-β-D-glucopyranose in the gas phase by Talbot et al., also turn out to be the most and the second most stable conformer of me-β-D-gluc obtained with the PCM of water, respectively. These two conformers differ with respect to the orientations of O5—C5—C6—O6 and C5—C6—O6—H dihedral angles related to the exocyclic hydroxymethyl group. Out of the six clockwise conformers shown in Figure 5.2,

cG-g⁺ and cG-g⁻ are ~5–6 kJ mol⁻¹ higher in energy than the most stable ccG+g⁻ conformer, whereas the remaining four clockwise conformers are 10–11 kJ mol⁻¹ higher. The Boltzmann factors of the G⁺ and G⁻ conformations of me-β-D-gluc in the PCM of water turn out to be ~60.5% and ~39.5%, respectively. The above predicted Boltzmann factors differ a bit from the experimental ones obtained for D-glucopyranose in water, which are 45% and 55%, respectively.^[42]

Table 5.1. The relative free energies, ΔG , (in kJ mol⁻¹) and the Boltzmann factors at 298 K (in %) of the conformer of me-β-D-gluc with the PCM of water.

Conformer	$\Delta G/ \text{kJ mol}^{-1}$	Boltz. factor %
ccG+g ⁻	0.00	41.1
ccG-g ⁺	1.21	25.2
ccG+t	4.11	7.8
ccG+g ⁺	4.59	6.5
ccG-g ⁻	5.46	4.5
cG-g ⁺	5.49	4.5
ccG-t	5.72	4.1
cG+g ⁻	5.90	3.8
cG+t	9.90	0.7
cG-t	10.1	0.7
cG+g ⁺	10.3	0.6
cG-g ⁻	11.1	0.5

The simulated IR and VCD spectra of the 12 conformers of me-β-D-gluc in the PCM of water are summarized in Figure 5.3. An inspection of the simulated IR spectra of the me-β-D-gluc conformers reveals some important aspects. The strongest IR bands of all conformers concentrate in the 950–1100 cm⁻¹ region. The major contribution for the

generation of these IR bands comes from the endo and exo-cyclic C—O and C—C stretching vibrations,^[43, 44] and different orientations of endo and exo-cyclic C—O and C—C groups generate some variations in the IR bands with respect to both band positions and intensities. The ccG+ conformations seem to produce four visually distinguishable IR bands, with two stronger ones in the middle and two weaker ones at each side that closely resemble the experimental features in this region. The ccG- conformations, on the other hand, tend to have a more evenly distributed intensity for bands in this region than that shown by the experimental ones. Finally, the cG- and cG+ conformations produce three or four visually separated IR bands, with one strongest band centred at $\sim 1020\text{ cm}^{-1}$ differing from the experimental features. The IR bands in the $1200\text{--}1500\text{ cm}^{-1}$ region come from the C—O—H and C—C—H bending vibrations, which are generally much weaker than the strong features in the $950\text{--}1100\text{ cm}^{-1}$ region. Experimentally, the $1200\text{--}1500\text{ cm}^{-1}$ region is characterized by unresolved bands that lift the baseline noticeably but without much specific band features.

For the VCD spectra in the $950\text{--}1100\text{ cm}^{-1}$ region, the cc conformers generally exhibit strong, roughly “W” shaped VCD signature if one ignores the narrow splitting of the bands visible in some cases. The c conformers, on the other hand, generally exhibit weaker VCD intensities in the above region than the cc-conformers, with no specific common features. As mentioned before, the main IR bands in the $1200\text{--}1500\text{ cm}^{-1}$ region are mainly from the C—O—H bending and C—C—H bending vibrations. The conformers identified exhibit very different spatial orientations of the C—O—H and C—C—H groups, resulting in very different VCD patterns for each conformer in this region. In addition, in the $1200\text{--}1500\text{ cm}^{-1}$ region, the simulated VCD features of cc conformers are generally weaker than their VCD features in the $950\text{--}1100\text{ cm}^{-1}$ region, whereas stronger VCD features are noted for some c conformers.

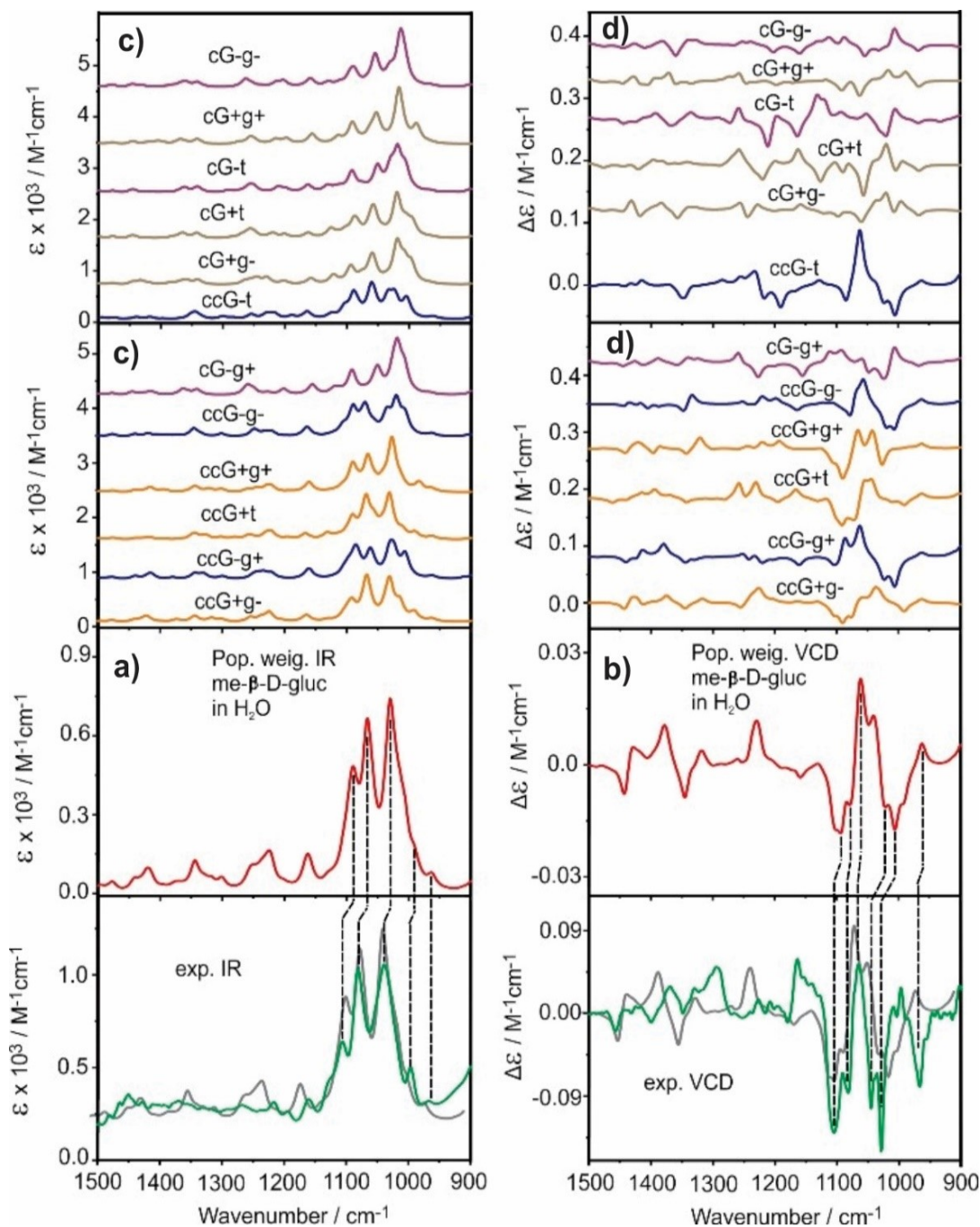


Figure 5.3. Comparisons of experimental IR and VCD spectra of methyl-β-D-glucopyranose in water with the population weighed VA(IR) (a) and VCD (b) spectra of the me-β-D-gluc monomer in the PCM of water and also with the simulated VA(IR) (c) and VCD (d) spectra of stable conformers of me-β-D-gluc in the PCM of water. The dashed lines indicate the corresponding experimental and theoretical features. The gray traces behind the experimental data are the population weighted IR and VCD spectra, which are shifted slightly by the same amount to guide the comparison.

Figure 5.3 also contains the comparison of experimental IR and VCD spectra of me- β -D-gluc in water with the population weighed IR and VCD spectra of me- β -D-gluc monomer in the PCM of water. We use dashed lines to connect the theoretical and corresponding experimental features and gray traces to make it easier to recognize the associated experimental and theoretical features by lining up the dominant IR features in the 900–1170 cm^{-1} region between the experiment and theory. While the experimental IR features in this lower frequency are reproduced well theoretically, one cannot say the same for the corresponding VCD features. For example, in the region below 1000 cm^{-1} , the main VCD features are predicted with the opposite signs of the experimental ones. The experimental IR bands in the 1170–1500 cm^{-1} region overlap severely, as indicated by the lifted base line over the whole region. It is, therefore, difficult to comment on the quality of the agreement between the experimental and theoretical IR bands. The VCD bands, on the other hand, show some noticeable disagreements in the 1170–1420 cm^{-1} region. As discussed above, the C—O—H bending vibrations of me- β -D-gluc play a vital role in the appearance of VCD features in the region, therefore, one may expect the intermolecular H-bonding interactions between the C—O—H groups of me- β -D-gluc and solvent water molecules to influence the VCD signatures in this region noticeably.

5.3.2 The *Clusters-in-a-Liquid* Solvation Model in the Simulation of IR and VCD Spectra of Methyl- β -D-glucopyranose in Water

Several solvation studies, which used a combined molecular dynamics (MD) and DFT approach to model the experimental Raman and ROA features of monosaccharides in water, have been reported.^[17, 18, 19, 20] In one study,^[20] the QM solute monosaccharide and the MM solvent water molecules were used in the 2-layer ONIUM model^[45] to reproduce Raman and ROA spectra of me- β -D-gluc in water with good agreement. With this model, the explicit H-bonding interactions with water solvent molecules are not considered since only MM water molecules were used. To include explicit solute-water H-bonding interactions, Melcrova et al. used the parallel variable selection (PVS)^[46] method to reduce the number of MD snapshots needed.^[19] The selected monosaccharide-(water)_n clusters,

which include only water molecules in the first hydration shell, were optimized using a partial optimization process,^[47] which restricts the relaxation of low frequency vibrational motions, and the PCM of water accounts for additional solvent effects. The final averaged Raman and ROA spectra reveal good correlations with the experimental spectra. The above approaches have not been used on VCD spectral features, which tend to be even more sensitive to solvent effects.^[17, 18, 19, 20]

Here, we apply a somewhat different approach, namely the *clusters-in-a-liquid* model^[21] to account for the water solvent effect. The model hypothesizes that the significant contribution to the observed spectra is made by the *long-lived* hydration complexes, rather than by the chiral solute itself. The observed induced solvent VCD signatures of the water bending vibration mode has provided proofs and insights about the existence of *long-lived* chiral solute-water_{*n*} clusters in water.^[22, 23] To apply the *clusters-in-a-liquid* model to account for the water solvent effects, one needs to identify the *long-lived* me-β-D-gluc-(water)_{*n*} clusters. This task is challenging. While it is fairly straightforward to identify such hydration clusters for simpler systems with limited H-bonding sites, the availability of multiple H-bond donor and acceptor sites in me-β-D-gluc makes it complicated. In addition, one needs to be concerned about the competition between intra- and inter-molecular H-bonding interactions, which may impact the composition of the *long-lived* hydration clusters.

Some hints about such hydration clusters can be extracted from several previous studies. Suzuki et al.^[27] investigated the experimental IR features of glucose by using the simulated IR features of glucose-(water)_{*n*} complexes (where *n* = 4 to 9) with the continuum reaction field under Onsager's model and identified the important roles of *n* = 8, 9 hydration complexes in the interpretation of experimental IR features obtained in the 1000–1300 cm⁻¹ region. Furthermore, the ultrasound,^[25] NIR,^[26] and NMR^[24] experiments of β-D-glucose and its methyl derivatives in water have identified the hydration number of β-D-glucose and its methyl derivatives to be in the range of 8 to 10. Finally, several MD simulations that investigated the interactions between β-D-glucose and water have recognized the existence of D-glucose-water_{8,9} complexes.^[48] The above results provide insights about the long-lived existence of monosaccharide-(water)_{*n*} clusters in water.

In the current study, we decided to choose the $\text{me-}\beta\text{-D-gluc-(water)}_8$ complexes to understand the effects of such clusters on the appearance of IR and VCD spectra. We have considered all 12 glucose conformers in the modelling of the $\text{me-}\beta\text{-D-gluc-(water)}_8$ complexes in the PCM of water. One reason to include all monomeric conformers is that it is recognized increasingly that solvation can alter the relative conformational stability of a solute drastically. For example, Carcabal et al. observed that the most stable monohydrated complex of phenyl- $\beta\text{-D-glucopyranose}$ contains the cG-g+ conformer, which lies 10 kJ mol^{-1} above the most stable ccG+g+ conformer in the gas phase.^[37] We also note that Klein reported the formation of strong bidentate cooperative H-bonding interactions between the ring hydroxy groups of glucopyranose and water.^[49] Taking these considerations into account in solvating $\text{me-}\beta\text{-D-gluc}$ with eight water molecules, we introduced four explicit water molecules to form cooperative H-bonding interactions with the ring hydroxy and ring methoxy groups of glucopyranose. Furthermore, Sukuzi reported MD simulations of glucose in water and identified more than one acceptor/donor H-bond for the O6/H(-O6) atoms of the exocyclic hydroxymethyl group, respectively.^[50] Based on the above evidence, we introduced two to three explicit water molecules to model the H-bonding interactions with the exocyclic hydroxymethyl group of $\text{me-}\beta\text{-D-gluc}$. The remaining (1–2) explicit water molecules can form H-bonds in two main ways. The first possibility is to form H-bonding interactions with the remaining unoccupied H-bond donor/acceptor sites of $\text{me-}\beta\text{-D-gluc}$. The second possibility is for these explicit water molecules to form H-bonds with other explicit water molecules. Overall, around 300 methyl- $\beta\text{-D-gluc-(water)}_8$ complexes in the PCM of water were considered. The optimized geometries of 20 low-energy $\text{me-}\beta\text{-D-gluc-(water)}_8$ complexes at the B3LYP/6-311++G(2d,p) level of theory with the G-g+ and G+g+ conformations are summarized in Figure 5.4a) and b), respectively, alongside with their individual relative free energies and Boltzmann factors at room temperature.

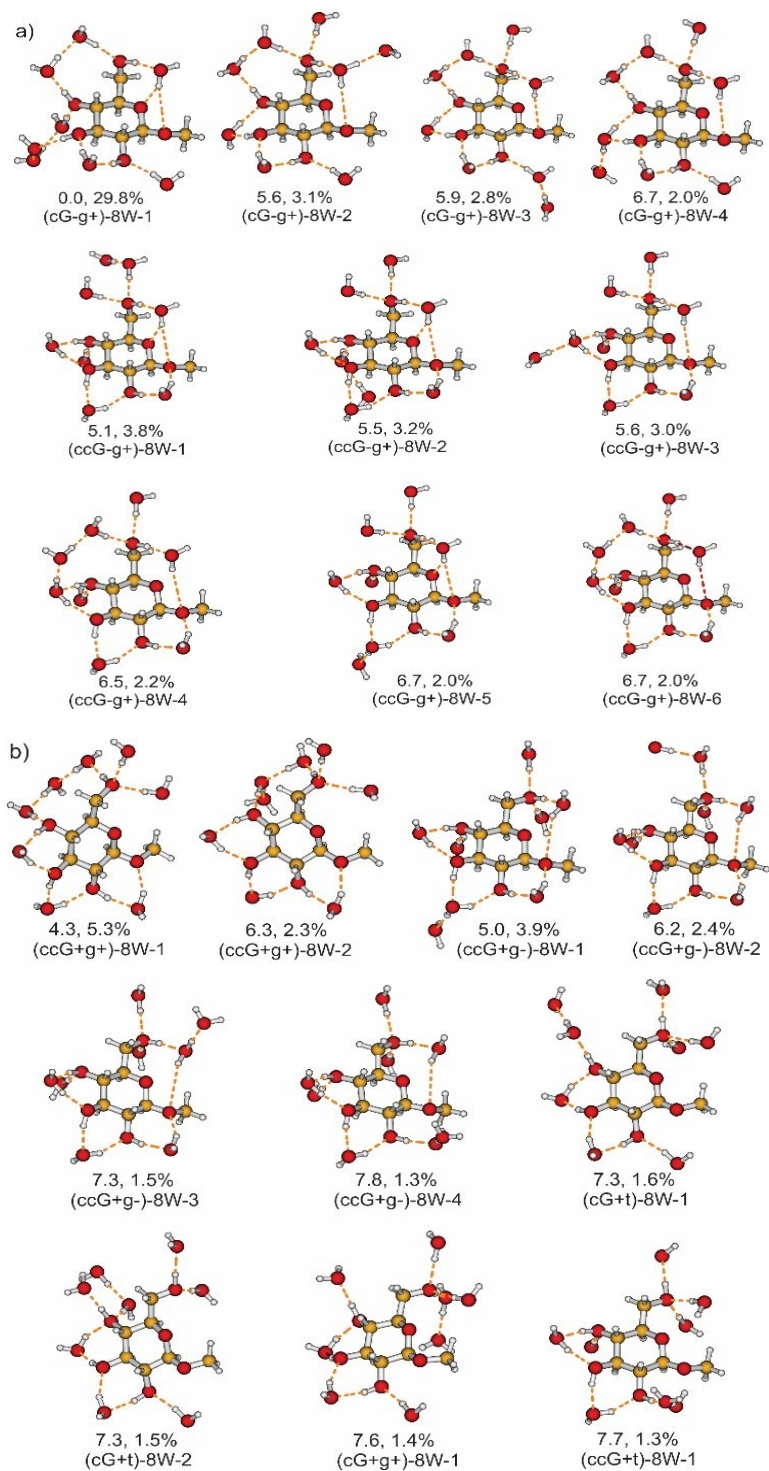


Figure 5.4. Optimized geometries of the 20 most stable me- β -D-gluc-(H₂O)₈ complexes containing a) G-g+ and b) G+g- me- β -D-gluc conformers in the PCM of water. The relative free energies (in kJ mol⁻¹) and Boltzmann factors (%) of each cluster at room temperature also are listed. The Arabic numbers indicate the relative stability of the hydration clusters containing a particular me- β -D-gluc conformer, with 1 being the most stable one.

Although the ccG+g- conformer is recognized as the most stable conformer of me- β -D-gluc with the PCM of water, its octahydrate complex is 5.5 kJmol⁻¹ less stable than the most stable (cG-g+)-8W-1 octahydrate complex obtained in the PCM of water. Similar to the monohydrate^[37] and dihydrate^[51] complexes of phenyl- β -D-glucopyranose in the gas phase, the most stable (cG-g+)-8W-1 complex identified contains an extensive cooperative H bonded chain O1 \rightarrow W1 \rightarrow O2H \rightarrow W2 \rightarrow O3H \rightarrow W3 \rightarrow W4W5 \rightarrow O4H \rightarrow W6 \rightarrow W7 \rightarrow O6H \rightarrow W8 \rightarrow O5 (Figure 5.5 a)). In comparison, the second most stable octahydrate complex, (ccG+g+)-8W-1, lies \sim 4.3 kJmol⁻¹ above the most stable octahydrate complex. The optimized geometry of the (ccG+g+)-8W-1 complex reveals the existence of O1 \rightarrow W1 \rightarrow HO2 \rightarrow W2 \rightarrow HO3 \rightarrow W3 \rightarrow HO4 \rightarrow W4 \rightarrow W5 \rightarrow W6 \rightarrow HO6 \rightarrow Hs of 7W and 8W cooperative H-bonded chain (Figure 5.5 b)). Therefore, the preference in binding explicit water molecules to the high energy cG-g+ and ccG+g+ monomeric conformers comes from the generation of these strongly cooperative H-bonded networks. The population percentages of the octahydrate complexes of the G- and G+ conformations turn out to be 66.7% and 33.3%, respectively. These percentages demonstrate a closer resemblance to the experimental percentages of the G- and G+ conformations of D-glucopyranose in water of 55:45^[42] than the ratio obtained with consideration of the monomeric forms only.

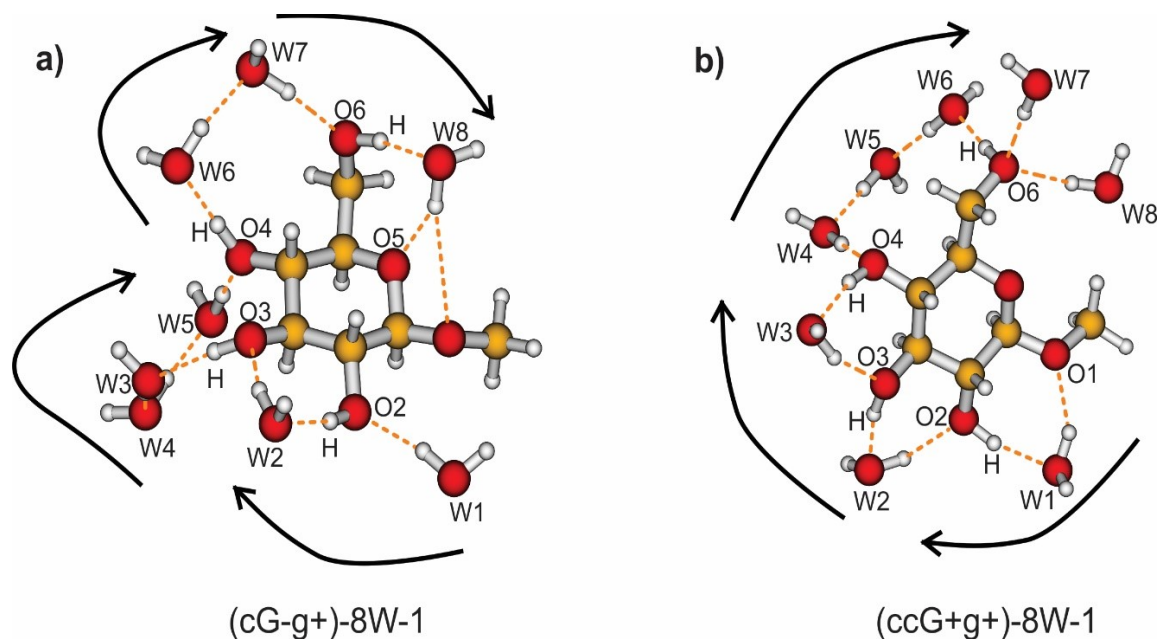


Figure 5.5. The strong cooperative H-bonding chains are indicated with the arrowed lines in the a) most stable cG-g+-8W-1 and the b) second most stable ccG+g+-8W-1 octahydrate complexes.

The simulated IR and VCD spectra of the 20 me- β -D-gluc-(water)₈ conformers are presented in Figure 5.6. The H-bonding interactions with water change the IR and especially the VCD spectral features from those of the monomeric solute conformers. It is noted that most main IR and VCD features can be reproduced by the related features produced from some octahydrates. For example, the simulated VCD features of (cG-g+)-8W-1, the most stable octahydrate, capture all the main experimental VCD features in the 900–1500 cm⁻¹ region, except for the strong negative experimental VCD feature observed around 1100 cm⁻¹. Similarly, the simulated VCD features of (cG-g+)-8W-2, (cG-g+)-8W-3, and (cG-g+)-8W-4 complexes correctly predict the experimental VCD features in the 900–1350 cm⁻¹ region, except for the strong negative VCD feature observed around 1100 cm⁻¹. On the other hand, the above strong negative experimental VCD feature at ~1100 cm⁻¹ is predicted correctly by the simulated VCD spectra of ccG+ octahydrate complexes. Finally, only the simulated VCD spectra of ccG+g+ octahydrate complexes predict the -ve/+ve/-ve/+ve experimental VCD features observed in the 990–1100 cm⁻¹ region correctly.

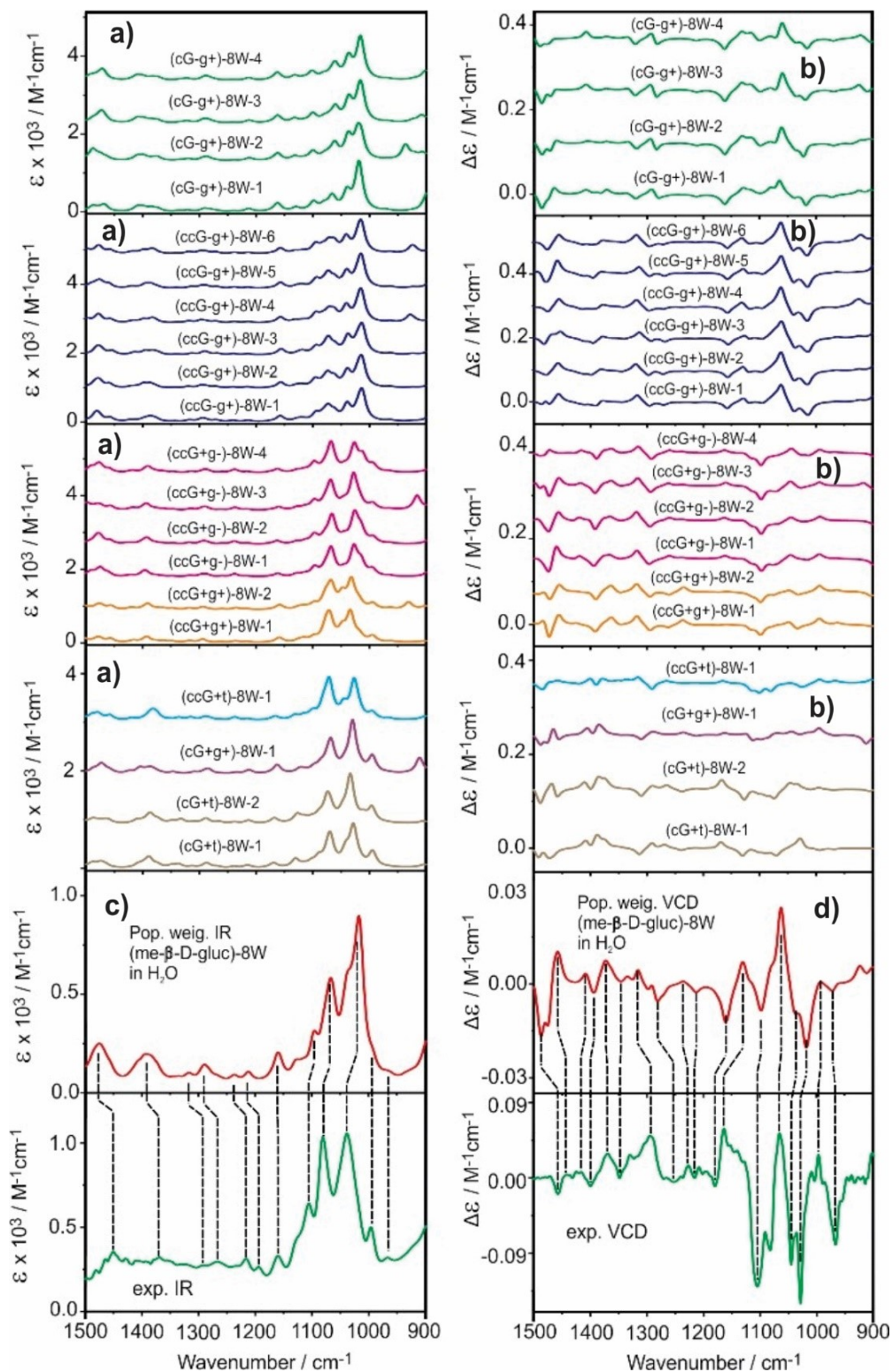


Figure 5.6. The simulated IR (a) and VCD (b) spectra of the $\text{me-}\beta\text{-D-gluc-(H}_2\text{O)}_8$ complexes are shown in the top section, while the comparisons of the Boltzmann weighted IR (c) and VCD (d) spectra with the experimental data are provided at the bottom section.

Instead of going over these tedious details, we focus now on the Boltzmann weighted IR and VCD spectra of me- β -D-gluc-(H₂O)₈ complexes. For the IR spectra, it appears that most experimental IR bands in the region above 1150 cm⁻¹, even though not well resolved in most cases, can be correlated to the corresponding theoretical features, while good agreements also have been achieved between the experiment and theory for the IR bands below 1150 cm⁻¹. The agreement between the VCD experimental data and theoretical simulation has improved noticeably with the inclusion of the explicit water molecules for the whole spectral region. For example, the negative VCD band at 960 cm⁻¹ and the positive band at about 1000 cm⁻¹ now are predicted correctly, in contrast to the opposite signs predicted without the inclusion of explicit water molecules. Much better agreements also have been achieved for the experimental VCD features above 1150 cm⁻¹ with those predicted with the inclusion of explicit water molecules than without the presence of explicit water.

5.4 Conclusions

In this study, we have undertaken the interpretation of experimental IR and VCD spectra of me- β -D-gluc in water using both the implicit solvation model and the *clusters-in-a-liquid* solvation model. Twelve low-energy me- β -D-gluc conformers were identified in the PCM of water. While the main IR and VCD features in the 1000–1150 cm⁻¹ region could be explained by the me- β -D-gluc conformers alone, noticeable disagreements were noted, suggesting that the me- β -D-gluc monomers are not the dominant species in water. By applying the *clusters-in-a-liquid* solvation model, the me- β -D-gluc-(water)₈ octahydrate complexes in the PCM of water were constructed, and 20 low-energy octahydrate conformers were identified. The simulated IR and VCD spectra, based on the me- β -D-gluc-(water)₈ octahydrate complexes in the PCM of water, capture all the main experimental features, providing much better agreements with the experimental data than use of the model based on the monomers alone. The better agreements achieved with the me- β -D-gluc-(water)₈ clusters in the PCM of water strongly indicate that these are the long-lived species in the aqueous solution of me- β -D-gluc.

5.5 Acknowledgement

This work was funded by the Natural Sciences and Engineering Research Council of Canada, Canada Foundation for Innovation, and by the University of Alberta. We gratefully acknowledge access to the computing facilities of the Shared Hierarchical Academic Research Computing Network, the Western Canada Research Grid (Westgrid), and Compute/Calcul Canada. YX is a Tier I Canada Research Chair in Chirality and Chirality Recognition.

5.6 References

-
1. a) R. A. Dwek, *Chem. Rev.*, **1996**, *96*, 683–720; b) H. Rudiger, H. -C. Siebert, D. Solis, J. Jimenez-Barbero, A. Romero, C. -W. von der Lieth, T. Diaz-Maurino, H. -J. Gabius, *Curr. Med. Chem.*, **2000**, *7*, 389–416; c) A. P. Davis, R. S. Wareham, *Angew. Chem., Int. Ed.*, **1999**, *38*, 2978–2996; d) J. B. Lowe, J. D. Marth, *Annu. Rev. Biochem.* **2003**, *72*, 643–691; e) J. Lehmann, *Carbohydrates Structure and Biology*; Georg Thieme: Stuttgart, Germany, **1998**; f) Hricovini, *M. Curr. Med. Chem.*, **2004**, *11*, 2565–2583.
 2. R. V. Stick, S. J. Williams, *Carbohydrates: The Essential Molecules of Life*, Elsevier Science, **2009**.
 3. R. U. Lemieux, *Explorations with Sugars: How Sweet it Was*; American Chemical Society, Washington, DC, **1990**.
 4. a) K. G. Rice, P. Wu, L. Brand, Y. C. Lee, *Curr. Opin. Struct. Biol.*, **1993**, *3*, 669–674; b) M. R. Wormald, A. J. Petrescu, Y. -L. Pao, A. Glithero, T. Elliott, *Chem. Rev.*, **2002**, *102*, 371–386; c) R. A. Dwek, C. J. Edge, D. J. Harvey, M. R. Wormald, R. B. Parekh, *Annu. Rev. Biochem.* **1993**, *62*, 65–100.
 5. a) C. Clarke, R. J. Woods, J. Gluska, A. Cooper, M. A. Nutley, G.-J. Boons, *J. Am. Chem. Soc.*, **2001**, *123*, 12238–12247; b) E. Klein, Y. Ferrand, N. P. Barwell, A. P. Davis, *Angew. Chem.*, **2008**, *120*, 2733–2736; c) F. A. Quioco, D. K. Wilson, N. K. Vyas, *Nature*, **1989**, *340*, 404.
 6. P. Colins, R. Ferrier, *Monosaccharides; Their Chemistry and their Roles in Natural Products*, Wiley, New York, **1995**.
 7. a) L. A. Nafie, *Vibrational Optical Activity: Principles and Applications*, John Wiley & Sons, Ltd., UK, **2011**; b) G. Yang and Y. Xu, *Top. Curr. Chem.*, **2011**, *298*, 189–236; c) J. M. Batista, A. N. L. Batista, J. S. Mota, Q. B. Cass, M. J. Kato, V. S. Bolzani, T. B. Freedman, S. N. Lopez, M. Furlan, L. A. Nafie, *J. Org. Chem.*, **2011**, *76*, 2603–2612; d) H. Sato, H. Uno, H. Nakano, *Dalton Trans.*, **2011**, *40*, 1332–1337;

-
- e) D. Dunmire, T. B. Freedman, L. A. Nafie, C. Aeschlimann, J. G. Gerber, J. Gal, *Chirality*, **2005**, *17*, 101–108; f) P. L. Polavarapu, *Chirality*, **2012**, *24*, 909–1020.
8. V. Parchaňský, J. Kapitán, P. Bouř, *RSC Adv.*, **2014**, *4*, 57125–57136.
9. a) J. R. Chessman, J. Frisch, J. Devlin, J. P. Stephens, *Chem. Phys. Lett.*, **1996**, *252*, 211–220; b) J. R. Cheeseman, M. J. Frisch, *J. Chem. Theo. Comput.*, **2011**, *7*, 3323–3334.
10. a) W. Hug, *Appl. Spectrosc.* **2003**, *57*, 1–13; b) X. L. Cao, R. K. Dukor, L. A. Nafie, *Theo. Chem. Acc.* **2008**, *119*, 69–79.
11. a) M. Srebro-Hooper and J. Autschbach, *Annual Rev. Phys. Chem.*, **2017**, *68*, 399–420; b) M. R. Poopari, Z. Dezhahang, Y. Xu, *Phys. Chem. Chem. Phys.*, **2013**, *15*, 1655–1665 c) M. Passarello, S. Abbate, G. Longhi, S. Lepri, R. Ruzziconi, V. P. Nicu, *J. Phys. Chem. A*, **2014**, *118*, 4339–4350; d) Y. Zhang, M. R. Poopari, X. Cai, A. Savin, Z. Dezhahang, J. Cheramy, Y. Xu, *J. Nat. Prod.*, **2016**, *79*, 1012–1023.
12. a) J. E. Rode, J. C. Dobrowolski, K. Lyczko, A. Wasiewicz, D. Kaczorek, R. Kawęcki, G. Zając, M. Baranska, *J. Phys. Chem. A*, **2017**, *121*, 6713–6726; b) K. Bünnemann and C. Merten, *Phys. Chem. Chem. Phys.*, **2017**, *19*, 18948–18956.
13. M. R. Poopari, Z. Dezhahang, Y. Xu, *Phys. Chem. Chem. Phys.*, **2013**, *15*, 1655–1665.
14. S. Lubber, M. Reiher, *J. Phys. Chem. A*, **2009**, *113*, 8268–8277.
15. a) P. K. Bose, P. L. Polavarapu, *Carbohydrate Research*, **1999**, *390*, 172–183; b) K. Monde, T. Taniguchi, N. Miura, S. I. Nishimura, *J. Am. Chem. Soc.*, **2004**, *126*, 9496–9497.
16. a) Z. Q. Wen, L. D. Barron, L. Hecht, *J. Am. Chem. Soc.*, **1993**, *115*, 285–292; b) A. F. Bell, L. D. Barron, L. Hecht, *Carbohydrate Research*, **1994**, *257*, 11–24.
17. S. T. Mutter, F. Zielinski, J. R. Cheeseman, C. Johannessen, P. L. A. Popelier, E. W. Blanch, *Phys. Chem. Chem. Phys.*, **2015**, *17*, 6016.
18. F. Zielinski, S. T. Mutter, C. Johannessen, E. W. Blanch, P. L. A. Popelier, *Phys. Chem. Chem. Phys.*, **2015**, *17*, 21799.
19. A. Melcrova, J. Kessler, P. Bour, J. Kaminsky, *Phys. Chem. Chem. Phys.*, **2016**, *18*, 2130.
20. J. R. Cheeseman, M. S. Shaik, P. L. A. Popelier, E. W. Blanch, *J. Am. Chem. Soc.*, **2011**, *133*, 4991–4997.
21. A. S. Perera, J. Thomas, M. R. Poopari and Y. Xu, *Front. Chem.*, **2016**, *4*, 1–17.

-
22. J. Sadlej, J. C. Dobrowolski and J. E. Rode, *Chem. Soc. Rev.*, **2010**, 39, 1478–1488.
23. a) M. Losada and Y. Xu, *Phys. Chem. Chem. Phys.*, **2007**, 9, 3127–3135; b) G. Yang and Y. Xu, *J. Chem. Phys.*, **2009**, 130, 164506; c) M. Losada, P. Nguyen and Y. Xu, *J. Phys. Chem. A*, **2008**, 112, 5621–5627; d) M. Losada, H. Tran and Y. Xu, *J. Chem. Phys.*, **2008**, 128, 014508.
24. J. M. Harvey, M. C. R. Symons, R. J. Naftalin, *Nature*, **1976**, 261, 435–436.
25. S. A. Galerna, H. Holland, *J. Phys. Chem.*, **1991**, 95, 5321–5326.
26. J. L. Hollenberg, D. O. Hall, *J. Phys. Chem.*, **1983**, 87, 695–696.
27. T. Suzukia, T. Sota, *J. Chem. Phys.*, **2003**, 119, 19, 10133.
28. Gaussian 09 (Revision D.01), M. J. Frisch, G. W. Trucks, H. B. Schlegel, G. E. Scuseria, M. A. Robb, J. R. Cheeseman, G. Scalmani, V. Barone, B. Mennucci, G. A. Petersson, H. Nakatsuji, M. Caricato, X. Li, H. P. Hratchian, A. F. Izmaylov, J. Bloino, G. Zheng, J. L. Sonnenberg, M. Hada, M. Ehara, K. Toyota, R. Fukuda, J. Hasegawa, M. Ishida, T. Nakajima, Y. Honda, O. Kitao, H. Nakai, T. Vreven, J. A. Montgomery, Jr., J. E. Peralta, F. Ogliaro, M. Bearpark, J. J. Heyd, E. Brothers, K. N. Kudin, V. N. Staroverov, T. Keith, R. Kobayashi, J. Normand, K. Raghavachari, A. Rendell, J. C. Burant, S. S. Iyengar, J. Tomasi, M. Cossi, N. Rega, J. M. Millam, M. Klene, J. E. Knox, J. B. Cross, V. Bakken, C. Adamo, J. Jaramillo, R. Gomperts, R. E. Stratmann, O. Yazyev, A. J. Austin, R. Cammi, C. Pomelli, J. W. Ochterski, R. L. Martin, K. Morokuma, V. G. Zakrzewski, G. A. Voth, P. Salvador, J. J. Dannenberg, S. Dapprich, A. D. Daniels, O. Farkas, J. B. Foresman, J. V. Ortiz, J. Cioslowski, D. J. Fox, Gaussian, Inc., Wallingford CT, **2013**.
29. A. D. Becke, *J. Chem. Phys.*, **1993**, 98, 5648–5652.
30. R. Krishnan, J. S. Binkley, R. Seeger, J. A. Pople, *J. Chem. Phys.*, **1980**, 72, 650–654.
31. a) P. J. Stephens, F. J. Devlin, C. F. Chabalowski, M. J. Frisch, *J. Phys. Chem.*, **1994**, 98, 11623–11627; b) T. Kuppens, K. Vandyck, J. Van der Eycken, W. Herrebout, B. J. van der Veken, P. Bultinck, *J. Org. Chem.*, **2005**, 70, 9103–9114.
32. a) B. Mennucci, J. Tomasi, R. Cammi, J. R. Cheeseman, M. J. Frisch, F. J. Devlin, S. Gabriel and P. J. Stephens, *J. Phys. Chem. A*, **2002**, 106, 6102–6113; b) B. Mennucci, *WIREs Comput Mol Sci*, **2012**, 2, 386.
33. C. J. Cramer, D. G. Truhlar, *J. Am. Chem. Soc.*, **1993**, 115, 13, 5745.
34. J. C. Corchado, M. L. Sanchez, M. A. Aguilar, *J. Am. Chem. Soc.*, **2004**, 126, 7311–7319.

-
35. P.L. Polavarapu, C.S. Ewig, *Journal of Computational Chemistry*, **1992**, *13*, 10,1255–1261.
36. F. O. Talbot, J. P. Simons, *Phys. Chem. Chem. Phys.*, **2002**, *4*, 3562–3565.
37. P. Carcabal, R. A. Jockusch, I. Hunig, L. C. Snoek, R. T. Kroemer, B. G. Davis, D. P. Gamblin, I. Compagnon, J. Oomens, J. P. Simons, *J. Am. Chem. Soc.*, **2005**, *127*, 7311–7319.
38. S. E. Barrows, F. J. Dulles, C. J. Cramer, A. D. French, D. G. Truhlar, *Carbohydr. Res.*, **1995**, *276*, 219–251.
39. J. P. Simons, R. A. Jockusch, P. CarCabal, I. Hunig, R. T. Kroemer, N. A. Macleod, L. C. Snoek, *International Reviews in Physical Chemistry*, **2005**, *24*, 3–4, 489.
40. a) R. H. Marchessault, S. Perez, *Biopolymers* **1979**, *18*, 2369–2374 ; b) J. Gonzalez-Outeirino, K. N. Kirschner, S. Thobhani, R. J. Woods, *Can. J. Chem.*, **2006**, *84*, 569–579; c) K. Bock, J. Duus, *J. Carbohydr. Chem.*, **1994**, *14*, 513–543.
41. N, Uddin, M. K. Ghosh, T. H. Choi, C. H. Choi, *Theor Chem Acc*, **2015**, *134*:122
42. a) Y. Nishida, H. Ohru, H. Mequero, *Tetrahedron Letters*, **1984**, *25*, 1575–1578; b) Y. Nishida, H. Hori, H. Ohru, H. Meguro, *J. Carbohydrate Chemistry*, **1988**, *7*(1), 239–250; c) R. J. Abraham, E. J. Chambers, *magn. Reson. Chem.*, **1992**, *30*, S60–S65.
43. C. M. Tummalapalli, D. M. Back, P. L. Polavarapu, *J. Chem. Soc., Faraday Trans. 1*, **1988**, *84*, 2585.
44. P. K. Bose, P. L. Polavarapu, *J. Am. Chem. Soc.*, **1999**, *121*, 6094–6095.
45. T. Vreven, K. S. Byun, I. Komaromi, S. Dapprich, J. A. Montgomery, Jr., K. Morokuma, M. J. Frisch, *J. Chem. Theory Comput.*, **2006**, *2*, 815–826.
46. J. Kessler, M. Dracinsky, P. Bour, *Journal of Computational Chemistry*, **2013**, *34*, 366–371.
47. J. Hudecova, K. Hopmann, P. Bour, *J. Phys. Chem. B*, **2012**, *116*, 336–342.
48. a) N. W. H. Cheetham, K. Lain, *Carbohydrate Research*, **1996**, *282*, 13–23; b) V. Krautler, M. Muller, P. H. Hunenberger, *Carbohydrate Research*, **2007**, *342*, 2097–2124; c) S. L. Lee, P. G. Debenedettia, *J. Chem. Phys.*, **2005**, *122*, 204511.
49. R. A. Klein, *J. Am. Chem. Soc.*, **2002**, *124*, 13931–13937.
50. T. Suzuki, *Phys. Chem. Chem. Phys.*, **2008**, *10*, 96–105.
51. J. P. Simons, B. G. Davis, E. J. Cocinero, D. P. Gamblin, E. C. Stanca-Kaposta, *Tetrahedron: Asymmetry*, **2009**, *20*, 718–722.

Chapter 6

Conclusions and Future Work

6.1 Conclusions

Vibrational circular dichroism (VCD) and Raman optical activity (ROA) are vibrational optical activity spectroscopies that have become powerful spectroscopic tools in providing stereochemical information for a wide range of chiral molecules in solution.^[1] The main theme of my PhD thesis centers on the characterization of intermolecular interactions associated with chiral molecules using VCD and ROA spectroscopy together with theoretical calculations. Since VOA spectroscopies, especially VCD spectroscopy, are quite sensitive to the conformational aspects of chiral molecules, the conformational modifications due to solute-solvent and solute-solute interactions can be identified through the interpretation of experimental VCD spectra. In this thesis, I have demonstrated the unique sensitivity of VCD spectral signatures to both bulk solvent effects and explicit hydrogen-bonding interactions in solution. In particular, I have discussed the induced solvent chirality (or chiral transfer), VCD spectral features observed in the water bending band region, in detail in Chapter 3. From the chirality transfer spectral signatures reported here and before^[2] and the related conformer specific gas phase spectroscopic studies of small chiral hydration clusters reported by others,^[3] a general picture of solvation in aqueous solution emerges. In such an aqueous solution, some small chiral hydration clusters, rather than the chiral solutes themselves, are the dominant species and are the ones that contribute mainly to the experimentally observed VCD features. These experimental data and the associated theoretical analyses are the foundation for the proposed *clusters-in-a-liquid* approach^[1] to account for solvent effects effectively. One significant challenge in applying the *clusters-in-a-liquid* model is how to identify and model the long-lived solute-(water)_n clusters in water. In Chapters 3 and 5, I have applied the *clusters-in-a-liquid* model to both methyl glycidate and methyl-β-D-glucose, two chiral molecules with a modest and a very large number of hydrogen-bonding sites, respectively.

In this work, I was involved in the development of matrix-isolation (MI) IR and VCD experiments. One goal is to apply MI-IR and MI-VCD spectroscopic methods to obtain better resolved IR and VCD spectral features to aid the assignment of solution spectra. For example, we applied different experimental conditions to produce different degrees of self-aggregation of lactic acid. Utilizing this approach, I have been able to follow the aggregation of lactic acid in a step-wise fashion. The results are summarized in Chapter 4, where the corresponding well-resolved MI-IR and MI-VCD spectral features have made it possible to clarify the previously ambiguous band assignments in solution spectra and achieve a new conclusion about the dominant species in lactic acid solution. In the following, the detailed conclusions of each research chapter are summarized.

In the research study presented in Chapter 3, I investigated the solvation effects on methyl glycidate in two very different solvents, water and CCl_4 , using VCD and ROA spectroscopy. The VCD features of methyl glycidate in water and in CCl_4 are noticeably different, providing the first insights into the different solvation effects of CCl_4 and water. The experimental IR and VCD features of methyl glycidate obtained in CCl_4 were predicted correctly using the simulated spectral features of the monomer of methyl glycidate in the PCM of CCl_4 . In contrast, the simulated IR and VCD features of the monomer of methyl glycidate in the PCM of water failed to reproduce the main IR and VCD features of methyl glycidate in water. In particular, the experimentally observed induced solvent VCD feature at the water bending vibration was not predicted via the implicit solvent model, i.e. the monomer of methyl glycidate in the PCM of water. Instead, we applied the *clusters-in-a-liquid* solvation model. This solvation model postulates that the long-lived solute-water complexes rather than the solute itself are the main species in water that generate the observed IR and VCD spectral features. The simulated spectral features of the methyl glycidate-(H_2O) and the methyl glycidate-(H_2O)₂ complexes in the PCM of water correctly predict all the main experimental IR and VCD features of methyl glycidate in water. The same methyl glycidate-(H_2O)_{1,2} clusters identified above also were used to reproduce the experimental Raman and ROA features of methyl glycidate in water satisfactorily. The correct prediction of all four experimental spectra of methyl glycidate in

water supports the conclusion that the methyl glycidate-(H₂O)_{1,2} clusters identified are the long-lived species in water and are responsible for the spectral features detected.

In Chapter 4, I analyzed the spectral features of different species of lactic acid using MI-IR and MI-VCD spectroscopic methods. Different sample conditions could be achieved with the MI technique to create different degrees of self-aggregation of lactic acid and, therefore, different sizes of the (lactic acid)_n clusters. At 10 K with a fast Ar flow rate, I was able to produce a cold matrix with mainly the lactic acid monomer. A very narrow line width was achieved at 10 K, and the well resolved MI-IR and MI-VCD spectral features could be assigned unambiguously to the lactic acid monomer via theoretical simulation. The comparison of MI-IR and MI-VCD spectral features obtained at 10 K with those recorded at 16 K and 24 K provides clear evidence of the self-aggregation of lactic acid at elevated matrix temperatures and higher lactic acid concentrations. It was recognized that the lactic acid dimer plays a major role in reproducing the experimental MI-IR and MI-VCD features observed at 16 K and 24 K. Clearly, the lactic acid dimer is the dominant species present in the Ar matrix at the above elevated matrix temperatures. The importance of MI-VCD features of LA obtained at 24K is recognized during the interpretation of the solution VCD spectra of LA; furthermore, the lactic acid trimer and tetramer are also present. The comparison of the MI-IR and MI-VCD spectral features obtained at 24 K with 0.1 M and 0.2 M solution VCD spectra provides a good foundation for understanding the self-aggregation of lactic acid in CDCl₃. The broad character of the VCD signatures obtained for the 0.2 M solution and the dominating nature of the negative VCD feature in the 1700–1800 cm⁻¹ region over the rest of the VCD intensities at 0.2 M strongly suggest that the lactic acid tetramer makes a noticeable contribution. To correctly predict the IR and especially the VCD spectra of the 0.2M solution, the dominant existence of the lactic acid tetramer and the lactic acid trimer species in 0.2 M solution are essential. In the same study, we investigated the influence of different DFT approaches on the energetic ordering of the lactic acid monomer and larger self-aggregated clusters. The study shows that there still are noticeable theoretical uncertainties in the energetic ordering of larger lactic acid clusters, in their IR and VCD intensities, and even in the signs of some VCD bands. Because of all these theoretical uncertainties, it is essential to use the MI-IR

and MI-VCD approaches described above to firm up the final assignment of the solution measurements.

In Chapter 5, I described the investigation of the solvation effects of water on the IR and VCD spectra of methyl- β -D-glucose in water. The methyl- β -D-glucose is selected as a representative molecule for monosaccharides and also as a representative chiral molecule with extensive hydrogen-bonding sites. Therefore, the current investigation of solvation effects of water on methyl- β -D-glucose could provide insights into the solvation effects of water on monosaccharides and carbohydrates in general since monosaccharides are the basic building unit of carbohydrates. The conformational flexibility of methyl- β -D-glucose gives rise to many possible conformations. We identified the main conformations using extensive DFT conformational searches and based them partially on insights obtained from the previous studies on similar monosaccharides.^[4] The simulated IR and VCD spectral features of the methyl- β -D-glucose conformers in the PCM water could not reproduce the experimental IR and VCD features of methyl- β -D-glucose in water, especially in the 1200–1500 cm^{-1} region. The deficiency observed above indicates that the methyl- β -D-glucose monomer species are not the long-lived species in an aqueous solution of methyl- β -D-glucose. In the next phase of the analysis, I implemented the *clusters-in-a-liquid* solvation model to predict the experimental IR and VCD features of methyl- β -D-glucose in water. The previous ultrasound^[5], NIR^[6], NMR^[7], combined DFT and IR^[8] investigations and molecular dynamics simulations^[9] suggest that the monosaccharide-(water)_n clusters with n = 8–10 are important species in water. Extensive DFT modeling has been carried out to identify possible long-lived (methyl- β -D-glucose)-water₈ clusters in water. The simulated IR and VCD features of the methyl- β -D-glucose-(water)₈ complexes in the PCM of water show much better agreement with the experimental IR and VCD features of methyl- β -D-glucose in water for the 900–1500 cm^{-1} region than those obtained with the methyl- β -D-glucose monomer. The results support the conclusion that the methyl- β -D-glucose-(water)₈ clusters are the long-lived species rather than the methyl- β -D-glucose monomer in water.

6.2 Future Work

In my research, it became clear to me that much work still is needed to improve the accuracy of theoretical modeling in terms of the completeness of conformational search, relative conformational stability, vibrational frequencies and intensities, and VCD magnitudes and signs. For example, it would be of interest to compare systematically how different hybrid DFT functionals and basis sets perform on the conformational aspects of the solute-solute and solute-solvent clusters. Both structural and relative energetic changes can influence the appearance of the simulated spectral features significantly. The experimental MI-IR and MI-VCD data may be used as the experimental “gold” standard because they are free of solvent effects, allowing direct comparison to the theoretical modeling.

In the study presented in Chapter 5, significant improved agreement with the experimental data has been achieved using the simulated IR and VCD features of the methyl- β -D-glucose-(water)₈ complexes instead of the methyl- β -D-glucose monomer in the PCM of water. Despite the above success, it would be of great interest to investigate the simulated spectral features of other methyl- β -D-glucose-(water)_{*n*} complexes, especially those with only a few water molecules. One rationale for such studies is to see the consequence on the simulated spectral features while solvating each hydrogen-bonding site independently rather than simultaneously. Since the previous ultrasound^[5], NIR^[6], NMR^[7], combined DFT and IR^[8] investigations of methyl- β -D-glucose related molecules in water had provided evidence for the existence of monosaccharide-(water)_{*n*} complexes with *n* = 8–10, it would also be interesting to study the simulated IR and VCD features of methyl- β -D-glucose-(water)_{9,10} complexes in the PCM of water.

While the PCM method has been used conveniently and largely successfully in the *clusters-in-a-liquid* approach to reproduce the effects of the bulk water environment, it would be desirable to explore the utility of other models, for example the two-layer ONIOM model utilized by Cheeseman et al.^[10] in their glucose study. The representation of bulk water with explicit MM water molecules rather than a structureless continuum characterized by its dielectric constant may capture some new spectral features that were

missed with PCM. In the study reported by Cheeseman et al., no explicit hydrogen-bonding interactions between water and glucose were considered at the quantum mechanics level.^[10] Therefore, no Raman or ROA bands associated with water show up in the predicted spectra. Essentially, their study considered the effects of the explicit water molecules on the conformation of methyl- β -D-glucose and on ROA sign and intensity without the explicit hydrogen-bonds with water. One may consider this approach as a more sophisticated way to treat the bulk water environment than PCM.

6.3 References

1. A. S. Perera, J. Thomas, M. R. Poopari, Y. Xu, *Front. Chem.*, **2016**, *4*, 1–17.
2. a) M. Losada, P. Nguyen, Y. Xu, *J. Phys. Chem. A*, **2008**, *112*, 5621–5627; b) M. Losada, Y. Xu, *Phys. Chem. Chem. Phys.*, **2007**, *9*, 3127–3135; c) M. Losada, H. Tran, Y. Xu, *J. Chem. Phys.*, **2008**, *128*, 014508; d) G. Yang, Y. Xu, *J. Chem. Phys.*, **2009**, *130*, 164506; e) G. Yang, Y. Xu, *J. Chem. Phys.*, **2009**, *130*, 164506.
3. a) P. Çarçabal, R. A. Jockusch, I. Hunig, L. C. Snoek, R. T. Kroemer, B. G. Davis, D. P. Gamblin, I. Compagnon, J. Oomens, J. P. Simons, *J. Am. Chem. Soc.*, **2005**, *127*, 11414–11425; b) E. J. Cocinero, P. Çarçabal, *Carbohydrates, Top. Curr. Chem.*, **2015**, *364*, 299–334; c) C. Pérez, J. L. Neill, M. T. Muckle, D. P. Zaleski, I. Pena, J. C. Lopez, J. L. Alonso, B. H. Pate, *Angew. Chem. Int. Ed.*, **2015**, *54*, 979–982; d) J. Thomas, O. Sukhorukov, W. Jäger, Y. Xu, *Angew. Chem. Int. Ed.*, **2014**, *53*, 1156–1159; e) Z. Su, Q. Wen, Y. Xu, *J. Am. Chem. Soc.*, **2006**, *128*, 6755–6760; f) Z. Su, Y. Xu, *Angew. Chem. Int. Ed.*, **2007**, *46*, 6163–6166.
4. a) F. O. Talbot, J. P. Simons, *Phys. Chem. Chem. Phys.*, **2002**, *4*, 3562–3565; b) P. Carcabal, R. A. Jockusch, I. Hunig, L. C. Snoek, R. T. Kroemer, B. G. Davis, D. P. Gamblin, I. Compagnon, J. Oomens, J. P. Simons, *J. Am. Chem. Soc.*, **2005**, *127*, 7311–7319.
5. S. A. Galerna, H. Holland, *J. Phys. Chem.*, **1991**, *95*, 5321–5326.
6. J. L. Hollenberg, D. O. Hall, *J. Phys. Chem.*, **1983**, *87*, 695–696.
7. J. M. Harvey, M. C. R. Symons, R. J. Naftalin, *Nature*, **1976**, *261*, 435–436.
8. T. Suzukia, T. Sota, *J. Chem. Phys.*, **2003**, *119*, 19, 10133.
9. a) N. W. H. Cheetham, K. Lain, *Carbohydrate Research*, **1996**, *282*, 13–23; b) V. Krautler, M. Muller, P.

H. Hunenberger, *Carbohydrate Research*, **2007**, 342, 2097–2124.

10. J. R. Cheeseman, M. S. Shaik, P. L. A. Popelier, E. W. Blanch, *J. Am. Chem. Soc.* **2011**, 133, 4991.

Bibliography

1. L. A. Nafie, "Molecular Chirality and Optical Activity", In *Vibrational Optical Activity: Principles and Applications*, John Wiley and Sons, Ltd., Chichester, 2011.
2. R. S. Cahn, C. K. Ingold, V. Prelog, *Angew. Chem., Int. Ed.*, **1966**, 5, 385.
3. a) J. B. Biot, *Bull. Soc. Philomath.*, **1815**, 190; b) D.F. Arago, *Mem. de L'Inst.*, **1811**, 12, part1, 93.
4. H. D. Flack, G. Bernardinelli, *Acta Crystallogr. Sect. A*, **1999**, 55, 908–915.
5. T. J. Wenzel, J. D. Wilcox, *Chirality*, **2003**, 15, 256–270.
6. L. A. Nafie, *J. Mol. Struct.*, **1995**, 347, 83–100.
7. G. Pescitelli, S. Gabriel, Y. Wang, J. Fleischhauer, R. W. Woody, N. Berova, *J. Am. Chem. Soc.*, **2003**, 125, 7613–7628.
8. T. B. Freedman, X. Cao, R. K. Dukor, L. A. Nafie, *Chirality*, **2003**, 15, 9, 743–58.
9. T. A. Keiderling, *Curr. Opin. Chem. Biol.*, **2002**, 6, 5, 682–688
10. P. J. Stephens, F. J. Devlin, *Chirality*, **2000**, 12, 172–179.
11. G. Yang, Y. Xu, "Vibrational Circular Dichroism Spectroscopy of Chiral Molecules", In *Top. Curr. Chem., Volume: Electronic and Magnetic Properties of Chiral Molecules and Supramolecular Architectures*, edited by R. Naaman, D. N. Beratan, D. H. Waldeck, Springer-Verlag Berlin Heidelberg, 2011, vol 298, pp 189–236.
12. R. K. Dukor, L. A. Nafie, "Vibrational Optical activity of pharmaceuticals and biomolecules", In *Encyclopedia of Analytical Chemistry*, edited by R. A. Meyers, John Wiley & Sons, 2000, pp 662–676.
13. L. A. Nafie, T. B. Freedman, R. K. Dukor, "Vibrational Circular dichroism", In *Handbook of Vibrational Spectroscopy*, edited by J. M. Chalmers and P. R. Griffiths, John Wiley & Sons, 2002.
14. Z. Dezhahang, C. Merten, M. R. Poopari, Y. Xu, *Dalton Trans.*, **2012**, 41, 10817–10824.
15. G. Holzwarth, E. C. Hsu, H. S. Mosher, T. R. Freedman, A. Moscovitz, *J. Am. Chem. Soc.*, **1974**, 96, 1, 251–252.
16. L. A. Nafie, J. C. Cheng, P. J. Stephens, *J. Am. Chem. Soc.*, **1975**, 97, 13, 3842–3843.
17. B. E. Maryanoff, D. F. McComsey, R. K. Dukor, L. A. Nafie, T. B. Freedman, X. Cao, V. W. Day, *Bioorg. Med. Chem.*, **2003**, 11, 11, 2463–2470.
18. R. D. Shah, L. A. Nafie, *Curr. Opin. Drug. Discov. Devel.*, **2001**, 4, 6, 764–775.
19. Gaussian 03, Revision E.01, M. J. Frisch, G. W. Trucks, H. B. Schlegel, G. E. Scuseria, M. A. Robb, J. R. Cheeseman, J. A. Montgomery, Jr., T. Vreven, K. N. Kudin, J. C. Burant, J. M. Millam, S. S. Iyengar, J. Tomasi, V. Barone, B. Mennucci, M. Cossi, G. Scalmani, N. Rega, G. A. Petersson, H. Nakatsuji, M. Hada, M. Ehara, K. Toyota, R. Fukuda, J. Hasegawa, M. Ishida, T. Nakajima, Y. Honda, O. Kitao, H. Nakai, M. Klene, X. Li, J. E. Knox, H. P. Hratchian, J. B. Cross, V. Bakken, C. Adamo, J. Jaramillo, R. Gomperts, R. E. Stratmann, O. Yazyev, A. J. Austin, R. Cammi, C. Pomelli, J. W. Ochterski, P. Y. Ayala, K. Morokuma, G. A. Voth, P. Salvador, J. J. Dannenberg, V. G. Zakrzewski, S. Dapprich, A. D. Daniels, M. C. Strain, O. Farkas, D. K. Malick, A. D. Rabuck, K. Raghavachari, J. B. Foresman, J. V. Ortiz, Q. Cui, A. G. Baboul, S. Clifford, J. Cioslowski, B. B. Stefanov, G. Liu, A. Liashenko, P. Piskorz, I. Komaromi, R. L. Martin, D. J. Fox, T. Keith, M. A. AlLaham, C. Y. Peng, A. Nanayakkara, M. Challacombe, P. M. W. Gill, B. Johnson, W. Chen, M. W. Wong, C. Gonzalez, and J. A. Pople, Gaussian, Inc., Wallingford CT, 2004.
20. Gaussian 09, Revision C.01, M. J. Frisch, G. W. Trucks, H. B. Schlegel, G. E. Scuseria, M. A. Robb, J.

- R. Cheeseman, G. Scalmani, V. Barone, B. Mennucci, G. A. Petersson, H. Nakatsuji, M. Caricato, X. Li, H. P. Hratchian, A. F. Izmaylov, J. Bloino, G. Zheng, J. L. Sonnenberg, M. Hada, M. Ehara, K. Toyota, R. Fukuda, J. Hasegawa, M. Ishida, T. Nakajima, Y. Honda, O. Kitao, H. Nakai, T. Vreven, J. A. Montgomery, Jr., J. E. Peralta, F. Ogliaro, M. Bearpark, J. J. Heyd, E. Brothers, K. N. Kudin, V. N. Staroverov, R. Kobayashi, J. Normand, K. Raghavachari, A. Rendell, J. C. Burant, S. S. Iyengar, J. Tomasi, M. Cossi, N. Rega, J. M. Millam, M. Klene, J. E. Knox, J. B. Cross, V. Bakken, C. Adamo, J. Jaramillo, R. Gomperts, R. E. Stratmann, O. Yazyev, A. J. Austin, R. Cammi, C. Pomelli, J. W. Ochterski, R. L. Martin, K. Morokuma, V. G. Zakrzewski, G. A. Voth, P. Salvador, J. J. Dannenberg, S. Dapprich, A. D. Daniels, Ö. Farkas, J. B. Foresman, J. V. Ortiz, J. Cioslowski, and D. J. Fox, Gaussian, Inc., Wallingford CT, 2009.
21. Amsterdam Density Functional Program; Vrije Universiteit: Amsterdam, The Netherlands; E.J. Baerends, T. Ziegler, J. Autschbach, D. Bashford, A. Bérces, F.M. Bickelhaupt, C. Bo, P.M. Boerrigter, L. Cavallo, D.P. Chong, L. Deng, R.M. Dickson, D.E. Ellis, M. van Faassen, L. Fan, T.H. Fischer, C. Fonseca Guerra, M. Franchini, A. Ghysels, A. Giammona, S.J.A. van Gisbergen, A.W. Götz, J.A. Groeneveld, O.V. Gritsenko, M. Grüning, S. Gusarov, F.E. Harris, P. van den Hoek, C.R. Jacob, H. Jacobsen, L. Jensen, J. W. Kaminski, G. van Kessel, F. Kootstra, A. Kovalenko, M. V. Krykunov, E. van Lenthe, D.A. McCormack, A. Michalak, M. Mitoraj, S.M. Morton, J. Neugebauer, V.P. Nicu, L. Noodleman, V.P. Osinga, S. Patchkovskii, M. Pavanello, P.H.T. Philipsen, D. Post, C.C. Pye, W. Ravenek, J.I. Rodríguez, P. Ros, P. R. T. Schipper, G. Schreckenbach, J.S. Seldenthuis, M. Seth, J.G. Snijders, M. Solà, M. Swart, D. Swerhone, G. te Velde, P. Vernooijs, L. Versluis, L. Visscher, O. Visser, F. Wang, T.A. Wesolowski, E.M. van Wezenbeek, G. Wiesenekker, S. K. Wolff, T.K. Woo, A.L. Yakovlev.
 22. a) L. D. Barron, M. P. Bogaard, A. D. Buckingham, *J. Am. Chem. Soc.*, **1973**, *95*, 2, 603–605; b) L. A. Nafie, *Annu. Rev. Phys. Chem.*, **1997**, *48*, 357–386.
 23. L. D. Barron, A. D. Buckingham, *Chem. Phys. Lett.*, **2010**, *492*, 199–213.
 24. L. D. Barron, F. Zhu, L. Hecht, G. E. Tranter, N. W. Isaacs, *J. Mol. Struct.*, **2007**, *834–836*, 7–16.
 25. K. Rezaei, E. Jenab, F. Temelli, *Critical Rev. Biotech.*, **2007**, *27*, 183–195.
 26. G. Hummer, A. Tokmakoff, *J. Chem. Phys.*, **2014**, *141*, 22D101.
 27. Z. Dezhahang, C. Merten, M. R. Poopari, Y. Xu, *Dalton Trans.*, **2012**, *41*, 10817–10824.
 28. C. Merten, C. J. Berger, R. McDonald, Y. Xu, *Angew. Chem. Int. Ed.*, **2014**, *53*, 9940–9943.
 29. P. Zhu, G. Yang, M. R. Poopari, Z. Bie, Y. Xu, *Chem. Phys. Chem.*, **2012**, *13*, 1272–1281.
 30. M. R. Poopari, Z. Dezhahang, G. Yang, Y. Xu, *Chem. Phys. Chem.*, **2012**, *13*, 2310–2321.
 31. M. R. Poopari, Z. Dezhahang, Y. Xu, *Spectrochim. Acta A Mol. Biomol. Spectrosc.*, **2013**, *136*, 131–140.
 32. B. Mennucci, *WIREs Comput. Mol. Sci.*, **2012**, *2*, 386–404.
 33. R. Otto, J. Brox, S. Trippel, M. Stei, T. Best, R. Wester, *Nat. Chem.*, **2012**, *4*, 534–538.
 34. P. Carcabal, R. A. Jockusch, I. Hunig, L. C. Snoek, R. T. Kroemer, B. G. Davis, et al., *J. Am. Chem. Soc.*, **2005**, *127*, 11414–11425;
 35. L. Drouin, E. C. Stanca-Kaposta, P. Saundh, A. J. Fairbanks, S. Kemper, T. D. W. Claridge et al., *Chem. Eur. J.*, **2009**, *15*, 4057–4069.
 36. E. J. Cocinero, P. Carcabal, “Carbohydrates”, In *Gas-Phase IR Spectroscopy and Structure of Biological Molecules. Top. Curr. Chem.*, edited by A. Rijs, J. Oomens, Springer, Cham, 2015, vol 364, pp 299–334.
 37. C. Perez, J. L. Neill, M. T. Muckle, D. P. Zaleski, I. Pena, J. C. Lopez et al., *Angew. Chem. Int. Ed.*, **2015**, *54*, 979–982.
 38. C. Perez, J. L. Neill, M. T. Muckle, D. P. Zaleski, I. Pena, J. C. Lopez et al., *Angew. Chem.*, **2015**, *127*, 993–996.
 39. K. Jalkanen, S. Suhai, *Chem. Phys.*, **1996**, *208*, 81–116.

40. J. Sadlej, J. C. Dobrowolski, J. E. Rode, *Chem. Soc. Rev.*, **2010**, *39*, 1478–1488.
41. M. Losada, P. Nguyen, Y. Xu, *J. Phys. Chem. A*, **2008**, *112*, 5621–5627.
42. M. Losada, Y. Xu, *Phys. Chem. Chem. Phys.*, **2007**, *9*, 3127–3135.
43. M. Losada, H. Tran, Y. Xu, *J. Chem. Phys.*, **2008**, *128*, 014508.
44. G. Yang, Y. Xu, *J. Chem. Phys.*, **2009**, *130*, 164506.
45. A. S. Perera, J. Thomas, M. R. Poopari, Y. Xu, *Front. Chem.*, **2016**, *4*, 1–17.
46. A. S. Perera, J. Cheramy, C. Merten, J. Thomas, Y. Xu, *Chem. Phys. Chem.*, **2018**, *19*, 17, 2234–2242.
47. G. Tarczay, G. Magyarfalvi, E. Vass, *Angew. Chem. Int. Ed.*, **2006**, *45*, 1775–1777.
48. C. H. Pollok, C. Merten, *Phys. Chem. Chem. Phys.*, **2016**, *18*, 13496–13502.
49. J. R. Cheeseman, M. S. Shaik, P. L. A. Popelier, E. W. Blanch, *J. Am. Chem. Soc.*, **2011**, *133*, 4991–4997.
50. S. T. Mutter, F. Zielinski, J. R. Cheeseman, C. Johannessen, P. L. A. Popelier, E. W. Blanch, *Phys. Chem. Chem. Phys.*, **2015**, *17*, 6016.
51. A. Melcrova, J. Kessler, P. Bour, J. Kaminsky, *Phys. Chem. Chem. Phys.*, **2016**, *18*, 2130.
52. F. Zielinski, S. T. Mutter, C. Johannessen, E. W. Blanch, P. L. A. Popelier, *Phys. Chem. Chem. Phys.*, **2015**, *17*, 21799.
53. G. Holzwarth, E. C. Hsu, H. S. Mosher et al., *J. Am. Chem. Soc.*, **1974**, *96*, 251–252.
54. L. A. Nafie, J. C. Cheng, P. J. Stephens, *J. Am. Chem. Soc.*, **1975**, *97*, 3842–3843.
55. L. A. Nafie, T. A. Keiderling, P. J. Stephens, *J. Am. Chem. Soc.*, **1976**, *98*, 2715–2723.
56. L. A. Nafie, M. Diem, *Appl. Spectrosc.*, **1979**, *33*, 130–135.
57. L. A. Nafie, M. Diem, D. W. Vidrine, *J. Am. Chem. Soc.*, **1979**, *101*, 496–498.
58. E. D. Lipp, C. G. Zimba, L. A. Nafie, *Chem. Phys. Lett.*, **1982**, *90*, 1–5.
59. K.W. Busch, M. A. Busch, (Eds), *Chiral Analysis: Instrumental aspects of chiroptical detection*, Elsevier, Amsterdam, 2006.
60. E. Whittle, D. A. Dows, G. C. Pimentel, *J. Chem. Phys.*, **1954**, *22*, 1943.
61. E. D. Becker, G. C. Pimentel, *J. Chem. Phys.*, **1956**, *25*, 224.
62. I. Norman, G. Porter, *Nature (London)*, **1954**, *174*, 58.
63. M. Van Thiel, E. D. Becker, G. C. Pimentel, *J. Chem. Phys.*, **1957**, *27*, 95.
64. M. Van Thiel, E. D. Becker, G. C. Pimentel, *J. Chem. Phys.*, **1957**, *27*, 486.
65. D. W. Schlosser, F. Devlin, K. Jalkanen, P. J. Stephens, *Chem. Phys. Lett.*, **1982**, *88*, 286.
66. I. R. Dunkin, *Matrix Isolation Techniques*, Oxford University Press, New York, 1998.
67. J. W. L. Kohler, *Sci. Amer.*, **1965**, *212*, 119.
68. M. Moskovits, G. A. Ozin, (Editors) *Cryochemistry*, Wiley-Interscience, New York, 1976.
69. H. E. Hallam, (Editor) *Vibrational Spectroscopy of Trapped Species*, J. Wiley, London, 1973.
70. D. W. Schlosser, F. Devlin, K. Jalkanen, P. J. Stephens, *Chem. Phys. Lett.*, **1982**, *88*, 286.
71. D. O. Henderson, P. L. Polavarapu, *J. Am. Chem. Soc.*, **1986**, *108*, 7110.
72. W.E. Gifford, R.C. Longworth, *Adv. Cryog. Eng.*, **1966**, *11*, 171.
73. M. A. Lowe, G. A. Segal, P. J. Stephens, *J. Am. Chem. Soc.*, **1986**, *108*, 248–256.

74. P. J. Stephens, *J. Phys. Chem.*, **1985**, *89*, 748–752.
75. N. V. Cohan, H. F. Hameka, *J. Am. Chem. Soc.*, **1966**, *88*, 2136.
76. T. R. Faulkner, C. Marcott, A. Moscovitz, J. Overend, *J. Am. Chem. Soc.*, **1977**, *99*, 8160.
77. J. A. Schellman, *J. Chem. Phys.*, **1973**, *58*, 2882.
78. G. Holzwarth, I. Chabay, *J. Chem. Phys.*, **1972**, *57*, 1632.
79. C. J. Barnett, A. F. Drake, R. Kuroda, S. F. Mason, *Mol. Phys.*, **1980**, *41*, 455.
80. L. A. Nafie, T. H. Walnut, *Chem. Phys. Lett.*, **1977**, *49*, 441.
81. T. H. Walnut, L. A. Nafie, *Chem. Phys.*, **1977**, *67*, 1501.
82. K. L. C. Hunt, R. A. Harris, *J. Chem. Phys.*, **1991**, *94*, 6995.
83. P. Lazzeretti, M. Malagoli, R. Zanasi, *Chem. Phys. Lett.*, **1991**, *179*, 297.
84. L. A. Nafie, T. B. Freedman, *J. Phys. Chem.*, **1983**, *78*, 7108.
85. R. Dutler, A. Rauk, *J. Am. Chem. Soc.*, **1989**, *111*, 6957.
86. D. Yang, A. Rauk, *J. Chem. Phys.*, **1992**, *97*, 6517.
87. P. J. Stephens, *J. Phys. Chem.*, **1987**, *91*, 1712–1715.
88. A. D. Buckingham, P. W. Fowler, P. A. Galwas, *Chem. Phys.*, **1987**, *112*, 1–14.
89. W. B. Person, J. H. Newton, *J. Chem. Phys.*, **1974**, *61*, 1040.
90. B. G. Johnson, M. J. Frisch, *Chem. Phys. Lett.*, **1993**, *216*, 133–140.
91. B. G. Johnson, M. J. Frisch, *J. Chem. Phys.*, **1994**, *100*, 7429–7442.
92. J. R. Cheeseman, M. J. Frisch, F. J. Devlin, P. J. Stephens, *Chem. Phys. Lett.*, **1996**, *252*, 211–220.
93. P. J. Stephens, F. J. Devlin, J. R. Cheeseman, *VCD Spectroscopy for Organic Chemists*, CRC Press, Taylor & Francis Group, Boca Raton, FL, USA, 2012.
94. W. J. Hehre, L. Radom, P. V. R. Schleyer, J. A. Pople, *Ab Initio Molecular Orbital Theory*, John Wiley & Sons, New York, 1986.
95. P. J. Stephens, K. J. Jalkanen, F. J. Devlin, C. F. Chabalowski, *J. Phys. Chem.*, **1993**, *97*, 6107–6110.
96. F. J. Devlin, P. J. Stephens, *J. Am. Chem. Soc.*, **1994**, *116*, 5003–5004.
97. D. Y. Yang, A. Rauk, *J. Chem. Phys.*, **1994**, *100*, 7995–8002.
98. P. Hohenberg, W. Kohn, *Phys. Rev.*, **1964**, *136*, 3B, B864.
99. W. Kohn, L. J. Sham, *Phys. Rev.*, **1965**, *140*, A1133.
100. J. K. Labanowski, J. W. Andzelm, *Density functional Methods in Chemistry*, Springer-Verlag: New York, 1991.
101. P. J. Stephens, F. J. Devlin, *Chirality*, **2000**, *12*, 172–179.
102. A. D. Becke, *J. Chem. Phys.*, **1993**, *98*, 1372–1377.
103. A. D. Becke, *J. Chem. Phys.*, **1993**, *98*, 5648–5652.
104. A. D. Becke, *Phys. Rev. A*, **1988**, *38*, 6, 3098.
105. C. Lee, W. Yang, and R. G. Parr, *Phys. Rev. B*, **1988**, *37*, 2, 785.
106. J. P. Perdew, Y. Wang, *Phys. Rev. B*, **1992**, *45*, 23, 13244.
107. P. J. Stephens, F. J. Devlin, C. F. Chabalowski, M. J. Frisch, *J. Phys. Chem.*, **1994**, *98*, 11623–11627.
108. T. Kuppens, W. Langenaeker, J. P. Tollenaere, P. Bultinck, *J. Phys. Chem. A*, **2003**, *107*, 542.

109. T. Kuppens, K. van der Vandyck, J. Eycken, W. Herrebout, B. J. van der Veken, P. Bultinck, *J. Org. Chem.*, **2005**, *70*, 9103.
110. T. Kuppens, W. Herrebout, B. van der Veken, P. Bultinck, *J. Phys. Chem. A*, **2006**, *110*, 10191.
111. Ducasse, F. Castet, A. Fritsch, I. Huc, T. Buffeteau, *J. Phys. Chem. A*, **2007**, *111*, 5092.
112. T. Brotin, D. Cavagnat, J. P. Dutasta, T. Buffeteau, *J. Am. Chem. Soc.*, **2006**, *128*, 5533.
113. W. J. Hehre, R. Ditchfield, J. A. Pople, *J. Chem. Phys.*, **1972**, *56*, 5, 2257.
114. T. H. Dunning Jr, *J. Chem. Phys.*, **1989**, *90*, 1007.
115. F. Weigend, F. Furche, R. Ahlrichs, *J. Chem. Phys.*, **2003**, *19*, 12753.
116. a). Gaussian 09, Revision B.01, M. J. Frisch, G. W. Trucks, H. B. Schlegel, G. E. Scuseria, M. A. Robb, J. R. Cheeseman, G. Scalmani, V. Barone, B. Mennucci, G. A. Petersson, H. Nakatsuji, M. Caricato, X. Li, H. P. Hratchian, A. F. Izmaylov, J. Bloino, G. Zheng, J. L. Sonnenberg, M. Hada, M. Ehara, K. Toyota, R. Fukuda, J. Hasegawa, M. Ishida, T. Nakajima, Y. Honda, O. Kitao, H. Nakai, T. Vreven, J. A. Montgomery, Jr., J. E. Peralta, F. Ogliaro, M. Bearpark, J. J. Heyd, E. Brothers, K. N. Kudin, V. N. Staroverov, R. Kobayashi, J. Normand, K. Raghavachari, A. Rendell, J. C. Burant, S. S. Iyengar, J. Tomasi, M. Cossi, N. Rega, J. M. Millam, M. Klene, J. E. Knox, J. B. Cross, V. Bakken, C. Adamo, J. Jaramillo, R. Gomperts, R. E. Stratmann, O. Yazyev, A. J. Austin, R. Cammi, C. Pomelli, J. W. Ochterski, R. L. Martin, K. Morokuma, V. G. Zakrzewski, G. A. Voth, P. Salvador, J. J. Dannenberg, S. Dapprich, A. D. Daniels, Ö. Farkas, J. B. Foresman, J. V. Ortiz, J. Cioslowski, D. J. Fox, Gaussian, Inc., Wallingford CT, 2009;
117. A. D. Becke, E. R. Johnson, *J. Chem. Phys.*, **2005**, *123*, 154101.
118. S. Grimme, S. Ehrlich, L. Goerigk, *J. Comput. Chem.*, **2011**, *32*, 1456–1465.
119. R. Krishnan, J. S. Binkley, R. Seeger, J. A. Pople, *J. Chem. Phys.*, **1980**, *72*, 650–654.
120. B. Mennucci, J. Tomasi, R. Cammi, J. R. Cheeseman, M. J. Frisch, F. J. Devlin, S. Gabriel, P. J. Stephens, *J. Phys. Chem. A*, **2002**, *106*, 6102–6113.
121. P. L. Polavarapu, *Chirality*, **2012**, *24*, 909–920.
122. V. Parchaňský, J. Kapitán, P. Bouř, *RSC Adv.*, **2014**, *4*, 57125–57136.
123. W. Hug, *Appl. Spectrosc.*, **2003**, *57*, 1–13.
124. X. L. Cao, R. K. Dukor, L. A. Nafie, *Theo. Chem. Acc.*, **2008**, *119*, 69–79.
125. J. R. Cheeseman, M. J. Frisch, *J. Chem. Theo. Comput.*, **2011**, *7*, 3323–3334.
126. M. Srebro-Hooper and J. Autschbach, *Annual Rev. Phys. Chem.*, **2017**, *68*, 399–420.
127. M. Passarello, S. Abbate, G. Longhi, S. Lepri, R. Ruzziconi, V. P. Nicu, *J. Phys. Chem. A*, **2014**, *118*, 4339–4350.
128. Y. Zhang, M. R. Poopari, X. Cai, A. Savin, Z. Dezhahang, J. Cheramy, Y. Xu, *J. Nat. Prod.*, **2016**, *79*, 1012–1023.
129. K. Bünnemann and C. Merten, *Phys. Chem. Chem. Phys.*, **2017**, *19*, 18948–18956.
130. J. E. Rode, J. C. Dobrowolski, K. Lyczko, A. Wasiewicz, D. Kaczorek, R. Kawęcki, G. Zając, M. Baranska, *J. Phys. Chem. A*, **2017**, *121*, 6713–6726.
131. M. R. Poopari, Z. Dezhahang and Y. Xu, *Phys. Chem. Chem. Phys.*, **2013**, *15*, 1655–1665.
132. M. Yves, *The hydrogen bond and the water molecule*, Elsevier, New York, 2007.
133. G. Hummer, A. Tokmakoff, *J. Chem. Phys.*, **2014**, *141*, 22D101.
134. K. H. Hopmann, K. Ruud, M. Pecul, A. Kudelski, M. Dračinský, P. Bouř, *J. Phys. Chem. B*, **2011**, *115*, 4128–4137.

135. M. Kamiński, A. Kudelski, M. Pecul, *J. Phys. Chem. B*, **2012**, *116*, 4976–4990.
136. P. L. Geissler, *Annu. Rev. Phys. Chem.*, **2013**, *64*, 317–337.
137. M. Thämer, L. De Marco, K. Ramasesha, A. Mandal, A. Tokmakoff, *Science*, **2015**, *350*, 78–82.
138. F. Dahms, R. Costard, E. Pines, B. P. Fingerhut, E. T. J. Nibbering, T. Elsaesser, *Angew. Chem. Int. Ed.*, **2016**, *55*, 10600–10605; *Angew. Chem.*, **2016**, *128*, 10758–10763.
139. S. Palchowdhury, B. L. Bhargava, *J. Phys. Chem. B*, **2018**, *122*, 2113–2120.
140. J. Thomas, J. Yiu, J. Rebling, W. Jäger, Y. Xu, *J. Phys. Chem. A*, **2013**, *117*, 13249–13254.
141. J. T. A. Gall, J. Thomas, F. Xie, Z. Wang, W. Jäger, Y. Xu, *Phys. Chem. Chem. Phys.*, **2017**, *19*, 29508–29515.
142. C. Guo, R. D. Shah, R. K. Dukor, T. B. Freedman, X. Cao, L. A. Nafie, *Vib. Spectrosc.*, **2006**, *42*, 254–272.
143. X. Cao, R. D. Shah, R. K. Dukor, T. B. Freedman, C. Guo, L. A. Nafie, *Appl. Spectrosc.*, **2004**, *58*, 1057–1064.
144. W. Huang, J. Thomas, W. Jäger and Y. Xu, *Phys. Chem. Chem. Phys.*, **2017**, *19*, 12221–12228.
145. J. Thomas, N. A. Seifert, W. Jäger and Y. Xu, *Angew. Chem. Int. Ed.*, **2017**, *56*, 6289–6293; *Angew. Chem.*, **2017**, *129*, 6386–6390.
146. J. Neugebauer, M. Reiher, C. Kind, B. A. Hess, *J. Comput. Chem.*, **2002**, *23*, 895–910.
147. J. Cheeseman, private communication.
148. C. Merten, *Phys. Chem. Chem. Phys.*, **2017**, *19*, 18803–18812.
149. A. Melcrova, J. Kessler, P. Bour and J. Kaminsky, *Phys. Chem. Chem. Phys.*, **2016**, *18*, 2130–2142.
150. M. Schneider, C. Masellis, T. Rizzo, and C. Baldauf, *J. Phys. Chem. A*, **2017**, *121*, 6838–6844.
151. C. Merten and Y. Xu, *Angew. Chem. Int. Ed.*, **2013**, *52*, 2073–2076.
152. A. Scherrer, R. Vuilleumier and D. Sebastiani, *J. Chem. Phys.*, **2016**, *145*, 084101.
153. S. Lubner, M. Reiher, *J. Phys. Chem. A*, **2009**, *113*, 8268–8277.
154. M. R. Poopari, P. Zhu, Z. Dezhahang and Y. Xu, *J. Chem. Phys.*, **2012**, *137*, 194308.
155. Z. Su, Q. Wen, Y. Xu, *J. Am. Chem. Soc.*, **2006**, *128*, 6755–6760.
156. Z. Su and Y. Xu, *Angew. Chem. Int. Ed.*, **2007**, *46*, 6163–6166; *Angew. Chem.*, **2007**, *119*, 2326–2329.
157. J. Thomas, O. Sukhorukov, W. Jäger and Y. Xu, *Angew. Chem. Int. Ed.*, **2014**, *53*, 1156–1159; *Angew. Chem.*, **2014**, *126*, 1175–1178.
158. J. M. Batista Jr., E. W. Blanch, V. da Silva Bolzan, *Nat. Prod. Rep.*, **2015**, *32*, 1280–1302.
159. A. C. Chamayou, G. Makhoulfi, L. A. Nafie, C. Janiak, S. Ludeke, *Inorg. Chem.*, **2015**, *54*, 2193–2203.
160. T. Wu, X. X. You, P. Bour, *Coord. Chem. Rev.*, **2015**, *284*, 1–18.
161. A. S. Perera, J. Cheramy, C. Merten, J. Thomas, Y. Xu, *Chem. Phys. Chem.*, **2018**, *19*, 2234–2242.
162. C. Merten, Y. Xu, *Chem. Phys. Chem.*, **2013**, *14*, 213–219.
163. C. Merten, Y. Xu, *Angew. Chem., Int. Ed.*, **2013**, *52*, 2073–2076.
164. W. Sander, M. Gantenberg, *Spectrochim. Acta, Part A*, **2005**, *62*, 902–909.
165. M. Kleerebezem, J. Hugenholtz, *Curr. Opin. Biotechnol.*, **2003**, *14*, 232–237.
166. A. Narladkar, E. Balnois, Y. Grohens, *Macromol. Symp.*, **2006**, *241*, 34–44.
167. B. P. van Eijck, *J. Mol. Spectrosc.*, **1983**, *101*, 133–138.

168. L. Pszczolkowski, E. Białkowska-Jaworska, Z. Kisiel, *J. Mol. Spectrosc.*, **2005**, *234*, 106–112.
169. Z. Kisiel, E. Białkowska-Jaworska, D. P. Zaleski, J. L. Neill, A. L. Steber, B. H. Pate, WH10, *66th Int. Sym. on Mol. Spectrosc.*, Columbus, Ohio, 2011.
170. A. Borda, A. Gomez-Zavaglia, L. Iapinski, R. Fausto, *Phys. Chem. Chem. Phys.*, **2004**, *6*, 2101–2108.
171. A. Shouten, J. Kanters, J. van Krieken, *J. Mol. Struct.*, **1994**, *323*, 165–168.
172. G. Cassanas, M. Morssli, E. Fabregue, L. Bardet, *J. Raman Spectrosc.*, **1991**, *22*, 409–413.
173. G. Cassanas, G. Kister, E. Fabregue, M. Morssli, L. Bardet, *Spectrochim. Acta, Part A*, **1993**, *49*, 271–279.
174. Z. Fekete, T. Kortvelyesi, J. Andor, I. Palinko, *J. Mol. Struct.: THEOCHEM*, **2003**, *666*, 159–162.
175. Gaussian 16, Revision B.01, M. J. Frisch, G. W. Trucks, H. B. Schlegel, G. E. Scuseria, M. A. Robb, J. R. Cheeseman, G. Scalmani, V. Barone, G. A. Petersson, H. Nakatsuji, X. Li, M. Caricato, A. V. Marenich, J. Bloino, B. G. Janesko, R. Gomperts, B. Mennucci, H. P. Hratchian, J. V. Ortiz, A. F. Izmaylov, J. L. Sonnenberg, D. Williams-Young, F. Ding, F. Lipparini, F. Egidi, J. Goings, B. Peng, A. Petrone, T. Henderson, D. Ranasinghe, V. G. Zakrzewski, J. Gao, N. Rega, G. Zheng, W. Liang, M. Hada, M. Ehara, K. Toyota, R. Fukuda, J. Hasegawa, M. Ishida, T. Nakajima, Y. Honda, O. Kitao, H. Nakai, T. Vreven, K. Throssell, J. A. Montgomery, Jr., J. E. Peralta, F. Ogliaro, M. J. Bearpark, J. J. Heyd, E. N. Brothers, K. N. Kudin, V. N. Staroverov, T. A. Keith, R. Kobayashi, J. Normand, K. Raghavachari, A. P. Rendell, J. C. Burant, S. S. Iyengar, J. Tomasi, M. Cossi, J. M. Millam, M. Klene, C. Adamo, R. Cammi, J. W. Ochterski, R. L. Martin, K. Morokuma, O. Farkas, J. B. Foresman, and D. J. Fox, Gaussian, Inc., Wallingford CT, 2016.
176. J. Cheeseman, M. Frisch, *J. Chem. Theory Comput.*, **2007**, *7*, 3323–3334.
177. M. K. Kesharwani, A. Karton, J. M. L. Martin, *J. Chem. Theory Comput.*, **2016**, *12*, 444–454.
178. J. Thomas, N. A. Seifert, W. Jager, Y. Xu, *Angew. Chem., Int. Ed.*, **2017**, *56*, 6289–6293 (*Angew. Chem.*, **2017**, *129*, 6386–6390)
179. D. Rappoport, F. Furche, *J. Chem. Phys.*, **2010**, *133*, 134105.
180. J. Sadlej, J. Dobrowolski, J. Rode, M. Jamroz, *Phys. Chem. Chem. Phys.*, **2006**, *8*, 101–113.
181. M. Pecul, A. Rizzo, J. Leszczynski, *J. Phys. Chem. A*, **2002**, *106*, 11008–11016.
182. A. Barnes, *J. Mol. Struct.*, **1984**, *113*, 161–174.
183. G. Holzwarth, I. Chabay, *J. Chem. Phys.*, **1972**, *57*, 1632–1635.
184. V. Setnicka, M. Urbanova, P. Bour, V. Kral, K. Volka, *J. Phys. Chem. A*, **2001**, *105*, 8931–8938.
185. T. Taniguchi, K. Monde, *J. Am. Chem. Soc.*, **2012**, *134*, 3695–3698.
186. S. Abbate, G. Mazzeo, S. Meneghini, G. Longhi, S. E. Boiadjev, D. A. Lightner, *J. Phys. Chem. A*, **2015**, *119*, 4261–4267.
187. V. P. Nicu, E. J. Baerends, *Phys. Chem. Chem. Phys.*, **2009**, *11*, 6107–6118.
188. G. Longhi, M. Tommasini, S. Abbate, P. L. Polavarapu, *Chem. Phys. Lett.*, **2015**, *639*, 320–325.
189. R. A. Dwek, *Chem. Rev.*, **1996**, *96*, 683–720.
190. H. Rudiger, H. -C. Siebert, D. Solis, J. Jimenez-Barbero, A. Romero, C. W. von der Lieth, T. Diaz-Maurino, H. J. Gabius, *Curr. Med. Chem.*, **2000**, *7*, 389–416.
191. A. P. Davis, R. S. Wareham, *Angew. Chem., Int. Ed.*, **1999**, *38*, 2978–2996.
192. J. B. Lowe, J. D. Marth, *Annu. Rev. Biochem.* **2003**, *72*, 643–691.
193. J. Lehmann, *Carbohydrates Structure and Biology*; Georg Thieme: Stuttgart, Germany, **1998**.
194. Hricovini, *M. Curr. Med. Chem.*, **2004**, *11*, 2565–2583.

195. R. V. Stick, S. J. Williams, *Carbohydrates: The Essential Molecules of Life*, Elsevier Science, **2009**.
196. R. U. Lemieux, *Explorations with Sugars: How Sweet it Was*; American Chemical Society, Washington, DC, **1990**.
197. K. G. Rice, P. Wu, L. Brand, Y. C. Lee, *Curr. Opin. Struct. Biol.*, **1993**, *3*, 669–674.
198. M. R. Wormald, A. J. Petrescu, Y. -L. Pao, A. Glithero, T. Elliott, *Chem. Rev.*, **2002**, *102*, 371–386.
199. R. A. Dwek, C. J. Edge, D. J. Harvey, M. R. Wormald, R. B. Parekh, *Annu. Rev. Biochem.* **1993**, *62*, 65–100.
200. C. Clarke, R. J. Woods, J. Gluska, A. Cooper, M. A. Nutley, G.-J. Boons, *J. Am. Chem. Soc.*, **2001**, *123*, 12238–12247.
201. E. Klein, Y. Ferrand, N. P. Barwell, A. P. Davis, *Angew. Chem.*, **2008**, *120*, 2733–2736.
202. F. A. Quijoch, D. K. Wilson, N. K. Vyas, *Nature*, **1989**, *340*, 404.
203. P. Colins, R. Ferrier, *Monosaccharides; Their Chemistry and their Roles in Natural Products*, Wiley, New York, **1995**.
204. J. M. Batista, A. N. L. Batista, J. S. Mota, Q. B. Cass, M. J. Kato, V. S. Bolzani, T. B. Freedman, S. N. Lopez, M. Furlan, L. A. Nafie, *J. Org. Chem.*, **2011**, *76*, 2603–2612.
205. H. Sato, H. Uno, H. Nakano, *Dalton Trans.*, **2011**, *40*, 1332–1337.
206. D. Dunmire, T. B. Freedman, L. A. Nafie, C. Aeschlimann, J. G. Gerber, J. Gal, *Chirality*, **2005**, *17*, 101–108.
207. P. L. Polavarapu, *Chirality*, **2012**, *24*, 909–1020.
208. P. K. Bose, P. L. Polavarapu, *Carbohydrate Research*, **1999**, *390*, 172–183.
209. K. Monde, T. Taniguchi, N. Miura, S. I. Nishimura, *J. Am. Chem. Soc.*, **2004**, *126*, 9496–9497.
210. Z. Q. Wen, L. D. Barron, L. Hecht, *J. Am. Chem. Soc.*, **1993**, *115*, 285–292.
211. A. F. Bell, L. D. Barron, L. Hecht, *Carbohydrate Research*, **1994**, *257*, 11–24.
212. J. M. Harvey, M. C. R. Symons, R. J. Naftalin, *Nature*, **1976**, *261*, 435–436.
213. S. A. Galerna, H. Holland, *J. Phys. Chem.*, **1991**, *95*, 5321–5326.
214. J. L. Hollenberg, D. O. Hall, *J. Phys. Chem.*, **1983**, *87*, 695–696.
215. T. Suzukia, T. Sota, *J. Chem. Phys.*, **2003**, *119*, 19, 10133.
216. Gaussian 09 (Revision D.01), M. J. Frisch, G. W. Trucks, H. B. Schlegel, G. E. Scuseria, M. A. Robb, J. R. Cheeseman, G. Scalmani, V. Barone, B. Mennucci, G. A. Petersson, H. Nakatsuji, M. Caricato, X. Li, H. P. Hratchian, A. F. Izmaylov, J. Bloino, G. Zheng, J. L. Sonnenberg, M. Hada, M. Ehara, K. Toyota, R. Fukuda, J. Hasegawa, M. Ishida, T. Nakajima, Y. Honda, O. Kitao, H. Nakai, T. Vreven, J. A. Montgomery, Jr., J. E. Peralta, F. Ogliaro, M. Bearpark, J. J. Heyd, E. Brothers, K. N. Kudin, V. N. Staroverov, T. Keith, R. Kobayashi, J. Normand, K. Raghavachari, A. Rendell, J. C. Burant, S. S. Iyengar, J. Tomasi, M. Cossi, N. Rega, J. M. Millam, M. Klene, J. E. Knox, J. B. Cross, V. Bakken, C. Adamo, J. Jaramillo, R. Gomperts, R. E. Stratmann, O. Yazyev, A. J. Austin, R. Cammi, C. Pomelli, J. W. Ochterski, R. L. Martin, K. Morokuma, V. G. Zakrzewski, G. A. Voth, P. Salvador, J. J. Dannenberg, S. Dapprich, A. D. Daniels, O. Farkas, J. B. Foresman, J. V. Ortiz, J. Cioslowski, D. J. Fox, Gaussian, Inc., Wallingford CT, **2013**.
217. C. J. Cramer, D. G. Truhlar, *J. Am. Chem. Soc.*, **1993**, *115*, 13, 5745.
218. J. C. Corchado, M. L. Sanchez, M. A. Aguilar, *J. Am. Chem. Soc.*, **2004**, *126*, 7311–7319.
219. P.L. Polavarapu, C.S. Ewig, *Journal of Computational Chemistry*, **1992**, *13*, 10, 1255–1261.
220. F. O. Talbot, J. P. Simons, *Phys. Chem. Chem. Phys.*, **2002**, *4*, 3562–3565.

221. S. E. Barrows, F. J. Dulles, C. J. Cramer, A. D. French, D. G. Truhlar, *Carbohydr. Res.*, **1995**, 276, 219–251.
222. J. P. Simons, R. A. Jockusch, P. CarCabal, I. Hunig, R. T. Kroemer, N. A. Macleod, L. C. Snoek, *International Reviews in Physical Chemistry*, **2005**, 24, 3–4, 489.
223. R. H. Marchessault, S. Perez, *Biopolymers* **1979**, 18, 2369–2374.
224. J. Gonzalez-Outeirino, K. N. Kirschner, S. Thobhani, R. J. Woods, *Can. J. Chem.*, **2006**, 84, 569–579.
225. K. Bock, J. Duus, *J. Carbohydr. Chem.*, **1994**, 14, 513–543.
226. N. Uddin, M. K. Ghosh, T. H. Choi, C. H. Choi, *Theor Chem Acc*, **2015**, 134:122
227. Y. Nishida, H. Ohruai, H. Mequero, *Tetrahedron Letters*, **1984**, 25, 1575–1578.
228. Y. Nishida, H. Hori, H. Ohruai, H. Meguro, *J. Carbohydrate Chemistry*, **1988**, 7(1), 239–250.
229. R. J. Abraham, E. J. Chambers, *magn. Reson. Chem.*, **1992**, 30, S60–S65.
230. C. M. Tummalapalli, D. M. Back, P. L. Polavarapu, *J. Chem. Soc. Faraday Trans. 1*, **1988**, 84, 2585.
231. P. K. Bose, P. L. Polavarapu, *J. Am. Chem. Soc.*, **1999**, 121, 6094–6095.
232. T. Vreven, K. S. Byun, I. Komaromi, S. Dapprich, J. A. Montgomery, Jr., K. Morokuma, M. J. Frisch, *J. Chem. Theory Comput.*, **2006**, 2, 815–826.
233. J. Kessler, M. Dracinsky, P. Bour, *Journal of Computational Chemistry*, **2013**, 34, 366–371.
234. J. Hudecova, K. Hopmann, P. Bour, *J. Phys. Chem. B*, **2012**, 116, 336–342.
235. N. W. H. Cheetham, K. Lain, *Carbohydrate Research*, **1996**, 282, 13–23.
236. V. Krautler, M. Muller, P. H. Hunenberger, *Carbohydrate Research*, **2007**, 342, 2097–2124.
237. S. L. Lee, P. G. Debenedettia, *J. Chem. Phys.*, **2005**, 122, 204511.
238. R. A. Klein, *J. Am. Chem. Soc.*, **2002**, 124, 13931–13937.
239. T. Suzuki, *Phys. Chem. Chem. Phys.*, **2008**, 10, 96–105.
240. J. P. Simons, B. G. Davis, E. J. Cocinero, D. P. Gamblin, E. C. Stanca-Kaposta, *Tetrahedron: Asymmetry*, **2009**, 20, 718–722.
241. E. J. Cocinero, P. Çarçabal, *Carbohydrates, Top. Curr. Chem.*, **2015**, 364, 299–334.
242. C. Pérez, J. L. Neill, M. T. Muckle, D. P. Zaleski, I. Pena, J. C. Lopez, J. L. Alonso, B. H. Pate, *Angew. Chem. Int. Ed.*, **2015**, 54, 979–982.
243. J. Thomas, O. Sukhorukov, W. Jäger, Y. Xu, *Angew. Chem. Int. Ed.*, **2014**, 53, 1156–1159.
244. Z. Su, Q. Wen, Y. Xu, *J. Am. Chem. Soc.*, **2006**, 128, 6755–6760.
245. Z. Su, Y. Xu, *Angew. Chem. Int. Ed.*, **2007**, 46, 6163–6166.

Appendix A

Supporting Information for Chapter 3

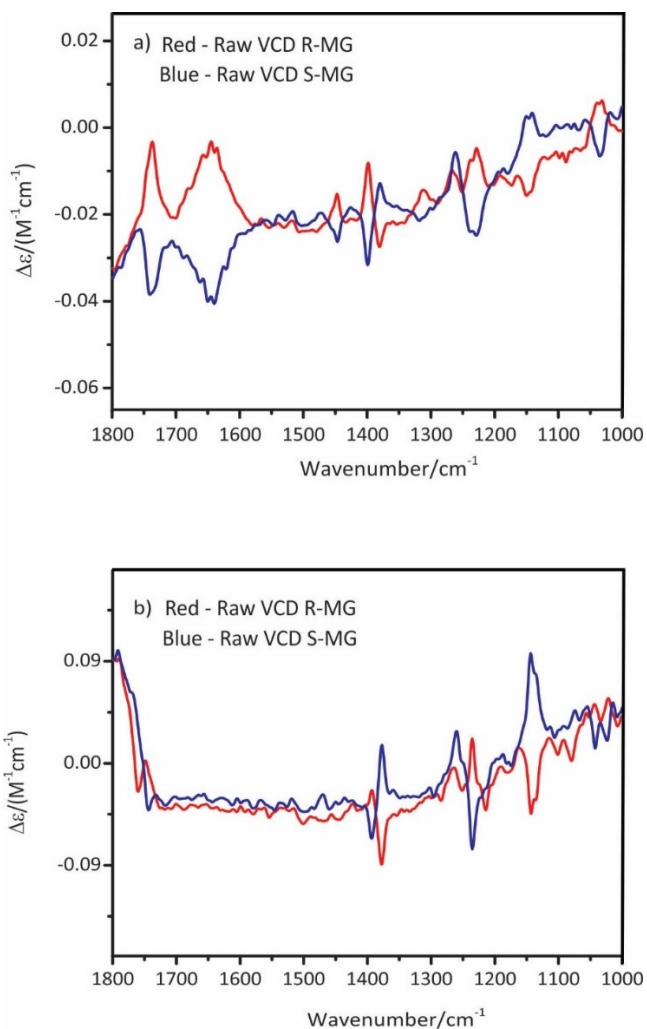


Figure A1. The raw, experimental VCD spectra of R-MG and S-MG a) in water, recorded with a concentration of 6 M and a pathlength of 3 μm and b) in CCl_4 , recorded with a concentration of 0.16 M and a pathlength of 25 μm .

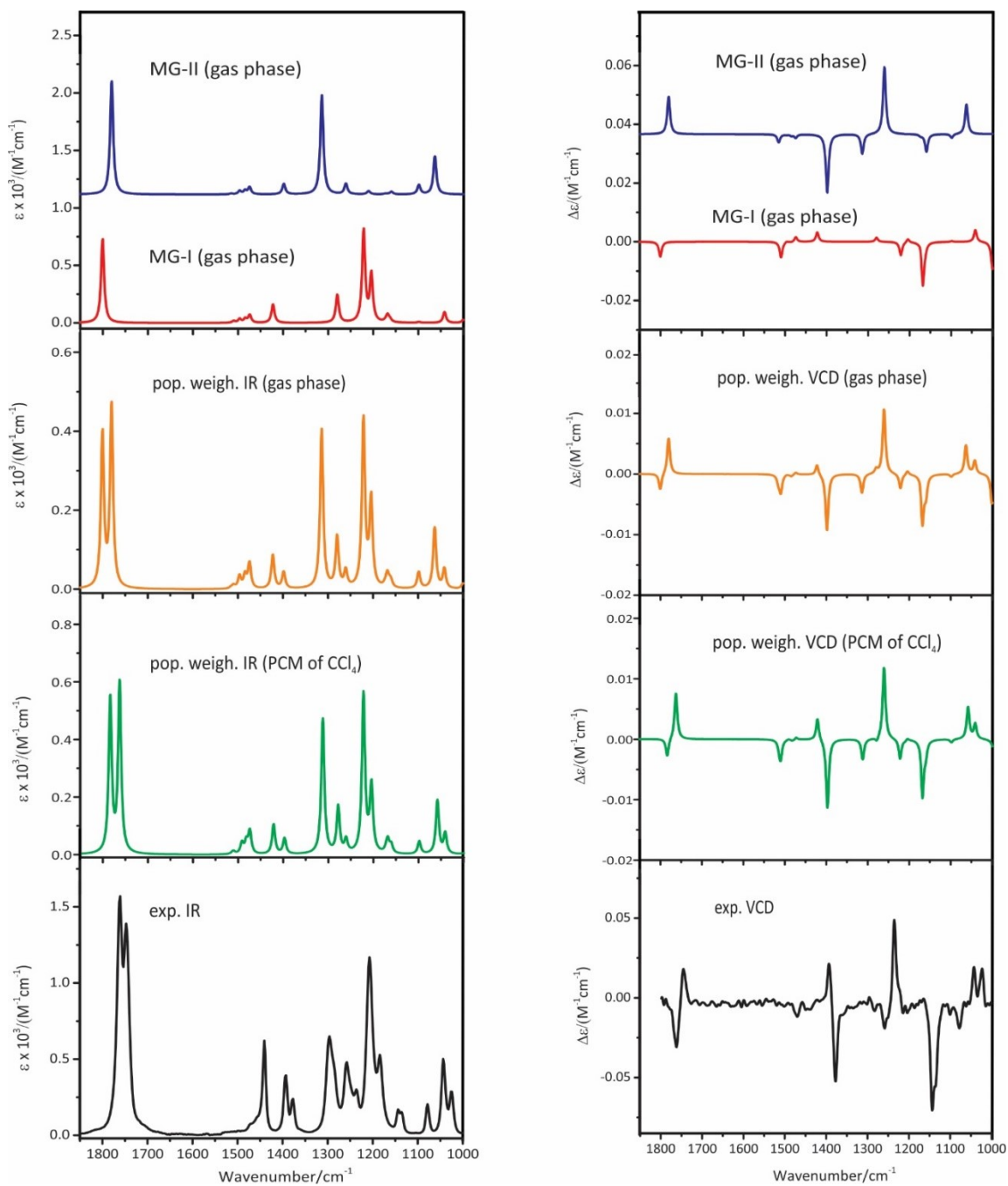


Figure A2. Comparisons of the experimental IR (bottom-left) and VCD (bottom-right) spectra of MG in CCl₄ with the simulated IR (top-left) and VCD (top-right) features of MG-I and MG-II in the gas phase and the corresponding population weighted IR and VCD spectra. The population weighted IR and VCD spectra of MG with the PCM of CCl₄ are also included for comparison.

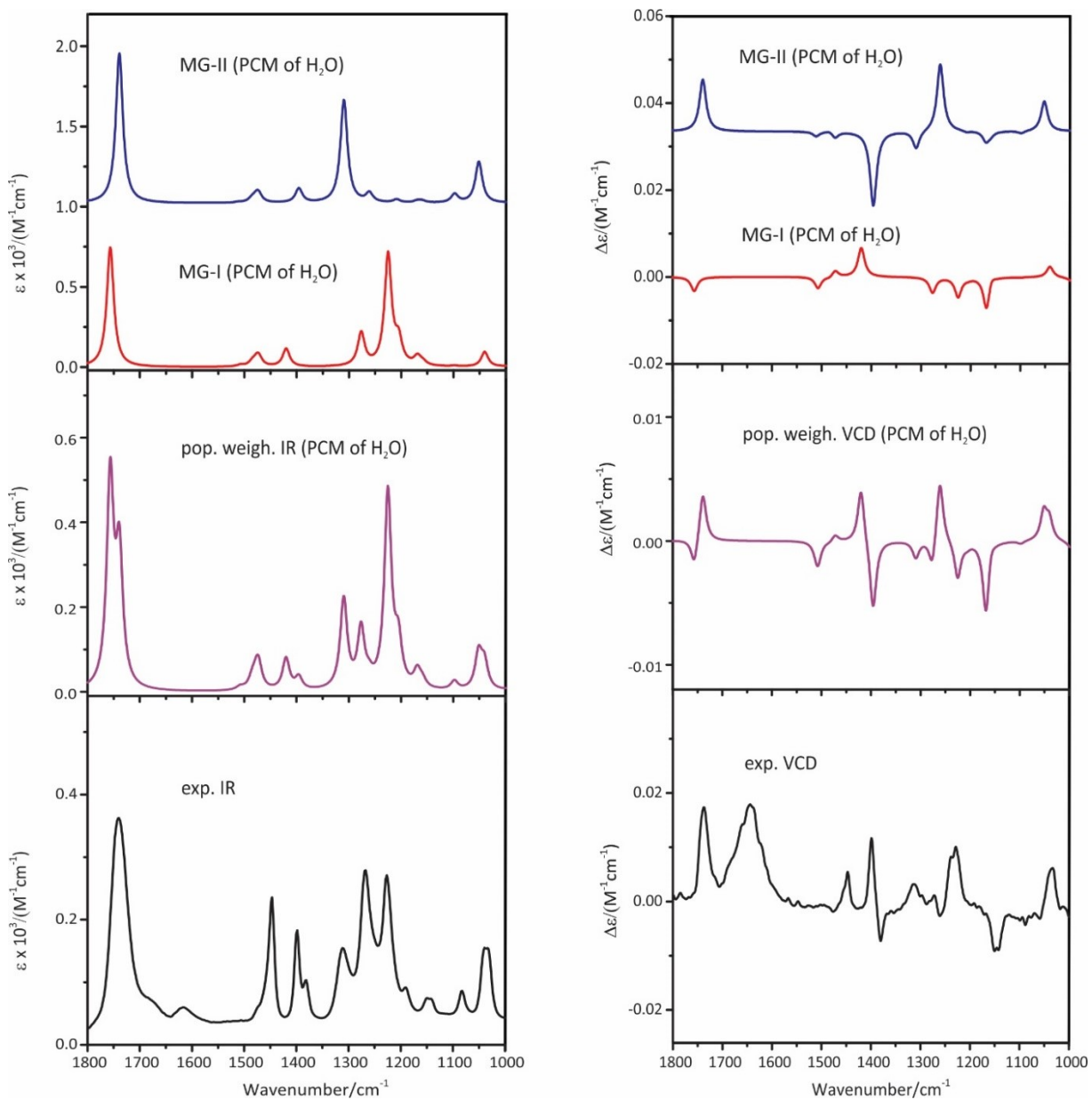


Figure A3. Comparisons of the experimental IR (bottom-left) and VCD (bottom-right) spectra of MG in water with the simulated IR (top-left) and VCD (top-right) spectra of MG-I and MG-II in the PCM of water and the corresponding population weighted IR and VCD spectra.

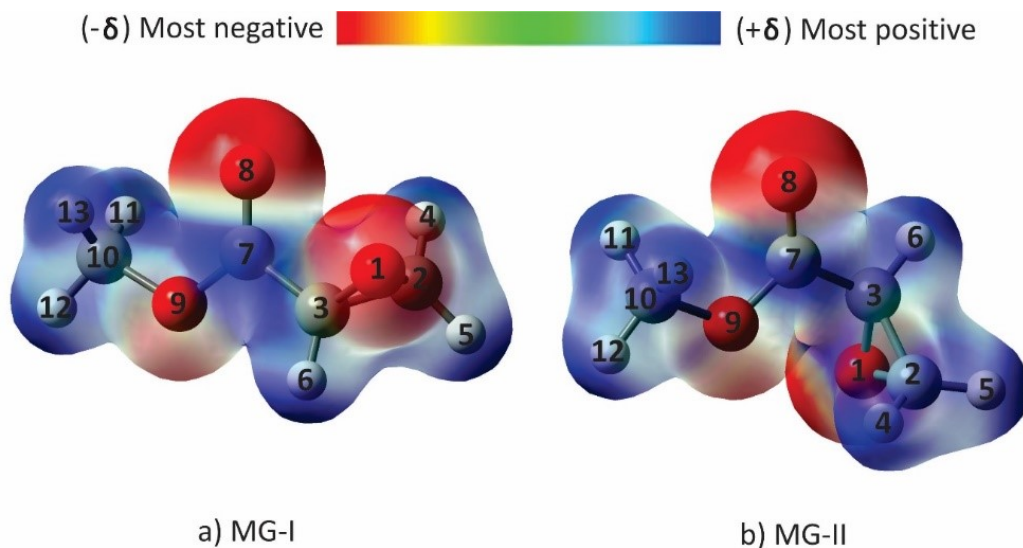


Figure A4. The electrostatic potential distribution diagrams of a) MG-I and b) MG-II.

Table A1. General assignment of the IR and VCD bands of MG-I and MG-II in the PCM of CCl₄.

Peak no ^a	IR freq. (cm ⁻¹)	IR intensity / (km mol ⁻¹)	VCD Rotational strength / (10 ⁻⁴⁴ esu ² cm ²)	General assignment ^b
1	1040.8	37.7	12.7	γ (C3—H6) + δ (H5—C2—H4)
1 ^l	1058.1	118.8	31.7	(rocking) + ν (O9—C10)
2	1099.1	1.78	0.17	γ (H5—C2—H4) (twisting) +
2 ^l	1098.3	26.2	-3.4	γ (C3—H6)
3	1160.8	9.3	1.1	γ (H5—C2—H4) (wagging) +
3 ^l	1160.2	7.4	-12.8	γ (C3—H6)
4	1168.1	22.7	-42.9	γ (H5—C2—H4) (wagging) +
4 ^l	1168.7	1.86	-2.7	γ (C3—H6)
5	1204.2	121.5	1.4	δ (O9—C10—H12) + γ (H11—C10—H13) (wagging) + δ (C3—H6)
5 ^l	1209.9	9.30	-0.94	δ (O9—C10—H12) + γ (H11—C10—H13) (wagging)
6	1221.9	293.1	-14.3	ν (C7—O9) + δ (O9—C10—H12) + δ (C3—H6) + γ (H11—C10— H13) (wagging)
6 ^l	1312.2	299.8	-16.3	δ (C3—H6) + ν (C3—C7) + ν (C7—O9) + γ (H11—C10— H13) (wagging) + δ (C10—H12)

7	1278.1	85.8	-2.9	$\nu(\text{C2—O1}) + \nu(\text{C3—O1}) +$
7 ¹	1260.7	28.9	60.5	$\nu(\text{C3—C2}) + \delta(\text{C3—H6})$
8	1421.3	54.9	13.6	$\nu(\text{C3—C7}) + \nu(\text{C2—O1}) +$
8 ¹	1397.1	34.7	-52.0	$\nu(\text{C3—O1}) + \nu(\text{C3—C2}) + \delta$ (C3—H6) + δ (H5—C2—H4)
9	1473.7	23.7	3.7	$\delta(\text{C10—H12}) + \gamma(\text{H11—C10—$
9 ¹	1474.4	22.3	-3.2	H13) (wagging)
10	1509.9	4.9	-10.4	$\delta(\text{H5—C2—H4}) + \nu(\text{C2—O1}) +$
10 ¹	1513.4	2.2	-4.9	$\nu(\text{C3—O1}) + \nu(\text{C3—C2})$
11	1783.5	286.8	-8.9	$\nu(\text{C=O})$
11 ¹	1762.6	379.2	27.9	

a) MG-I bands are labeled as 1, 2, 3, ... etc, while those of MG-II are labeled as 1¹, 2¹, 3¹, ... etc. b) ν denotes the stretching vibrations; δ and γ notations define the in plane and out of plane bending vibrations respectively. Detailed labels of wagging, rocking and twisting are given in the table. The atom numberings are given in Figure A4.

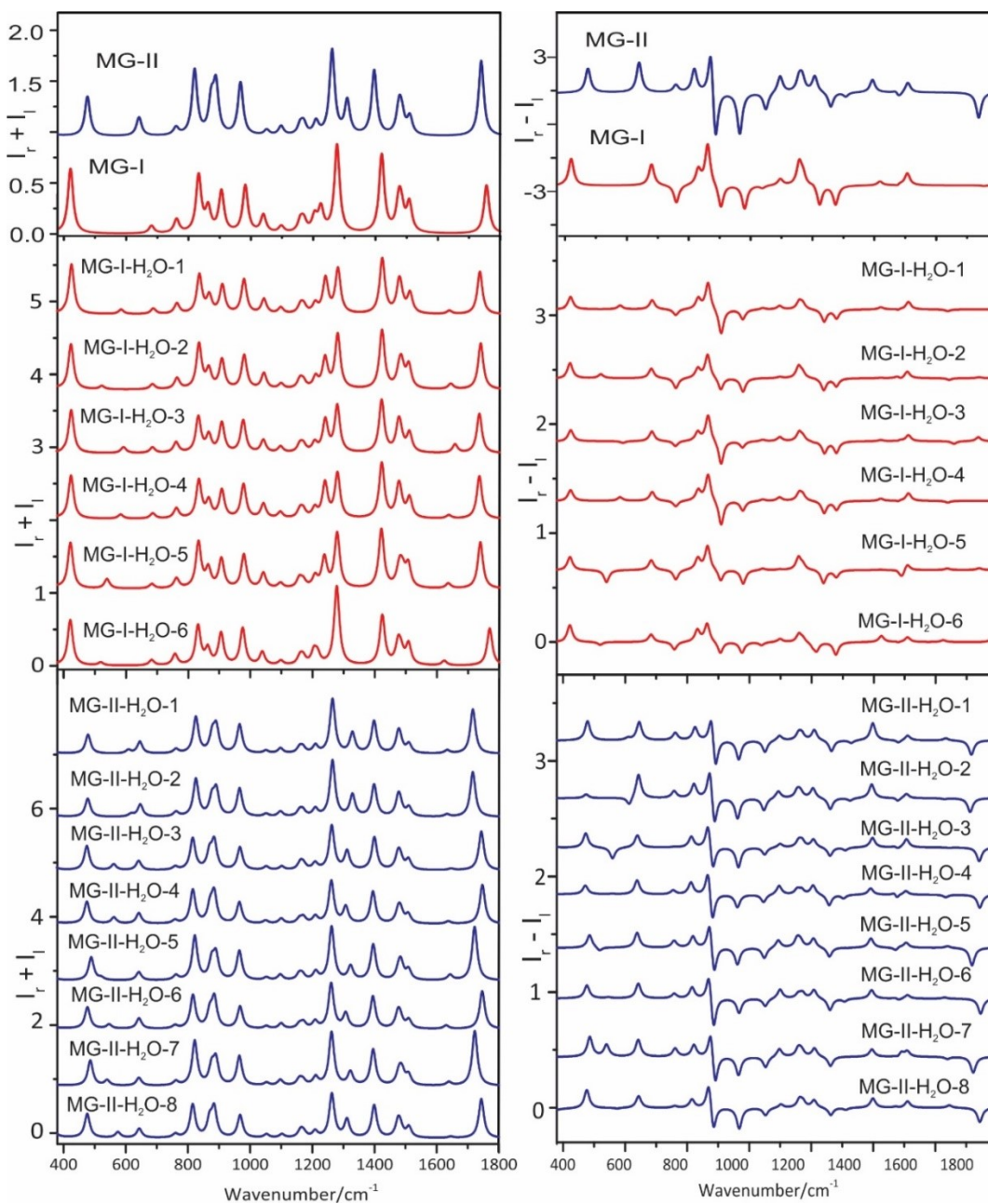


Figure A5. The simulated Raman (left panels) and ROA (right panels) spectra of MG-I, MG-II, MG-I-H₂O and MG-II-H₂O complexes in the PCM of water.

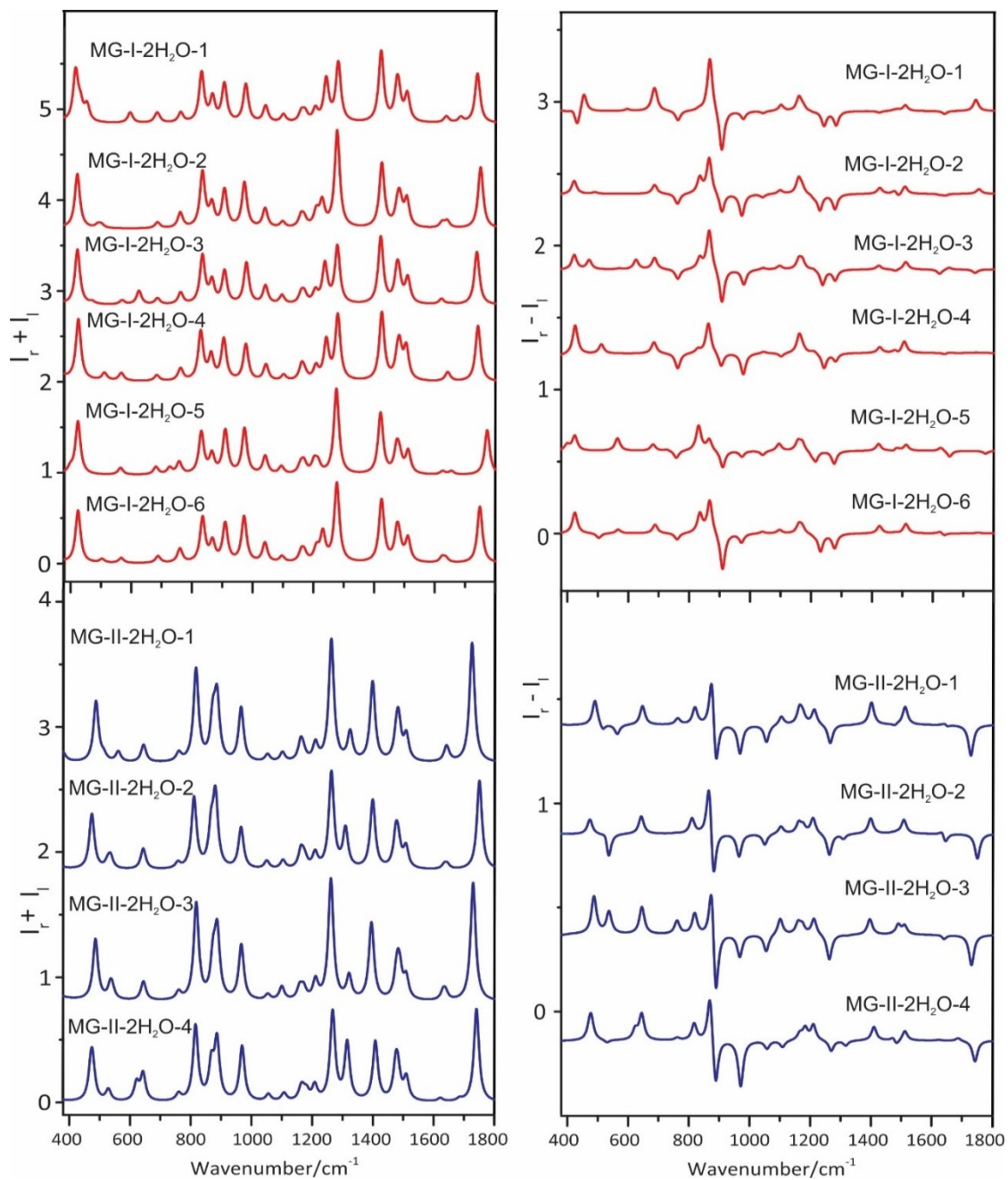


Figure A6. The simulated Raman (left panels) and ROA (right panels) spectra of MG-I-2H₂O and MG-II-2H₂O complexes in the PCM of water.

Appendix B

Supporting Information for Chapter 4

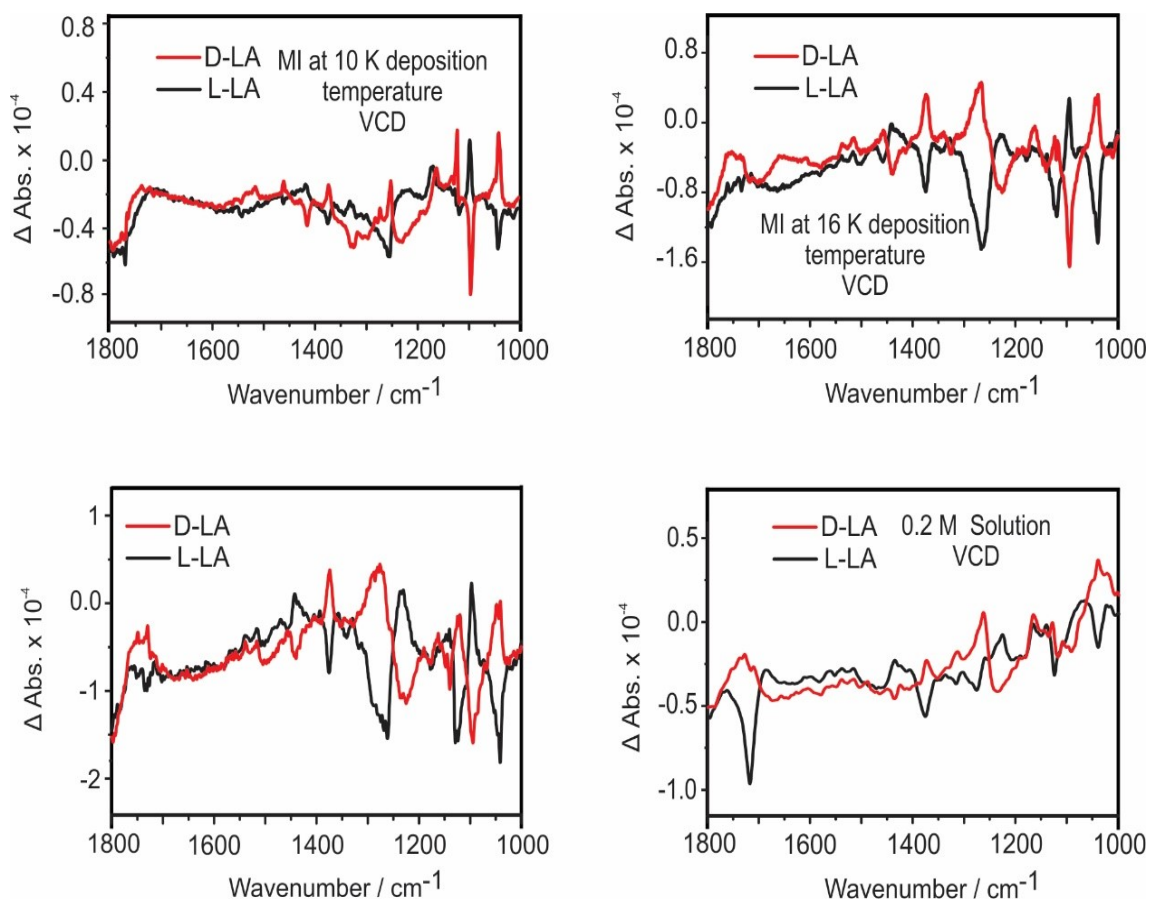


Figure B1. The raw, experimental VCD spectra of D-LA and L-LA in the cold Ar matrices at 10 K, 16 K and 24 K and in a 0.2 M solution in CDCl₃.

Table B1. Comparison of the relative energies (ΔE in kJ mol^{-1}) and Boltzmann factor (Bf in %) at 298 K of the LA monomer conformers computed at the B3LYP/6-311++G(2d,p) and B3LYP-D3BJ/6-311++G(2d,p) and the B3LYP-D3BJ/def2-TZVPD levels of theory.

Conf.	B3LYP/ 6-311++G(2d,p)		B3LYP-D3BJ/ 6-311++G(2d,p)		B3LYP-D3BJ/ def2-TZVPD	
	ΔE	Bf	ΔE	Bf	ΔE	Bf
M1	0.0 (0.0) ¹	95.0 (79.1)	0.0 (0.0)	94.9 (75.0)	0.0 (0.0)	95.1 (53.6)
M2	9.4 (8.0)	2.2 (3.2)	9.6 (8.2)	2.0 (2.7)	9.8 (6.3)	1.8 (1.9)
M3	9.9 (7.8)	1.8 (3.4)	9.8 (7.7)	1.9 (3.4)	10.0 (7.0)	1.7 (2.3)
M4	11.2 (4.2)	1.0 (14.4)	10.6 (3.4)	1.3 (18.9)	10.4 (7.0)	1.4 (39.5)

¹ The values in brackets are obtained with the PCM of CDCl_3 added to the calculations.

Table B2. Comparison of the relative energies (ΔE in kJ mol^{-1}) and Boltzmann factor (Bf in %) at 298 K¹ of the LA dimer conformers computed at the B3LYP/6-311++G(2d,p) and B3LYP-D3BJ/6-311++G(2d,p) and the B3LYP-D3BJ/def2-TZVPD levels of theory.

Dimer Conf.	B3LYP/6-311++G(2d,p)		B3LYP-D3BJ/6-311++G(2d,p)		B3LYP-D3BJ/def2-TZVPD	
	ΔE	Bf	ΔE	Bf	ΔE	Bf
D1	0.0 (0.0) ²	85.2 (79.5)	0.0 (0.0)	84.5 (78.8)	0.0 (0.0)	83.9 (78.4)
D2	6.2 (5.4)	7.0 (8.9)	6.2 (5.5)	6.8 (8.5)	6.1 (5.5)	7.1 (8.7)
D3	6.5 (5.5)	6.1 (8.5)	6.2 (5.3)	6.8 (9.4)	6.2 (5.2)	7.0 (9.6)
D4	12.1 (10.9)	0.6 (1.0)	12.2 (11.0)	0.6 (0.9)	11.9 (10.9)	0.6 (1.0)
D5	12.4 (10.7)	0.6 (1.1)	12.1 (10.5)	0.6 (1.1)	11.9 (10.4)	0.6 (1.2)
D6	12.9 (10.7)	0.5 (1.1)	12.3 (10.3)	0.6 (1.2)	12.2 (10.2)	0.5 (1.3)

¹ For the relevant cold matrix temperatures of 10, 16 and 24 K, only the most stable conformer D1 contributes dominantly to the experimental spectra. See text for discussion.

² The values in brackets are obtained with the PCM of CDCl_3 added to the calculations.

Table B3. Comparison of the relative free energies (ΔE in kJ mol^{-1}) and Boltzmann factor (Bf in %) at 298 K¹ of the LA trimers and tetramers computed at the B3LYP/6-311++G(2d,p) and B3LYP-D3BJ/6-311++G(2d,p) and the B3LYP-D3BJ/def2-TZVPD levels of theory.²

(LA) ₃ &(LA) ₄ Conf.	B3LYP/ 6-311++G(2d,p)		B3LYP-D3BJ/ 6-311++G(2d,p)		B3LYP-D3BJ/ def2-TZVPD	
	ΔE	Bf	ΔE	Bf	ΔE	Bf
T1	0.0 (0.0) ³	52.4 (52.3)	0.0 (0.0)	62.2 (82.7)	0.0 (0.0)	63.4 (57.9)
T2	0.3 (0.2)	47.4 (47.6)	1.2 (3.9)	37.7 (17.2)	1.4 (1.2)	36.4 (35.2)
T3	14.3 (14.5)	0.2 (0.2)	18.1 (20.9)	0.0 (0.0)	18.1 (18.3)	0.0 (0.0)
Te1	0.0 (0.0)	38.2 (38.6)	0.0 (0.0)	49.6 (50.1)	0.0 (0.0)	51.5 (52.8)
Te2	0.5 (0.5)	31.7 (31.7)	1.1 (1.3)	31.2 (29.5)	1.3 (1.5)	30.5 (28.3)
Te3	0.6 (0.7)	30.4 (29.7)	2.4 (2.2)	19.2 (20.4)	2.6 (2.6)	18.0 (18.8)

¹ For the relevant cold matrix temperatures of 10, 16 and 24 K, only the most stable conformers T1 and Te1 contribute mostly to the experimental spectra at the B3LYP-D3BJ/def2-TZVPD level.

² Only the three conformers listed are included in the Boltzmann factor calculations for easy comparison among different levels of theory.

³ The values in brackets are obtained with the PCM of CDCl₃ added to the calculations.

Table B4. The α^1 values of the C=O stretching modes of the most stable conformers of each LA species calculated.

Conf.	Vibrational Frequency (cm ⁻¹)	θ (°)
M1	1797.0	90.2
D1	1683.8	180.0
D1	1738.9	85
T1	1669.2	82.1
T1	1722.8	106.6
T1	1747.5	65.6
Te1	1662.8	0.0
Te1	1708.5	74.6
Te1	1737.1	180
Te1	1750.7	14.5

¹ α is defined as the angle between the electric and magnetic dipole transition moment vectors.

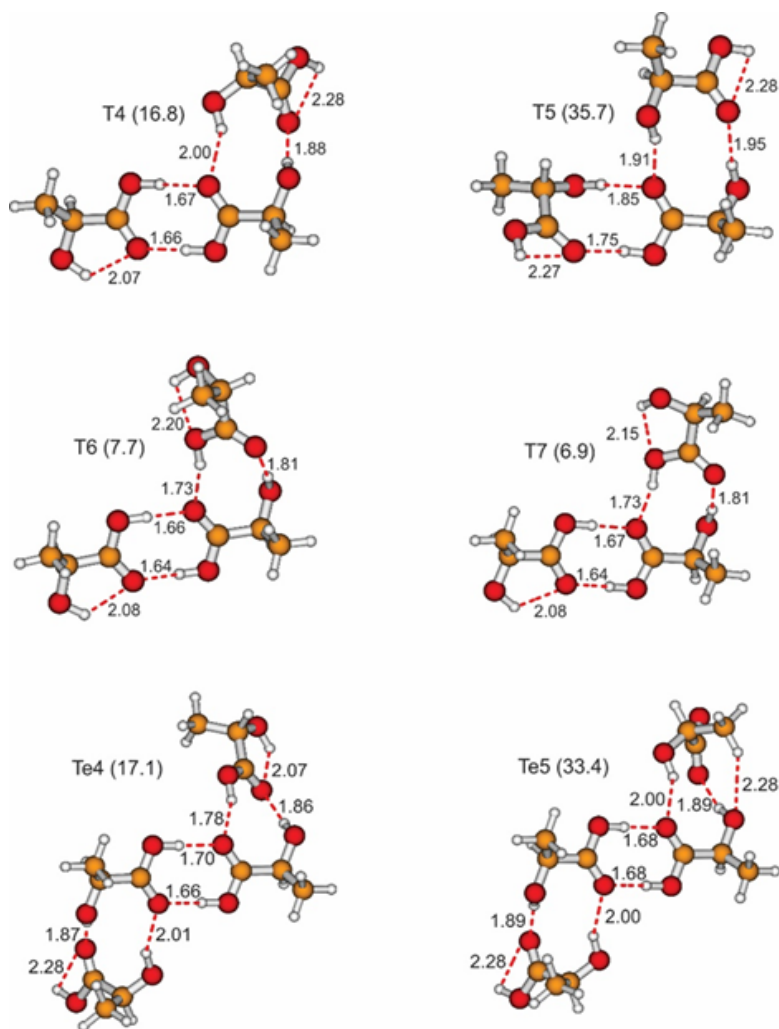


Figure B2. Geometries of the additional conformers of the LA trimer and tetramer in the gas phase. The relative free energy values in kJ mol^{-1} at the B3LYP-D3BJ/def2-TZPVD level of theory are indicated in brackets.

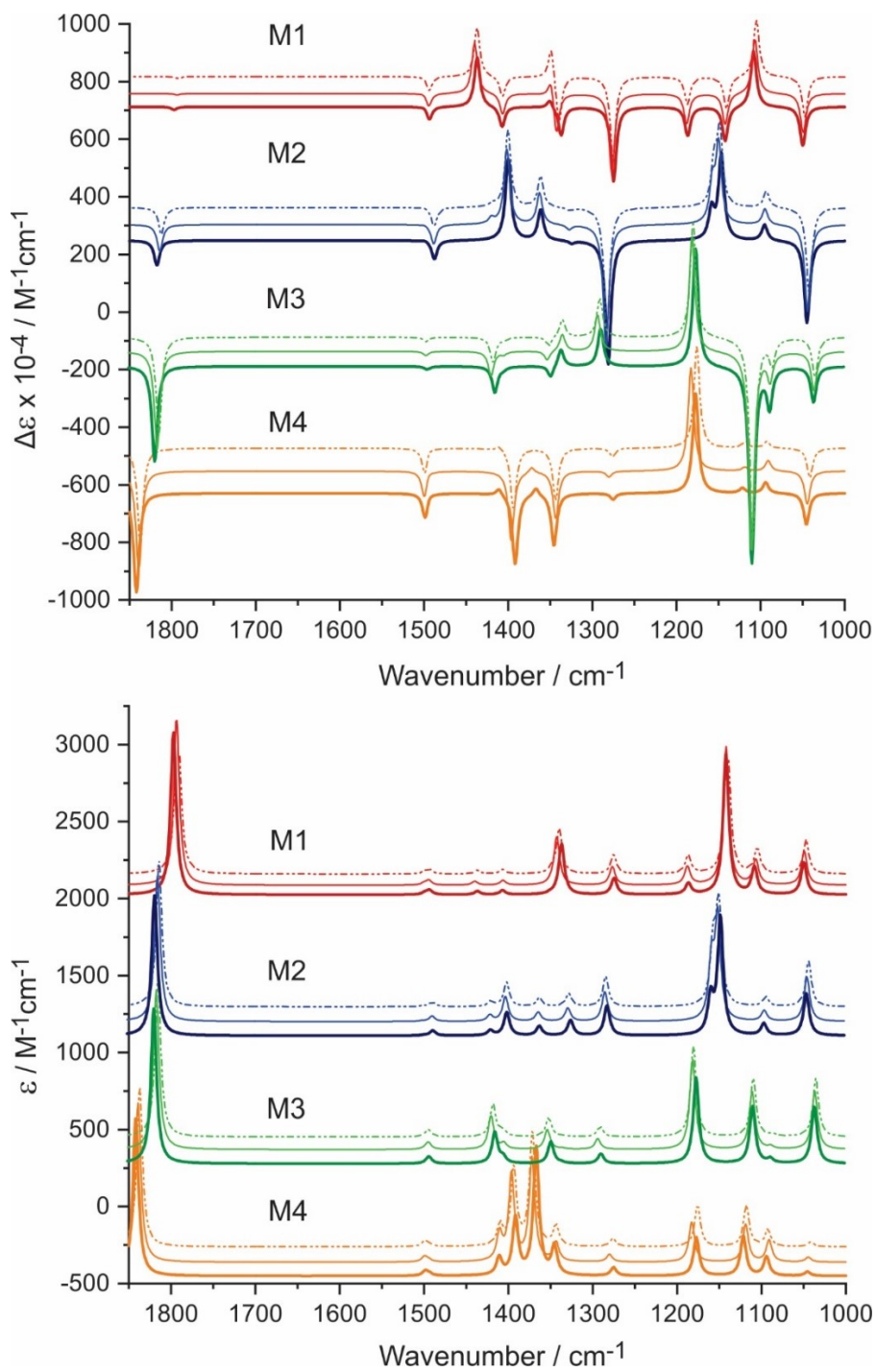


Figure B3. Predicted IR (bottom panel) and VCD (top panel) spectra of the four most stable conformers of the LA monomer in the gas phase at the B3LYP/6-311++G(2d,p) and B3LYP-D3BJ/6-311++G(2d,p) and the B3LYP-D3BJ/def2-TZVPD levels of theory from top to bottom.

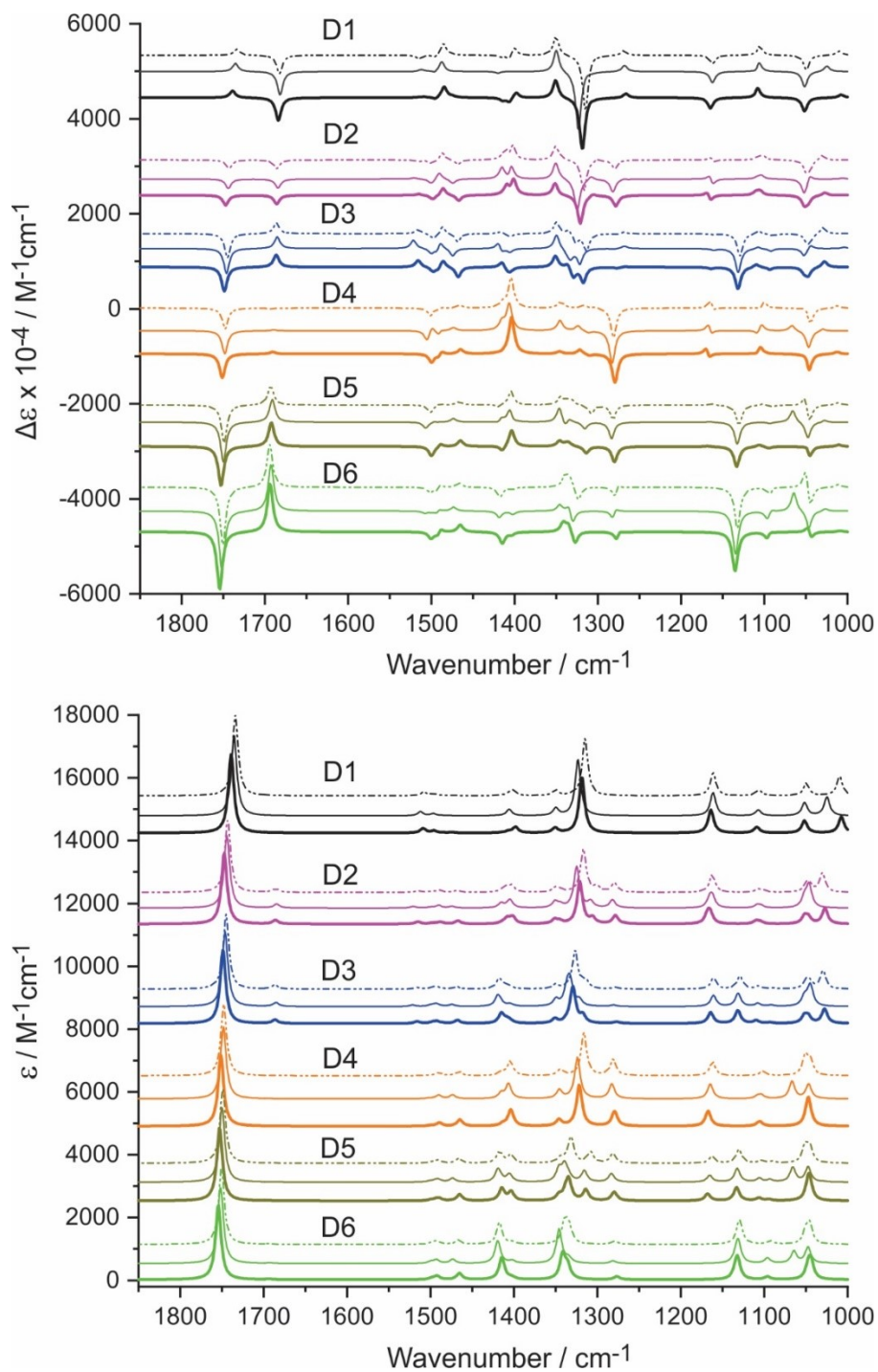


Figure B4. Predicted IR (bottom panel) and VCD (top panel) spectra of the six most stable conformers of the LA dimer in the gas phase at the B3LYP/6-311++G(2d,p) and B3LYP-D3BJ/6-311++G(2d,p) and the B3LYP-D3BJ/def2-TZVPD levels of theory from top to bottom.

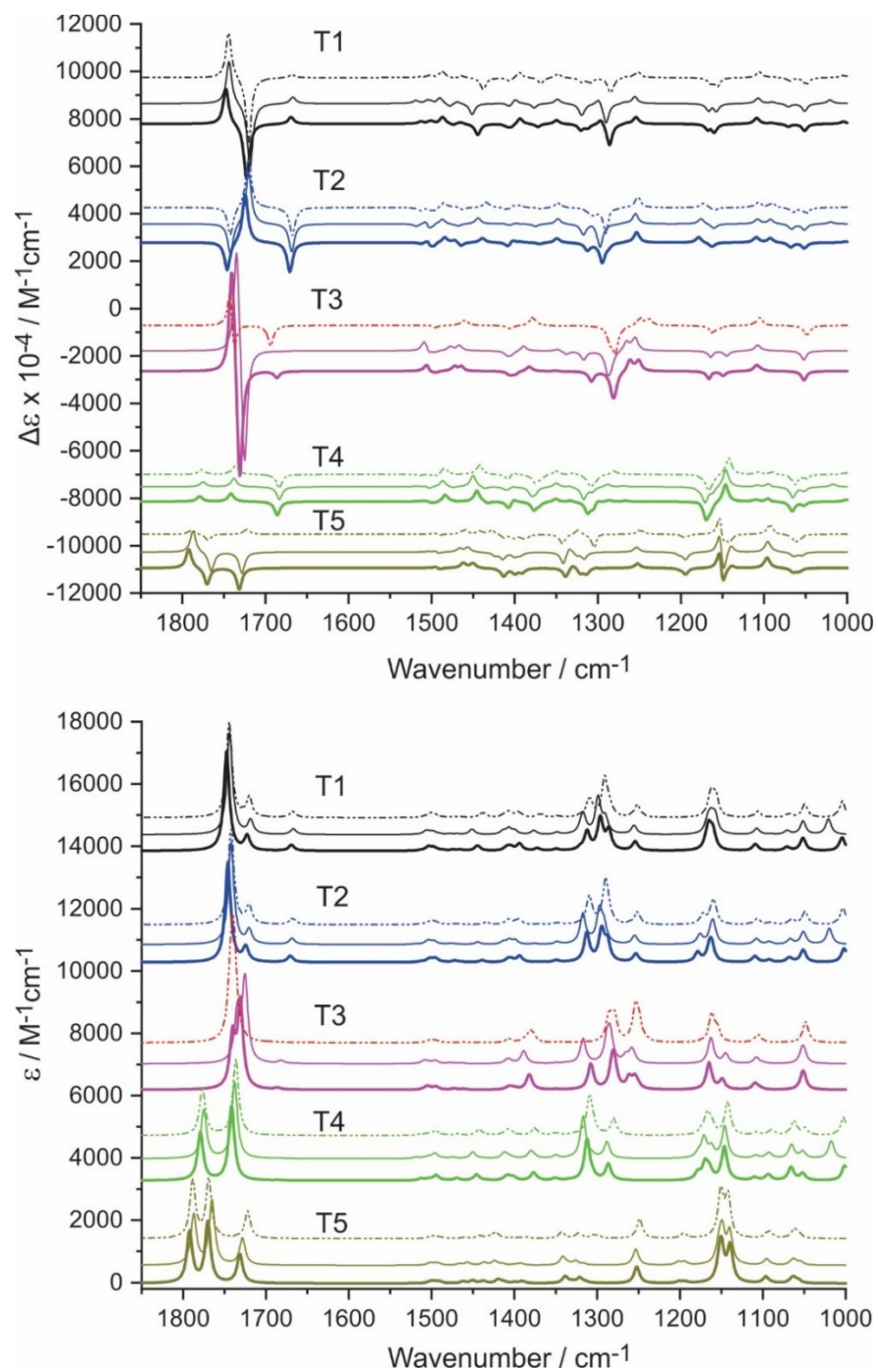


Figure B5. Predicted IR (bottom panel) and VCD (top panel) spectra of the five stable conformers of the LA trimer in the gas phase at the B3LYP/6-311++G(2d,p) and B3LYP-D3BJ/6-311++G(2d,p) and the B3LYP-D3BJ/def2-TZVPD levels of theory from top to bottom.

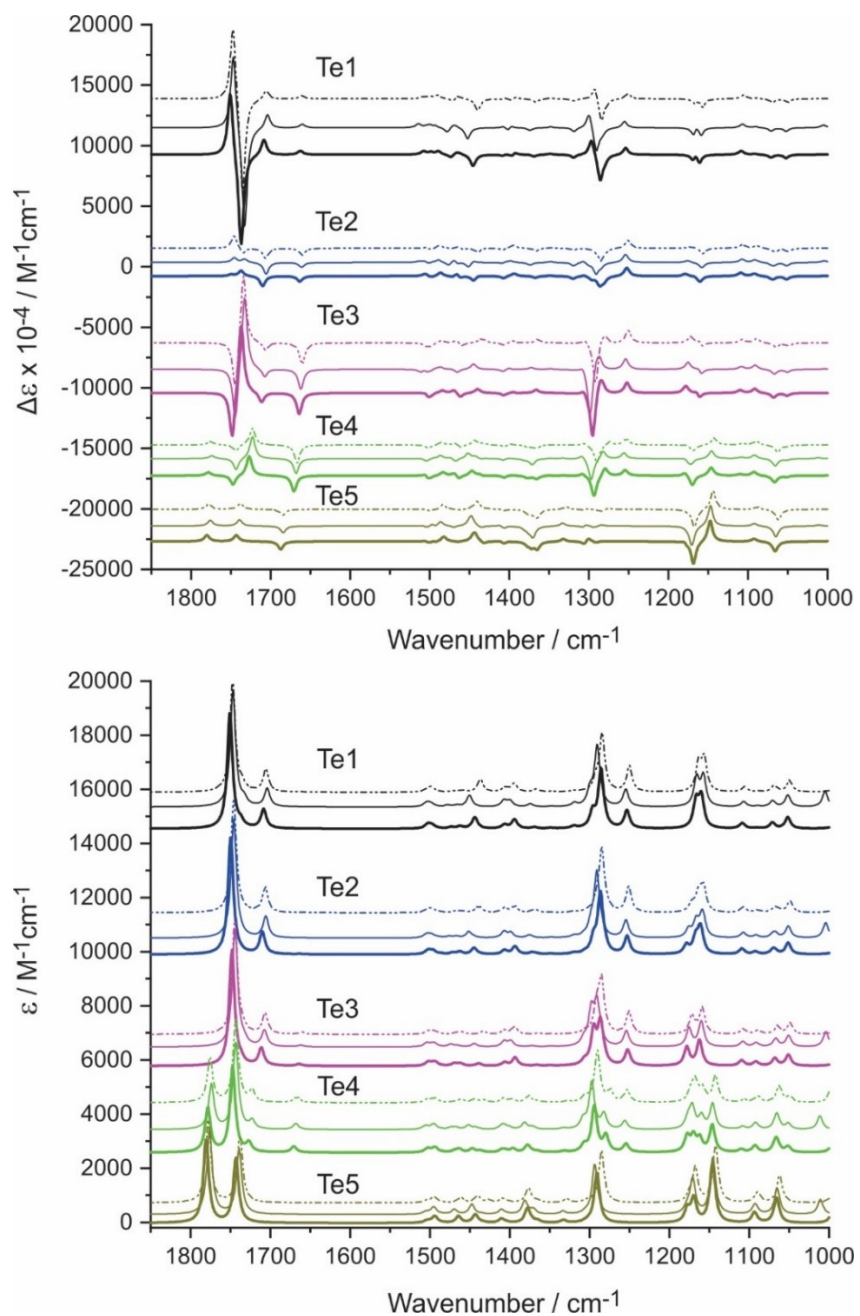
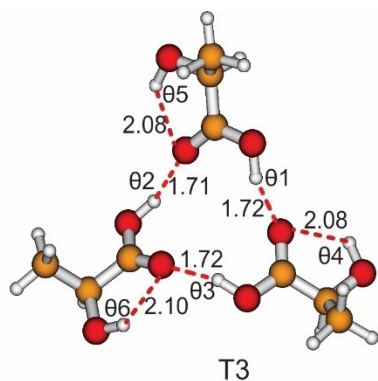
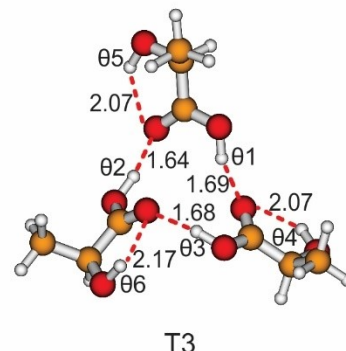


Figure B6. Predicted IR (bottom panel) and VCD (top panel) spectra of the five stable conformers of the LA tetramer in the gas phase at the B3LYP/6-311++G(2d,p) and B3LYP-D3BJ/6-311++G(2d,p) and the B3LYP-D3BJ/def2-TZVPD levels of theory from top to bottom.



$\theta 1 - \theta 6$: 160.7°, 162.0°, 163.3°,
117.2°, 117.0°, 116.3°

(Dipole = 0.8 Debye at B3LYP/6-311++G(2d,p))



$\theta 1 - \theta 6$: 161.3°, 168.9°, 170.8°,
117.1°, 117.3°, 112.2°

(Dipole = 1.5 D at B3LYP-D3BJ/6-311++G(2d,p))

Figure B7. Optimized geometries of T3 in the gas phase obtained with and without the dispersion correction (D3BJ) with the basis set 6-311++G(2d,p). The optimized geometry obtained at the B3LYP-D3BJ/def2-TZVPD level is very similar to that at the B3LYP-D3BJ/6311++G(2d,p) and the dipole moment is 1.4 D.

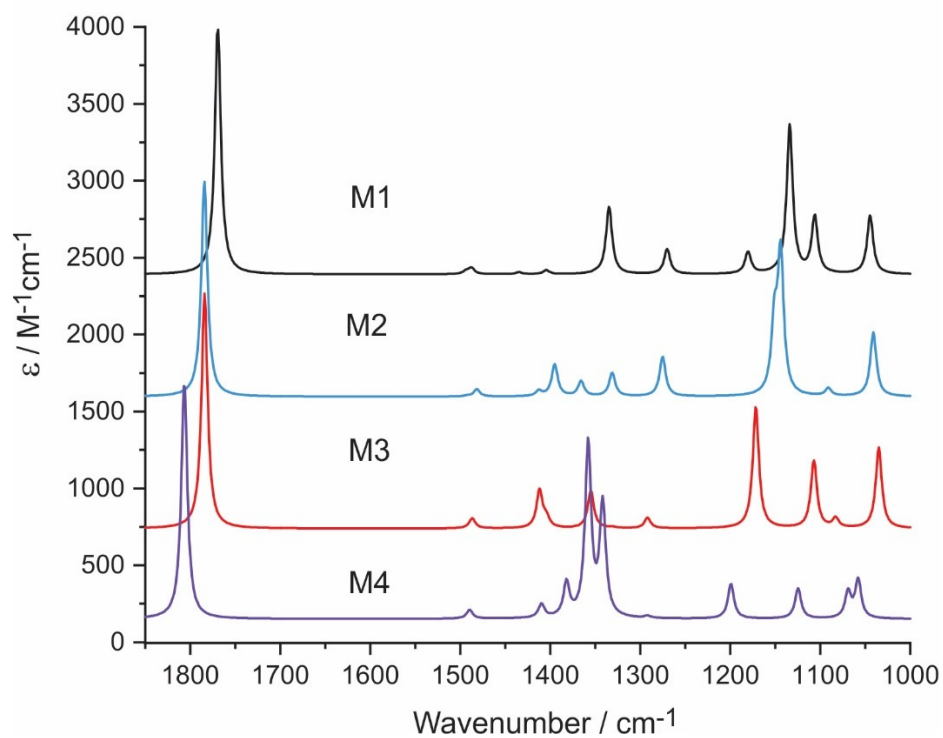
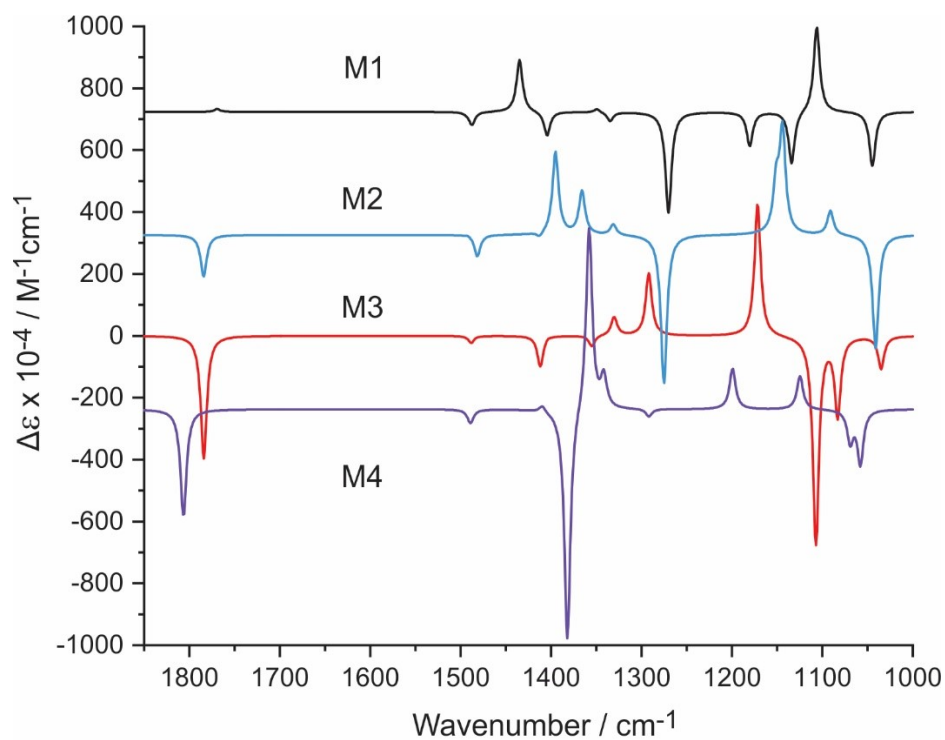


Figure B8. Predicted IR (bottom panel) and VCD (top panel) spectra of the four most stable conformers of the LA monomer in the PCM of CDCl_3 at the B3LYP-D3BJ/def2-TZVPD level of theory.

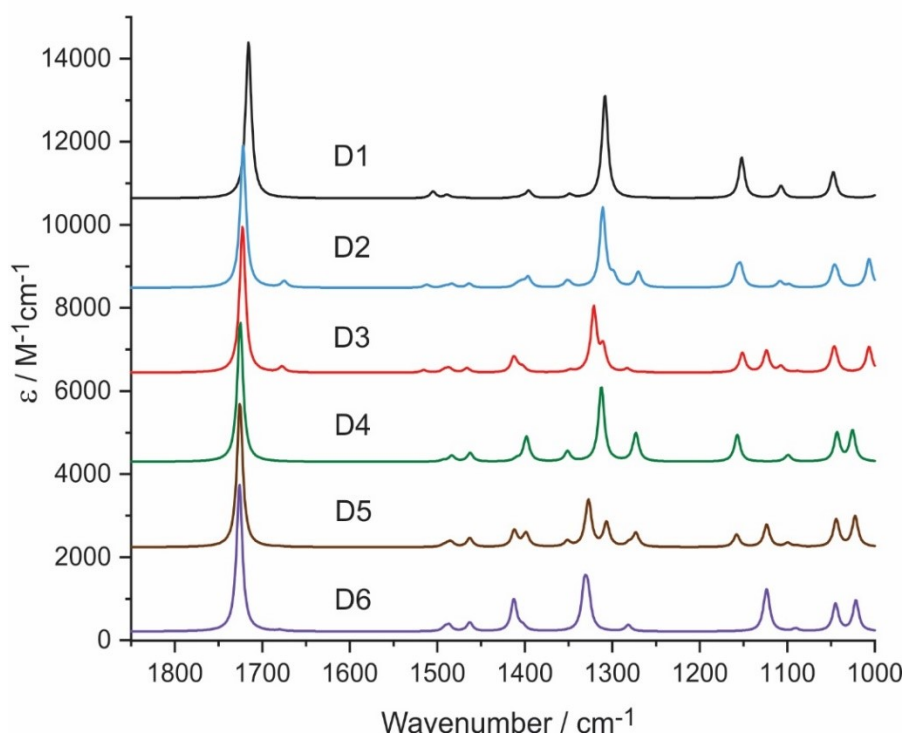
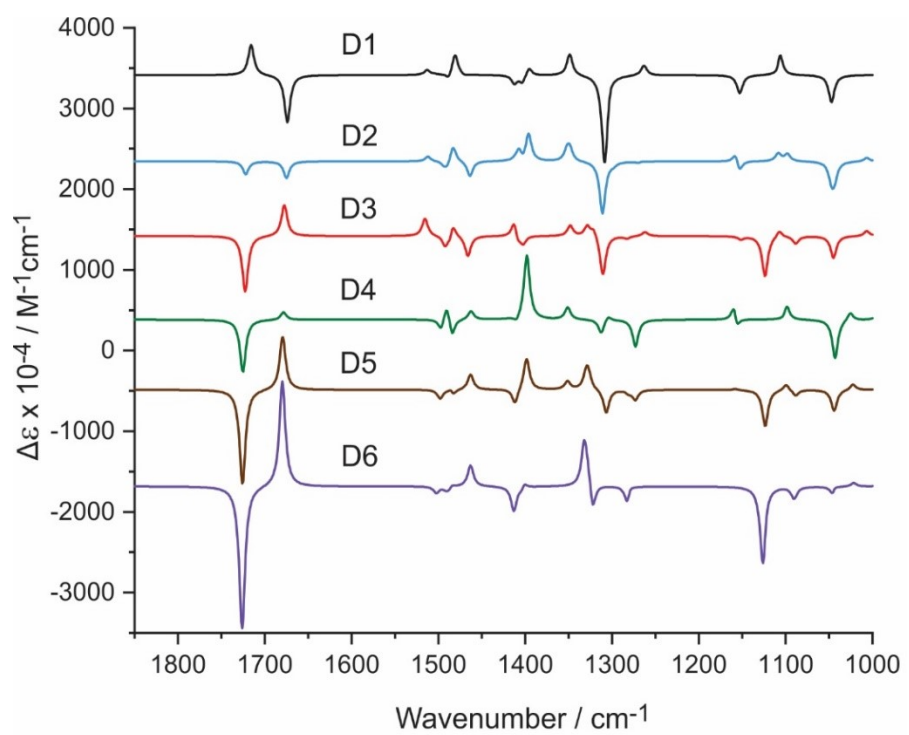


Figure B9. Predicted IR (bottom panel) and VCD (top panel) spectra of the six most stable conformers of the LA dimer in the PCM of CDCl_3 at the B3LYP-D3BJ/def2-TZVPD level of theory.

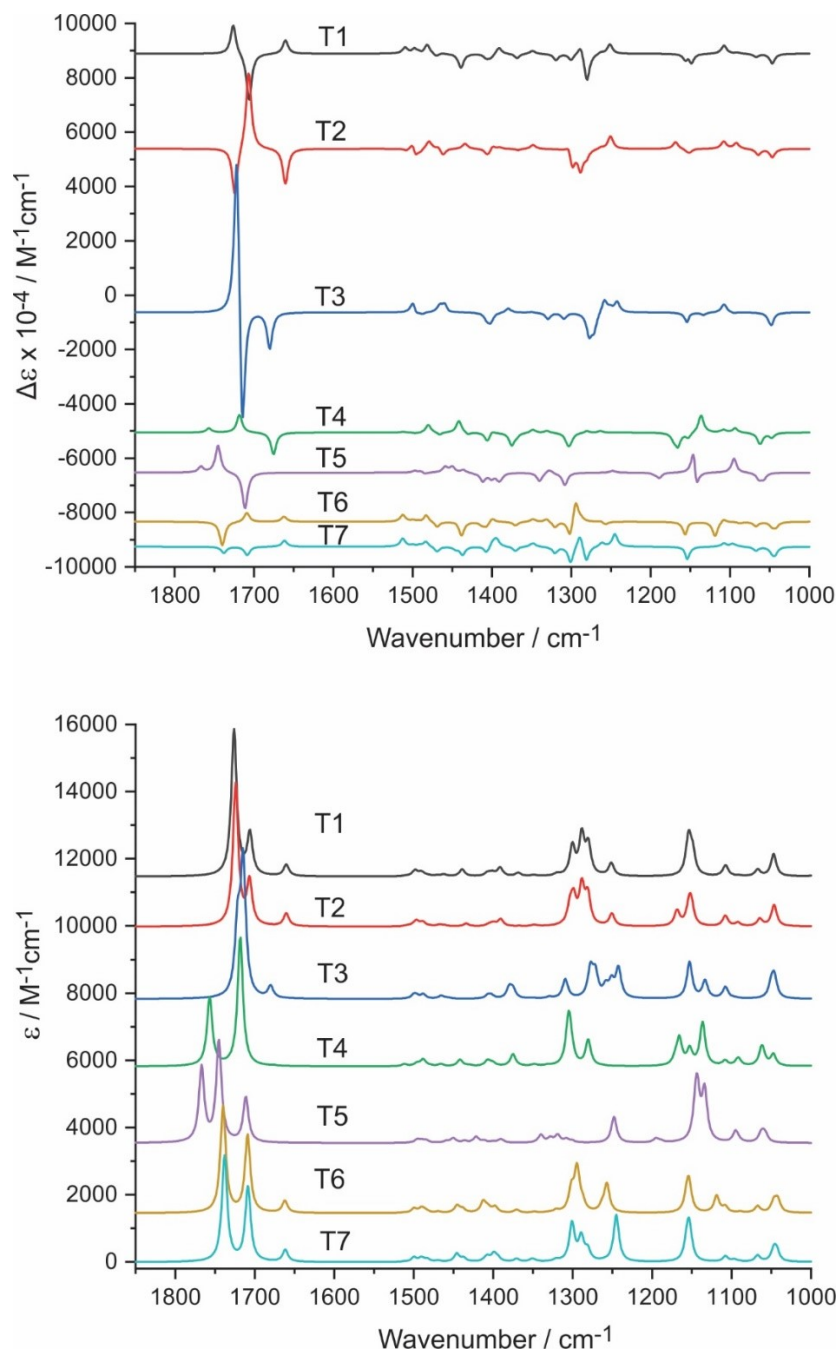


Figure B10. Predicted IR (bottom panel) and VCD (top panel) spectra of the seven $(\text{LA})_3$ conformers in the PCM of CDCl_3 at the B3LYP-D3BJ/def2-TZVPD level of theory. The Boltzmann factors for T1-T7 (in %) at 298 K are: 60.9, 28.9, 0.2, 0.2, 0.0, 3.4, and 6.4.

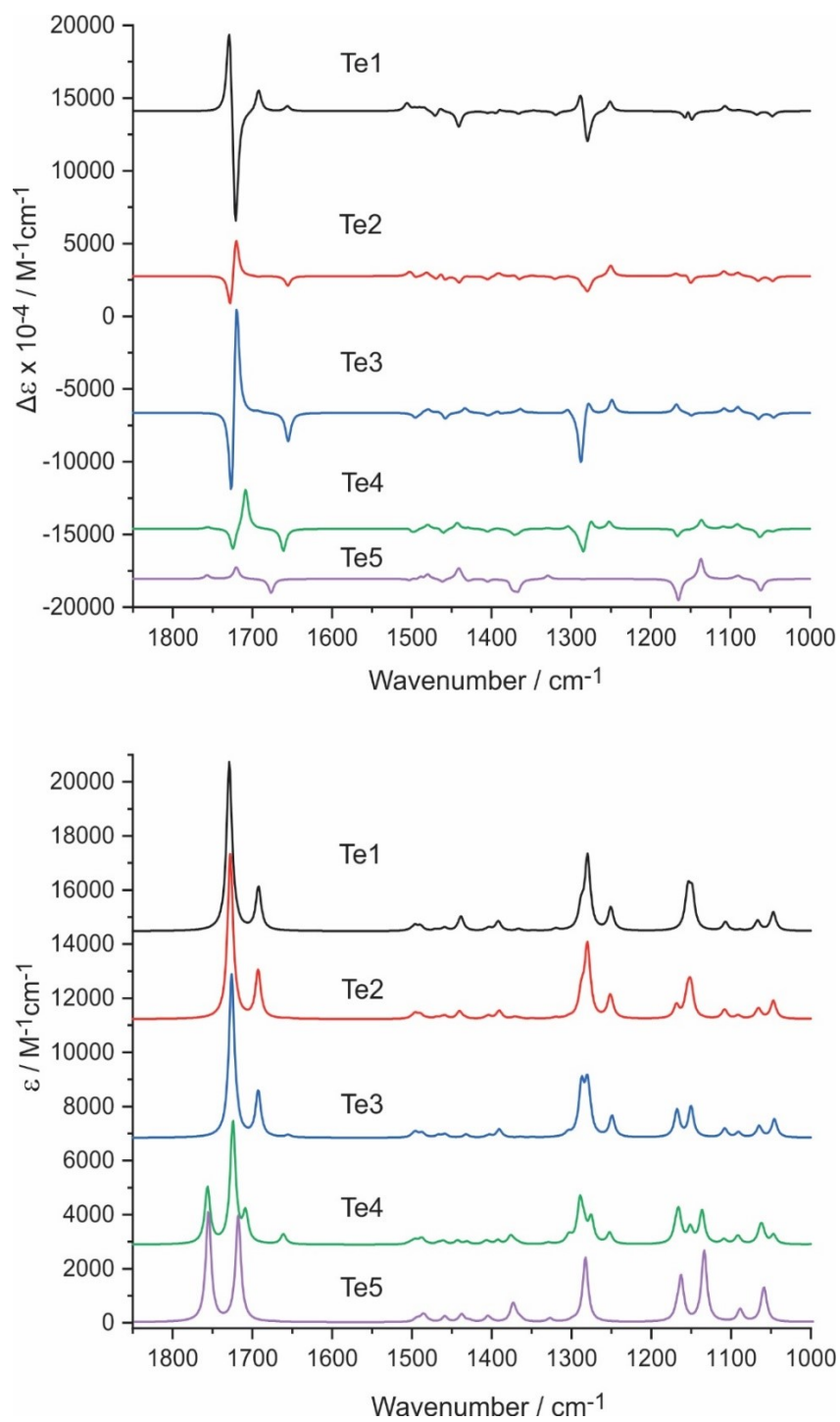


Figure B11. Predicted IR (bottom panel) and VCD (top panel) spectra of the five $(\text{LA})_4$ conformers in the PCM of CDCl_3 at the B3LYP-D3BJ/def2-TZVPD level of theory. The Boltzmann factors for Te1-Te5 (in %) at 298 K are: 76.9, 5.1, 17.9, 0.1, and 0.0.

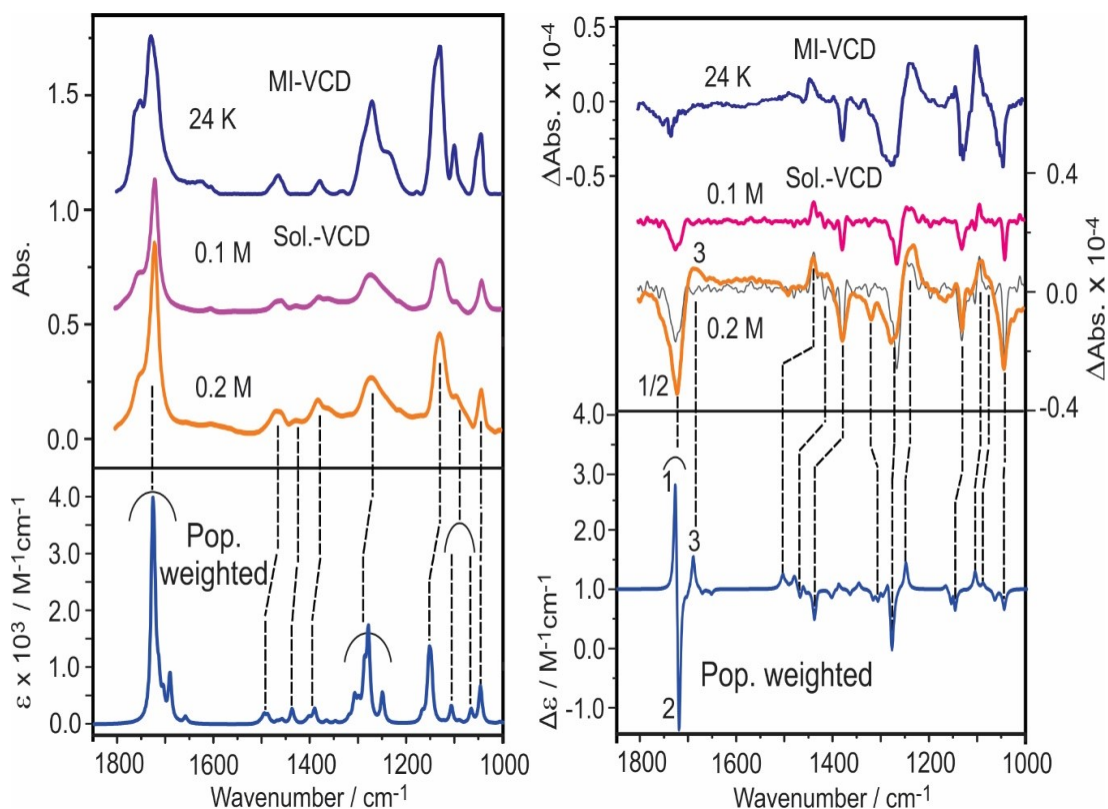


Figure B12. Comparison of the experimental IR (top-left) and VCD (top-right) spectra at 24 K, in 0.1 M and in 0.2M solution with the empirically population weighted IR (bottom-left) and VCD (bottom-right) spectra of the LA monomer, dimer, trimer and tetramer calculated at the B3LYP-D3BJ/def2-TZVPD level of theory. The population weighted spectra contain 20% LA dimer, 30% LA trimer and 50 % LA tetramer.

Cartesian coordinates for M1 calculated at the B3LYP-D3BJ/def2-TZVPD level of theory.

C	-0.6838390	0.0669900	-0.3994220
O	-1.3740950	-1.1481310	-0.2168140
C	0.7755140	-0.1176100	-0.0284510
O	1.2218370	-1.1360210	0.4380040
H	-0.7414130	-1.7899060	0.1396220
O	1.5215850	0.9726700	-0.2756180
H	2.4335270	0.7721350	-0.0109910
H	-0.7083480	0.3400240	-1.4617840
C	-1.3313400	1.1855700	0.4156880
H	-0.8520720	2.1435210	0.2155130
H	-2.3842330	1.2511440	0.1442460
H	-1.2640910	0.9652310	1.4819310

Cartesian coordinates for M2 calculated at the B3LYP-D3BJ/def2-TZVPD level of theory.

C	-0.6806620	0.1018410	0.3719140
H	-0.7349600	0.0783480	1.4718380
C	-1.6276580	-0.9410580	-0.1913640

C	0.7733050	-0.2332520	0.0551000
H	-1.5819920	-0.9415400	-1.2806310
H	-1.3619790	-1.9313070	0.1730570
H	-2.6456920	-0.7042200	0.1148940
O	1.2360220	-1.3404670	0.0101380
O	1.5242610	0.8825050	-0.1123700
H	2.4385490	0.5973440	-0.2666670
O	-1.0768880	1.3737840	-0.1080480
H	-0.3709940	2.0096130	0.0558470

Cartesian coordinates for M3 calculated at the B3LYP-D3BJ/def2-TZVPD level of theory.

C	0.6818700	-0.1437270	-0.4216020
O	1.2714090	1.1400640	-0.5069740
C	-0.8099720	-0.0966480	-0.1251640
O	-1.6086070	-0.9182450	-0.4855270
H	1.0325810	1.6475220	0.2781340
O	-1.1387820	0.9599340	0.6557700
H	-2.0909580	0.9063680	0.8334390
H	0.7825690	-0.5877950	-1.4115850
C	1.3698570	-1.0365990	0.6129320
H	0.9357770	-2.0370490	0.6101790
H	2.4299570	-1.1074420	0.3721920
H	1.2673860	-0.6137830	1.6144940

Cartesian coordinates for M4 calculated at the B3LYP-D3BJ/def2-TZVPD level of theory.

C	0.6409090	-0.0960240	-0.4214040
H	0.7209100	-0.3795710	-1.4749030
C	1.3931200	-1.0968340	0.4430390
C	-0.8522530	-0.1166670	-0.0817940
H	1.3212250	-0.8259280	1.4979940
H	0.9690760	-2.0907220	0.3093080
H	2.4464470	-1.1305370	0.1558170
O	-1.5311360	-1.0886420	-0.2611490
O	-1.3357440	1.0183710	0.4414410
H	-0.6044050	1.6618660	0.4722290
O	1.1176950	1.2439230	-0.2536290
H	2.0495650	1.2328280	-0.0127960

Cartesian coordinates for D1 calculated at the B3LYP-D3BJ/def2-TZVPD level of theory.

C	-1.9027630	0.0890560	-0.2195340
O	-1.3106280	-0.9858340	-0.2212460
C	-3.4175400	0.1466930	-0.2103440
H	-3.7100850	0.7330020	-1.0902400
C	-3.9335940	0.8476180	1.0458880
H	-5.0225090	0.8458220	1.0241080
H	-3.5790190	1.8766800	1.0917070
H	-3.6064740	0.3135830	1.9391120
O	-3.9599120	-1.1500090	-0.3169050
H	-3.2213750	-1.7760360	-0.3320270
O	-1.3171810	1.2597730	-0.2247770
H	-0.3174200	1.1629000	-0.2253160
C	1.9027640	-0.0890450	-0.2195400
O	1.3106330	0.9858470	-0.2212510
C	3.4175390	-0.1466890	-0.2103490
H	3.7100780	-0.7329730	-1.0902660

C	3.9335930	-0.8476580	1.0458570
H	5.0225080	-0.8458670	1.0240730
H	3.5790120	-1.8767190	1.0916430
H	3.6064800	-0.3136500	1.9391000
O	3.9599150	1.1500160	-0.3168630
H	3.2213780	1.7760430	-0.3320080
O	1.3171760	-1.2597610	-0.2247660
H	0.3174100	-1.1628870	-0.2252970

Cartesian coordinates for D2 calculated at the B3LYP-D3BJ/def2-TZVPD level of theory.

C	-1.8785700	-0.0672570	0.1618160
O	-1.2490110	-1.1101920	0.0533910
C	-3.3855880	-0.0577570	0.3709840
H	-3.5176110	-0.3985300	1.4100470
C	-4.0865080	-1.0366400	-0.5574240
H	-5.1532360	-1.0330270	-0.3378660
H	-3.6942750	-2.0421690	-0.4184780
H	-3.9453700	-0.7374780	-1.5964230
O	-3.9607750	1.2215650	0.2028620
H	-3.3135940	1.8934400	0.4486780
O	-1.3324150	1.1296880	0.1619850
H	-0.3317640	1.0728850	0.0636610
C	1.9001950	-0.0863490	-0.2022330
O	1.2786750	0.9673850	-0.0893710
C	3.4094510	-0.0875890	-0.3470340
H	3.6282730	-0.6117910	-1.2857740
C	4.0732410	-0.8392230	0.8059700
H	5.1536450	-0.7961830	0.6749590
H	3.7569090	-1.8814820	0.8248890
H	3.8232100	-0.3693710	1.7582270
O	3.8979940	1.2322830	-0.4278200
H	3.1406280	1.8299260	-0.3454810
O	1.3540210	-1.2735530	-0.2109870
H	0.3519540	-1.2147440	-0.1093900

Cartesian coordinates for D3 calculated at the B3LYP-D3BJ/def2-TZVPD level of theory.

C	1.8836530	-0.1953540	-0.1981710
O	1.2199680	-1.2214140	-0.1418040
C	3.3993050	-0.2270140	-0.2906880
H	3.6565260	-1.0653320	-0.9387310
C	3.9752690	-0.4689450	1.1078090
H	5.0608270	-0.5228680	1.0371830
H	3.5976890	-1.4021360	1.5269790
H	3.7107900	0.3514190	1.7779220
O	3.9341290	0.9301240	-0.9001720
H	3.4740940	1.7049290	-0.5538460
O	1.3830810	1.0188660	-0.1296540
H	0.3821980	0.9944160	-0.0254150
C	-1.8890510	-0.1002000	0.1984090
O	-1.2311120	0.9362300	0.1495340
C	-3.3974370	-0.0573480	0.3457660
H	-3.6372470	-0.6396240	1.2440130
C	-4.0854920	-0.6987610	-0.8587210
H	-5.1639170	-0.6268620	-0.7240090
H	-3.8063580	-1.7474900	-0.9540050
H	-3.8170170	-0.1699370	-1.7743250
O	-3.8373050	1.2701920	0.5242000
H	-3.0606810	1.8453590	0.4634310
O	-1.3853350	-1.3041230	0.1313360
H	-0.3817880	-1.2751390	0.0268520

Cartesian coordinates for D4 calculated at the B3LYP-D3BJ/def2-TZVPD level of theory.

C	1.8896420	-0.0509930	-0.1881680
O	1.2271070	-1.0808180	-0.1934560
C	3.4095580	-0.0802920	-0.2452860
H	3.6370160	-0.3932120	-1.2764350
C	3.9865280	-1.1077300	0.7158610
H	5.0698990	-1.1279340	0.6060130
H	3.5852350	-2.0967920	0.5036160
H	3.7475170	-0.8371220	1.7447500
O	3.9982000	1.1761350	0.0206060
H	3.3841550	1.8728030	-0.2410950
O	1.3773750	1.1580550	-0.1829940
H	0.3653450	1.1299560	-0.1860710
C	-1.8896160	0.0509950	-0.1878890
O	-1.2270810	1.0808190	-0.1933250
C	-3.4095270	0.0802900	-0.2452450
H	-3.6368620	0.3932110	-1.2764230
C	-3.9866260	1.1077260	0.7158220
H	-5.0699820	1.1279180	0.6058310
H	-3.5853120	2.0967900	0.5036250
H	-3.7477450	0.8371220	1.7447430
O	-3.9982090	-1.1761340	0.0205770
H	-3.3841250	-1.8728090	-0.2410130
O	-1.3773410	-1.1580510	-0.1829130
H	-0.3653090	-1.1299570	-0.1860670

Cartesian coordinates for D5 calculated at the B3LYP-D3BJ/def2-TZVPD level of theory.

C	1.8804960	-0.1840670	-0.2181720
O	1.1503040	-1.1671110	-0.2136110
C	3.3920750	-0.3156500	-0.1540260
H	3.6593890	-1.1703670	-0.7765060
C	3.8033820	-0.5938870	1.2950760
H	4.8847420	-0.7171480	1.3368270
H	3.3255840	-1.5008600	1.6667610
H	3.5242330	0.2423780	1.9389900
O	4.0624200	0.8045120	-0.6951130
H	3.5885510	1.6044490	-0.4352120
O	1.4557700	1.0580610	-0.2219610
H	0.4448140	1.1032190	-0.2222570
C	-1.8805000	0.1840670	-0.2182300
O	-1.1503090	1.1671110	-0.2136480
C	-3.3920790	0.3156500	-0.1540360
H	-3.6594080	1.1703720	-0.7765010
C	-3.8033470	0.5938790	1.2950800
H	-4.8847050	0.7171440	1.3368630
H	-3.3255360	1.5008470	1.6667590
H	-3.5241830	-0.2423920	1.9389810
O	-4.0624460	-0.8045010	-0.6951160
H	-3.5885720	-1.6044440	-0.4352400
O	-1.4557710	-1.0580610	-0.2219720
H	-0.4448120	-1.1032330	-0.2222350

Cartesian coordinates for D6 calculated at the B3LYP-D3BJ/def2-TZVPD level of theory.

C	-1.8756390	0.0610930	-0.1885690
O	-1.1785120	1.0663750	-0.1370260
C	-3.3939810	0.1443930	-0.2407630
H	-3.6112570	0.5105610	-1.2565240
C	-3.9362670	1.1459260	0.7664080
H	-5.0182610	1.2081630	0.6587720
H	-3.5012870	2.1293020	0.5989490
H	-3.7071570	0.8209000	1.7817290
O	-4.0240440	-1.1024540	-0.0298600
H	-3.4390760	-1.8057940	-0.3365420
O	-1.4051650	-1.1631320	-0.2539040
H	-0.3925920	-1.1701440	-0.2610700
C	1.8970530	-0.1729710	-0.2233490
O	1.2005960	-1.1789480	-0.2764630
C	3.4122820	-0.2565190	-0.1652150
H	3.7078240	-1.0686650	-0.8303150
C	3.8341830	-0.5938440	1.2681620
H	4.9190740	-0.6831820	1.3043070
H	3.3870630	-1.5337150	1.5933610
H	3.5279120	0.1988870	1.9534860
O	4.0432990	0.9114690	-0.6494300
H	3.5535660	1.6815480	-0.3345650
O	1.4300650	1.0519640	-0.1557220
H	0.4184850	1.0614910	-0.1523900

Cartesian coordinates for T1 calculated at the B3LYP-D3BJ/def2-TZVPD level of theory.

C	0.3163530	1.8576500	-0.2927140
O	0.1813010	0.6389660	-0.4202980
O	1.4779870	2.4338600	-0.1293860
H	2.2270830	1.7644150	-0.0994640
C	-0.8524860	2.8326010	-0.2782220
C	-1.1275280	3.2639900	1.1664130
H	-0.5295770	3.7014330	-0.8564930
H	-1.9303600	4.0001810	1.1643210
H	-1.4444960	2.4076230	1.7642170
H	-0.2413710	3.7060150	1.6212650
O	-1.9786120	2.3079360	-0.9198340
H	-2.4491220	1.6987790	-0.3197190
C	3.3307490	-0.5218900	-0.1965890
O	3.4564740	0.6888420	-0.0467020
O	2.1865140	-1.1262830	-0.4061310
H	1.4357620	-0.4662840	-0.4189420
C	4.5287200	-1.4481800	-0.1510810
C	4.3985290	-2.4622220	0.9848630
H	4.5387720	-1.9855930	-1.1077180
H	5.2888800	-3.0893160	0.9954930
H	4.3276930	-1.9489640	1.9447960
H	3.5201930	-3.0917120	0.8470600
O	5.7201020	-0.7064960	-0.0226200
H	5.4808550	0.2301100	0.0300080
C	-2.9694770	-0.8084330	0.1387210
O	-3.2176070	0.3019180	0.5794510
O	-1.8605940	-1.1260010	-0.4987190
H	-1.2342860	-0.3579590	-0.5320720
C	-3.9453790	-1.9608100	0.2817340
C	-4.4195730	-2.4502720	-1.0864960
H	-3.4058610	-2.7727990	0.7837510
H	-5.1413030	-3.2528880	-0.9401770
H	-4.9096720	-1.6407630	-1.6292140
H	-3.5844540	-2.8242210	-1.6780290
O	-5.0380000	-1.5708280	1.0833480
H	-4.9286940	-0.6279870	1.2782520

Cartesian coordinates for T2 calculated at the B3LYP-D3BJ/def2-TZVPD level of theory.

C	3.0643520	-0.6223450	-0.1706790
O	3.1653880	0.4884750	-0.6806250
O	1.9862260	-1.0657860	0.4287650
H	1.2647200	-0.3733720	0.4153250
C	4.2169990	-1.6052450	-0.1934570
C	4.6699640	-1.9548540	1.2238100
H	3.8387990	-2.5131220	-0.6798140
H	5.5124090	-2.6421220	1.1604340
H	4.9972730	-1.0567890	1.7494200
H	3.8649980	-2.4276220	1.7853110
O	5.2898750	-1.0886190	-0.9471420
H	5.0414500	-0.2015490	-1.2449000
C	0.1678080	1.8975100	-0.1306080
O	0.0622670	0.7821870	0.3818280
O	1.2569960	2.3113870	-0.7233450
H	1.9794890	1.6131600	-0.7048480

C	-0.9580390	2.9239430	-0.1414010
C	-0.5341180	4.1773450	0.6205720
H	-1.1075130	3.1847040	-1.1982800
H	-1.3390330	4.9082310	0.5632470
H	-0.3643100	3.9340870	1.6702270
H	0.3728280	4.6058150	0.1986980
O	-2.1295070	2.4304060	0.4399120
H	-2.5073760	1.7133570	-0.1034340
C	-2.9977830	-0.7969900	0.1091790
O	-3.1568200	0.1091260	-0.6923520
O	-2.0122890	-0.8540090	0.9834030
H	-1.3817670	-0.1020470	0.8505660
C	-3.9475940	-1.9774500	0.1802940
C	-3.2271210	-3.2894990	-0.1255150
H	-4.3264010	-2.0106440	1.2095050
H	-3.9509030	-4.1029070	-0.0934430
H	-2.7900850	-3.2575630	-1.1246160
H	-2.4416100	-3.4819050	0.6045210
O	-5.0264100	-1.7834290	-0.7064760
H	-4.8756020	-0.9421050	-1.1628300

Cartesian coordinates for T3 calculated at the B3LYP-D3BJ/def2-TZVPD level of theory.

C	0.5223400	2.1529460	-0.2219090
O	0.1564300	1.4048420	0.6772090
C	0.2304760	3.6418080	-0.1971240
H	-0.1704030	3.9149180	-1.1769360
C	1.5225630	4.4245350	0.0540590
H	1.2866690	5.4871280	0.0902390
H	2.2480250	4.2455720	-0.7392970
H	1.9621720	4.1356770	1.0103550
O	-0.7571460	3.9351650	0.7661050
H	-0.7330150	3.2361550	1.4344450
O	1.2191510	1.7670600	-1.2599070
H	1.4549790	0.7975640	-1.1960850
C	1.9624610	-1.6458350	-0.3148780
O	2.1401220	-0.6892720	-1.0564650
C	3.1287810	-2.4794260	0.1825640
H	2.9363970	-3.5091880	-0.1439160
C	3.2159980	-2.4502780	1.7076410
H	4.0838130	-3.0303370	2.0187300
H	2.3207420	-2.8776700	2.1575330
H	3.3416330	-1.4257670	2.0604920
O	4.3340510	-2.0257270	-0.3906380
H	4.1167080	-1.2862120	-0.9769240
O	0.7972890	-2.0578010	0.1177430
H	0.0344940	-1.5318340	-0.2445020
O	-1.5277080	-1.1010180	-0.7274970
C	-2.4373510	-0.6093910	-0.0746040
O	-2.2809040	0.3360580	0.8242470
H	-1.3439200	0.6630560	0.8343530
C	-3.8751540	-1.0546490	-0.2579640
H	-4.4361000	-0.1619800	-0.5638180
O	-3.9588600	-2.0302430	-1.2715410
C	-4.4646040	-1.5862260	1.0471530
H	-4.4779730	-0.8119010	1.8131380

H	-5.4843540	-1.9191730	0.8587450
H	-3.8851430	-2.4380680	1.4055190
H	-3.0671890	-2.1613610	-1.6257590

Cartesian coordinates for T4 calculated at the B3LYP-D3BJ/def2-TZVPD level of theory.

C	3.2100640	-0.4278220	-0.2095180
O	3.2087750	0.7525590	-0.5460270
O	2.1563570	-1.0870190	0.1978170
H	1.3435380	-0.4997550	0.2047710
C	4.4852020	-1.2475160	-0.2423780
C	4.8459780	-1.7620240	1.1503680
H	4.2839010	-2.1047470	-0.8968670
H	5.7768340	-2.3238510	1.0852320
H	4.9954940	-0.9265790	1.8357840
H	4.0629230	-2.4113670	1.5400910
O	5.5430700	-0.4885160	-0.7836340
H	5.1966600	0.3940360	-0.9808990
C	0.0142920	1.6719180	-0.1291430
O	0.0263160	0.4970040	0.2202040
O	1.0748670	2.3161690	-0.5555950
H	1.8847530	1.7234570	-0.5514570
C	-1.2435560	2.5311400	-0.1154010
C	-1.0963370	3.6658700	0.8939250
H	-1.3250600	2.9596640	-1.1234590
H	-1.9928420	4.2833980	0.8624980
H	-0.9936390	3.2574980	1.9002520
H	-0.2279860	4.2810330	0.6657230
O	-2.3835950	1.7897300	0.2197300
H	-2.5512190	1.0988480	-0.4468580
C	-3.5731770	-1.3218620	-0.7810250
O	-3.1471040	-0.3610230	-1.3819380
O	-4.6130320	-2.0404710	-1.2319220
H	-4.9262820	-1.6276330	-2.0535300
C	-3.0463570	-1.8303550	0.5545990
C	-3.7461890	-1.0747140	1.6885840
H	-3.2908910	-2.8912300	0.6179000
H	-3.3969240	-1.4745960	2.6400570
H	-3.5042110	-0.0122440	1.6427940
H	-4.8295460	-1.1960370	1.6331420
O	-1.6479020	-1.7452510	0.6142120
H	-1.3470220	-0.8231450	0.5419780

Cartesian coordinates for T5 calculated at the B3LYP-D3BJ/def2-TZVPD level of theory.

C	0.4165680	-2.0846630	-0.3954520
O	0.3331890	-0.8660820	-0.4144040
O	-0.6288080	-2.8825160	-0.4780540
H	-1.4632760	-2.3470720	-0.4506880
C	1.7391400	-2.8108070	-0.2157090
C	1.9029710	-3.1695690	1.2661020
H	1.6975620	-3.7258760	-0.8087040
H	2.8396360	-3.7103270	1.3952650
H	1.9408220	-2.2615810	1.8711990
H	1.0798420	-3.7941860	1.6152240
O	2.8128640	-2.0568510	-0.7124190
H	2.8475610	-1.1962320	-0.2623050

C	2.5539240	1.6412570	-0.0586710
O	3.0140710	0.6244870	0.3997150
O	3.2071250	2.3862320	-0.9691540
H	4.0482240	1.9423470	-1.1628600
C	1.1863980	2.2239470	0.2745480
C	1.2967320	3.6326120	0.8438280
H	0.6423290	2.2624010	-0.6801810
H	0.2956970	4.0055150	1.0577990
H	1.8652920	3.6189210	1.7743970
H	1.7815870	4.3021930	0.1359180
O	0.5074710	1.4197020	1.2054950
H	0.5394400	0.5063870	0.8800790
C	-3.2071740	-0.3368540	0.2827630
O	-2.8835590	-1.4742160	0.0162210
O	-4.1479950	-0.0776460	1.2026110
H	-4.4475120	-0.9259080	1.5677200
C	-2.6036180	0.9311470	-0.3099950
C	-3.6753540	1.9137950	-0.7668200
H	-2.0299730	1.3796290	0.5155250
H	-3.1845660	2.8043850	-1.1564890
H	-4.2732500	1.4743610	-1.5662030
H	-4.3293500	2.1966140	0.0553030
O	-1.7736530	0.6442970	-1.4001930
H	-1.0332150	0.0839870	-1.1031110

Cartesian coordinates for T6 calculated at the B3LYP-D3BJ/def2-TZVPD level of theory.

C	0.2351500	1.9716760	-0.2232080
O	0.0867810	0.7709820	-0.4614130
O	1.3987130	2.5085610	0.0347950
H	2.1343850	1.8245940	0.0353350
C	-0.9181840	2.9635180	-0.1701780
C	-1.2467540	3.2709610	1.2952350
H	-0.5564200	3.8736760	-0.6545050
H	-2.0361930	4.0208700	1.3255480
H	-1.6047380	2.3719650	1.7998340
H	-0.3734170	3.6525760	1.8237590
O	-2.0231400	2.5192810	-0.9009110
H	-2.5308100	1.8702330	-0.3754620
C	3.2004000	-0.4710060	-0.2138390
O	3.3438410	0.7195310	0.0426660
O	2.0533870	-1.0290240	-0.5170640
H	1.3174320	-0.3515730	-0.5040450
C	4.3773030	-1.4251180	-0.2020510
C	4.1809320	-2.5309800	0.8342470
H	4.4165870	-1.8773550	-1.2011350
H	5.0581090	-3.1764020	0.8253280
H	4.0797590	-2.1017640	1.8319850
H	3.2975380	-3.1264020	0.6066160
O	5.5762930	-0.7250140	0.0387990
H	5.3538530	0.2097020	0.1575830
C	-3.1078630	-0.6428260	-0.0966200
O	-3.3498230	0.4425840	0.3930350
O	-1.9804110	-0.9394560	-0.7296620
H	-1.3415390	-0.1817140	-0.6992320
C	-4.0541550	-1.8265000	0.0174040

C	-3.9117540	-2.4408450	1.4129600
H	-5.0635340	-1.4313680	-0.1024940
H	-4.6129960	-3.2689350	1.5079520
H	-2.9001810	-2.8243480	1.5603990
H	-4.1251090	-1.7010980	2.1852150
O	-3.8703420	-2.7834400	-1.0077960
H	-2.9255720	-2.8679800	-1.1859730

Cartesian coordinates for T7 calculated at the B3LYP-D3BJ/def2-TZVPD level of theory.

C	0.2736720	1.9475150	-0.2353270
O	0.1326210	0.7464290	-0.4757690
O	1.4317720	2.4887060	0.0369900
H	2.1700660	1.8071150	0.0479820
C	-0.8838700	2.9351160	-0.1966470
C	-1.2276030	3.2469130	1.2642930
H	-0.5213870	3.8447780	-0.6813670
H	-2.0202390	3.9938000	1.2843190
H	-1.5864830	2.3484380	1.7691810
H	-0.3607850	3.6340290	1.7994340
O	-1.9807240	2.4834320	-0.9357360
H	-2.4886850	1.8329880	-0.4119920
C	3.2491890	-0.4824160	-0.1854190
O	3.3825760	0.7089400	0.0733310
O	2.1101250	-1.0463260	-0.5065290
H	1.3699950	-0.3740150	-0.5015500
C	4.4301710	-1.4308260	-0.1539840
C	4.2259980	-2.5290350	0.8891990
H	4.4830160	-1.8908490	-1.1486930
H	5.1053560	-3.1715150	0.8950540
H	4.1124840	-2.0920420	1.8822200
H	3.3469540	-3.1291640	0.6571100
O	5.6234720	-0.7231320	0.0936150
H	5.3937360	0.2092690	0.2165170
C	-3.0611450	-0.6779920	-0.1459370
O	-3.3079840	0.4048720	0.3472260
O	-1.9251170	-0.9674180	-0.7667270
H	-1.2873110	-0.2089640	-0.7215980
C	-4.0621240	-1.8257230	-0.1672820
C	-4.8104100	-1.9411380	1.1495910
H	-4.7764360	-1.5489190	-0.9586690
H	-5.5530680	-2.7339240	1.0703720
H	-4.1193910	-2.1920240	1.9549650
H	-5.3087420	-1.0035090	1.3875910
O	-3.4703060	-3.0758850	-0.4639810
H	-2.7338420	-2.9369150	-1.0711480

Cartesian coordinates for Te1 calculated at the B3LYP-D3BJ/def2-TZVPD level of theory.

C	1.2182460	-1.5045840	-0.7057630
O	1.6211740	-0.3408110	-0.6794160
O	-0.0523670	-1.8163030	-0.7466730
H	-0.6306020	-1.0002200	-0.7278280
C	2.1394420	-2.7148010	-0.6622650
C	2.1071390	-3.3187720	0.7460680
H	1.7258360	-3.4359680	-1.3711870
H	2.7284840	-4.2133270	0.7560930
H	2.5088670	-2.6098440	1.4721350
H	1.0919820	-3.5882580	1.0365380
O	3.4301510	-2.4030280	-1.0988140
H	3.9279490	-1.9683160	-0.3804110
C	-1.2182320	1.5046070	-0.7057590
O	-1.6211620	0.3408340	-0.6794580
O	0.0523830	1.8163220	-0.7466240
H	0.6306130	1.0002360	-0.7277800
C	-2.1394260	2.7148270	-0.6622520
C	-2.1071500	3.3187640	0.7460960
H	-1.7258010	3.4360090	-1.3711480
H	-2.7284900	4.2133230	0.7561290
H	-2.5088980	2.6098220	1.4721370
H	-1.0919980	3.5882380	1.0365940
O	-3.4301280	2.4030740	-1.0988360
H	-3.9279480	1.9683560	-0.3804510
C	4.8938840	0.3093380	0.4302030
O	4.8316720	-0.8630240	0.7621020
O	3.9849080	0.9255530	-0.2992940
H	3.2238760	0.3248520	-0.5025260
C	6.0593870	1.1930180	0.8312790
C	6.8270260	1.6779560	-0.3985330
H	5.6357650	2.0599820	1.3520960
H	7.6725620	2.2798540	-0.0680510
H	7.2095890	0.8281460	-0.9655360
H	6.1893660	2.2815400	-1.0437130
O	6.9104320	0.4977540	1.7147370
H	6.5786230	-0.4102820	1.7788570
C	-4.8939180	-0.3093350	0.4300120
O	-4.8316900	0.8630040	0.7619900
O	-3.9849110	-0.9255350	-0.2994590
H	-3.2238710	-0.3248280	-0.5026440
C	-6.0593870	-1.1930510	0.8311080
C	-6.8270480	-1.6779800	-0.3986930
H	-5.6357360	-2.0600170	1.3518990
H	-7.6725660	-2.2798970	-0.0681970
H	-7.2096390	-0.8281670	-0.9656710
H	-6.1893940	-2.2815430	-1.0438980
O	-6.9104250	-0.4978190	1.7145990
H	-6.5786380	0.4102250	1.7787190

Cartesian coordinates for Te2 calculated at the B3LYP-D3BJ/def2-TZVPD level of theory.

C	-0.9992480	-1.4746090	-0.2091470
O	-1.4114380	-0.3654180	0.1333740

O	0.2306880	-1.6852210	-0.6041330
H	0.7640460	-0.8383900	-0.6088560
C	-1.8709860	-2.7211980	-0.2450730
C	-2.2568300	-3.0208770	-1.6978060
H	-1.2508680	-3.5357660	0.1365210
H	-2.8373060	-3.9422360	-1.7214140
H	-2.8710960	-2.2140530	-2.1012850
H	-1.3730900	-3.1417920	-2.3238760
O	-2.9737260	-2.6103570	0.6066770
H	-3.6731230	-2.0813030	0.1778690
C	1.2775710	1.6547930	-0.2491890
O	1.6795740	0.5509460	-0.6171090
O	0.0582740	1.8611100	0.1809540
H	-0.4813150	1.0191640	0.1646260
C	2.1452870	2.9063450	-0.2421190
C	1.5542690	3.9616980	-1.1741410
H	2.1081240	3.2830770	0.7894800
H	2.1704760	4.8575390	-1.1194090
H	1.5665740	3.5978720	-2.2023470
H	0.5329790	4.2088180	-0.8912400
O	3.4554020	2.6416290	-0.6496390
H	3.9132340	2.0823390	0.0062410
C	-4.8777170	0.2285820	0.1861870
O	-4.9002040	-0.8490170	-0.3853730
O	-3.8004730	0.7608530	0.7287560
H	-3.0040770	0.1933720	0.5703160
C	-6.1236980	1.0801090	0.3362840
C	-6.4896280	1.2605170	1.8094780
H	-5.8915460	2.0606570	-0.0962060
H	-7.4049370	1.8475350	1.8730450
H	-6.6687650	0.2911480	2.2766530
H	-5.6959050	1.7770110	2.3483650
O	-7.1917870	0.5032020	-0.3809710
H	-6.8800460	-0.3461390	-0.7276250
C	4.9547460	-0.2603410	0.1487090
O	4.8129820	0.7329290	0.8428700
O	4.1231240	-0.6248620	-0.8081860
H	3.3362870	-0.0257840	-0.8342390
C	6.1347510	-1.1969140	0.3228360
C	5.6761250	-2.5993110	0.7196590
H	6.6376140	-1.2488510	-0.6509180
H	6.5542080	-3.2276020	0.8634570
H	5.1208000	-2.5648430	1.6580700
H	5.0470540	-3.0372710	-0.0546010
O	7.0285450	-0.6754120	1.2802830
H	6.6451500	0.1496880	1.6132820

Cartesian coordinates for Te₃ calculated at the B3LYP-D3BJ/def2-TZVPD level of theory.

C	-1.2153820	-1.5038480	-1.1127700
O	-1.6176430	-0.3403450	-1.1046990
O	0.0556360	-1.8176310	-1.1218870
H	0.6329280	-1.0002520	-1.1193900
C	-2.1407220	-2.7134860	-1.1067340
C	-1.9395620	-3.5346310	-2.3783860
H	-1.8305290	-3.3164300	-0.2420700

H	-2.5818190	-4.4124010	-2.3302650
H	-2.2267380	-2.9454450	-3.2502270
H	-0.9036310	-3.8512090	-2.4824620
O	-3.4868400	-2.3472160	-1.0261590
H	-3.6814450	-1.9441850	-0.1588490
C	1.2153970	1.5042000	-1.1123080
O	1.6176560	0.3406940	-1.1046030
O	-0.0556210	1.8179880	-1.1213290
H	-0.6329150	1.0006120	-1.1190690
C	2.1407360	2.7138360	-1.1058870
C	1.9395830	3.5353860	-2.3772790
H	1.8305420	3.3165050	-0.2410330
H	2.5818370	4.4131420	-2.3288750
H	2.2267640	2.9464770	-3.2493060
H	0.9036510	3.8519950	-2.4812590
O	3.4868540	2.3475400	-1.0254230
H	3.6814530	1.9442370	-0.1582390
C	4.4317650	-0.3199060	0.7928790
O	4.1697890	0.8061840	1.1826590
O	3.8997080	-0.8803850	-0.2761550
H	3.2092400	-0.2925700	-0.6718660
C	5.4239950	-1.2077140	1.5190830
C	4.7558520	-2.4812450	2.0350230
H	6.1923200	-1.4810200	0.7849900
H	5.4957110	-3.0714390	2.5742380
H	3.9468610	-2.2323850	2.7233750
H	4.3581720	-3.0736730	1.2116800
O	6.0242240	-0.4963740	2.5778920
H	5.6290410	0.3881010	2.5915820
O	-3.8996930	0.8804740	-0.2758690
H	-3.2092250	0.2927800	-0.6717630
C	-4.4317460	0.3196660	0.7929940
O	-4.1697980	-0.8065580	1.1824080
C	-5.4240110	1.2072330	1.5194440
H	-6.1923120	1.4807730	0.7854130
C	-4.7558940	2.4805990	2.0358210
O	-6.0242740	0.4955460	2.5780010
H	-4.3581890	3.0732970	1.2126840
H	-5.4957750	3.0706130	2.5752020
H	-3.9469250	2.2315200	2.7241200
H	-5.6290730	-0.3889250	2.5914320

Cartesian coordinates for Te4 calculated at the B3LYP-D3BJ/def2-TZVPD level of theory.

C	1.2811630	1.7894530	-0.4485110
O	1.6328590	0.6699180	-0.8248650
O	0.0333150	2.1165550	-0.2453170
H	-0.5882680	1.3507850	-0.4313640
C	2.2588520	2.9236270	-0.1668250
C	1.9808670	4.1018960	-1.0968990
H	2.0574570	3.2334730	0.8679360
H	2.6640380	4.9119410	-0.8467320
H	2.1598340	3.8080260	-2.1320310
H	0.9550350	4.4497140	-0.9934130
O	3.5898710	2.5309610	-0.3386340
H	3.8442620	1.8739640	0.3361870

C	-1.2747410	-1.0198950	-1.1045540
O	-1.6122930	0.1021660	-0.7471500
O	-0.0247250	-1.3717930	-1.3058290
H	0.5912430	-0.6048540	-1.1313010
C	-2.2642130	-2.1494490	-1.3564290
C	-2.2538190	-2.5386980	-2.8319110
H	-1.9065240	-3.0003500	-0.7610730
H	-2.9440440	-3.3676500	-2.9812720
H	-2.5876940	-1.6973980	-3.4406850
H	-1.2572180	-2.8392320	-3.1498210
O	-3.5707860	-1.7900450	-1.0043010
H	-3.6304280	-1.6135290	-0.0474180
C	-4.8906440	-0.1914500	1.7936750
O	-4.1069610	-1.1018140	1.6404640
O	-5.8024250	-0.1943330	2.7776900
H	-5.7113970	-1.0287950	3.2666520
C	-4.9932100	1.0408330	0.9043960
C	-5.9037740	0.7243860	-0.2858690
H	-5.4371660	1.8375060	1.5021210
H	-6.0072350	1.6231650	-0.8929980
H	-5.4678670	-0.0658400	-0.8983310
H	-6.8943160	0.4103700	0.0482070
O	-3.7231340	1.4976420	0.5225140
H	-3.2508710	0.8282810	-0.0011420
C	4.5883170	-0.5819730	0.4379890
O	4.4272090	0.3637470	1.1920420
O	3.9127360	-0.7697670	-0.6779800
H	3.2067210	-0.0817180	-0.7824510
C	5.6143310	-1.6630040	0.7211690
C	4.9497900	-3.0279570	0.8921120
H	6.2798120	-1.6973380	-0.1504340
H	5.7172160	-3.7657390	1.1231000
H	4.2382470	-3.0016450	1.7187090
H	4.4313300	-3.3253930	-0.0188000
O	6.3652350	-1.3274940	1.8665910
H	6.0131150	-0.4903030	2.2044950

Cartesian coordinates for Te5 calculated at the B3LYP-D3BJ/def2-TZVPD level of theory.

C	-1.3504500	-1.3648870	-0.5609900
O	-1.6358220	-0.1724960	-0.5781920
O	-0.1215580	-1.8209070	-0.5441530
H	0.5441650	-1.0720370	-0.5530730
C	-2.3976910	-2.4711470	-0.5496430
C	-2.3016280	-3.3037800	-1.8243520
H	-2.1504120	-3.1078980	0.3105330
H	-3.0370020	-4.1057650	-1.7775190
H	-2.5240080	-2.6817680	-2.6925380
H	-1.3076910	-3.7329190	-1.9353160
O	-3.6999360	-1.9633670	-0.4529260
H	-3.8181280	-1.4799800	0.3846540
C	1.3504640	1.3649400	-0.5607820
O	1.6358400	0.1725510	-0.5781060
O	0.1215720	1.8209560	-0.5439330
H	-0.5441510	1.0720880	-0.5529760
C	2.3977030	2.4712020	-0.5492770

C	2.3016710	3.3039860	-1.8238890
H	2.1503990	3.1078500	0.3109680
H	3.0370410	4.1059680	-1.7769410
H	2.5240760	2.6820790	-2.6921440
H	1.3077350	3.7331350	-1.9348290
O	3.6999460	1.9634150	-0.4525870
H	3.8181220	1.4799410	0.3849440
C	5.1667990	-0.5171300	1.4906870
O	4.4413510	0.4165650	1.7495990
O	6.1955060	-0.8609020	2.2821460
H	6.2296250	-0.2263410	3.0167840
C	5.0626970	-1.3978450	0.2523740
C	5.8469770	-0.7470530	-0.8914700
H	5.5110060	-2.3606860	0.5001310
H	5.8046970	-1.4042950	-1.7595130
H	5.4052460	0.2145300	-1.1554180
H	6.8923490	-0.5954870	-0.6162480
O	3.7245090	-1.6596030	-0.0737540
H	3.2462550	-0.8399860	-0.2886380
C	-5.1668380	0.5169720	1.4905700
O	-4.4414010	-0.4167520	1.7494050
O	-6.1955720	0.8606600	2.2820320
H	-6.2297160	0.2260200	3.0166000
C	-5.0626970	1.3978200	0.2523560
C	-5.8469490	0.7471550	-0.8915810
H	-5.5110080	2.3606360	0.5002040
H	-5.8046400	1.4044900	-1.7595530
H	-5.4052150	-0.2144020	-1.1556200
H	-6.8923290	0.5955660	-0.6164040
O	-3.7244990	1.6596070	-0.0737080
H	-3.2462420	0.8400110	-0.2886640